

The Voltammetry of Metallic Nanoparticle Arrays

Thesis submitted for D. Phil Physical & Theoretical Chemistry

Fallyn W. Campbell

Supervisor: Prof. R. G. Compton

September 2010

Contents

Abstract *7-8*
Acknowledgements *9*

Chapter 1 Introduction to Electrochemistry. *10-60*

1.1 Equilibrium

1.1.1 Chemical Equilibrium
1.1.2 Electrochemical Equilibrium
1.1.3 Electrode Potentials
1.1.4 The Nernst Equation
1.1.5 Standard and Formal Potentials

1.2 Electrochemical Cells

1.2.1 Types of Electrochemical Cell
1.2.2 Three Electrode Set – Up
1.2.3 Solvents and Supporting Electrolytes
1.2.4 Removal of Oxygen
1.2.5 Working Electrodes
1.2.6 Reference Electrodes

1.3 Faradaic and Non – Faradaic Processes

1.3.1 Electrode Processes
1.3.2 Currents & Reaction Fluxes

1.4 Mass Transfer

1.4.1 Migration
1.4.2 Diffusion
1.4.3 Convection
1.4.4 The Nernst Diffusion Layer

1.5 Electrode – Solution Interface

1.5.1 Electrical Double Layer
1.5.2 Need for Supporting Electrolyte

1.6 Electrode Kinetics

1.6.1 The Arrhenius equation
1.6.2 The Butler – Volmer Equation

1.6.3 The Tafel Law
1.6.4 Marcus Theory

1.7 Electrode Reaction Mechanisms

1.7.1 E Reaction
1.7.2 EC Reaction
1.7.3 CE Reaction
1.7.4 ECE Reaction
1.7.5 Catalytic Mechanism

1.8 Electro – analytical Techniques

1.8.1 Linear Sweep Voltammetry (LSV)
1.8.2 Cyclic Voltammetry (CV)
1.8.3 Chronoamperometry (CA)

Chapter 2 The Use of Nanoparticles in Electro – analysis: An Overview of Recent Literature. *61-114*

2.1 Introduction
2.2 Nanoparticles in Electro – analysis

2.2.1 Synthesis and Application of Silver Nanoparticles
2.2.2 Synthesis and Application of Gold Nanoparticles
2.2.3 Synthesis and Application of Platinum Nanoparticles
2.2.4 Synthesis and Application of Palladium Nanoparticles
2.2.5 Synthesis and Application of Ruthenium Nanoparticles
2.2.6 Synthesis and Application of Copper Nanoparticles
2.2.7 Synthesis and Application of Nickel Nanoparticles
2.2.8 *Synthesis of Some Less Common Nanoparticles*

2.3 Conclusions

Chapter 3 Voltammetry at Nanoparticle – Modified Electrodes: Theory. *115-129*

3.1 Isolated Spherical Particles
3.2 Diffusion Domain Approximation
3.3 Numerical Simulation
3.4 Categorizing Diffusional Behaviour
3.5 Simulation of Nanoparticle Arrays

Chapter 4 Experimental Methods *130-144*

4.1 Reagents & Materials
4.2 Solution Preparation
4.3 Synthesis of Nanoparticles

4.3.1 Colloidal Synthesis
4.3.2 Electroless Synthesis

4.4 Nanoparticle Characterisation

4.4.1 UV – vis Spectroscopy
4.4.2 Scanning Electron Microscopy

4.5 Electrochemical Experiments

4.5.1 Instrumentation
4.5.2 Working Electrodes
4.5.3 Reference Electrodes

4.6 Electrode Modification
4.7 Techniques

4.7.1 Scanning Electron Microscopy
4.7.2 UV – VIS Spectroscopy

Chapter 5 Hydrogen Peroxide Electro – Reduction at a Silver Nanoparticle Array: Investigating Nanoparticle Size & Coverage Effects. *145-161*

5.1 Introduction
5.2 Hydrogen Peroxide Reduction at Silver Nanoparticle Arrays
5.3 Results & Discussion
5.4 Conclusions

Chapter 6 The Hydrogen Evolution Reaction at a Silver Nanoparticle Array and Silver Macro – Electrode Compared: Changed Electrode Kinetics between Macro – and Nano – Scales. *162-185*

6.1 Introduction
6.2 Theory
6.3 Results & Discussion
6.4 Conclusions

Chapter 7 **Facile Method for the Construction of Random Nanoparticle Arrays on a Carbon Support for the Development of Well Defined Catalytic Surfaces.** *186-204*

7.1 Introduction
7.2 Results & Discussion

7.2.1 Electrode Characterisation
7.2.2 The Redox Behaviour of Ferro - / Ferricyanide at Platinum Nanoparticle Arrays
7.2.3 Proton Reduction at Platinum Nanoparticle Arrays
7.2.4 pH Determination
7.2.5 The Oxidation of Methanol at Platinum Nanoparticle Arrays

7.3 Conclusions

Chapter 8 **A Changed Electrode Mechanism between the Nano - and Macro – Scales: The Reduction of 4 – Nitrophenol in Aqueous Solution at Silver Electrode.** *205-222*

8.1 Introduction
8.2 Results & Discussion
8.3 Conclusions

Chapter 9 **Particle Size & Surface Coverage Effects in the Stripping Voltammetry of Silver Nanoparticles: Theory & Experiment.** *223-247*

9.1 Introduction
9.2 Theory

9.2.1 Introduction
9.2.2 Diffusion Domain Approximation
9.2.3 *Adapted "Thick Layer" Mathematical Model*

9.3 Results & Discussion

9.3.1 Experimental Results
9.3.2 Computation
9.3.3 Comparison of Theories
9.3.4 Electrochemically Irreversible Stripping
9.3.5 Comparison between Theory & Experiment

9.4 Conclusions

Chapter 10 **The Underpotential Deposition of Heavy Metals on Silver Nanoparticles: Size – Dependent Adsorption Behaviour.** *248-266*

10.1 Introduction
10.2 Results & Discussion

10.2.1 Thallium Underpotential Deposition
10.2.2 Lead Underpotential Deposition
10.2.3 Cadmium Underpotential Deposition

10.3 Conclusions

Chapter 11 **Conclusions** *267-268*

Glossary 269-271

Appendix 1 **Overview of Simulation Methods used to Model Nanoparticle Arrays.** *272-292*

Abstract

The experimental work discussed in this thesis examines the effect of voltammetry of nanoparticle arrays with a specific focus on the effect of nanoparticle size and surface coverage on the substrate electrode. These effects are investigated in relation to the reduction of hydrogen peroxide, 4-nitrophenol and the hydrogen evolution reaction. In each case, the experimental data obtained is subsequently fitted using numerical simulations to extract quantitative kinetic data.

Distinct differences are noted between macro – and nano – scale. The reduction of H_2O_2 reveals the absence of autocatalysis at the nano – scale. Furthermore, peak potential shifts positively with surface coverage under *Case 3* diffusion conditions. On the other hand, at essentially isolated particles (*Case 1*) E_p varies logarithmically with nanoparticle radius. By decreasing nanoparticle size, we promote convergent diffusion and enhance irreversibility of the process. The shift in E_p with surface coverage can be accounted for as the diffusion layers begin to overlap heavily, tending towards more macro – disk type behaviour.

We also study the hydrogen evolution reaction at an array of AgNPs. By fitting of the experimental data with numerical simulations we demonstrate altered kinetics between the macro – and nano – scale. Voltammetry at AgNP – arrays also display dependence between surface coverage and current. We attribute this to increased electro – active surface area and decrease in irreversibility of the process, with increasing surface coverage.

Numerical simulations are also used to fit experimental data obtained for the reduction of 4 – nitrophenol in acidic media. The AgNP – arrays exhibit significantly different electrode kinetics compared to a macro – disk. Examination of the data obtained for AgNP – arrays at two different acid concentrations implies the rate - determining step is likely the electron transfer process. We therefore infer a change in

the mechanism of the rate – determining step between macro – and nano – scale. An unusually low value of α at the NP – array may indicate that adsorption plays some role in the process.

Furthermore, we discuss the size – dependent adsorption behaviour exhibited by silver nanoparticle arrays, such that small particles with diameters below ~ 50 nm do not display the typical underpotential deposition characteristics of corresponding bulk materials or larger nanoparticles. This phenomenon is reported for the deposition of heavy metals (thallium, lead and cadmium) at silver nanoparticle arrays.

The stripping voltammetry of arrays of silver nanoparticles has also been investigated. The stripping peak potential is dependent on the degree of surface coverage. Modelling of this system has shown that a one – dimensional diffusion model is appropriate for high surface coverage; essentially it is experiencing planar diffusion. However, for an array of widely dispersed particles, the individual nanoparticle size and convergent diffusion begin to dominate behaviour.

A detailed overview of the literature is first discussed, relating to the synthesis of a wide variety of metallic nanoparticles and their practical applications, such as the determination of pH using platinum nanoparticles as covered in **Chapter 7**. We also discuss the fundamental principles governing the voltammetric behaviour of nanoparticles.

Acknowledgements

First of all I would like to thank my supervisor Professor Richard Compton for giving me the opportunity to work in his group and for his guidance, support and insight over the course of my D. Phil. I would also like to thank all the members of the RGC group for all their help and advice during my time here and for the constant stream of banter. In particular I would like to thank Dr. Ronan Baron for helping me get my research started and Dr. Neil Rees for his help on a great many subjects. I would also like to thank the EPSRC for funding and a CASE award.

I would like to say thank – you to Aoife and Kass thanks for making me smile and really think I've made some friends for life in you girls. Furthermore, could never have completed the world Pimm's drinking challenge without Aoife's assistance!! To my fellow countryman, Stephen for all his help on the simulation front and to Martin for providing a little ray of sunshine in all our lives and helping me win at tea on a daily basis!! I'd also like to say thanks to a great friend, Abigail Culshaw, thanks for Friday night cocktails, listening to me moan, globetrotting with me and for all the dancing fun. Thank – you to my other dancing girls Beckie, Lorna, Ali and Rodina…you are all brilliant!! A big shout out to Craig, Lyndsay and Pete thanks, for providing many memorable weekends in the city. Last but not least, thanks to Ewen for everything…could not have made it to the end without you….enough said.

To my parents, Lynn and Tony for their love and support (financial or otherwise), their exceptional removals service throughout my many years as a student and for giving me the space I needed to grown up. Thanks to Dad for his impromptu visits to Oxford and to Mum for listening when I need a friendly ear and for being the only person I can rely on to be awake after midnight for some chat. To my little sister Courtenay, thanks for the free haircuts, constant phone calls and general madness. To my little nephew Mason, you have no idea how much joy you bring to my life. I love you all and thanks for everything. I would also like to say thanks to my grandparents Addis and Lily, a true inspiration to me, who saw this process start but were sadly not here to see it completed, it would have made them incredibly proud.

Chapter 1

Introduction to Electrochemistry

This introductory chapter provides an outline of the fundamental principles underpinning the study of electrochemical processes. This chapter covers the basics of electrochemical equilibrium, electrochemical cells, electrode potentials, kinetics and commonly used electro – analytical techniques.

1.1 Equilibrium

1.1.1 Chemical Equilibrium

Thermodynamics predicts the direction but not the rate of a chemical process. Under equilibrium the Gibbs free energy of a system (G_{sys}) will be minimized, at constant temperature and pressure (**Equation 1.1**).

$$\partial G_{sys} = 0 \qquad [\mathbf{1.1}]$$

The standard Gibbs free energy change associated with a reaction can be expressed in terms of the equilibrium constant (K).

$$\Delta G^0 = -RT \ln K \qquad [\mathbf{1.2}]$$

Depending on the nature of the system, the equilibrium constant can be expressed in terms of the partial pressures or concentrations of the species at equilibrium. For the general reaction shown in **Equation 1.3**, K_p and K_c can be expressed as follows.

$$aA + bB + ... \rightleftharpoons xX + yY + ... \qquad [1.3]$$

$$K_p = \frac{p_X^x p_Y^y}{p_A^a p_B^b}$$

$$K_c = \frac{[X]^x [Y]^y}{[A]^a [B]^b} \qquad [1.4]$$

1.1.2 Electrochemical Equilibrium

An electrochemical equilibrium can be established by inserting an electrode into a solution of ions (*e.g.* Fe^{3+} / Fe^{2+}) as shown in the example given below (**Equation 1.5**). The equilibrium established at the electrode surface involves the two dissolved ions and the electrons in the metal electrode.

$$Fe(CN)_{6\ (aq)}^{3-} + e^- \rightleftharpoons Fe(CN)_{6\ (aq)}^{4-} \qquad [1.5]$$

Under equilibrium conditions, the rate at which the Fe^{3+} gains electrons from the metal electrode is equal to the rate at which Fe^{2+} gives up electrons. Once a dynamic equilibrium is established no further changes occur and the concentration of Fe^{3+} and Fe^{2+} will not be significantly changed from their values before the introduction of the electrode into the solution. Changes in the electron energies are shown as a function of the equilibrium, by the energy level diagram in **Figure 1.1**.

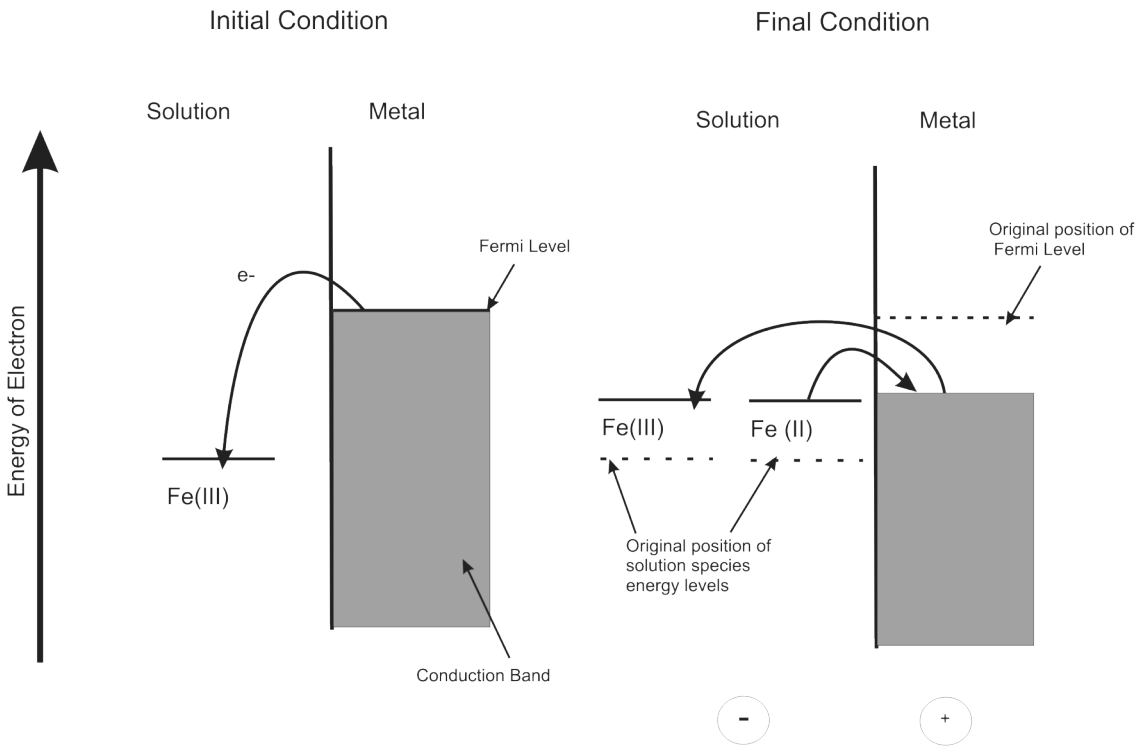


Figure 1.1

Energy level diagram showing the energies of the electrons in the solution phase species and metal electrode, before and after establishment of equilibrium[1].

Electrochemical equilibrium is significantly different from chemical equilibrium. The essential feature of electrochemical equilibrium is that it involves two separate phases (*i.e.* electrode and solution). Another important difference is that electrochemical equilibrium involves the transfer of a charged particle (*i.e.* electron) between the two phases. A net electrical charge exists on each of these two phases at equilibrium. This complicates matters as it becomes necessary to consider both the chemical energy and the electrical energy differences between the reactants and products. This will be discussed further in **Section 1.1.4**.

1.1.3 Electrode Potentials

The electrode potential is defined as the work done by a coulomb of positive charge when moved from a position infinitely distant from the electrode and brought immediately close to it. At equilibrium there will exist a charge separation between the metal and the solution. This means that an electrode potential has been established on the metal electrode relative to the solution. The potential drop across the electrode / solution interface ($\Delta\phi_{m/s}$) is given by **Equation 1.6**.

$$\Delta\phi_{m/s} = \phi_m - \phi_s \qquad [\mathbf{1.6}]$$

The quantity ϕ_m is defined as the potential of the metal electrode and ϕ_s as the potential of the solution. Direct measurement of the quantity $\Delta\phi_{m/s}$ is not possible without the use of a reference electrode (*R.E.*), which maintains a constant potential against which the potential drop ($\Delta\phi_{m/s}$) can be measured (**Equation 1.7**). Such that $(\phi_m - \phi_s)_{W.E.}$ represents the potential drop at the working electrode (*W.E.*) The equilibrium potential is rapidly reached assuming no current is drawn, dependent on the concentrations of species in solution (*e.g.* Fe^{3+} / Fe^{2+}).

$$E = (\phi_m - \phi_s)_{W.E.} - (\phi_m - \phi_s)_{R.E.} \qquad [\mathbf{1.7}]$$

1.1.4 The Nernst Equation

In order to account for the chemical and electrical potentials of species *A*, we introduce the quantity electrochemical potential, $\bar{\mu}_A$.

$$\bar{\mu}_A = \mu_A + z_A F\phi \qquad [\mathbf{1.8}]$$

The electrical potential is comprised of two terms. $z_A F\phi$ describes the electrical energy of *A*. z_A is the charge on the molecule while μ_A is the chemical potential of species *A*. At equilibrium, under constant *T* and *P*, there will be a balance between the electrochemical potentials of the species involved. For the example described in **Equation 1.9** above it follows that

$$\bar{\mu}_{Fe^{3+}} + \bar{\mu}_{e^-} = \bar{\mu}_{Fe^{2+}} \qquad [\mathbf{1.9}]$$

Applying **Equation 1.8** to **1.9** allows us to expand this expression to obtain the Nernst equation, applicable for a single electrode – solution interface.

$$\phi_m - \phi_s = \frac{\Delta\mu^0}{F} + \frac{RT}{F}\ln\left(\frac{[Fe(CN)_6^{3-}]}{[Fe(CN)_6^{4-}]}\right) \qquad [\mathbf{1.10}]$$

where $\Delta\mu^0 = \mu^0_{Fe^{3+}} + \mu_{e^-} - \mu^0_{Fe^{2+}}$, constant at a given *T* and *P*. The Nernst equation is given below in its more general form. For the general one – electron redox process shown in **Equation 1.11** the Nernst equation can be used to determine the equilibrium potential of a half – cell in an electrochemical cell based on the concentration /

activities of the chemical species involved and the standard potential, E^0 (**Equation 1.12**).

$$Ox + e^- \rightleftharpoons Red \qquad [1.11]$$

$$E = E^0 + \frac{RT}{F}\ln\frac{[O]}{[R]}$$

$$E = E^0 + \frac{RT}{F}\ln\frac{(a_{ox})}{(a_{red})} \qquad [1.12]$$

1.1.4 Standard and Formal Potentials

It is conventional to quote the system potential (couple or half – cell) against the standard hydrogen electrode (*SHE*), also known as the normal hydrogen electrode (*NHE*). All species contributing to the potential determining equilibria at each electrode are present at a concentration corresponding to unit activity for the solution phase and unit pressure for gases. Tabulated values of standard electrode potentials for typical reactions can easily be found in electrochemical literature[2, 3].

Activity coefficients are dependent on the solution concentration. In practice their use (*e.g.* Nernst equation) is inconvenient, as values tend to be unknown. It therefore makes sense to replace activity coefficients with the concentration terms. The concentration of species in solution can be related to the activity by **Equation 1.13**.

$$a_A = \gamma_A [A] \qquad [\mathbf{1.13}]$$

where a_A is the activity of species A, γ_A is the activity coefficient and [A] is the concentration. For our Fe^{3+} / Fe^{2+} example, the variation in cell potential with activity, is outlined by Nernst :

$$E = E^0 + \frac{RT}{F} \ln \frac{(a_{Fe^{3+}})}{(a_{Fe^{2+}})} \qquad [\mathbf{1.14}]$$

Considering **Equation 1.13**, we are able to obtain

$$E = E^0 + \frac{RT}{F} \ln \frac{\gamma_{Fe^{3+}} [Fe^{3+}]}{\gamma_{Fe^{2+}} [Fe^{2+}]} \qquad [\mathbf{1.15}]$$

We can define the formal potential, $E^{0'}$ in terms of E^0

$$E^{0'} = E^0 + \frac{RT}{F} \ln \frac{\gamma_{Fe^{3+}}}{\gamma_{Fe^{2+}}} \qquad [\mathbf{1.16}]$$

$$E = E^{0'} + \frac{RT}{F} \ln \frac{[Fe^{3+}]}{[Fe^{2+}]} \qquad [\mathbf{1.17}]$$

The value of $E^{0'}$ will differ between media, based on the ionic strength. The value of the standard potential for half – reactions and cells are obtained by measuring the

formal potential value over a range of ionic strength and extrapolating to zero ionic strength, where activity coefficients approach unity.

1.2 Electrochemical Cells

1.2.1 Types of Electrochemical Cell

An electrochemical cell is a device capable of generating electrical energy from a chemical reaction or of introducing electrical energy into a system to facilitate chemical reactions. An electrochemical cell where a faradaic current is flowing can be classified as either galvanic or electrolytic.

Galvanic cell: reactions occur spontaneously at electrodes when connected by an external conductor (*i.e.* converting chemical energy into electrical energy).

Electrolytic cell: reactions take place with the application of an external voltage greater than open – circuit potential of the cell (*i.e.* used to carry out desired chemical reactions by expending electrical energy such as in electrolytic synthesis).

The behaviour of the cell as a whole can be determined by combining the two half – cell reactions. As each half –cell has a characteristic voltage the potential of the cell can be predicted from tables of standard potentials. The difference in voltage between the two half – cells predicts the measured potential. The fundamental behaviour of a single electrode and its reactions is independent of whether the electrode is part of a galvanic or electrolytic cell set up. The electrode at which reductions occur is referred to as the cathode and that at which oxidations occur the anode. In an

electrolytic cell, the cathode is negative with respect to the anode while in a galvanic cell, the cathode is positive with respect to the anode.

1.2.2 Three Electrode Set Up for Electrolysis

A standard three – electrode cell is typically employed in controlled potential techniques and can be used in the study of electrode kinetics to obtain quantitative data. It is made up of the following components:

Working electrode (*W. E.*): electrode at which the reaction of interest takes place.

Reference Electrode (*R. E.*): provides a stable and reproducible potential (independent of sample composition), against which the potential of the *W. E.* can be compared.

Counter Electrode (*C. E.*): an inert conducting material, *e,g.* platinum wire or graphite rod, generally used as current – carrier.

The specific design and the materials used will depend on the experiment and the nature of the sample under investigation. The three electrodes are controlled by a potentiostat. The potentiostat consists of two circuits: a polarizing circuit that applies the potential to the cell and a measuring circuit to monitor the current. Potentiostatic control of the *W.E.* minimizes errors arising from cell resistance.

$$E_{app} = E_{W.E.} - E_{R.E.} - iR \qquad [\mathbf{1.18}]$$

Equation 1.16 explains the cause of the ohmic distortion: *iR* reflects electrical resistance of the bulk solution between *W.E.* and *R.E.*, *i.e.* ohmic potential drop.

A fixed potential can be maintained between the *W.E.* and the *R.E.* as negligible current can be drawn from the latter. As a constant $(\phi_m - \phi_s)$ is maintained at the *R.E.*, any change in *E* relates to corresponding changes in $(\phi_m - \phi_s)_{W.E.}$.

$$E = (\phi_m - \phi_s)_{W.E.} - (\phi_m - \phi_s)_{R.E.} \qquad [\mathbf{1.19}]$$

Imposition of a potential drop $(\phi_m - \phi_s)_{W.E.}$ allows us to examine the current through the *W.E.* solution interface, as a function of the applied potential. The purpose of the *C.E.* is to pass the same current as that induced to flow through the *W.E.*, such that the potentiostat drives the *C.E.* to whatever voltage is required to pass this current. Introduction of this third electrode is the only reason why a controlled potential can be applied to the *W.E.* as discussed. If only two electrodes are present, then one attempts to act as both the *R.E.* and *C.E.* Appreciable current drawn through the *R.E.* can induce chemical changes, altering $(\phi_m - \phi_s)_{R.E.}$.

$$E = (\phi_m - \phi_s)_{W.E.} + iR - (\phi_m - \phi_s)_{R.E.} \qquad [\mathbf{1.20}]$$

In this situation changes in *E* would cause unknown changes in *iR* as well as altering $(\phi_m - \phi_s)_{W.E.}$, so the latter would no longer be controlled.

The exception to this is the case of 'microelectrode' systems, where a two – electrode set up may be sufficient as small currents ($\sim 10^{-9} A$) means negligible change occurs at the *R.E.* and the *iR* term is small enough to be neglected.

1.2.3 Solvents and Supporting Electrolytes

Electrochemical measurements are carried out in a solvent containing a supporting electrolyte. The choice of solvent depends on a number of factors such as the solubility and redox behaviour of the analyte, as well as solvent properties (*i.e.* electrical conductivity, electrochemical activity and chemical reactivity). The chosen solvent should not react with the analyte or any products and should be electrochemically inert over a wide potential window. Supporting electrolytes are employed in controlled – potential experiments in order to suppress migration effects, decrease resistance and maintain a constant ionic strength. Supporting electrolytes may be inorganic salt, mineral acid or buffer (**Table 1.1**).

Typical Solvents	Aqueous	H_2O (*double – distilled*)
	Non – Aqueous	CH_3CN, DMF, DMSO
Typical Supporting Electrolytes	Aqueous	KCl, KNO_3, NH_4Cl, NaOH, HCl
	Non – Aqueous	Tetra – alkylammonium salts
	Buffer Systems	Acetate, phosphate, citrate

Table 1.1

Typical solvents and supporting electrolytes employed in electrochemical experiments.

1.2.4 Removal of Oxygen

The electrochemical reduction of oxygen is known to proceed via a two – step mechanism as outlined below (**Equation 1.21**).

$$O_2 + 2H^+ + 2e^- \rightarrow H_2O_2$$

$$H_2O_2 + 2H^+ + 2e^- \rightarrow 2H_2O \qquad [\mathbf{1.21}]$$

The first step corresponds to the formation of hydrogen peroxide and the second step to the reduction of peroxide to form water. The half – wave potentials of these two steps are recorded at ~ - 0.1 V and – 0.9 V (*vs. SCE*). A significant current can arise from these processes, which are likely to interfere with the measurement of analytical cathodic currents. Furthermore, products may affect the chemical processes under investigation. It is therefore prudent to remove dissolved oxygen from the electrochemical cell. The most common approach is to purge the cell with an inert gas such as N_2 or Ar.

1.2.5 Working Electrodes

The working electrode material strongly influences the voltammetric response. The chosen material should provide a reproducible response and high signal – to – noise ratio. Two factors largely determine the choice of electrode material: redox behaviour of the target analyte and background current over the potential region of interest. It is also important to consider the potential window, electrical conductivity, reproducibility of the electrode surface, mechanical properties, cost, availability and toxicity. Electrode materials, which have found extensive uses as working electrodes include: mercury, carbon and noble metals (Pt, Au, Ag, Pt, etc.).

1.2.6 Reference Electrodes

Commonly used reference electrodes in aqueous solution are the saturated calomel (*SCE*) and the standard hydrogen electrode (*SHE*). Many other reference electrodes have been devised for electrochemical studies in both aqueous and non – aqueous media. The reference electrode will be chosen based on the specific experimental conditions.

Where the experimental set up must be chloride – free, a mercury / mercury sulphate reference electrode (**Equation 1.22**) may be employed:

$$Hg / Hg_2SO_4 / K_2SO_4 \text{ (sat. aq)} \qquad [\mathbf{1.22}]$$

In a non – aqueous solvent, we may be concerned with the leakage of H_2O from the reference electrode into the system. In this case the following (**Equation 1.23**) may be employed as a suitable reference electrode:

$$Ag / Ag^+ \qquad [\mathbf{1.23}]$$

In non – aqueous solvents a quasi – reference electrode (*QRE*) is often employed to prevent contamination of the test solution. A metal wire (*e.g.* platinum or silver) is used under the assumption that essentially no change takes place in the bulk solution, so that the potential of the wire, although unknown, does not change over the course of a series of experiments. It is critical for the potential of the *QRE* to be calibrated with respect to a true reference. The ferrocene / ferrocenium redox couple (Fc/Fc^+) is often used in such calibrations.

1.3 Faradaic and Non – Faradaic Processes

1.3.1 Electrode Processes

Two types of processes are known to occur at electrodes. These are termed faradaic and non – faradaic electrode processes. Faradaic currents are able to provide a direct measure of the rate of a redox reaction. Where the electro – active species under consideration is reduced or oxidized resulting in a change in oxidation state this is termed a faradaic process. These reactions involve the transfer of electrons and are thus governed by Faraday's law.

It is possible for a given electrode – solution interface, even when no charge – transfer processes are taking place, it is possible under such conditions for the adsorption / desorption processes as well as changes in the structure of the interface to generate a current. Although non – faradaic processes do not involve any charge transfer across the interface, external currents may still arise due to changes in the potential, electrode area or solution composition.

During the course of an electrode reaction, both faradaic and non – faradaic processes will occur. Therefore, we must account for both processes in order to fully analyse electrochemical data.

1.3.2 Currents and Reaction Fluxes

The electron transfer between the electrode and electro – active species in solution requires the electro – active species to diffuse from the bulk to the electrode surface. The flux (j) can be thought of as a measure of the heterogeneous interfacial electrochemical reaction and is related to the current by **Equation 1.24**. Heterogeneous rate constants, such as those of electrode reaction, are temperature and

pressure dependent but also extremely sensitive to the electrical potential, with exponential dependence on $(\phi_m - \phi_s)$.

$$i = -FAj \qquad [\mathbf{1.24}]$$

The flux (j) is given in units of *mol* cm^{-2} s^{-1}, F is the Faraday constant (*96485 C* mol^{-1}) and A represents the electrode area (cm^{-2}).

As a redox process takes place, this leads to the depletion of the electro – active species close to the electrode surface such that the concentration of reactant at the electrode surface ($[\ ]_0$) is not equal to the bulk reactant concentration ($[\ ]_{bulk}$). This will be discussed further in later sections.

For a simple reaction, *e.g.* $\mathrm{Ox} + \mathrm{e}^- \rightleftharpoons \mathrm{Red}$, the current (electrode reaction rate) will be dictated by the rate of processes such as:

1. Mass transfer (*e.g.* from bulk to electrode surface).
2. Rate of electron transfer at the electrode surface.
3. Chemical reaction preceding or following the electron transfer step.
4. Other surface reactions (*e.g*. adsorption, desorption, crystallization, *etc.*).

These factors will be discussed in more depth in the following sections of this introductory chapter.

1.4 Mass Transfer

Mass transfer is the movement of material in solution and arises due to differences in electrical or chemical potential between two different locations. In order for a reaction to take place the reactant molecule must be transported from the bulk solution to the electrode surface. The rate of a reaction may therefore be determined by the kinetics of the electron transfer process or by the rate at which material is brought to (and from) the electrode surface (*i.e.* mass transfer control). Mass transfer plays a critical role in the electrochemical dynamics of a system. Below we will review the three significant modes of mass transfer and discuss their mathematical treatment.

1.4.1 Migration

The movement of charged particles under the influence of an electric field is known as the process of migration. Such an external field exists at the electrode – solution interface resulting from the potential drop between the two phases ($\Delta\phi_{m/s}$). The result is the exertion of an electrostatic force on charged species in the interfacial region subsequently inducing the movement of ions to or from the electrode surface. Migration effects are likely to accompany electrochemical reactions.

1.4.1.1 Elimination of Migration Effects.

The interplay of migration and electrolysis in any given chemical reaction can result in complex physical transport processes, which can prove difficult to interpret. A charge transfer process occurring at the electrode surface can in turn alter the local concentrations of electro – active species, altering the electrical potential in solution and electric field local to the electrode. Consequently the migratory flux and rate of

mass transport of the electro – active species will be altered. Such variation can make interpretation of the experimental data difficult. We are able to eliminate these migration effects by the introduction of a large concentration of inert "background electrolyte". The effect of the high concentration of background ions is to compress the double layer such that electrical neutrality is maintained throughout the interfacial region with the exception of the very small region immediately adjacent to the electrode surface. Excess background ions prevent the build up of electric fields in solution as the reaction proceeds. For migration effects to be disregarded calculations show that a concentration of background electrolyte approximately 100 times that of the electro – active species is required.

1.4.2 Diffusion

Diffusion is the movement of species under the influence of a gradient of chemical potential (*i.e.* a concentration gradient). The rate of diffusion (*i.e.* flux) is directly proportional to the slope of the concentration gradient at a particular location (x).

1.4.2.1 Fick's Laws

Diffusional behaviour has been established by Fick's laws as described in detail below. The measured current is directly proportional to the flux as shown by **Equation 1.25**.

$$i = -FAj \qquad [\mathbf{1.25}]$$

The diffusive flux (j) at any given point (x) can be quantified by Fick's 1st Law, which states that the flux is proportional to the concentration gradient, $\frac{\partial c}{\partial x}$ (**Equation 1.26**)[4].

$$j = -D\frac{\partial c}{\partial x} \qquad [\mathbf{1.26}]$$

The flux (j) is given in units of $mol\ cm^{-2}\ s^{-1}$, D is the diffusion coefficient ($cm\ s^{-1}$) and the local concentration gradient is represented by $\partial c/\partial x$.

Fick's 1st Law is based on the assumption that the flux is driven by concentration differences alone with no influence from external electrical fields. Such fields can have a strong influence on the flux of charged species. This effect can be negated by the addition of excess background electrolyte as discussed in **Section 1.5.2**.

Generally speaking the larger the molecule the smaller the value of the diffusion coefficient. Typically values of diffusion coefficient are found in the range of $10^{-5} - 10^{-6} cm^2 s^{-1}$ at room temperature. The value of the diffusion coefficient is temperature sensitive, displaying an Arrhenius type relationship (**Equation 1.27**).

$$D = D_\infty \exp\left(\frac{-E_A}{RT}\right) \qquad [\mathbf{1.27}]$$

where D_∞ is the hypothetical value of the diffusion coefficient at infinite temperature, $E_A\,(kJ\ mol^{-1})$ is the activation energy.

Fick's 2nd Law[4] can be derived from the first and addresses how the concentration of a species at point x varies with time (**Equation 1.28**).

$$\frac{\partial c}{\partial t} = D\frac{\partial^2 c}{dx^2} \qquad [\mathbf{1.28}]$$

The change in concentration at a given location (x) is given by the difference in the flux in and out of a cross – section of the solution of width, ∂x.

$$\frac{\partial c}{\partial t} = \frac{J(x,t) - J(x+\partial x,t)}{\partial x} \qquad [\mathbf{1.29}]$$

Flux at point $x + \partial x$ is given in terms of that at point x as shown by **Equation 1.30** below:

$$J(x+\partial x,t) = J(x,t) + \frac{\partial J(x,t)}{\partial x}\partial x \qquad [\mathbf{1.30}]$$

From Fick's 1st Law we know that the flux is proportional to the concentration gradient. This allows us to obtain the following expressions

$$-\frac{\partial J(x,t)}{\partial x} = \frac{\partial}{\partial x} D_0 \frac{\partial c(x,t)}{\partial x} \qquad [\mathbf{1.31}]$$

$$\frac{\partial c(x,t)}{\partial t} = \left(\frac{\partial}{\partial x}\right)\left[D_0 \frac{\partial c(x,t)}{\partial x}\right] \qquad [\mathbf{1.32}]$$

We can therefore expression Fick's 2nd Law in one dimension as shown in **Equation 1.28**. In three dimensions the appropriate expression is given in **Equation 1.33**.

$$\frac{\partial c}{\partial t} = D\left(\frac{\partial^2 c}{\partial x^2} + \frac{\partial^2 c}{\partial y^2} + \frac{\partial^2 c}{\partial z^2}\right) \qquad [\mathbf{1.33}]$$

This expression can be adapted for disc electrodes with cylindrical co – ordinates or spherical co – ordinates when dealing with spherical or hemispherical electrodes.

1.4.2.2 Fick's Laws in Practice: The Cottrell Equation

The Cottrell Equation as given in **Equation 1.34**, describes Fick's 2nd Law in experimental practice. Application of a sufficiently large overpotential to the working electrode causes all of the electro – active species to be reduced or oxidized very quickly (*vs.* rate of diffusion). Therefore, the concentration of electro – active species at the electrode surface will be reduced to zero. Regardless of the kinetics of such redox processes (*i.e.* facile or sluggish), it is possible to activate them by application of a large enough overpotential.

$$i(t) = i_d(t) = \frac{nFAD_0^{1/2}c_{bulk}}{\pi^{1/2}t^{1/2}} \qquad [\mathbf{1.34}]$$

For example, for an electrode with $A = 0.5 cm^2$, $D = 1\times10^{-5} cm^2 s^{-1}$, $c_{bulk} = 1\times10^{-3} mol\ cm^{-3}$ and $t = 1\ sec$, we are able to predict the current as approximately, $2.7\times10^{-4} A$. This corresponds to experimental potential step chronoamperometry, as the current resulting form a potential step decays to zero, with dependence inversely proportional to the square root of time.

1.4.3 Convection

Convection is the result of mechanical force acting upon the solution. Convection can be described as natural or forced. Natural convection can be present in any solution and arises due to the thermal gradients and / or density differences throughout the solution. Thermal gradients may occur as the result of exo – or endothermicity of a given process. Differences in density may arise as the reaction proceeds. The concentrations of the products of the electrode reaction will increase at the electrode surface, which may have different densities than the bulk solution.

Forced convection can be achieved by employing external forces such as stirring or bubbling with inert gas. This technique may used to swamp any contribution from unpredictable natural convection in order to achieve reproducibility in experimental practice. Forced convection possesses hydrodynamic behaviour, allowing quantitative description of the flow in solution and prediction of mass transport patterns.

1.4.4 The Nernst Diffusion Layer

When a potential step is carried out it is predicted that the observed current will depend on the reciprocal of square root of time. This is typically observed for up to a few seconds, except over very short time scales where the Faradaic current will be obscured by so – called "charging current" due to movement of ions comprising the supporting electrolyte, near the electrode. Experimentally, the current will tend towards a steady – state value, rather than current falling off to zero as predicted by the Cottrell Equation. This is consistent with **Figure 1.2** shown below.

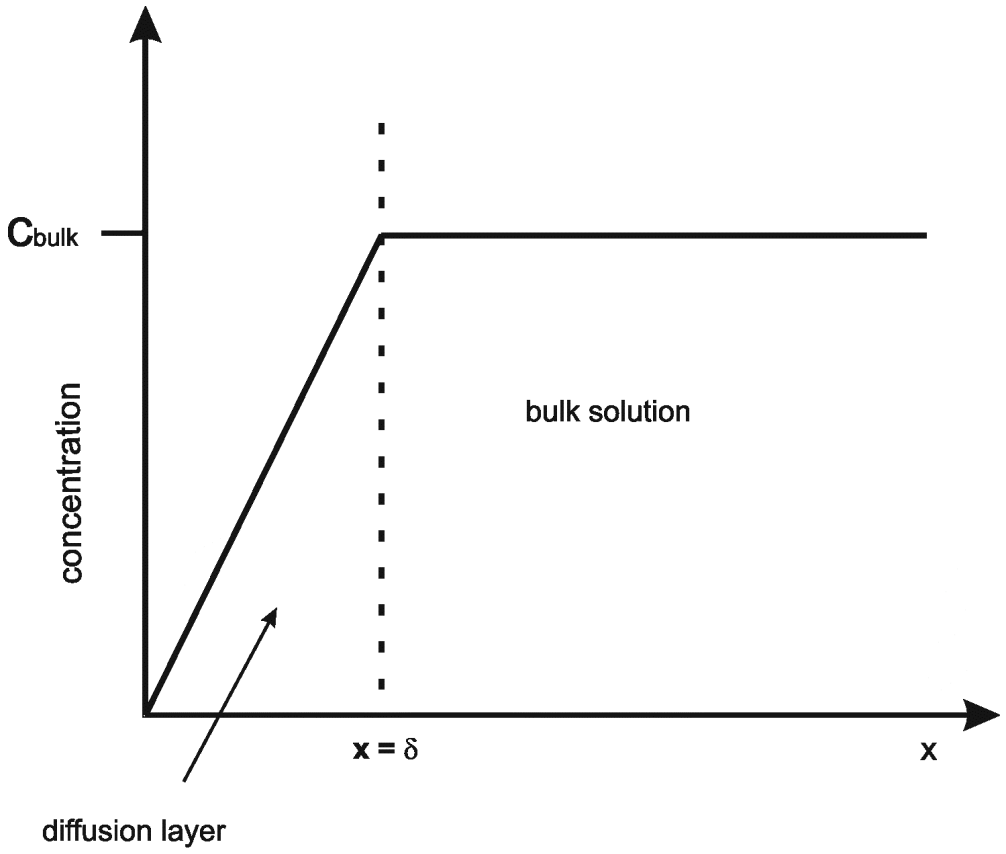


Figure 1.2

The Nernst model of the diffusion layer.

Beyond a critical distance, δ, from the electrode surface, the solution will be well – mixed maintaining the concentration of the electro – active species at a constant bulk value. This mixing in the bulk solution is due to natural convection induced by density differences.

On the other hand, close to the electrode surface rigidity and frictional forces cause natural convection to die away in this zone between $x = 0$ and $x = \delta$, known as the diffusion layer. In this region, changes in concentration occur solely by diffusional transport as described by Fick's Law's (**Equation 1.35**). The electro – active material must diffuse across the diffusion layer in order for the reaction to take place at the electrode surface. Therefore, the maximum current will be limited by the rate of diffusion. Driving the potential to sufficiently large overpotential such that the

concentration of electro – active species at the electrode surface is reduced to zero, will result in a limiting current as shown below:

$$j = D\frac{\partial c}{\partial x} = \frac{Dc_{bulk}}{\delta} \qquad [\mathbf{1.35}]$$

The corresponding steady – state current (I_{ss}) is given by **Equation 1.36**:

$$I_{ss} = \frac{nFADc_{bulk}}{\delta}$$
$$= nFAm_T c_{bulk} \qquad [\mathbf{1.36}]$$
$$m_T = \frac{D}{\delta}$$

m_T is defined as the mass transport coefficient ($cm\ s^{-1}$).

In reality the diffusion zone and the well – mixed solution merge into one another. The Nernst diffusion layer is a simplified model. For diffusion – only models to be applicable to experimental data it is important that the time scale of the experiments is restricted to confine any concentration changes to the diffusion zone, between $x = 0$ and $x = \delta$.

The Cottrell Equation predicts the case of a limiting current falling away with time. In contrast, the Nernst diffusion layer gives a limiting current attained when the concentration decays from the bulk value (c_{bulk}) to zero at the electrode surface over the distance of the diffusion layer, δ.

The diffusion layer thickness will increase as square root of time ($\sqrt{t}$) for diffusion to a planar electrode in an unstirred solution.

1.5 Electrode – Solution Interface

1.5.1 Electrical Double Layer

A charged surface (*i.e.* an electrode) when placed in contact with a solution of ions will attract ions of opposite charge and will repel like charges. The result is an ion atmosphere in the immediate vicinity of the electrode surface. This is referred to as the electrical double layer and is described in terms of several layers. Models describing the structure of the double layer have been proposed by Helmholtz, Gouy and Chapman, and Stern[2].

The layer closest to the electrode is known as the inner Helmholtz plane (*IHP*) and contains specifically adsorbed solvent molecules, ions, etc. on the electrode surface. The *IHP* is defined as the axis through the centre of the specifically adsorbed species. The specific adsorption of molecules results in a reduced charge density required in the solution double layer to compensate for the electrode charge.

Solvated solvent molecules approaching the electrified surface make up the outer Helmholtz plane (*OHP*) and involve electrostatic interactions between electrode and solvated ions, such that no specific adsorption is involved in the *OHP*. Those molecules which are not specifically adsorbed are distributed in a three – dimensional arrangement known as the diffuse layer, which extends from the *OHP* to the bulk solution. A schematic representation of the Stern model is shown in **Figure 1.3**.

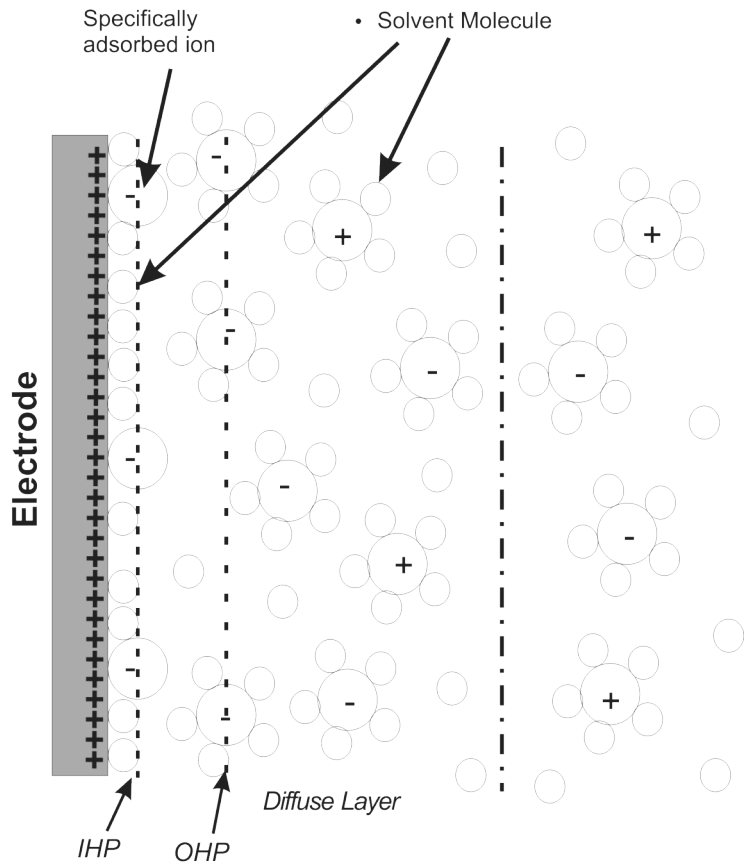


Figure 1.3

A schematic representation of the electrical double layer as described by Stern[2, 5].

1.5.2 Need for Supporting Electrolyte

The addition of excess background electrolyte acts to compress the potential drop to within 10 – 20 angstroms of the working electrode surface. As the electron transfer process between electrode and solution takes place by means of quantum mechanical tunnelling this implies that the species under investigation must be located within a similar distance of the electrode surface to facilitate the overlap of the orbitals of the metal and those of the electro – active species. Where experiments are conducted in poorly conducting electrolytes, it is necessary to perform Frumkin corrections[1] to account for potential drop over greater distances. Typical concentrations of such inert

supporting electrolytes are greater than 10^{-1}M and the supporting electrolytes are electrochemically inert in the potential region of interest.

1.6 Electrode Kinetics

We consider the following electrode process:

$$A + e^- \underset{k_a}{\overset{k_c}{\rightleftharpoons}} B \qquad [\mathbf{1.37}]$$

k_c and k_a represent the rate constants for the reductive (cathodic) and oxidative (anodic) processes, respectively. The rate equation for the above process can be expressed as shown in **Equation 1.38**.

$$j = k_c[A]_0 - k_a[B]_0 \qquad [\mathbf{1.38}]$$

1.6.1 The Arrhenius Equation

Experimental rate constants for solution phase reactions nearly always vary with temperature as described by the Arrhenius Equation (**Equation 1.39**).

$$k = Ae^{-E_A/RT} \qquad [\mathbf{1.39}]$$

E_A has units of energy and is known as the activation energy, A is the frequency factor. As the activation energy describes the probability of overcoming the energy barrier, the frequency factor relates to the frequency of attempts on said energy barrier.

This concept of activation energy allows us to construct a picture of the reaction pathway along a reaction co – ordinate. The reactants and products will occupy minima on the potential energy surface as they are the only configurations stable

enough to have significant lifetime. Other configurations are possible but will have high energies and lack stability. The activation energy E_A will represent the maximum energy between the two minima. E_A describes the change in Gibbs energy going from minimum to maximum, called the transition state or activated complex (‡). $\Delta G^{\ddagger}$ is termed the standard free energy of activation. The Arrhenius Equation can be used to relate the rate constant to the Gibbs energy of activation (**Equation 1.37**).

$$k_c = A_c e^{\frac{-\Delta G_c^{\ddagger}}{\mathrm{RT}}} = A_c e^{\frac{\Delta S_c^{\ddagger}}{R}} . e^{\frac{-\Delta H_c^{\ddagger}}{RT}}$$

$$k_a = A_a e^{\frac{-\Delta G_a^{\ddagger}}{\mathrm{RT}}} \qquad [\mathbf{1.40}]$$

Comparison of **Equation 1.40** with **1.37** indicates that the entropy term can be grouped together with the frequency factor (*A*).

1.6.2 The Butler – Volmer Equation

Most current interpretations of electrode kinetics are underpinned by the Butler – Volmer model. For all faradaic electrode processes, the potential of the electrode strongly affects the kinetics of the reactions occurring at its surface, except at very large overpotentials where the process becomes transport controlled. As the interfacial potential difference can be used to control reactivity, we can predict the precise way in which k_c and k_a (rate constants of the cathodic and anodic reactions, respectively) depend on potential.

The most convenient forms of the Butler – Volmer expression are given in **Equation 1.41**.

$$k_c = k^0 \exp\left[\frac{-\alpha F(E - E_f^0)}{RT}\right]$$

$$k_a = k^0 \exp\left[\frac{\beta F(E - E_f^0)}{RT}\right] \quad (\beta = 1 - \alpha) \qquad [\mathbf{1.41}]$$

The standard electrochemical rate constant (k^0 / cm s^{-1}) is simply a measure of the rate of the redox couple. A large value of k^0 will achieve equilibrium rapidly while a small value will be sluggish. Electrochemical rate constant are related to $(\phi_m - \phi_s)$ as follows:

$$k_c \propto \exp\left[\frac{-\alpha F(\phi_m - \phi_s)}{RT}\right]$$

$$k_a \propto \exp\left[\frac{\beta F(\phi_m - \phi_s)}{RT}\right] \qquad [\mathbf{1.42}]$$

However, as a reference electrode is required in order to complete the circuit, the expression is modified to give **Equation 1.43**, E_f^0 is the formal potential for the redox couple and $(E - E_f^0)$ measures the potential applied to the working electrode relative to the formal potential of the redox couple:

$$(E - E_f^0) = (\phi_m - \phi_s)_{W.E.} + \text{constant} \qquad [\mathbf{1.43}]$$

The rate constant being potential dependent, we may expect k_c to predominate at negative electrode potentials while k_a would dominate at relatively positive potentials. At a fixed value of ϕ_m and ϕ_s, the reaction profile would appear as shown in **Figure 1.4**.

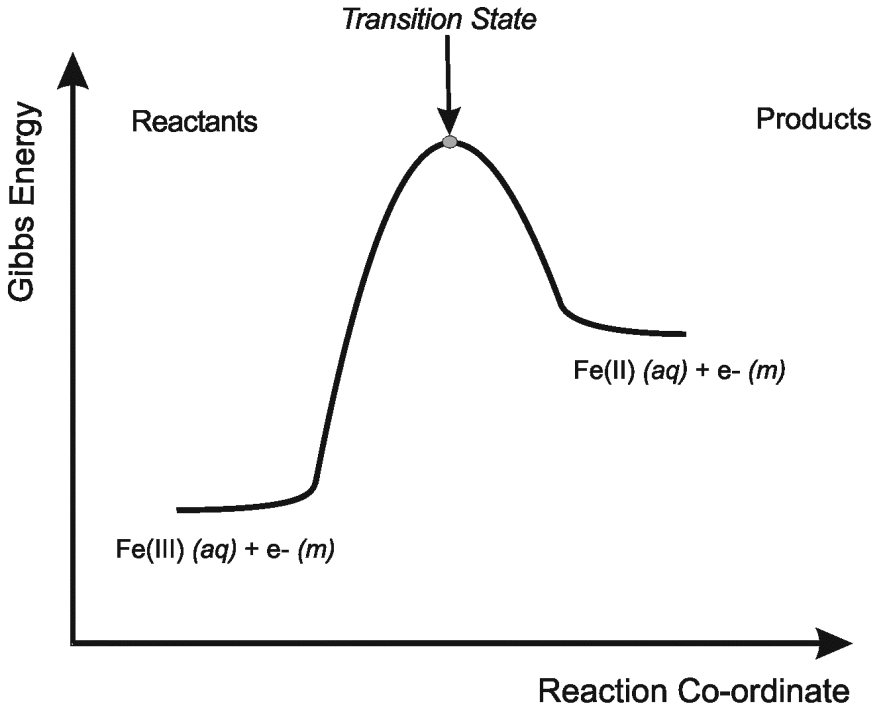


Figure 1.4

A reaction profile for the Fe^{3+} / Fe^{2+} electrode process, ϕ_m and ϕ_s are both fixed values.

By altering the value of ($\phi_m - \phi_s$) the reaction profile can be changed to favour either the cathodic or anodic processes.

The transfer coefficient (α / β) provides a measure of the symmetry of the energy barrier and can possess values from zero to unity. Experimentally, the value of the transfer coefficient will remain constant as the kinetic data is collected over a

relatively narrow potential range. Where $\alpha \to 0$, this indicates that the transition state (‡) will be reactant like in nature while a value closer to unity implies a product like transition state. $\alpha + \beta = 1$, $\alpha = 0.5$ and $\beta = 0.5$.

1.6.3 The Tafel Law

For the simple one – electron redox process described in **Equation 1.37** and the corresponding rate equation (**1.38**), the net flux (*j / mol cm*$^{-2}$ *s*$^{-1}$) is described in **Equation 1.44**:

$$j = k^0 \exp\left[\frac{-\alpha F(E - E_f^0)}{RT}\right][A]_0 - k^0 \exp\left[\frac{+\beta F(E - E_f^0)}{RT}\right][B]_0 \quad [\mathbf{1.44}]$$

The term k^0 is used exclusively, as $k_c^0 = k_a^0 = k^0$. $[\ ]_0$ refers specifically to the concentration at electrode surface. The net flux, and by association, the current, are balanced between the reduction current and oxidation current. Under extreme conditions (*i.e.* $E >> E_f^0$ or $E << E_f^0$) it becomes possible to neglect one of these terms.

For the electrochemical reduction of *A* to *B* (**Equation 1.45**) the flux is calculated according to **Equation 1.46** as shown below:

$$A + e^- \xrightarrow{k_c} B \quad [\mathbf{1.45}]$$

$$j = k^0 \exp\left[\frac{-\alpha F(E - E_f^0)}{RT}\right][A]_0 \qquad [\mathbf{1.46}]$$

Assuming that the concentration of species *A* and *B* are not altered substantially from the constant bulk values, the Tafel Law indicates:

$$\ln|I_{red}| = \frac{-\alpha FE}{RT} + \text{constant} \qquad [\mathbf{1.47}]$$

Similarly,

$$\ln|I_{ox}| = \frac{+\beta FE}{RT} + \text{constant} \qquad [\mathbf{1.48}]$$

The corresponding plot of $|\ln I_{red}|$ / $|\ln I_{ox}|$ $vs.E$ is known as a Tafel plot. Schematic diagrams of the Tafel plots for a reductive or oxidative process are shown in **Figure 1.5**. The Tafel plot provides information on the magnitude of the transfer coefficient (α and β). $[A]_0$ and $[B]_0$ must be constant over the potential range of interest.

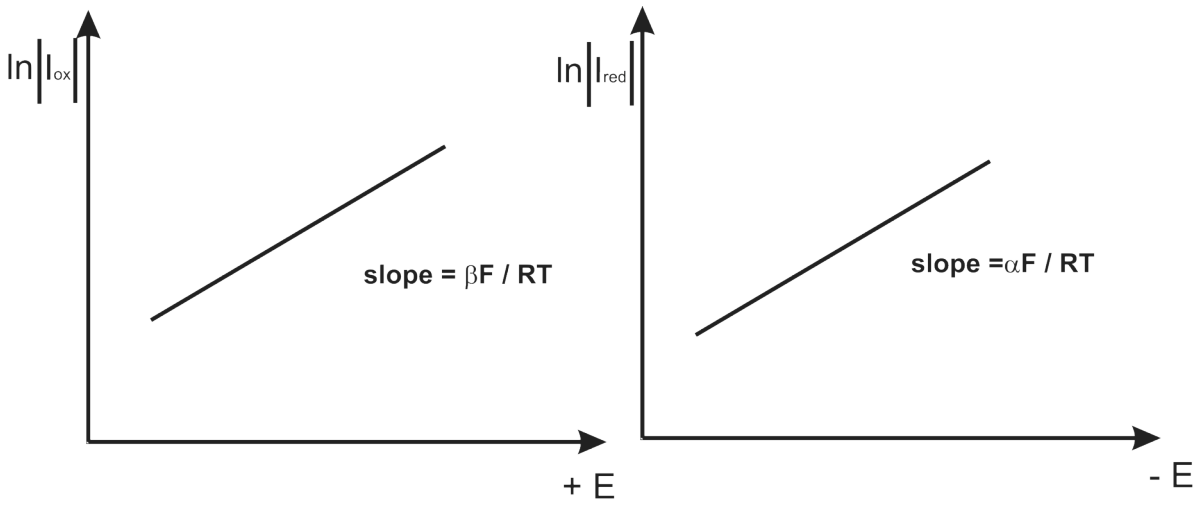


Figure 1.5

Typical Tafel plots for oxidative and reductive processes, respectively.

1.6.4 Marcus Theory

In order to explain the basic principles underlying electron transfer at the electrode – solution interface, we will consider the following process (**Equation 1.49**).

$$Fe(H_2O)^{2+}_{6\ (aq)} \rightarrow Fe(H_2O)^{3+}_{6\ (aq)} + e^{-}_{(m)} \qquad [\mathbf{1.49}]$$

The potential energy curves of the reactants (*R*) and products (*P*) are shown in **Figure 1.6** as a function of the reaction co – ordinate, which in this case can be described as *Fe – O* bond distance within the octahedral complex[1]. Marcus theory can be used to describe the existence of the activation barrier to electron tunnelling at the electrode-solution interface. The reason for such a barrier can be found with the Franck – Condon principle, stating that electronic transitions are essentially instantaneous compared with the time scale of nuclear motions. The electron transfer occurs over a significantly shorter timescale (~ 10^{-15} *s*) than molecular nuclear vibration (~ 10^{-13} *s*). Therefore, the transition corresponds to the nuclei being "frozen" on the timescale of

electron transfer. If the molecule is to move to a new "electronic state", it must be instantaneously compatible with the nuclear positions and momenta in the originating electronic state.

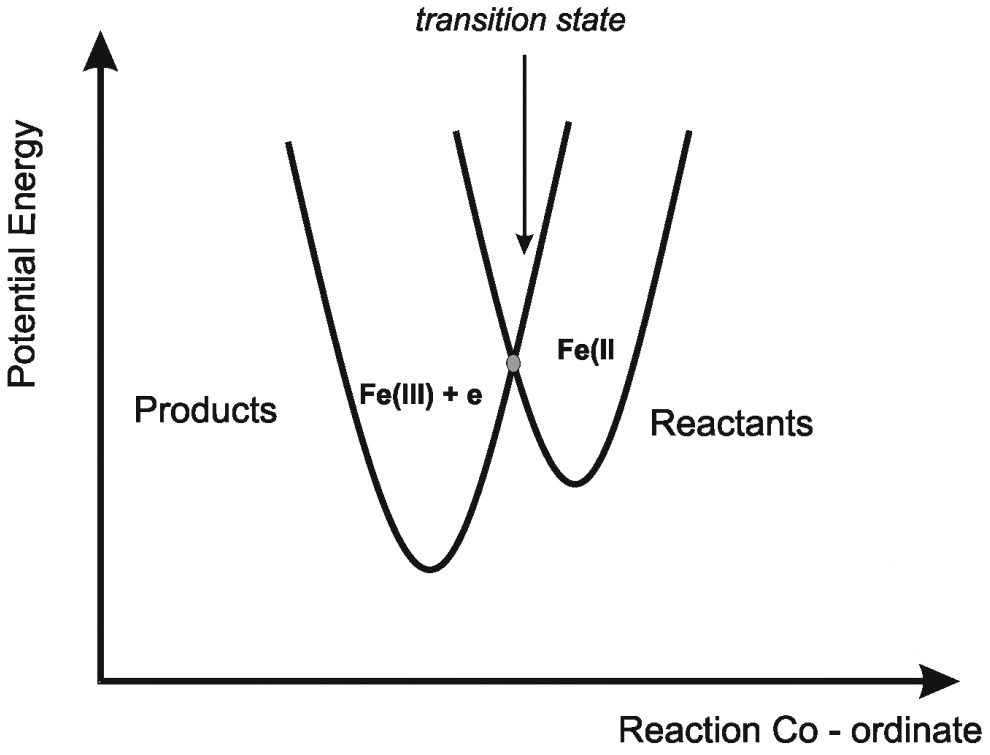


Figure 1.6

The potential energy curves for the oxidation of $Fe^{2+}(aq)$.

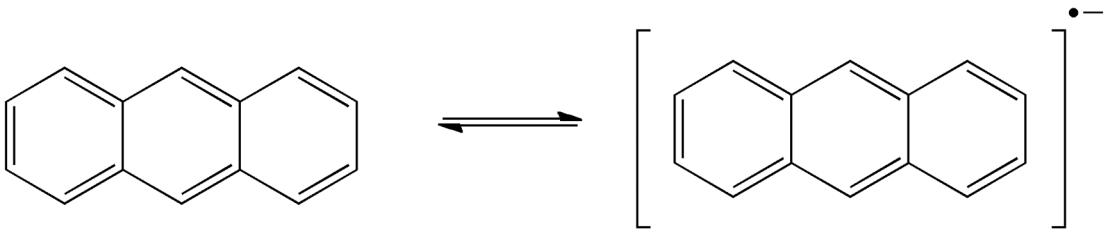
For the example given in **Equation 1.49**, the tunnelling of the electron takes place from the ground state (lowest vibrational energy level, vibrational quantum number, $\upsilon = 0$). Therefore, the $Fe(H_2O)_6^{3+}$ ion must be formed in a highly vibrationally excited state. As conservation of energy must be adhered to, this indicates the reaction proceeds via thermal activation such that the energy of $Fe(H_2O)_6^{2+}$ is raised to the energy of the cross – over point of the curves (transition state). In the transition state it becomes possible for electron tunnelling to take place generating a vibrationally

excited $Fe(H_2O)_6^{3+}$ ion. Collision with solvent molecules quenches thermal energy and produces the ground state $Fe(H_2O)_6^{3+}$ ion.

In summary, the energy barrier exists due to the need to match the energy of *R* and *P* in the transition state. This must occur by means of thermal activation prior to the electron tunnelling process. Thermal activation means that bond length / angles within *R* can become stretched, compressed and / or distorted as well as solvation shells. This concept provides the basis of Marcus theory, describing heterogeneous electron transfer.

Marcus theory can be used to quantitatively predict electron transfer rate constants. A simple rule of thumb to predict whether these rates will be fast or slow is based on the difference in the reaction co – ordinate (*e.g. Fe – O* bond length, Δ). The greater the difference in the reaction co – ordinate between ground state *R* and *P*, the higher the energy of transition state (‡), with a correspondingly larger energy barrier. If follows that the higher the activation energy, the slower the rate constant. When *R* and *P* have similar molecular geometry, the activation barrier will be low and the k^0 will be large. On the other hand, where *R* and *P* are structurally dissimilar the activation energy will be larger and corresponding k^0 will be small. To demonstrate these principles we can consider some examples as shown below:

Example 1



Example 1 shows the anthrancene/anthrancene radical anion couple. This process has a fast electrochemical rate constant of $\sim 4\ cm\ s^{-1}$ in dimethylformamide (DMF) solution (25 ^oC). The corresponding low energy barrier is due to the fact that the bond

angles are virtually unchanged between *R* and *P* as are bond lengths as the electron is delocalized across the entire structure.

Example 2

$$MnO_{4\,(aq)}^{-} + e^{-} \rightleftharpoons MnO_{4}^{2-}{}_{(aq)}$$

The example given above has fast electron transfer kinetics ($k^0 = 0.2\ cm\ s^{-1}$). As both anions have a tetrahedral geometry, the *Mn – O* bond angles do not change. Only a very small change occurs in the bond lengths, implying typically fast electron transfer kinetics according to the principles described above.

Marcus Theory represents the limiting model of Butler – Volmer Theory and thus it was not necessary to interpret the following electrochemical systems in this manner.

1.7 Electrode Reaction Mechanisms

Cyclic voltammetry can be an important tool in the diagnosis of chemical reactions, which may precede or succeed the redox process. Chemical reactions can significantly alter the surface concentrations of the electro – active species in solution. Homogeneous processes occur everywhere in the medium while heterogeneous processes occur only at the electrode – solution interface. The rate of the latter will therefore depend on mass transport to the electrode surface. In this section, redox steps will be referred to as *E* processes and chemical steps as *C*.

The shape of recorded voltammograms will be altered as a result of chemical competition for the electrochemical reactant or product. Analysis of voltammetry can help us to elucidate reaction pathways and provide information on reactive intermediates formed. We will now discuss several commonly observed reaction pathways[1, 2, 6].

1.7.1 E Reaction

The most simple reaction mechanism is the heterogeneous one – electron oxidation (or reduction) to form a stable cation (or anion), known as an *E reaction* (**Equation 1.50**).

$$O + e^- \rightleftharpoons R \qquad [\mathbf{1.50}]$$

Examples of this reaction mechanism are given as follows[1]:

$$Fe(CN)_6^{3-} + e^- \rightleftharpoons Fe(CN)_6^{4-}$$

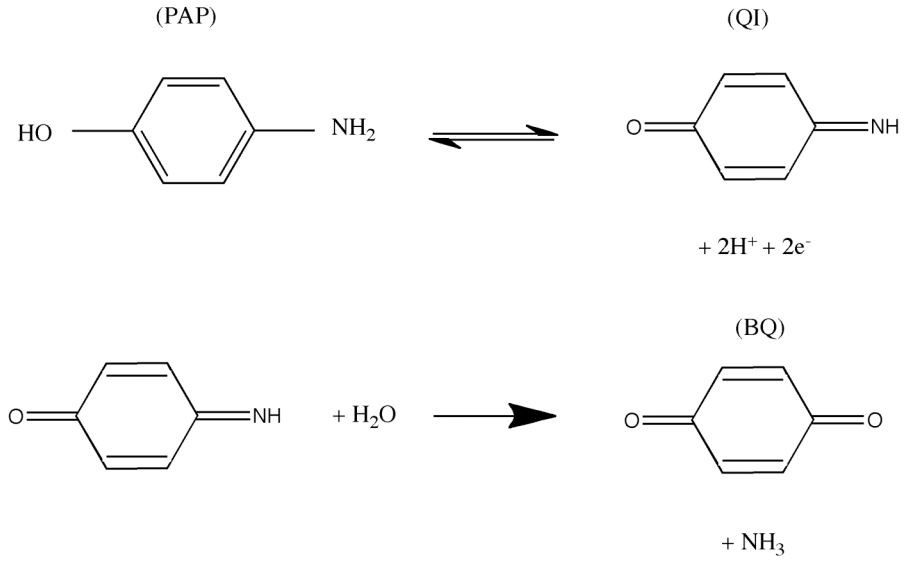
$$FeCp_2 - e^- \rightarrow FeCp_2^{\bullet +}$$

1.7.2 EC Reaction

Where a redox system is perturbed by a chemical reaction succeeding the redox step, this is known as an *EC reaction* (**Equation 1.51**). An extreme case is where the chemical step is so fast that no reverse peak would be observed.

$$O + e^- \rightleftharpoons R \rightarrow Z \qquad [\mathbf{1.51}]$$

For example, the oxidation of *p* – aminophenol (*PAP*) at platinum electrode in aqueous acidic solution[2].



In this case the reverse peak will be smaller as the product is chemically removed from the electrode surface by the chemical step. The ratio of the anodic to cathodic

peak current ($i_{p,a} / i_{p,c}$) will be smaller than unity for an *EC mechanism* This value can be used to determine the rate constant of the chemical step.

1.7.3 CE reaction

In the case of a *CE mechanism*, a slow chemical reaction precedes the electron transfer process (**Equation 1.52**). The ratio of $i_{p,a} / i_{p,c}$, is generally larger than unity, approaching unity as the scan rate decreases. The reverse peak is usually unaffected by the coupled reaction but the forward peak will no longer be proportional to the square root of the scan rate.

$$R \rightarrow Z$$

$$O + e^- \rightleftharpoons R \qquad [\mathbf{1.52}]$$

A typical example is the reduction of carboxylic acids such as acetic acid[1].

$$CH_3COOH_{(aq)} \rightleftharpoons H^+_{(aq)} + CH_3CO_2^-{}_{(aq)}$$

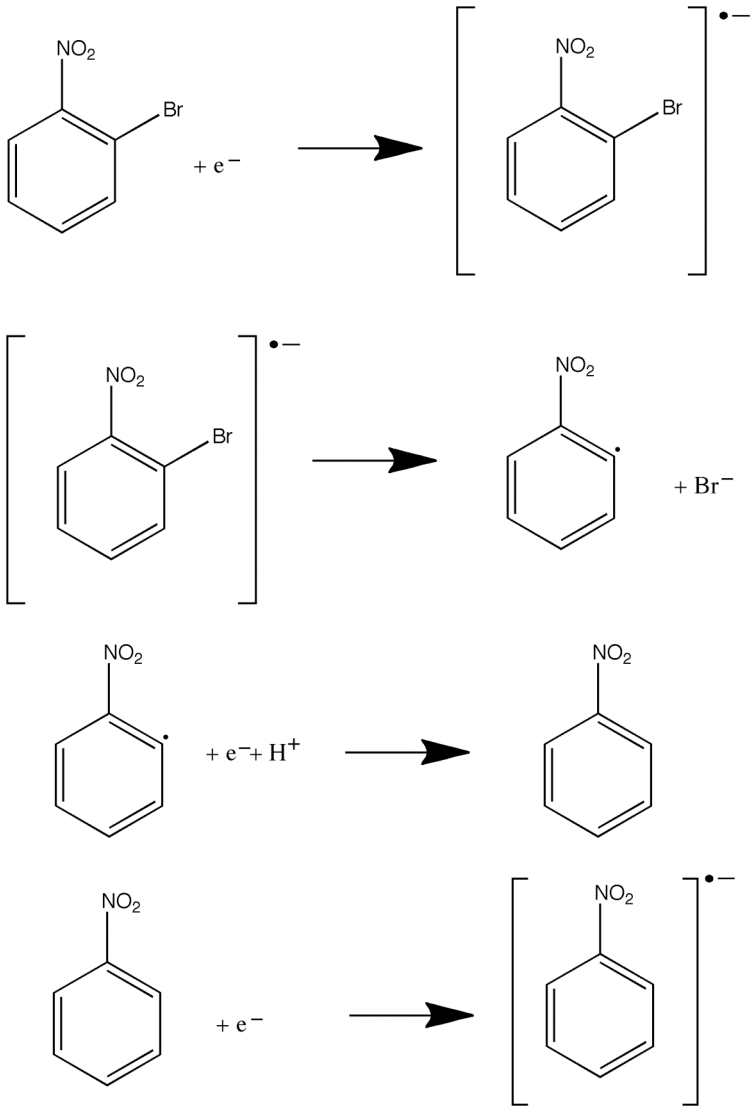
$$H^+_{(aq)} + e^- \rightleftharpoons \tfrac{1}{2} H_{2(g)}$$

1.7.4 ECE reaction

An *ECE reaction* is a chemical step interspersed between two electron transfer steps. The chemical step yields a product, which is also electro – active in the experimental potential range (**Equation 1.53**).

$$O_1 + e^- \rightleftharpoons R_1 \rightarrow O_2 + e^- \rightarrow R_2 \qquad [\mathbf{1.53}]$$

An example is the reduction of 1, 2 – bromonitrobenzene in aprotic solvents[1]



The two redox couples can be observed independently and the rate constant of the chemical process can be estimated from the relative sizes of the two CV peaks. If the *C* step is very fast, relative to the electron transfer, the system will appear as an *EE* reaction (two successive charge transfer steps).

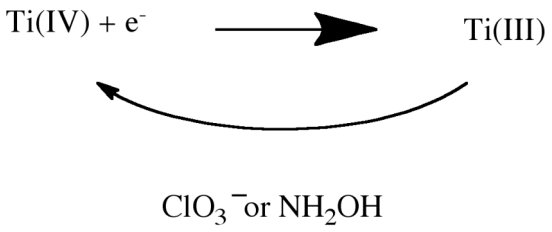
1.7.5 Catalytic Mechanism

A special case is the electron transfer process followed by the regeneration of the starting material by a chemical step, known as a *catalytic mechanism* (**Equation 1.54**).

$$O + e^- \rightleftharpoons R \qquad \textbf{[1.54]}$$

$$R + A \rightarrow O$$

For example, the reduction of Ti(IV) in the presence of a substance such as NH_2OH or ClO_3^-, capable of oxidizing Ti(III)[2].



1.8 Electroanalytical Techniques

1.8.1 Linear Sweep Voltammetry

Linear sweep voltammetry (LSV) is closely related to cyclic voltammetry as discussed below. Such experiments are typically performed in an unstirred solution, containing an electro – active species. LSV relies on the mass transport of species to the electrode surface. The potential of the working electrode is swept linearly from E_1 to E_2 according to **Equation 1.55**[5]. This is displayed schematically in **Figure 1.7**.

$$E(t) = E_1 - \upsilon_s t \qquad [\mathbf{1.55}]$$

Considering the simple one – electron reduction of species A to species B (*i.e.* $A + e^- \rightarrow B$), sweeping of the potential to more negative potentials will increase the rate while the concentration of species A at the electrode surface ($[A]_0$) will steadily decrease. The maximum current (I_p) represents a balance between these two factors. At potentials more negative than E_p, the shape of the voltammogram is dictated by the rate of diffusion to the electrode surface, while the portion preceding E_p is controlled by the electrode kinetics. Irreversible LSV will display E_p at more negative values than reversible systems. No current flows in the irreversible case until the potential is considerably more negative than the equilibrium potential, E_e. On the other hand, the reversible case displays an appreciable current at potentials much less negative than E_e. This is expected for the rapid electrode kinetics typical of reversible process, such that as soon as the reaction becomes thermodynamically favourable, current will begin to flow.

1.8.2 Cyclic Voltammetry

Cyclic voltammetry (CV) is by far the most common electro – analytical technique employed, and is often the first port of call in an electrochemical study, facilitating the rapid location of redox potentials. Cyclic voltammetry can be used to provide qualitative data on the system of interest, including kinetics of heterogeneous electron transfer, thermodynamics of a redox process, of coupled chemical reactions and of adsorption processes. The CV experiment involves the application of a potential to the working electrode, which changes with time, according to a triangular potential waveform as shown in **Figure 1.7**. The plot of *I vs. E* is known as a voltammogram. Single or multiple cycles can be employed depending on the information required.

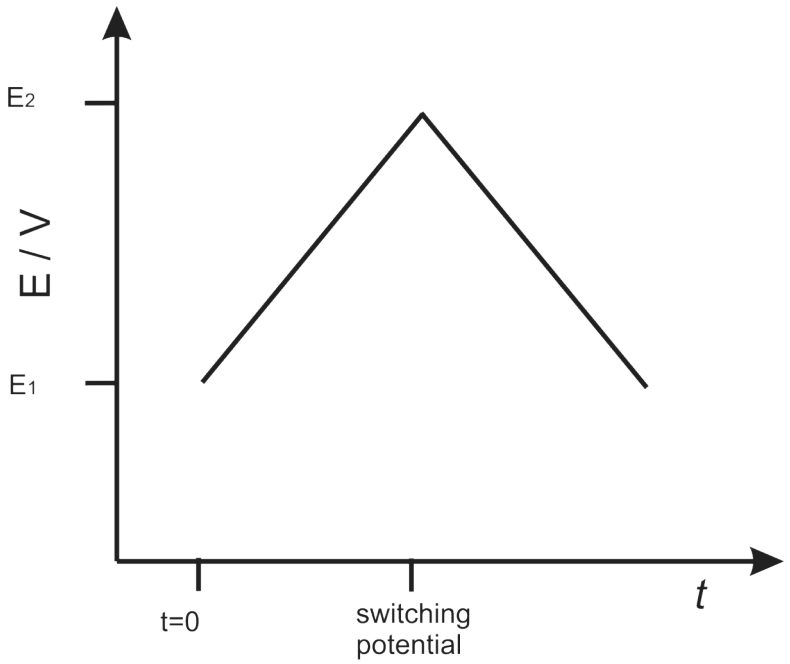


Figure 1.7

A triangular cyclic voltammetric waveform. Slope of the line equals the scan rate (υ / Vs^{-1}).

The starting potential (E_1) is typically chosen where there is negligible current flow. The potential is then swept in a linear manner to a voltage, E_2, known as the switching

potential at which point the direction of the scan is reversed. The potential window ($E_2 - E_1$) is usually chosen to include a redox process.

We will consider the generalized simple electrode process (**Equation 1.56**), where both *A* and *B* are solution phase species.

$$A + e^- \rightleftharpoons B \qquad [\mathbf{1.56}]$$

The variation in current with applied potential will depend on the standard electrochemical rate constant (k^0) and the formal potential of the A/B redox couple, diffusion coefficient (D) of species A and B, as well as the voltage sweep rate (υ / $V\ s^{-1}$). In a typical reversible redox couple, the current will increase as the applied potential approaches the characteristic E^0 of the process. The current will increase until a peak is reached. At a point (at least $90 / n\ mV$) beyond the peak, the scan direction is reversed and the molecules formed in the forward sweep (*i.e. B*) are re – oxidised back to *A*, generating an anodic peak. The peaks recorded in a cyclic voltammogram result from the formation of a diffusion layer near the electrode surface. The i_p reflects the continuous change in the surface concentrations coupled with expansion of the diffusion layer, over time. Once the electrode potential reaches a value at which the surface concentration of the electro – active species is close to zero the current will begin to decay. Therefore, a current maximum corresponds to the achievement of diffusion control while the current drop beyond the peak is independent of the applied potential and exhibits an inverse square root of time ($1/\sqrt{t}$) dependence.

1.8.2.1 Reversibility

Electron transfer processes display different limiting behaviours corresponding to the value of the standard electrochemical rate constant (k^0). A "large" value is characterized as electrochemically reversible with fast electrode kinetics while a "small" value of k^0 characterizes electrochemically irreversible behaviour with slow electrode kinetics. When we use the terms "large" or "small", more specifically we mean with respect to the rate of mass transport[2]. **Figure 1.8** shows typical reversible, irreversible and quasi – reversible voltammetry obtained by varying the value of k^0, keeping all other variables constant.

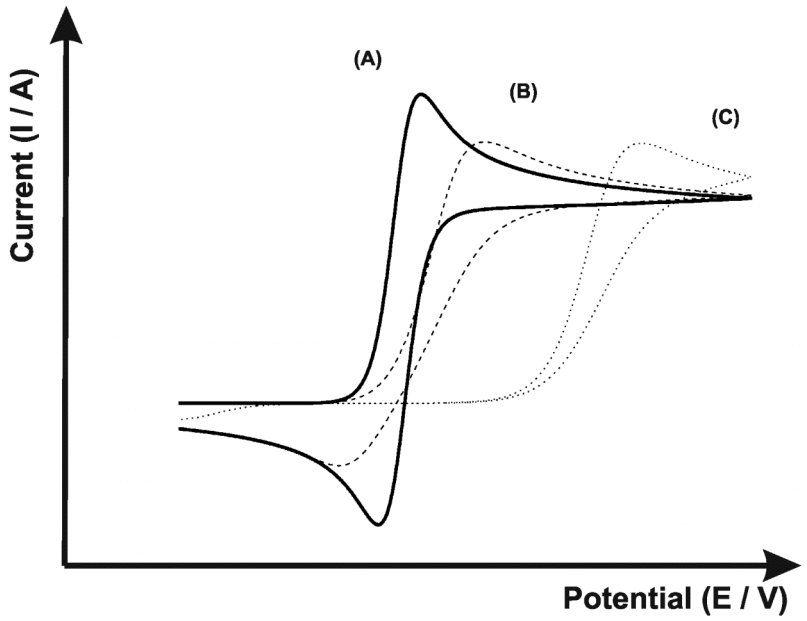


Figure 1.8

Examples of reversible (A), quasi – reversible (B) and irreversible (C) cyclic voltammetry.

For the fully reversible *A / B* redox couple the peak current (i_p) can be predicted by the Randles – Sevčík Equation as shown below[6]:

$$i_p = (2.69 \times 10^5) n^{3/2} A C D^{1/2} \upsilon^{1/2} \qquad [\mathbf{1.57}]$$

In the above expression, n represents the number of electrons, A is the electrode area (cm^2), C is the concentration ($mol\ cm^{-3}$), D the diffusion coefficient ($cm^2\ s^{-1}$) and υ is the scan rate ($V\ s^{-1}$).

The current is directly proportional to the concentration and increases with square root of scan rate ($\sqrt{\upsilon}$). For a simple one – electron reversible couple, the ratio reverse – to – forward peak currents ($i_{p,r} / i_{p,f}$), is unity. The peak position (E_p) can be related to the formal potential of the redox process and centred between $E_{p,a}$ and $E_{p,c}$ according to **Equation 1.58**.

$$E^0 = \frac{E_{p,a} + E_{p,c}}{2} \qquad [\mathbf{1.58}]$$

The separation between peaks for a typical reversible couple is given by **Equation 1.59**. The peak – to – peak separation can be used to determine the number of electrons transferred in the process as well as a criterion for Nernstian behaviour.

$$\Delta E_p = E_{p,a} - E_{p,c} = \frac{0.059}{n} V \quad (\text{at } 25^\circ\text{C}) \qquad [\mathbf{1.59}]$$

That is to say that a fast one – electron process will have a peak separation, $\Delta E_p = \sim 59mV$ at 25ºC.

Cyclic voltammetry can be particularly useful in the diagnostics of non – ideal systems, such as those where the redox reaction is slow or coupled with a chemical reaction.

Irreversible and quasi – reversible systems display sluggish electron transfer. The voltammetry in these cases is distinguished by reduced magnitude of individual peaks and the wider separation between peaks. The peak current (I_p) of an irreversible electrode process, can be predicted by a modified Randles – Sevčík equation as shown in **Equation 1.60**[6].

$$i_p = (2.99 \times 10^5) n(\alpha n_a)^{1/2} ACD^{1/2} \upsilon^{1/2} \qquad [\mathbf{1.60}]$$

A quasi – reversible system displays behaviour intermediate between these reversible and irreversible limits. Typical rate constants for quasi – reversible processes lie in the range of $10^{-1} > k^0 > 10^{-5} cm\ s^{-1}$. The recorded current is controlled by both the charge transfer and mass transport, such that the voltammetric wave shape is a function of $\frac{k^0}{\sqrt{\pi a D}}$ where $a = \frac{nF\upsilon}{RT}$. Very fast scan rates (*i.e.* small values of $\frac{k^0}{\sqrt{\pi a D}}$) result in the system exhibiting irreversible behaviour. Conversely, increasing the value of $\frac{k^0}{\sqrt{\pi a D}}$, the process approaches a more reversible case.

1.8.3 Chronoamperometry

Potential step chronoamperometry refers to the limiting case, where the potential is stepped from E_1 to E_2, corresponding to a potential where no electrolysis takes place and one where full conversion occurs at the electrode surface, respectively. **Figure 1.9** shows the variation in applied potential in a typical potential step experiment[5].

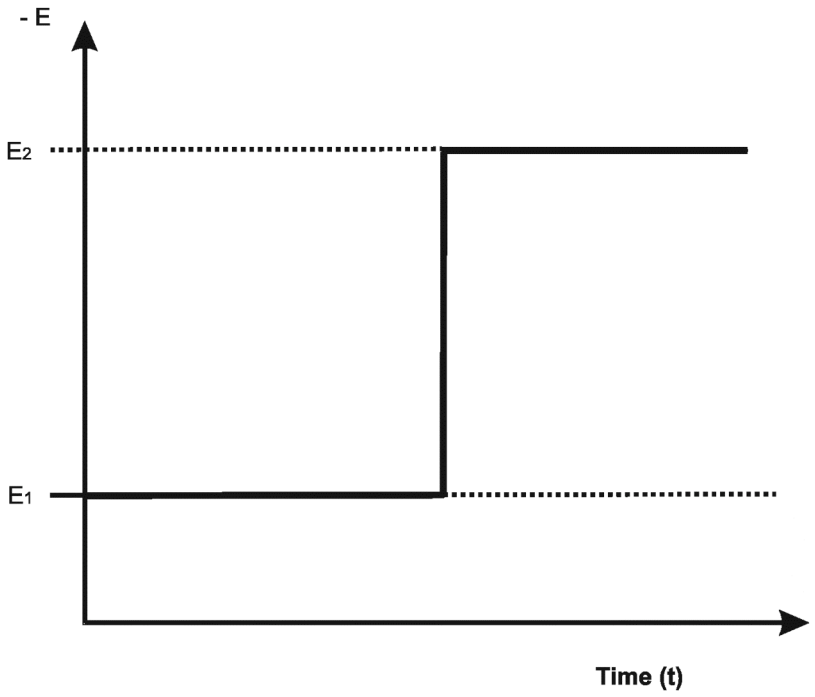


Figure 1.9

The variation in applied potential used in a potential step experiment.

The result is a large increase in current that decreases steadily with time. **Figure 1.10** shows a typical example of the voltammetric response following a potential step. Such large initial currents are due to the steep concentration gradients experienced as short time implies little time for diffusion to occur.

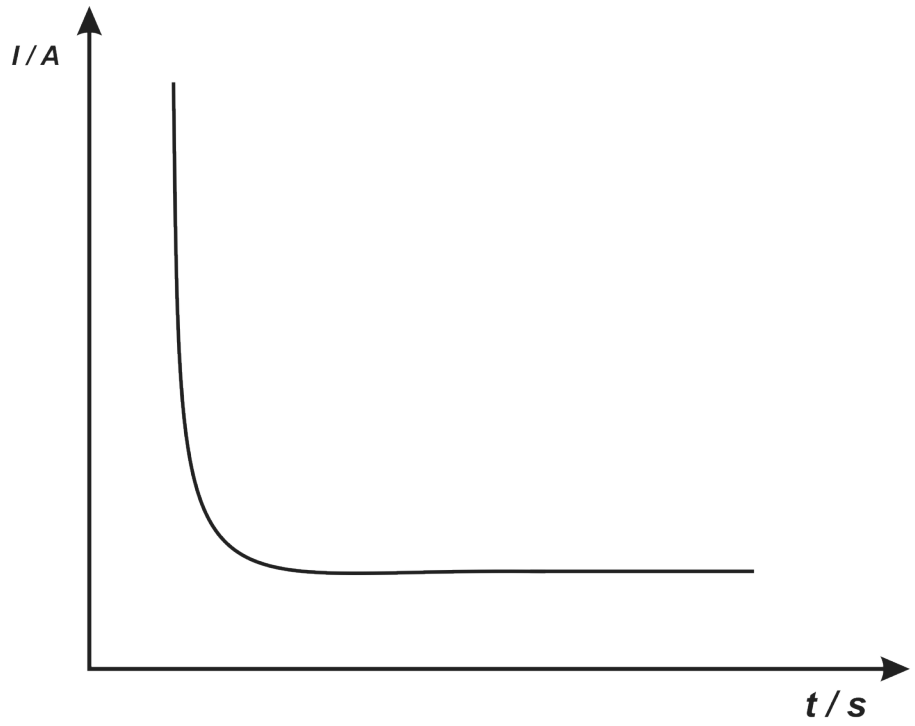


Figure 1.10

Typical example of voltammetric trace obtained following a potential step[5].

Over time the diffusion layer thickness increases, and the current falls, ultimately to zero. Chronoamperometry can be used to determine information on the diffusion coefficient of species in solution[5]. The Cottrell Equation has been used to describe such current responses as discussed earlier in this chapter (**Section 1.4.2.2**).

Chapter 1: References

1. R. G. Compton and C. E. Banks, *Understanding Voltammetry*, 1st edn., World Scientific, Singapore, 2008.

2. A. J. Bard and L. R. Faulkner, *Electrochemical Methods: Fundamentals and Applications*, 2nd edn., John Wiley & Sons, Inc., New York, 2001.

3. R. G. Compton and G. H. W. Sanders, *Electrode Potentials*, Oxford University Press, Oxford, 1996.

4. P. H. Rieger, *Electrochemistry*, 2nd edn., Chapman & Hall, New York, 1994.

5. A. C. Fisher, *Electrode Dynamics*, Oxford University Press, Oxford, 1996.

6. J. Wang, *Analytical Electrochemistry*, 2nd edn., Wiley-VCH, New York, 2001.

Chapter 2

The Theory and Use of Nanoparticles in Electroanalysis: An Overview of the Recent Literature.

Abstract

The use of nanoparticles in the field of electro – analysis continues to expand at a rapid rate, with recent research trends indicating the development of novel synthetic procedures, sensing devices and biological applications. It is well known that nanoparticulate materials possess a variety of unique properties (*e.g.* enhanced mass transport, high surface area, improved signal – to – noise ratio, *etc.*), which can often be advantageous in electro – analytical techniques. In this chapter we concentrate our effort on an in – depth review and discussion of the recent advances made with regards to the synthesis, characterization and electro – analytical application of silver, gold, platinum, palladium, ruthenium, copper and nickel nano – materials. The conditions under which these materials are likely to be stable have been identified for each metal discussed, in order to aid practitioners in the field of nano – electrochemistry.

2.1 Introduction

Electro – analysis is a straightforward means of determining species in aqueous solution, both quantitatively and qualitatively. Electro – analytical techniques have a number of advantages over other detection methods such as chromatography, luminescence and spectroscopy: particularly, the low associated cost, ease of use, accuracy and reliability. A variety of techniques are available to the researcher to study the electrochemistry of electro – active species in solution. Analytical techniques employed include cyclic voltammetry (CV), differential pulse voltammetry (DPV), chronoamperometry (CA), linear sweep voltammetry (LSV) and stripping voltammetry. These are all effective electro – analytical techniques provided they are optimized to obtain the best electrochemical response. These processes can be influenced by several factors, including the nature of the analyte under investigation, the type of electrode and choice of electrolyte. The size and morphology of the electrode as well as the fabrication method used can be very influential on the voltammetric response of the system. When we use an array of nanoparticles (NPs), as is common, we should also consider the effect of increasing surface coverage on the voltammetry observed. Campbell *et al.* have studied H_2O_2 reduction at a silver nanoparticle array[1], which has shown that the voltammetric trace for H_2O_2 reduction will vary with both NP size and extent of surface coverage. In the study of H_2O_2 , decreasing the NP size causes a negative shift in the peak potential whereas increasing the coverage causes a positive shift. This is discussed in greater detail in **Chapter 5** of this thesis. Additionally, NP size – effects have been simulated by Ward Jones[2] for the anodic stripping voltammetry of various sizes of AgNPs and compared with experimental data. An in depth discussion of this behaviour is provided in **Chapter 9**.

In recent years the study of metallic nanoparticles has been extensive. The specific properties exhibited at the nano – scale, which are not typical of the corresponding bulk materials, underpins the significance of nanoparticulate materials in electro – analysis. These include enhanced diffusion based on convergent rather than linear diffusion at the smaller NPs, high active surface area, improved selectivity, catalytic activity, higher signal – to – noise ratio, unique optical properties, *etc*. The use of nanoparticles also provides control over the local micro – environment. This can be highly advantageous when incorporating sensitive or biological material into a system. These unique properties make nano – materials ideally suited for electro – analytical applications. Enhanced convergent mass transport to nano – electrodes facilitates the study of faster electrochemical processes. At the nano – scale, crystal planes may be exposed, which are not accessible at the macro – scale, in turn giving improved current responses and catalytic behaviour. Commonly used metals for nanoparticles are gold, silver and platinum. The electro – analytical application of such nano – materials has been found to be quite extensive. This suggests the potential for study of a wide variety of metal nanoparticles. Not only typically used electrode materials such as those mentioned above but also metals such as palladium (Pd), ruthenium (Ru), nickel (Ni) and copper (Cu). NPs of bismuth (Bi) and iridium (Ir) have also been recently synthesized. Manufacture of NP – based devices can have cost savings over conventional macro – electrodes as only a fraction of the expensive metal is required. Clearly there is a great deal of scope for further study in this area of electrochemistry.

The review by Welch et al.[3], has provided a comprehensive overview of synthesis and application of metallic nanoparticles to date. It has received *ca.* 100 citations at the time of writing. This chapter provides an updated review of this area, covering the most recent trends and advances in both the preparation of subsequent utilization of

NPs in electro – analytical techniques. We will discuss in detail, the synthesis and practical application of several metallic NPs, on a metal – by – metal basis.

In practical applications it is important to note that the pH or electrode potential conditions applied to various NPs may cause either dissolution or the formation of surface oxides. For example, copper and nickel NPs are difficult to prepare oxide – free. To assist practitioners in the field we start each section by indicating the apparent range of pH and potential where the *bulk* metal exists as a stable form. This provides an appropriate guide to the range of stability of the metal particles; usage outside of these ranges may require consideration of issues of dissolution or oxide formation. These have been adapted form the corrosion / immunity / passivation diagrams given in '*Atlas of Electrochemical Equilibria in Aqueous Solutions*' by M. Pourbaix[4].

2.2 Nanoparticles in Electro – analysis

A wide variety of metallic nanoparticles have been studied in order to assess the applications of these materials in electro – analysis. This introduction to NPs provides an in depth discussion of some recent synthetic procedures and common trends in the electro – analytical application of common NPs such as silver, gold and platinum. We have also outlined advances in the synthesis and application of less commonly used metal nanoparticles including Pd, Cu, Ru, Ni and Bi.

2.2.1 Synthesis and Application of Silver Nanoparticles

Silver is an ideal material for the construction of electrodes. It has the highest electrical conductivity of all metals and is highly stable[5]. Silver is known to catalyze reactions including the decomposition of H_2O_2 and is an important material in the electro – analytical determination of a variety of analytes including halides, toxic compounds, organic compounds and biomolecules. AgNPs can be synthesized via a number of methods as detailed below. However, as it is a relatively expensive metal AgNPs could provide an economical alternative as well as the additional benefits provided by nano – materials as discussed above. The stability of silver across a range of pH and potentials is outlined in **Figure 2.1**.

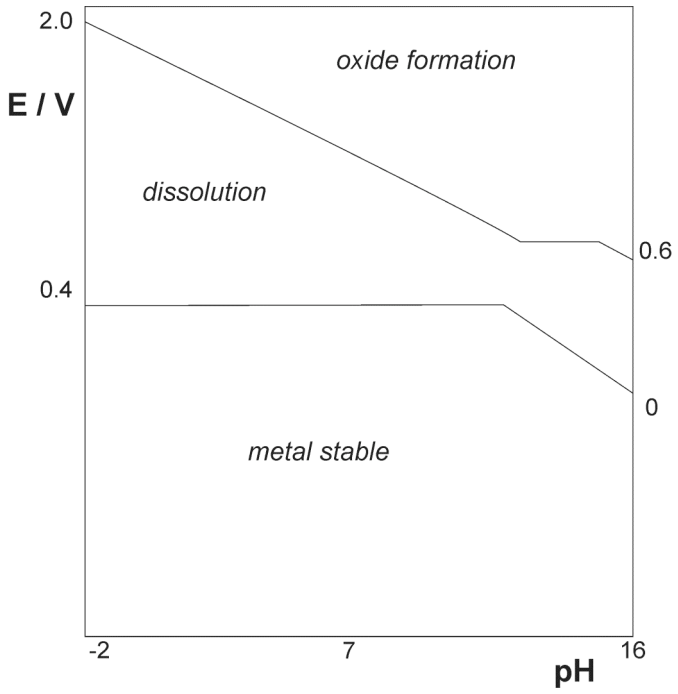


Figure 2.1

A simplified diagrammatic representation of the stability of silver metal, reported across a range of pH and potential values, at 25°C [4]. By convention, the lines are drawn for ions at unit activity.

2.2.1.1 Colloidal Silver Nanoparticles

The most typical method of AgNP preparation in recent years is by reduction of a silver salt in the presence of a protecting / stabilizing agent. This is commonly performed in an aqueous surfactant polymer solution as the composition of the reaction mixture can be very easily altered to employ different reducing and capping agents, to obtain Ag (0) NPs. Stabilising agents such as citrate[6], oleate[7], humic acid[8] and CTAB[7] are typically used. In recent years, more 'exotic' stabilizing agents have been employed in the preparation of AgNPs. These include the lipopeptide biosurfactant surfactin, as described by Reddy et al.[8]. A silver salt ($AgNO_3$) was reduced by $NaBH_4$, in the presence of surfactin, demonstrating a renewable and environmentally compatible synthesis. The NPs produced were uniform in both size

and shape and were shown to vary in size with both pH and reaction temperature. NPs were characterized by UV –vis, XRD and TEM.

Similarly, the stabilization of AgNPs has also been achieved by use of α-cyclodextrin (α-CD) to produce AgNPs (d_{avg} = 5.3 nm) in water[9]. Stabilization occurs via the hydrophobic interactions of the NPs with apolar primary faces of α-CD. These interactions also facilitate the assembly of two – and three – dimensional structures.

The ability to control the size and morphology of NPs in a synthetic procedure is vitally important as these factors can greatly influence the electrochemical behaviour of NPs. For example, reduction of $AgNO_3$ by D(+) – glucose or by NaOH in 1% starch solution (70°C, 30 min) generates spherical NPs with diameters of 15 and 43 nm, respectively. The smaller NPs are attributed to slower reduction rates of the milder glucose reducing agent compared to NaOH[10]. Furthermore, a mixture of ethylene glycol and polyvinylpyrolidone (EG / PVP) and a suitable reducing agent can be used to produce cubic NPs[11]. Various NP shapes have been achieved including nano – prisms, rods, wires, plates and belts[12].

Some alternative solution methods of preparation for AgNPs, have included the use of biomolecules and microwave heating[13]. This particular method uses stabilizing agents, such as starch, and basic amino acids such as L – lysine and L – arginine as mild and renewable reducing agents. Characterization by TEM, UV – vis and SEM shows NPs, which are highly crystalline, spherical, with an average diameter of 26.3 nm. Synthesis by a reverse micro – emulsion system has also been employed[14].

The biocompatibility of certain colloidal NPs makes them ideal for the examination of electron transfer processes of biomolecules. Oleate stabilized AgNPs (d_{avg} = 15 nm) have shown application in the analysis of Cytochrome c[15]. The NPs enhance the electron transfer process between Cytochrome c and the electrode as compared to

bulk silver. Linear sweep voltammetry shows a linear relationship between peak current and concentration of Cytochrome c in the range of 8 nM L^{-1} – 3 μM L^{-1}, and limit of detection, *LOD* = 2.3 nM L^{-1}. The oxidation of Cytochrome c on AgNP – modified electrode gave a peak at – 0.019 V (*vs. SCE*), increasing linearly with scan rate (υ) from 10 – 300 mV s^{-1}, demonstrating the adsorption controlled nature of this process.

The Turkevich method was pioneered in the 1950s for the synthesis of colloidal NPs. This approach has been modified to prepare AgNPs with DNA immobilized on their surface. This method typically used a silver salt ($AgNO_3$) and sodium citrate acting as a reducing agent with heating. Charged citrate ions adsorb onto the NP surface to stabilize AgNPs and prevent aggregation. Predominantly spherical NPs of (d_{avg} = 66 ± 16 nm) were synthesized and applied to the electrochemical sensing of silver tag labelled DNA, immobilized on a pencil graphite electrode (PGE)[16]. DNA can be immobilized on the surface of the AgNPs, followed by the surface modification of PGE by passive adsorption. Electrochemical detection is made possible by conversion of the base pairing recognition event to an electrical signal, based on the oxidation signals of silver (~ 131 mV) and guanine (~ 1000 mV) *vs. Ag/AgCl*. Such analysis can potentially be extended to provide an accurate and simplistic method of patient diagnosis.

2.2.1.2 Electro - deposition of Silver Nanoparticles

AgNPs can be very easily deposited via electrochemical methods, typically by potentiometric techniques, such as pulsed or constant potential application. Furthermore, stripping of a film can result in NPs of various sizes depending on the duration of applied stripping potential.

The determination of chromium (VI) at AgNPs on screen – printed electrodes has

been investigated by Domínguez – Renedo[17]. The AgNPs were deposited from a buffered solution (pH 2) of $AgClO_4$ by application of – 0.8 V (*vs. Ag/AgCl*) for 400 s under stirring. SEM analysis showed NPs produced via this method were aggregated. Differential pulse voltammetry was used in determination of Cr (VI), with high sensitivity and low $LOD = 8.5 \times 10^{-7} M$, without other interferences. Advantages of such methods include facilitating simple mass production of disposable electrodes as well as the ability to easily alter the composition of inks used in screen printing, to allow incorporation of enzymes, polymer, complexing agents, etc.

It has also been possible to electrochemically deposit Ag – DNA hybrid NPs, by the addition of DNA to the deposition solution, acting as a template. DNA prevents aggregation of particles, improving catalytic ability for the reduction of H_2O_2 and glucose[18]. The Ag – DNA NPs of uniform dimension were deposited on to a glassy carbon electrode (GCE). Direct reduction of H_2O_2 using Ag – DNA NPs, displays a linear response of 2.0 μM to 2.5 mM, LOD = 0.6 μM and sensitivity 773 mM^{-1} cm^{-2}. Glucose sensing is based on O_2 consumption with oxidation of glucose, catalyzed by immobilized glucose oxidase (*GOx*). A linear response in range of 50 μM to 1.2 mM and LOD = 9.0 μM was obtained, while excluding typical interferences.

Casella et al.[19] used a GCE modified with Ag particles (d_{avg} = 600 nm), in the study of the electro – reduction of nitrophenolic compounds. The GC/Ag electrode is constructed using a multi – pulse of potentials of equal amplitude and duration. The potential is pulsed between E_1 = - 0.6 V and E_2 = 0.2 V (*vs. SCE*) for relevant times of t_1 = 50ms and t_2 = 50 ms, for 200 cycles in deoxygenated $AgNO_3$ solution (5 mM). This resulted in an assembly of globular homogeneous, well – dispersed particles. Although nitrophenols can be reduced at the GCE surface the potential required for reduction at Ag is far less negative. Furthermore, the shape of the voltammetric wave for the GC/Ag electrode is far less drawn out than of the response of the

polycrystalline Ag electrode. This indicates that the kinetics are much faster for the former.

A combinatorial approach designed by Sljukic[20] developed a practical means of bromide detection. A multi – metal electrode composed of AgNP, AuNPs and PdNPs, deposited on glassy carbon microspheres (GCMS) by electroless deposition, shows a voltammetric response in the presence of bromide. The AgNPs (200 – 700 nm) are identified as electro – active for bromide and an individual AgNP – GCMS/epoxy composite electrode was then constructed and bromide detection examined. Signals were found to be stable and reproducible and a *LOD* = 3 μM was calculated.

2.2.1.3 Alternative Preparation Methods

Bio – catalytic deposition of AgNPs has been utilized in electrochemical immunoassays to provide an ultra sensitive, low *LOD* method of determining immunoglobulin (*IgG*)[21]. This method uses a heterogeneous sandwich procedure to immobilise the antibody *IgG* in polystyrene microwells. *IgG* determination is based on biocatalytic deposition, followed by Ag enhancement, characterization of the NPs by SEM and finally quantification by electrochemical assays.

Nano – silver on multi – walled carbon nanotubes (MWCNTs) have been synthesized to construct composite films, used in electroanalysis of H_2O_2 [22]. A dispersion of Ag/MWCNTs can be cast onto a GC electrode, where cathodic DPV peaks are measured (- 0.5 → - 0.7 V *vs. SCE*) as the analytical signals. H_2O_2 reduction is recorded at – 0.64 V (*vs. SCE*) on Ag/MWCNTs/GC. A linear concentration range is exhibited from 0.35 – 15 mM H_2O_2, *LOD* = 0.2 mM. An increased current is facilitated by nano – scale particles and smaller overpotentials are required for H_2O_2 reduction.

Similarly, the plating of Ag onto CNTs has been used in the detection of DNA hybridization, based on a Ag/CNT probe[23]. The probe is constructed by labelling of single strand DNA (ss – DNA) with Ag/CNT. The binding of the ss – DNA is monitored electrochemically by DPV and it is possible to distinguish between perfectly complementary DNA and that which is a near perfect match.

2.2.2 Synthesis and Application of Gold Nanoparticles

Gold is also an efficient conductor of electricity and is known for its malleability and ductility[5]. Gold nanoparticles (AuNPs) can be very useful in place of bulk gold electrodes, as they require much less of the expensive material. Previous work has shown extensive uses of AuNPs in electro – analysis. Recent studies have shown the biocompatibility of AuNPs is highly advantageous, enabling the incorporation of biomolecules such as enzymes and proteins into electrochemical systems. Reviews focusing specifically on AuNP – based biosensors can be found in the literature [24 25]. The next section discusses the preparation of AuNPs by electro – less and electrochemical methods and their subsequent applications in electro – analysis. **Figure 2.2** displays the stability of gold as a function of pH and potential conditions.

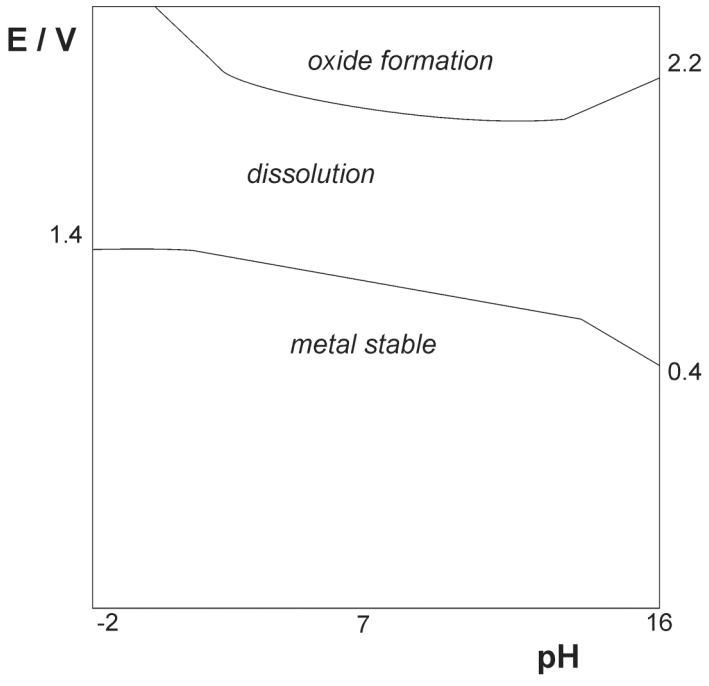


Figure 2.2

A simplified diagrammatic representation of the stability of gold metal, reported across a range of pH and potential values at 25℃ [4]. By convention, the lines are drawn for ions at unit activity.

2.2.2.1 Colloidal Synthesis of AuNPs

The ability of AuNPs to provide stable environments for the immobilization of biomolecules has lead to many developments in the design of enzyme biosensors, DNA sensors and immunosensors. Enzyme – based electrodes can be prepared by immobilization of enzymes such as glucose oxidase (*GOx*), horseradish peroxidase (*HRP*) and tyrosinase (*TYR*) on colloidal AuNPs. The NPs were then mixed in a carbon paste used to construct electrodes. Electro – polymerisation methods are also used to construct immobilization matrices for NPs and appropriate biomolecules. Commonly used polymers include polypyrrole, polyaniline and chitosan. NPs can also be immobilized om self – assembled monolayers (SAMs) of thiols[26, 27]. Citrate – stabilized AuNPs (d_{avg} = 13 nm), prepared according to the Turkevich method, can be functionalized using single strand DNA (ss – DNA) and used to facilitate the construction of a multilayer uniform self – assembled structure on the surface of a gold electrode. This method is based on the hybridization of complementary ss – DNA. Such assemblies are particularly useful for the study of biomolecules as they allow adsorption of the molecule in its native conformation. This methodology has been applied to the detection of Cytochrome c[28]. The redox peaks recorded in the voltammetry were assigned to the heme centre within the protein. This allowed detection of ultra low concentrations of the protein ($LOD = 6.7 \times 10^{-10} M$). AuNPs play an important role in this system as they help to promote electronic communication between the electro – active heme centre of the protein and the electrode surface.

A colloidal gold/cysteamine/carbon paste electrode ($Au_{colloid}$/Cyst/CPE) has demonstrated an improved voltammetric response for the redox of homocysteine compared to a Au macro – electrode, in pH 7 PBS [29]. This improvement is based on the claimed enhanced electron transfer kinetics. In the above system the $Au_{colloid}$ was

synthesized according to the citric reduction method, producing AuNPs, d_{avg} = 24nm. Two defined oxidation peaks were observed at + 650 and + 950 mV, the latter of which is well known as the oxidation to Au oxides. Therefore, the peak reported at + 650 mV can be assigned to oxidation of homocysteine. The Au macro – electrode displays a broad anodic peak from + 600 mV under the same conditions. This method was also applied to the amperometric detection of homocysteine at a $Au_{colloid}$ – array. Similar species such as glutathione, cysteine, penicillamine and cystine could also be detected using this system.

$Au_{colloid}$ synthesized as above can in turn be immobilized on L – cysteine (LC) modified GCE, by immersion in a suspension of $Au_{colloid}$ for 10 hours at 4°C. Characterization by SEM and XPS confirmed immobilization of $Au_{colloid}$ on the electrode surface. Determination of uric acid (UA) and ascorbic acid (AA) on a GC electrode proves to be difficult due to the proximity of oxidation peaks, resulting in a broad anodic peak from 0.116 – 0.579 V (*vs. SCE*). However, use of a $Au_{colloid}$/LC/GC electrode allowed both UA and AA to be detected simultaneously[30] as the peaks are separated by ~ 0.306 V. Differential pulse voltammetry (DPV) for increasing UA concentrations in the presence of $2.0 \times 10^{-3} M$ AA had a linear concentration range of $6.0 \times 10^{-7} - 8.5 \times 10^{-4} M$ and a $LOD = 2.0 \times 10^{-7} M$. Similarly, for increasing concentrations of AA in the presence of $2.5 \times 10^{-4} M$ UA, a linear range of $8.0 \times 10^{-6} - 5.5 \times 10^{-3} M$ and a $LOD = 3.0 \times 10^{-6} M$ were obtained.

The preparation methods used by Jena et al.[31] to synthesize gold nano – seeds (GNS) were applied to the amperometric detection of toxic chromium (VI). This method adopts use of a sol – gel derived thiol functionalized silicate network on a Au macro – electrode, to facilitate self-assembly of Au nano – seeds. The nano – seeds can then be grown via a seed – mediated mechanism in a solution of 0.3 mM NH_2OH and 0.03 mM $HAuCl_4$, resulting in the construction of a gold nano – electrode ensemble (GNE)

comprised of AuNPs (d_{avg} = 85 nm), as characterized by XRD, SEM, UV – vis and electrochemistry. This system is highly sensitive and capable of detecting sub – ppb concentrations of Cr(VI) without typical interferences from Cr(III) ions. The response of GNS (~ 0.25 V *vs. Ag/AgCl*) and GNE (~ 0.4 V *vs. Ag/AgCl*) to the presence of Cr(VI) is attributed to the three – electron reduction to Cr(III). The voltammetric behaviour of the GNE electrode is strongly dependent on NP coverage, exhibiting a positive shift in peak potential with increasing coverage.

2.2.2.2 Electro - deposition of AuNPs

Electro – deposited AuNPs alongside immobilization of various enzymes have been employed to construct AuNP – based biosensors. In these examples a GC electrode is modified by electrodeposition of AuNPs followed by attachment of the appropriate enzyme by cross – linking with glutaraldehyde (*GA*). Phenolic compounds such as phenol, catechol and caffeic acid have been determined by a tyrosinase biosensor [32]. Optimized conditions were determined as a deposition of AuNPs at – 200 mV for 60 s and a detection potential of – 0.10 V (*vs. Ag/AgCl*) in phosphate buffer (pH 7.4). As the enzyme reaction involves the catalytic oxidation of the phenolic compound to corresponding *o* – quinones, this allowed the reaction to be followed by the electro – reduction of these quinones. This method gave analytical characteristics similar to those reported in the literature and can be used to determine polyphenols in samples of wines.

Similarly, an amperometric biosensor for hypoxanthine (*Hx*) was constructed by electro – deposition of Au nano – crystals on a carbon paste electrode (*CPE*) at – 400 mV (*vs. Ag/AgCl*) for 15 mins[33]. Immobilization of the xanthine oxidase (*XO*) by cross – linking with *GA* and bovin serum albumin (*BSA*) allows an applied detection potential of 0.0 V to be employed as opposed to the typical + 600 mV. Consequently,

interferences (*e.g.* ascorbic acid) can be minimized. Under optimized experimental conditions, a linear concentration range of 0.5 – 10 μM and $LOD = 2.2 \times 10^{-7} M$ was attained. This method can be applied practically to the determination of *hypoxanthine* in foodstuffs.

Colloidal AuNPs were electrodeposited on a planar Au electrode to facilitate attachment of the acetylcholinesterase enzyme (*AChE*). The electrochemical detection of thiocholine could be recorded at the Au electrode following the hydrolysis of acetylthiocholine[34]. In the absence of the enzyme no response was recorded at the Au electrode. A far improved voltammetric signal is obtained for the AuNP/*AChE* electrode as compared to Au/*AChE* for the oxidation of thiocholine at ~ 680 mV (*vs. Ag/AgCl*). This indicated the roughened surface of AuNP – modified electrode provides favourable conditions for the immobilization of the enzyme. At the detection potential of + 680 mV, a linear concentration range of 1 – 6 μM and *LOD* = 100 nM could be achieved for this system. This method can also be used to investigate the inhibition of the enzyme by toxins.

An electro – aggregation method used with commercially available AuNPs (d_{avg} = 5 nm) to generate a mesoporous gold deposit on the surface of a boron doped diamond (BDD) electrode has been used to detect arsenic (III) in phosphate buffered media[35]. It is possible to control the amount of Au deposited and thus the accessible Au surface by changing the deposition time at – 5 V (40 mM $NaClO_4$, 0.01% $HAuCl_4$ *vs. SCE*). This method can be applied to real samples (*e.g.* water) around neutral pH values. Typical voltammetry of 10 mM As(III) in phosphate buffer media shows a reduction peak at – 0.44 V (*vs. SCE*) and the corresponding stripping response at – 0.12 V in the reverse scan direction, as well as the oxidation of arsenite to arsenate at + 0.5 V.

These peaks are shown to change linearly with As concentration and the *LOD* = 0.03 μM.

2.2.2.3 Electro - less Plating

AuNPs (20 – 200 nm diameter) have been synthesized by electro – less reduction of $AuNa(S_2O_3)_2$ by L – ascorbic acid on to a GCMS substrate. GCMS can subsequently be abrasively attached to a BPPG electrode. This material was then used in the determination of As(III). A peak for the detection of As(III) was recorded at + 0.2 V (*vs. SCE*), in acidic media. A linear response in E_p was shown with increasing As(III) concentration. This system provides a *LOD* = 0.8 μM and a sensitivity of 0.90875 C M^{-1}.

Polymer beads of poly(methyl methacrylate) (PMMA) or polystyrene (PS) were used as typical substrates for immobilization of AuNPs[36]. NPs can be directly deposited by dropwise addition of $NaBH_4$ to a solution of $Au(en)_2Cl_3$, without the need for PMMA surface modification. Drop wise addition of reducing agent results in the formation of small NPs of ~ 6.9 nm and also seems to prevent aggregation, as confirmed by TEM imaging. This material showed catalytic activity towards the reduction of 4-nitrophenol (4 – NP) to 4 – aminophenol (4 – AP), with an excess of $NaBH_4$. The pseudo – first order rate constant for the reduction of 4 – NP to 4 – AP was calculated to be $k = 7.9 \times 10^{-3} s^{-1}$, the highest value reported to date for polymer – supported Au catalysts.

Specific nano – scale related properties of AuNPs, have been studied by Batchelor – McAuley *et al.* with regards to the underpotential deposition (*UPD*) of thallium on AuNPs of various sizes[37]. AuNPs were chemically deposited on MWCNTs by reduction of $HAuCl_4.H_2O$ with $NaBH_4$. The deposition and anodic stripping voltammetry of thallium was then investigated. Very small AuNPs of 10 nm do not

exhibit typical Tl *UPD* as compared to a Au macro – disk electrode or larger AuNPs (30 – 60 nm), under identical conditions. Similar behaviour has been reported by Campbell et al. for the *UPD* of lead, thallium and cadmium on AgNPs[38, 39]. The study of UPD on AgNPs is discussed in more detail in **Chapter 10**. This implies that these small NPs do not possess active sites with sufficient size to allow the deposition of such heavy metals to take place, in stark contrast to the macro – scale or micro – scale. Clearly the size and structure gives rise to properties significantly removed from the bulk equivalent.

2.2.3 Synthesis and Application of Platinum Nanoparticles

Platinum metal is used in industrial catalysis and can be found in the catalytic converters of vehicles, used to remove pollutants from car exhaust fumes. Platinum is more expensive than both silver and gold. Therefore, obvious economical advantages arise from use of PtNPs. Pt wires are often used in electrochemistry as electrodes due to their stability and conductivity. PtNPs are synthesized in a similar fashion to AuNPs and AgNPs. The stability of Pt metal is described schematically over a range of pH and potentials in **Figure 2.3**.

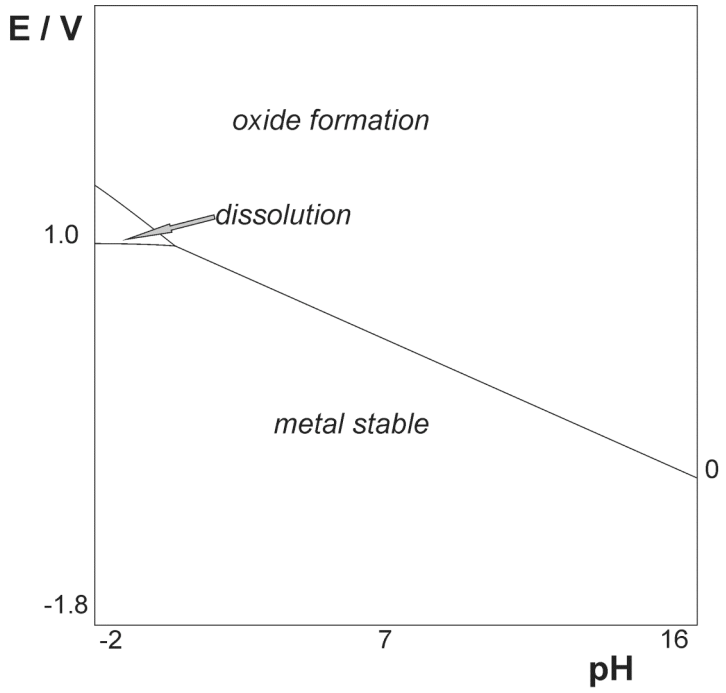


Figure 2.3

A simplified diagrammatic representation of the stability of platinum metal, reported across a range of pH and potential values, at 25°C [4]. *By convention, the lines are drawn for ions at unit activity.*

2.2.3.1 Colloidal Synthesis of PtNPs

Colloidal PtNPs are synthesized by reduction of hexachloroplatinate ($PtCl_6^{2-}$) in the presence of a citrate – capping agent. The $Pt_{colloid}$ can then be functionalized with nucleic acids. These materials were used as labels for the amplified bio – recognition of DNA hybridization, aptamer/protein recognition events and tyrosinase activity. In the case of DNA hybridization[40], this method conveniently eliminates the need for enzymes or antibodies in the analytical procedure. The electro – catalysed H_2O_2 reduction at PtNP labels enabled the amplified analysis of tyrosinase activity via the oxidation of tyrosine methyl ester – functionalized PtNPs, in association with a boronic acid functionalized gold electrode[41]. This methodology presents a lower sensitivity than others, but is comparatively the most simple and cost effective approach. Typical literature preparation methods of small PtNPs use dodecylamine and hexanethiol (3.0 ± 1.0 nm and 2.7 ± 0.4 nm, respectively) capping ligands. Studies of CO adsorption on Pt have been performed using these materials[42].

2.2.3.2 Electro – deposition of PtNPs

A simple method of depositing PtNPs on an electrode substrate is by electrochemical deposition from an aqueous solution of Pt salt. Carbon substrates are typically used in electroanalysis as they are cheap and easily modified. Platinum macro – electrodes have been shown to be useful in the detection of highly toxic arsenic, showing a low *LOD* with anodic stripping voltammetry. However, a common problem encountered is the interference from other metals (*e.g.* copper, lead, zinc, iron, *etc.*). Cu is a particular problem in stripping voltammetry as it can co – deposit alongside As. This can be resolved as the catalytic oxidation of As(III) to As(IV) by Pt is not affected by the presence of Cu. Use of NPs in particular can also help to improve the selectivity

of the system. By effecting a potential shift, the analytical peaks can be distinguished from common interferences. A glassy carbon electrode is modified by PtNPs by immersion in 1 mM $PtCl_6$ in 0.1 M KCl, followed by stepping the potential to + 0.5 V for 0.01 s then to 2.7 V (*vs. SCE)* for 120 s, while cycling[43]. Characterization of the electrode surface by AFM shows PtNPs with roughly spherical morphology (d_{avg} = 122 nm). The oxidation of As(III) to As(V) is recorded in the anodic scan at + 0.85 V (*vs. SCE*) in 0.1 M H_2SO_4, increasing peak height with As(III) concentration (100 mM to 500 mM). Current densities calculated for the NP – modified electrode were shown to be higher than equivalent geometric area of Pt macro – electrode. This is likely relating to difference in diffusional behaviour between the macro – and nano – scales. For the linear range of 1 to 50 μM, *LOD* = 0.028 ± 0.003 μM (2.1 ± 0.23 ppb) was calculated, compared to 0.48 ± 0.02 μM (35 ± 1.5 ppb) for a macro – electrode under the same conditions. This method provides a practical method for detection of arsenic; the WHO guideline value in water is reported as 0.01 mg/L[44].

Carbon nanotubes (CNTs) are a useful substrate for the immobilization of metallic NPs for use in electro – analysis, due to their electrical conductivity, small size, high surface area and durability. These materials have found extensive application in fuel cell technologies in recent years as an alternative to carbon black. Well – dispersed PtNPs can be electrochemically deposited on to CNTs very easily, with a considerably larger number of catalytic sites than those prepared by alternative methods. Small NPs are favourable for enhanced catalytic activity. PtNPs (d_{avg} = 2 nm) are synthesized on CNTs via a potential step electrochemical deposition technique[45], from 0.25 to 1.5 V (*vs. SCE*), for a 0.001s pulse in aqueous solution (1 mM K_2PtCl_6 + 0.5 M H_2SO_4). When compared to a Pt/C catalyst prepared by a wet – impregnation method, the ECD catalyst demonstrated significantly greater (~ 3×)

catalytic activity, as outlined by the CO adsorption results. We can attribute this increased activity to the small size and dispersion of the Pt catalyst.

As platinum is recognized as an excellent catalyst for methanol oxidation, we can apply these nano – scale electro – catalysts to this process, which in turn has implications for the direct methanol fuel cell (DMFC). However, it is important to attempt to overcome the typical problems associated with DMFC such as catalyst poisoning and slow electrode kinetics. PtNPs were deposited on a MWCNT paste electrode at a constant potential or by cyclic voltammetry (1 mM K_2PtCl_4 + 0.1 M K_2SO_4) and the resulting Pt/MWCNT paste electrode implemented as the working electrode in methanol oxidation. The optimum loading of platinum was calculated as 18 $\mu g/cm^2$ while TEM analysis showed small and well – dispersed PtNPs with d_{avg} = 5 nm[46]. A Pt/MWCNT electrode has good activity in the presence of methanol (0.5 M CH_3OH + 0.5 M H_2SO_4), displaying the typical two oxidation peaks at 0.5 and 0.75 V (*vs. SCE*) in the CV trace. A similar preparation of a Pt/SWCNT composite was adopted by Guo et al.[47], where TEM imaging displaying NPs d_{avg} = 6.5 nm.

Following on from the DMFC, direct formic acid fuel cells (DFAFC) have shown potential for powering portable devices. Roughly spherical PtNPs (16 ± 5 nm) are uniformly grown on a nichrome substrate by CV in a solution of 1 mM K_2PtCl_4 + 0.1 M K_2SO_4, as displayed in SEM imaging. PtNP/nichrome composites have been studied as suitable electro – catalysts for formic acid oxidation[48]. The nano – scale Pt modified nichrome showed 50 times greater activity towards formic acid oxidation compared to a bulk platinum electrode. Investigation of formic acid was performed in 0.1 M $HClO_4$ and CV showed two oxidation peaks at 0.4 and 0.7 V demonstrating nano – Pt retained the properties of its bulk counterpart. However, the nano – scale presents greater catalytic activity as well as reducing the cost of noble metal. Increased catalytic activity is indicated by higher current density for the

adsorption/desorption of hydrogen and the increase peak current for formic acid oxidation.

2.2.3.3 Electro – less Plating

Baron *et al.*[49] have recently constructed PtNP – arrays supported on glassy carbon microspheres (GCMS), by a simple electroless deposition method in aqueous solution. H_2PtCl_6 was reduced by L – ascorbic acid in the presence of GCMS (pH 5.2). This method has been shown to produce highly dispersed PtNPs of homogeneous size. This material could subsequently be used as a practical, low cost Pt nano – electrode array for proton detection, by abrasive attachment of the GCMS to a BPPG electrode. A linear response to H^+ concentration in the range 0.1 mM to 10 mM allows the determination of pH in the range 1 – 3, sensitivity of 0.46 mA mol^{-1} and *LOD* = 200 μM. When applied to the electro – oxidation of methanol, to assess possible applications in fuel cell technologies, poisoning of the electrode surface occurred rapidly. This represents a significant problem when using metal catalysts.

Carbon nanotubes (CNTs) are also commonly used as substrates for the immobilization of PtNPs. The electroless deposition of Pt has been achieved by utilizing the electrostatic interaction of $PtCl_6^-$ ions with functionalized MWCNTs, acting as the anchoring mechanism. The reduction of the salt by $NaBH_4$ forms PtNPs on the surface of the CNTs, d_{avg} = 6.5 nm. The electrochemical properties of the Pt/CNT composite material were then investigated with respect to catalytic activity towards alcohol oxidation. A CNT glassy carbon electrode has no activity for 1 M ethanol (C_2H_5OH) in 0.5 M sulphuric acid (H_2SO_4) whereas the Pt/CNT composite electrode showed high catalytic activity for ethanol oxidation, three distinct peaks occurring at 0.32, 0.64 and 1.12 V, respectively[50].

A chemical deposition technique developed by Wang *et al.*[51] utilizes conducting polymers to immobilize enzymes, while the introduction of PtNPs improves electron transfer between the electrode and the bio – molecules. This can in turn be used to construct an amperometric glucose biosensor based on the detection of H_2O_2 by PtNPs. This method presents a one – step preparation of the modified electrodes since the H_2PtCl_6 initiates the electro – polymerisation of pyrrole to polypyrrole, while itself being reduced to Pt metal. SEM characterization of the electrode surface showing a 3D – interacting network, with PtNPs of 50 – 500 nm. Successive additions of glucose in aqueous solution displayed a well – defined current response with a linear range of 0 – 12 mM, and a sensitivity of 0.05 mM. The improved current response on the GOx/Pt/PPy as opposed to the GOx/PPy electrode was thought to be due to the improved electron transfer between the entrapped enzymes and the electrode, facilitated by the presence of the PtNPs.

2.2.4 Synthesis and Application of Palladium Nanoparticles

Palladium metal shares similar properties to platinum, ruthenium, rhodium, osmium and iridium. Pd metal is believed to be a potential device for hydrogen storage due to its ability to absorb hydrogen, thought to form PdH_2. Uses of Pd include multi – layer ceramic capacitors, carbon monoxide detection, catalysis and organic synthesis. An overview of Pd stability to changing pH and potential is shown in **Figure 2.4**. The study of synthesis and electro – analytical application of PdNPs is an area which has generated a significant body of work in recent years, as discussed below.

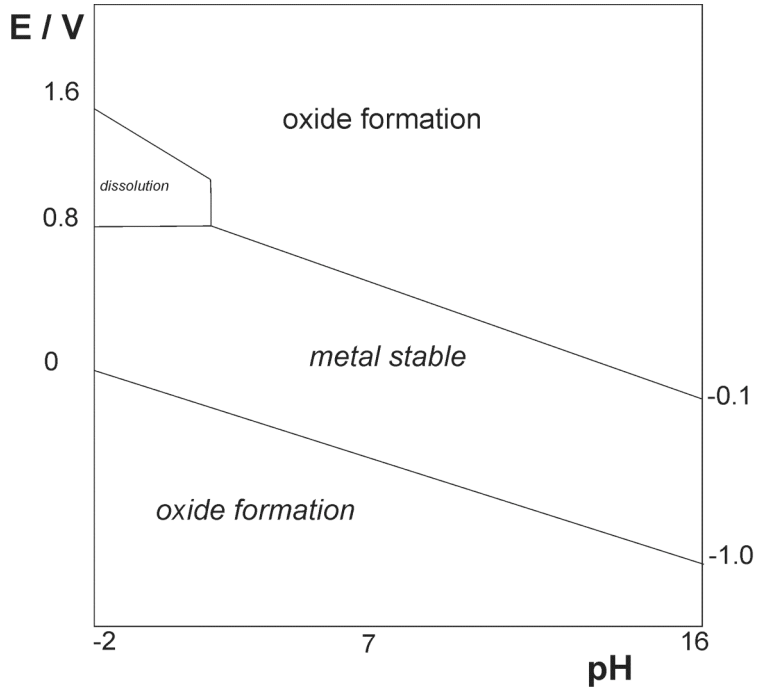


Figure 2.4

A simplified diagrammatic representation of the stability of palladium metal, reported across a range of pH and potential values at 25℃ [4]. By convention, the lines are drawn for ions at unit activity.

2.2.4.1 Colloidal and Electro - less Synthesis of PdNPs

There are a handful of examples of colloidal synthesis of PdNPs. The synthesis of a $Pd_{colloid}$ more typically involves the preparation of a bimetallic catalyst such as Pd/Cu or Pd/Au. Synthetic procedures for colloids of nano – Pd have been outlined by Guy *et. al.*[52] and Burton et al.[53] as the starting material for preparation of a bimetallic alloy catalysts of Pd/Cu, Pd/Al_2O_3 and Pd/ZnO. Pd/Cu composites stabilized by PVP, have proved to be useful in the catalytic reduction of nitrates and nitrites and Pd/Au for the oxidation of benzyl alcohols[54]. Pd based catalysts have also been used in the direct synthesis of H_2O_2[55]. PdNP colloids integrated with a MWCNT network, constructed on the surface of a GC electrode, exhibit biocompatibility and can be used as a highly sensitive DNA hybridisation biosensor[56]. PdNPs (d_{avg} = 4 nm) were synthesized by reduction of $NaPdCl_4$ in DMF by $NaBH_4$. The suspension was then mixed with MWCNTs and cast on to a polished GC electrode. The hybridization event is followed electrochemically using DPV, to observe redox of the indicator, methylene blue (*MB*). This particular technique is able to distinguish between complementary ($LOD = 1.2 \times 10^{-13} M$) and non – complementary DNA. The MWCNT/PdNP network was thought to promote electron transfer and the faster redox reaction of MB.

Morphology controlled synthesis of Pd nanostructures is also made possible by colloidal preparation techniques. Nanocubes and nanodendrites (d_{avg} = 60 nm) can be synthesized in aqueous solution at room temperature from Pd – CTAB complexes[57]. Dendritic nano – structured Pd is reported to evolve from spherical particles, mediated by the presence of polyglycol and hydrazine[58] and can be applied to the sensing of H_2O_2. As H_2O_2 is a by – product of numerous enzyme – catalyzed reactions it can be used as an indication of reaction progress, and has potential in biosensing. The Pd nanostructures were characterized by several techniques including SEM, TEM, XRD

and AFM. Suspensions of nano – Pd were used in the modification of substrate electrodes for analytical purposes.

Electro – less chemical deposition of Pd on to a carbon substrate is a simple and effective means of generating separated and clearly defined PdNPs, for analytical purposes. Electro – less deposition on to GCMS has been utilized by Baron et. al, in combinatorial analysis. PdNPs of size 20 – 500 nm were recognized as electro – active in the presence of hydrazine[59]. Modified GCMS were incorporated into the working electrode by abrasive attachment to a BPPG surface or by mixing into a carbon epoxy electrode. The carbon epoxy/PdNP electrode gave a low detection limit of hydrazine (2 μM) and higher sensitivity compared to a Pd macro – disk of equivalent area, due to enhanced diffusion at the array compared to the macro – disk. Palladium NPs doped with boron (Pd – B NPs) were synthesized via an aqueous solution phase method, where dimethylamine borane (DMAB) was used to reduce $PdCl_2$, in the presence of NH_4F and H_3BO_3. This produced highly disperse Pd – B NPs with narrow size distribution, deposited on a carbon black support. By replacing the DMAB reducing agent with $NaBH_4$ it is possible to facilitate the synthesis of a Pd/C catalyst via the same method. This material exhibits enhanced activity with respect to the electro – oxidation of formic acid and DFAFCs, with long – term stability of the catalyst improved by thermal treatment[60].

2.2.4.2 Electro – deposition of PdNPs

The detection of hydrogen / protons has been achieved using PdNPs, as shown by Batchelor – McAuley and co – workers. PdNPs have been electrochemically deposited on a boron – doped diamond (BDD) electrode from a solution of $PdCl_2$ in 1 M H_2SO_4, by potential sweep techniques and by fixed potential deposition. AFM analysis was used to ascertain the nature of the Pd deposits, d_{avg} = 100 nm. For the

study of the electrochemical response of hydrogen to PdNPs, Pd was deposited for 40 s at 0.0 V from a solution containing 0.18 mM $PdCl_2$ in 1 M H_2SO_4. The PdNP system allows distinction between two types of bound hydrogen: a peak at + 0.02 V corresponds to oxidation of hydrogen to ions (H^+) on surface of PdNPs, while second peak at + 0.26 V results from the oxidation of hydrogen from the bulk of the PdNPs. To fully understand the behaviour of Pd with respect to the kinetics of hydrogen adsorption, nano – scale material was used to avoid interference from the dominant bulk metal response[61]. SWCNTs have been used as a substrate for the electro – deposition of PdNPs, in a simple construction of a hydrogen gas sensor by Mubeen et al.[62]. This system exhibits a notably improved sensitivity and detection limit over other reported findings.

PdNPs electrodeposited on BDD have shown activity towards the detection of hydrazine[63]. The optimum conditions for the deposition of PdNPs on a BDD electrode were the same as those described above. SEM characterization of the electrode surface indicated a random distribution of NPs in range of 10 – 200 nm diameter. In the presence of 1.36 mM hydrazine (phosphate buffer, pH 7), the oxidation wave can be observed on Pd – modified BDD, at + 0.11 V (*vs. SCE*), and is easily voltammetrically distinguished from solvent decomposition. The greatest advantage of the nano – scale particles in this case is the high linear ranges and lower limit of detection for hydrazine as compared to a Pd macro – electrode. Ji and co – workers have reported the fabrication of a film of MWCNTs on a GC electrode, decorated with PdNPs (1 nm or less), via activation of CNTs, complex formation and reduction to Pd(0). This work has shown that the Pd/MWCNT composite material is especially stable and thus can facilitate the detection of hydrazine at low pH values, which would otherwise be inaccessible due to the stripping of the metal that would normally take place[64].

The alcohol electro – oxidation process is important in the development of direct alcohol fuel cells (DAFCs). A uniform dispersion of PdNPs (~ 8nm) deposited on a titanium substrate exhibits activity towards ethanol electro – oxidation in 1.0 M KOH, but shows no activity in a 0.5 M H_2SO_4 medium[65]. An investigation into the effects of the KOH concentration indicated that increased OH^- concentration improved the kinetics of the oxidation process. Such materials exhibit potential for application in DAFC technology and ethanol sensing devices.

The electro – oxidation of oxalic acid ($H_2C_2O_4$) is facilitated by the deposition of PdNPs on a carbon paste electrode (Pd – CPE), from a solution of $PdCl_2$. Cyclic voltammetry shows 2 peaks (+ 0.65 and 0.90 V *vs. Ag/AgCl*) corresponding to the electro – oxidation of $C_2O_4^{2-}$ in H_2SO_4 [66]. PdNP could be deposited by potential cycling from – 0.3 to 0.0 V for 5 cycles or by potentiostatic electro – deposition at an electrolysis potential of – 0.4 V (*vs. Ag/AgCl*). By varying the number of cycles or electrolysis time between 5 s and 3 min it is possible to control the PdNP size. AFM analysis confirmed that by reducing either of these parameters the NP size decreased. A promising catalytic effect was observed for a relatively uniform deposition of NPs, with well – separated NPs. The peak current of $H_2C_2O_4$ oxidation at a PdNP – modified electrode was linear in the range of $1\times10^{-2} - 2\times10^{-5} M$ as compared to the Pd macro – electrode with a range of $1\times10^{-2} - 2\times10^{-4} M$. The detection limit is lower by one order of magnitude for the nano – scale electrode ($2\times10^{-5} M$).

2.2.4.3 Alternative Preparation Techniques

Less commonly used techniques to synthesis PdNPs have included PdNP/CNF (carbon nanofiber) composite materials fabricated by electro – spinning and thermal treatment. The Pd/CNF is cast on to the surface of a CPE electrode thus facilitating

the simultaneous determination of dopamine, uric acid and ascorbic acid[67]. A sonochemical synthesis was employed by Liu and co – workers to entrap PdNPs within a mesoporous structure such as SBA-15. Pd/SBA-15 was then functionalized with the protein haemoglobin (*Hb*), to construct a sensor based on peroxidase activity of Pd[68]. Ultrasound synthesis was also used to prepare a carbon – supported distribution of PdNPs (d_{avg} =10.5 nm). The reduction of nitrate on a PdNP catalyst was studied using differential electrochemical mass spectrometry (DEMS). DEMS evidenced the detection of N_2O and NO. NO is produced in both the anodic and cathodic scans whereas N_2O is produced only in cathodic scan[69]. A poly(acrylic acid) (PAA) network can be used as a nanoreactor to generate PdNPs in situ[70] by means of "shrink well" cycling. PAA is biocompatible and presents a platform for biosensing, based on the reduction of peroxide generated in enzymatic processes.

2.2.5 Synthesis and Application of Ruthenium Nanoparticles

The output of nanoparticle research in recent years has seen the investigation of rare metal nanoparticles such as ruthenium nanoparticles (RuNPs) become much more common. Ruthenium possesses the ability to harden metals and has found application in fabrication of wear – resistant alloy materials. Ru – complexes have found use in microelectronics and solar cell design, among other things. Typical literature methods [71-73] cite the chemical reduction of a metal salt, employing a variety of stabilizing agents and electrode substrate materials, as an attractive and simplistic route to colloidal nanoparticle synthesis. RuNPs have great potential catalytic applications. **Figure 2.5** shows the stability of ruthenium metal with variation of pH and potential.

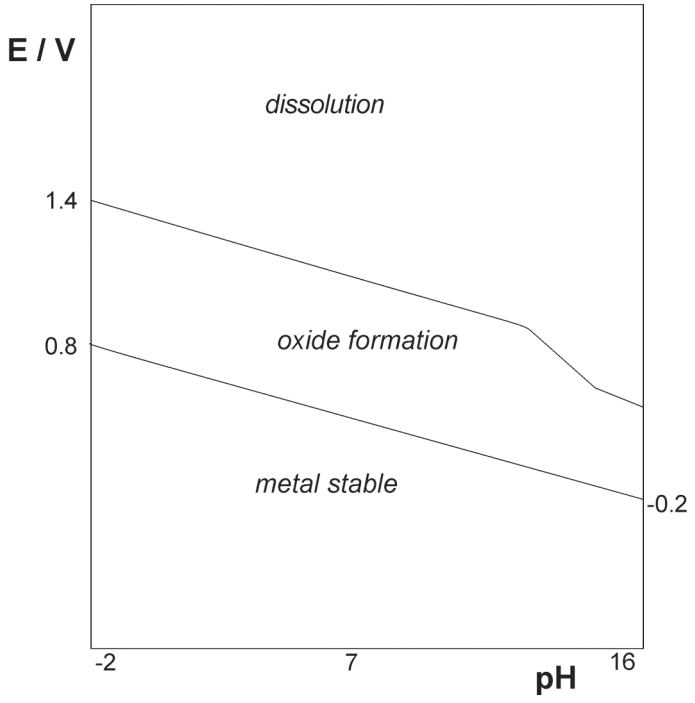


Figure 2.5

A simplified diagrammatic representation of the stability of ruthenium metal, reported across a range of pH and potential values at 25°C (in the absence of complexing substances)[4]. By convention, the lines are drawn for ions at unit activity.

A microwave – assisted preparation of RuNPs occurs via the reduction of $RuCl_3$ with ethylene glycol (EG) in the presence of polyvinylpyrollidone (PVP). Ru colloids were supported on a γ-Al_2O_3 substrate by two methods: (1) immobilization of a ready prepared Ru/PVP colloid; (2) in situ deposition of Ru by reduction of $RuCl_3$ with EG in presence of γ-Al_2O_3 support[74]. In both cases, the characterization of RuNPs by TEM indicated spherical/quasi – spherical morphology dispersed uniformly on the surface of γ-Al_2O_3, with average particle sizes of 1.7 and 1.9 nm, respectively. The latter of these two examples produced a chlorine free system unlike the ex situ alternative. This can be highly advantageous in catalysis. Several stabilizing agents have been reported in the aqueous synthesis of colloidal RuNPs: (1) PVP where glycerol acts as solvent and reducing agent, producing *ca.* 2 nm diameter RuNPs under microwave heating[75]; (2) alkylamine stabilized colloids formed by high temperature decomposition of a $Ru_3(CO)_{12}$ precursor[76]; (3) heavily fluorinated compounds act to entrap NPs (*ca.* 3 nm) in the crystal lattice of solid fluorous compound, when synthesized by hydrogenation of a Ru(COD)(COT) precursor[77]; (4) dithiocarbamate stabilized RuNPs have been prepared according to a modified Brust reaction. Results have indicated the ability to control the core size of the particles and TEM characterization indicated NPs with d_{avg} = 3nm[78].

As with other NPs, it is useful to be able to attach RuNPs to a carbon substrate for use in electro – analytical techniques. Lu has used two different approaches to decorate MWCNTs with RuNPs[79 80, 81]. First, MWCNTs were modified by a sodium decyl sulphate (SDS) surfactant. $RuCl_3$ was then reduced by EG, in the presence of the modified CNTs. Secondly, the modification of acid – treated MWCNTs with nickel ions facilitated the growth of RuNPs. The resulting densely decorated CNTs have potential application as electro – catalysts in fuel cells. Thermal decomposition and

micro – emulsion techniques have also been employed to attach RuNPs to carbon nanofibers.

Mesoporous SiO_2 (SBA-15) has also been employed as a template for the size – controlled synthesis of RuNPs, via a polyol reduction with a PVP capping agent[82]. The use of pure RuNPs as electro – catalysts is an area worthy of more in depth investigations. Bimetallic nano – materials of PtRu have found application in fuel cell technologies. Pt in known to be one of the most effective electro – catalysts for the oxidation of alcohols in fuel cells. However, this process produces CO as a by – product, which is known to foul Pt surfaces. Ruthenium, on the other hand, exhibits a much higher tolerance to CO. Therefore, PtRu combines the properties of both, providing a material with both high reactivity and a high CO tolerance. Numerous studies have shown the significance of PtRu NPs as a possible fuel cell catalyst for the oxidation of alcohols such as methanol and 2 – propanol[83, 84]. The NPs are often deposited onto a high surface area carbon support, (*e.g.* CNTs)[85, 86]. Colloidal PtRu composite NPs, used to decorate MWCNTs, have recently shown application for the electro – catalytic oxidation and detection of glucose. PtRu NPs (d_{avg} = 2.5 nm) were characterized by TEM. The PtRu/MWCNT catalyst displays a selective activity to the oxidation of glucose in alkaline media[87], with greater stability and sensitivity than its monometallic counterparts.

Studies over the past few years have led researchers to consider selenium – modified RuNPs as cathode materials, suitable as electro – catalysts for the oxygen reduction reaction (ORR) in fuel cells[88]. Ru/Se nanoclusters have been prepared using a mesoporous silica template, in which case excellent electro – catalysis for the ORR has been exhibited, with improved stability as compared to a templated Fe/N/C catalyst[89, 90]. Delacôte suggests an aqueous synthetic route involving the reduction of a mixture of $RuCl_3$ and SeO_2 by $NaBH_4$, in alkaline media. Under mild reaction

conditions, a particle size of 2 nm was achieved. The Ru/Se/C shows a good performance in a polymer electrolyte fuel cell (PEFC), comparable to other catalysts of this kind[91].

2.2.6 Synthesis and Application of Copper Nanoparticles

Copper is second only to silver as a good electrical conductor. Although Cu does not react with H_2O, the ease with which it can be oxidized in air presents a problem since the metal is usually covered with an oxide layer. Consequently, analytical applications referred to in the literature often point to the use of copper oxide nanoparticles (CuO NPs). Compared to noble metals such as Ag, Au and Pt, the study of CuNPs is less extensive. CuNPs have potential in a number of sensing applications and interest has grown in this area in recent years. In the following section we discuss several studies carried out on the synthesis of CuNPs and CuO NPs and the use of these materials. The range of copper stability is shown in **Figure 2.6**.

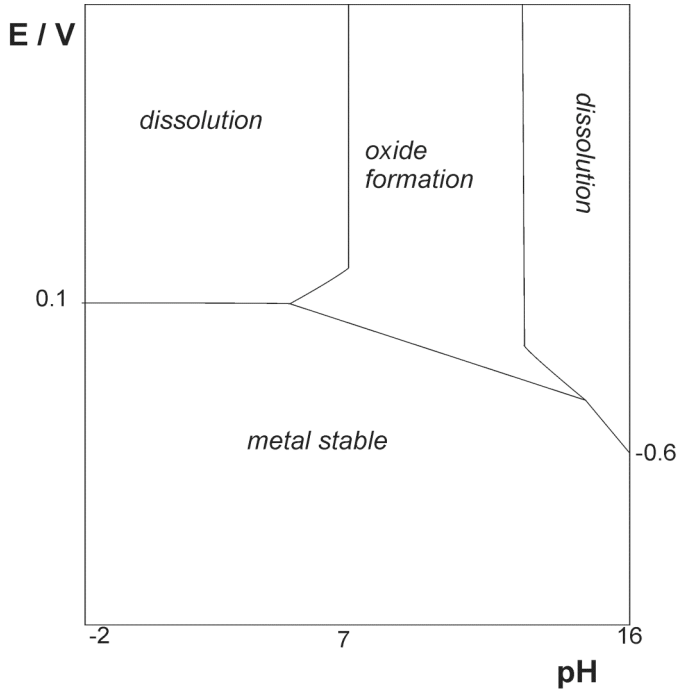


Figure 2.6

A simplified diagrammatic representation of the stability of copper metal, reported across a range of pH and potential values at 25℃ [4]. By convention, the lines are drawn for ions at unit activity.

Welch et al.[92] demonstrated that CuNPs could be deposited in situ from an acidic solution, on to a BDD substrate electrode. Furthermore, it was possible to control the size of NP deposits by application of specific deposition and stripping potentials. This method produces deposits of discrete CuNPs whereas repeated potential cycling results in irregular deposits, due to incomplete stripping of Cu from BDD surface during the anodic scan. The surface of Cu/BDD electrodes have been characterized by AFM showing that successive scanning of potential generates an irregular formation of Cu (d = 74 – 172 nm). Application of a discrete deposition potential followed by stripping potential creates a uniform deposit.

The in – depth study of the electrochemical behaviour of CNTs in the presence of the anaesthetic halothane has given rise to very important results. Dai and co – workers have shown that CNTs appear to be electro – active towards the reduction of halothane. This behaviour is in fact due to the presence of occluded CuNPs in the walls of the CNTs[93, 94]. These impurities are a result of the production of CNTs via chemical vapour deposition (CVD). The optimum response for the detection of halothane was found to take place in a NaOH (0.1 M) electrolyte, pH 13, LOD = 4.6 μM, with a comparable sensitivity to silver macro – electrode. The voltammetry displayed towards halothane was previously thought to be due to the electron transfer at the edge plane sites of CNTs.

CuO NP impurities have also been noted to occur during the synthesis of CNTs by CVD. These impurities have been recognized as electro – active towards the oxidation of glucose at a CNT – modified BPPG electrode[95]. No voltammetric response is observed for glucose oxidation at a EPPG electrode. Therefore, it is inferred that the observed voltammetry is due to the presence of CuO NP impurities of CNTs. This is further evidenced by the similar voltammetric behaviour exhibited by a

CuO microcrystal – modified BPPG electrode towards glucose, with a distinctive oxidation wave at + 0.6 V (*vs. SCE*).

Cu nanorod bundles were synthesized via a hydrothermal method, in the presence of polyethylene glycol (PEG). This material was characterized by TEM showing Cu nanorods of *ca.* 1 μm in length and 200 nm in width. These nanorod agglomerates were subsequently cast on to the surface of BPPG electrodes and proved to be electro – active towards carbohydrates such as glucose, fructose and sucrose in 0.1 M NaOH[96]. As well as the detection of carbohydrates, CuO nanorod bundles have been studied for the voltammetric and amperometric detection of H_2O_2. The determination of H_2O_2, in this particular instance, is best studied via the oxidation of the analyte, with $LOD = 2.2 \times 10^{-7} M$. The detection of glucose, fructose and sucrose all gave wide linear ranges and $LOD = 1.2 \times 10^{-6} M$, $1.1 \times 10^{-6} M$ and $3.7 \times 10^{-6} M$, respectively.

An interesting approach to the electrochemical synthesis of CuNP uses a self – assembled monolayer (SAM) of polyamidoamine (PAMAM) dendrimer as a template[97]. PAMAM dendrimers have been used to synthesis a number of metal NPs including Co, Pt and Pd. Metal ions can complex with the dendrimer and then be reduced to form Cu nanoparticles, whereby the dendrimer acts to anchor the NPs. A self – assembled monolayer of PAMAM is formed on the surface of a Au electrode. Upon immersion in 1 mM solution of Cu^{2+}, the ions become encapsulated by the dendrimer. The modified electrode is then introduced to an electrochemical cell containing 0.5 M H_2SO_4 to electrochemically reduce Cu^{2+} ions to Cu(0). AFM characterization of the electrode surface indicates NPs in size range 75 – 125 nm, with a random distribution on the electrode surface. An obvious advantage of the dendrimer – based synthesis is control over NP size and prevention of agglomeration. The PAMAM template can be employed as a means of pre – concentrating Cu^{2+} ions

to allow quantitative electrochemical sensing of copper ions in real samples, selectively determined by electrochemical stripping analysis, without interference from ions such as Cd^{2+} and Bi^{3+}. It is also possible to further electrochemically derivatise the Cu/dendrimer nanocomposite material to form a film of copper hexacyanoferrate, which exhibits biomimetic catalytic properties, used in sensing applications.

CuNPs have shown activity towards several target analytes including nitrates, nitrites, oxygen and hydrogen peroxide[52, 98-100]. They have also proven to be useful in the construction of a non – enzymatic glucose sensor as outlined by Kang *et al.*[101]. Typically enzyme – based sensors for glucose detection suffer from several draw – backs as enzymes are very sensitive to their environments (*i.e.* factors such as temperature, pH, humidity and toxic chemicals). Furthermore, complex procedures often have to be employed in order to immobilize enzymes on electrode surfaces. Nanoclusters of Cu have been electrodeposited on a MWCNT film – modified GC electrode. The distribution of Cu nanoclusters was then characterized by TEM and showed NPs with a random distribution and a size range of 20 – 80 nm, composed of crystalline nano – Cu with an average size of ~ 6.8 nm. The CV of a CuNP/CNT/GC electrode was performed in deoxygenated alkaline solution and displayed similar voltammetric features to a Cu electrode. The response of 1.0 mM glucose in 20 mM NaOH displays the oxidation of glucose taking place between 0.40 and 0.80 V (*vs. Ag/AgCl*), along with the oxidation of Cu(II) to Cu(III). The mechanism by which glucose is oxidized by copper is not fully understood but is thought to be related to the action of Cu(III) acting as an electron transfer mediator. The optimal conditions for the sensing of glucose were shown to be an applied potential of 0.65 V (*vs. Ag/Ag/Cl*) in 20 mM NaOH. Steady state current responses were examined with successive increases in glucose concentration under the optimized conditions, demonstrating a

linear range of 7.0×10^{-7} to $3.5 \times 10^{-3} M$ glucose, sensitivity of 17.76 μA mM^{-1} and $LOD = 2.1 \times 10^{-7} M$. This relatively wide range and high sensitivity are thought to be due to the increased electro – active surface and 'synergistic electro – activity' achieved by combining Cu nanoclusters with CNTs. This easily fabricated amperometric biosensor is highly stable and reproducible and might therefore be realistically used in biological analysis of glucose.

2.2.7 Synthesis and Application of Nickel Nanoparticles

Nickel is a hard and ductile metal presenting a possible alternative to expensive noble metals such as platinum, palladium and silver, which are often used as cathode materials in fuel cells and capacitors. Furthermore, nickel is also a ferromagnetic material, which can be a useful property in the recovery of nickel metal from catalytic processes. The following section discusses the synthesis and application of NiNPs. As above the stability of the nickel metal over pH and potential ranges is displayed in **Figure 2.7**.

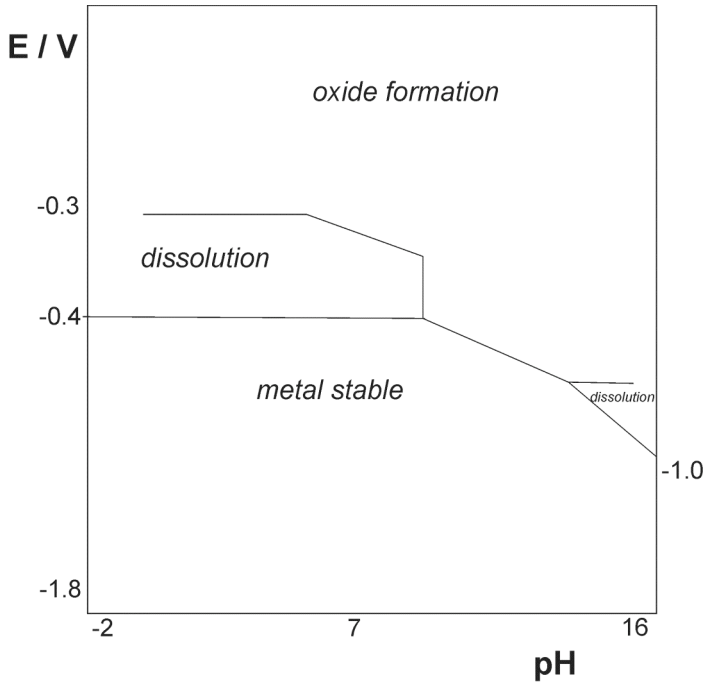


Figure 2.7

A diagrammatic representation of nickel metal stability, reported across a range of pH and potential values at 25°C (in solutions not containing chloride ions) [4]*. By convention, the lines are drawn for ions at unit activity.*

Various synthetic methods have been reported to prepare NiNPs in aqueous solution. A modified polyol synthesis uses a $NiCl_3$ precursor, $NaBH_4$ reducing agent and a PVP stabilizing agent to synthesise a stable dispersion of small NiNPs. The NPs were characterized by TEM and displayed a range of sizes from 3.4 – 3.8 nm, depending on the initial nickel/PVP ratio. PVP is found to be particularly important in the synthesis to prevent agglomeration and to control the growth of NiNPs. In the absence of the stabilizing agent, aggregation of the NiNPs was recognized by TEM analysis, with an average NP size of 7.7 nm[102].

A variety of surfactantless syntheses of NiNPs have been proposed, including the work of Bai[103] and that of Cheng[104] and their co – workers, utilizing hydrazine and high temperature synthesis, respectively. As NiNPs can be easily oxidized in air it can be advantageous to coat them with a layer of carbon, thus maintaining the nano – crystalline properties and magnetism but also protecting against oxidation of the surface. Use of Ni/CNT catalyst in the decomposition of acetylene at 600°C results in the encapsulation of the NPs with graphene layers. Carbon coated NiNPs have shown to be useful in the electrochemical detection of brucine, an anti – inflammatory and analgesic drug, dangerous at doses of 30 – 90 mg. A GCE modified with C-NiNPs increases the peak current of the brucine redox as well as improving the reversibility of the process. DPV is carried out for a range of brucine concentrations, and shows a linear catalytic current range of $4.7\times10^{-8} - 2.4\times10^{-4}\,M$ and $LOD = 1.4\times10^{-8}\,M$. C-Ni NPs act as promoters, accelerating the rate of the electron transfer and thus lowering the overpotential[105].

Alternative approaches to the synthesis of NiNPs include microwave irradiation, by reduction of the nickel precursor by hydrazine hydrate and stabilization by PVP[106]. Electro – less plating methods can also be used to control size, dispersion and morphology[107].

Composite or functionalized nickel based nano – materials have been employed in electro – analytical applications. Synergy exists between the electro – catalytic properties of silver towards methanol oxidation and the magnetic properties of nickel as demonstrated by the work of Jin and co – workers[108]. Bimetallic nickel/silver NPs, composed of distinct Ni and Ag particles, were used to functionalize a CNT substrate via a single step chemical deposition under ultrasound. The oxidation of methanol was facilitated by the AgNPs and displayed improved catalysis as compared to a bulk Ag electrode. Addition of a small quantity of NiNPs (1.5 % of the total NPs) aids in the recovery of the bi-functionalized nanotubes, using a magnet.

NiNPs functionalized by hexacyanoferrate (Ni-HF NPs) were synthesized at room temperature by a simple dropwise addition of an aqueous solution of $NiCl_2$ solution to $K_3Fe(CN)_6$ under stirring. Ni-HF NPs were attached to CNTs by means of interlinking histidine to give a highly stable Ni/CNT nanostructure[109]. When compared to the physically mixed NP/CNT material, the former exhibits more efficient electron transfer as well as an improved electrochemical response to H_2O_2 reduction, making this material attractive for the construction of oxidase – based biosensors. One such example is the immobilization of cholesterol oxidase for the detection of cholesterol. The cholesterol oxidase modified NiNP/CNT biosensor displayed a fast and sensitive response to H_2O_2 and cholesterol. Furthermore, a wide linear range for cholesterol was obtained (0.005 – 3 mM), and *LOD* = 1μM, as well as good stability and reproduceability.

As NiNPs can be quite easily oxidized, the electro – analytical application of NiO NPs has also been investigated. Salimi et al. have shown that a glucose oxidase enzyme can be successfully co – deposited on a GCE alongside NiO NPs, with retention of the native enzyme conformation[110]. This particular biosensor is stable, reproducible, has a long lifetime and displays an excellent electro – catalytic response

to glucose, in the presence of a ferrocene – methanol mediator. The *GOx* modified NiO GCE was characterized by CV over various scan rates. The proportionality of the peak current with scan rate implied a surface controlled process, with the *GOD* adsorbed on the surface of NiO undergoing a reversible electron transfer. The biocatalytic activity of *GOx* was measured by cyclic voltammetry for increasing concentrations of glucose. The oxidation of glucose is recorded at E_p > 0.6 V *vs. Ag/AgCl*, where an increase in anodic current is observed with increasing concentration. A linear response is reported in the range of 1 to 20 mM, *LOD* = 100 μM. NiO NPs offer a biocompatible environment for the enzyme as well as improving the electron transfer efficiency. This approach could be extended to a variety of enzymes and presents potential applications in bio – electrochemistry, biosensing, bioelectronics and biofuels.

A final example of nanosize Ni is the electro – synthesis of a nickel – based hydrotalcite (Ni – HT) films on the surface of electrodeposited PtNPs. Ni – HT films can be deposited from a solution of Ni and Al nitrates, in one step. SEM analysis shows a uniform coating of Ni-HT on the PtNPs[111]. The GC – Pt/Ni – HT electrode appears to improve the reversibility of the process and a larger peak area is observed, compared to the Pt free material. The latter is due to a greater number of electro – active Ni sites, resulting from the increased area of the electrode. The importance of the Ni sites in the HT film is to act as mediators for redox processes. The examples studied by Scavetta described the similar chronoamperometric behaviour of ethanol and glucose oxidation. A wider linear range is obtained for platinised electrodes modified with HT films. Furthermore, practical limits of detection were attainable for ethanol detection with an upper limit of 65 mM while for glucose the limit of linearity was reached at 8 mM.

2.2.8 Synthesis of Some Less Common Metal Nanoparticles.

A few other examples of metallic NPs are considered in this chapter, which are significant in electro – analysis. BiNPs have recently been synthesized by in situ deposition on the surface of a BDD electrode[112]. This system has been used to outline the nucleation and growth mechanism of BiNPs by examination of the electrode surface with AFM and has been applied to the simultaneous determination of Pb^{2+} and Cd^{2+}. This method has achieved improved limits of detection compared to a Bi macro – electrode.

A nano – pH sensor has been developed, which uses nano AFM tips made of iridium oxide (IrO) to detect fluctuations of pH in the range of pH 3 – 14. Using these tips, the hydration of samples of tri – calcium silicate and aluminate was seen to release OH^- ions, detectable at the nano – scale. This method could be useful in the study of samples of only a few micrometers or microlitres[113].

The nucleation and growth of cobalt nanoparticles (CoNPs) on a BDD electrode has been carried out by electro – deposition. Simm has investigated the kinetics of this nucleation and growth process using AFM[114]. Alternative synthetic routes include a polyol synthesis [115], thermal decomposition[116] and laser irradiation[117]. Examples of CoNPs as used in electro – analysis leads to the use of cobalt in composite or bimetallic materials, such as the electro – reduction of O_2 at arrays of PtCo NPs[118]. The ORR has also been studied on Ag – Co bimetallic nanoparticulate catalyst dispersed on a carbon powder, in basic media[119].

2.3 Conclusions

By consideration of the work discussed in this chapter we conclude that NPs have an important role to play in the field of electro – analysis as the application of NPs in electro – analysis continues to expand. The unique properties of nanoparticulate materials can be exploited to enhance the response of electro – analytical techniques. At present much of the work is empirical in nature. It is to be hoped that systematic voltammetric and structural characterization as well as clear control experiments with corresponding bulk materials will provide a more systematic basis for future work. Possible areas of future study may include investigation of rare metal nano – materials, metal oxides and bimetallic NPs as well as examination of the effects of NP size and morphology.

In the next section we will provide an overview of the theoretical principles underpinning the behaviour of nanoparticles in electrochemistry.

Chapter 2: References

1. F. W. Campbell, S. R. Belding, R. Baron, L. Xiao and R. G. Compton, *Journal of Physical Chemistry C*, 2009, **113**, 9053-9062.

2. S. E. W. Jones, F. W. Campbell, R. Baron, L. Xiao and R. G. Compton, *Journal of Physical Chemistry C*, 2008, **112**, 17820-17827.

3. C. W. Welch and R. G. Compton, *Analytical and Bioanalytical Chemistry*, 2006, **384**, 601-619.

4. M. Pourbaix, *Atlas of Electrochemical Equilibria in Aqueous Solutions*, 1st edn., Pergamon, New York, 1966.

5. M. Winters, *Webelements: The periodic table on the World Wide Web*, http://www.webelements.com/.

6. A. Pyatenko, M. Yamaguchi and M. Suzuki, *Journal of Physical Chemistry B*, 2005, **109**, 21608-21611.

7. X. He, X. Zhao, Y. Chen and J. Feng, *Materials Characterization*, 2008, **59**, 380-384.

8. A. S. Reddy, C.-Y. Chen, S. C. Baker, C.-C. Chen, J.-S. Jean, C.-W. Fan, H.-R. Chen and J.-C. Wang, *Materials Letters*, 2009, **63**, 1227-1230.

9. C. H. B. Ng, J. Yang and W. Y. Fan, *The Journal of Physical Chemistry C*, 2008, **112**, 4141-4145.

10. Z. Shervani, Y. Ikushima, M. Sato, H. Kawanami, Y. Hakuta, T. Yokoyama, T. Nagase, H. Kuneida and K. Aramaki, *Colloid & Polymer Science*, 2008, **286**, 403-410.

11. J. Zhu, C. Kan, X. Zhu, J.-G. Wan, M. Han, Y. Zhao, B. Wang and G. Wang, *Journal of Materials Research*, 2007, **22**, 1479-1485.

12. C. Ying and et al., *Nanotechnology*, 2007, **18**, 325602 (325605pp).

13. B. Hu, S.-B. Wang, K. Wang, M. Zhang and S.-H. Yu, *The Journal of Physical Chemistry C*, 2008, **112**, 11169-11174.

14. D. Wang, J. An, Q. Luo, X. Li and M. Li, *Journal of Applied Polymer Science*, 2008, **110**, 3038-3046.

15. L. Lin, P. Qiu, X. Cao and L. Jin, *Electrochimica Acta*, 2008, **53**, 5368-5372.

16. H. Karadeniz, A. Erdem, A. Caliskan, C. M. Pereira, E. M. Pereira and J. A. Ribeiro, *Electrochemistry Communications*, 2007, **9**, 2167-2173.

17. O. Domínguez-Renedo, L. Ruiz-Espelt, N. García-Astorgano and M. J. Arcos-Martínez, *Talanta*, 2008, **76**, 854-858.

18. S. Wu, H. Zhao, H. Ju, C. Shi and J. Zhao, *Electrochemistry Communications*, 2006, **8**, 1197-1203.

19. I. G. Casella and M. Contursi, *Journal of The Electrochemical Society*, 2007, **154**, D697-D702.

20. B. Sljukic, R. Baron, C. Salter, A. Crossley and R. G. Compton, *Analytica Chimica Acta*, 2007, **590**, 67-73.

21. Z.-P. Chen, Z.-F. Peng, Y. Luo, B. Qu, J.-H. Jiang, X.-B. Zhang, G.-L. Shen and R.-Q. Yu, *Biosensors and Bioelectronics*, 2007, **23**, 485-491.

22. P. Yang, W. Wei, C. Tao, B. Xie and X. Chen, *Microchimica Acta*, 2008, **162**, 51-56.

23. M. Gao, H. Qi, Q. Gao and C. Zhang, *Electroanalysis*, 2008, **20**, 123-130.

24. S. Guo and E. Wang, *Analytica Chimica Acta*, 2007, **598**, 181-192.

25. J. M. Pingarrón, P. Yáñez-Sedeño and A. González-Cortés, *Electrochimica Acta*, 2008, **53**, 5848-5866.

26. M. Okamura, T. Kondo and K. Uosaki, *The Journal of Physical Chemistry B*, 2005, **109**, 9897-9904.

27. B. Su and H. H. Girault, *The Journal of Physical Chemistry B*, 2005, **109**, 23925-23929.

28. J. Zhao, X. Zhu, T. Li and G. Li, *Analyst*, 2008, **133**, 1242-1245.

29. J. Manso, L. Agüí, P. Yáñez-Sedeño and J. M. Pingarrón, *Analytical Letters*, 2005, **37**, 887-902.

30. G. Hu, Y. Ma, Y. Guo and S. Shao, *Electrochimica Acta*, 2008, **53**, 6610-6615.

31. B. K. Jena and C. R. Raj, *Talanta*, 2008, **76**, 161-165.

32. V. Carralero Sanz, M. L. Mena, A. González-Cortés, P. Yáñez-Sedeño and J. M. Pingarrón, *Analytica Chimica Acta*, 2005, **528**, 1-8.

33. L. Agüí, J. Manso, P. Yáñez-Sedeño and J. M. Pingarrón, *Sensors and Actuators B: Chemical*, 2006, **113**, 272-280.

34. O. Shulga and J. R. Kirchhoff, *Electrochemistry Communications*, 2007, **9**, 935-940.

35. L. Rassaei, M. Sillanpää, R. W. French, R. G. Compton and F. Marken, *Electroanalysis*, 2008, **20**, 1286-1292.

36. K. Kuroda, T. Ishida and M. Haruta, *Journal of Molecular Catalysis A: Chemical*, 2009, **298**, 7-11.

37. C. Batchelor - McAuley, G. G. Wildgoose and R. G. Compton, *New Journal of Chemistry*, 2008, **32**, 941-946.

38. F. W. Campbell and R. G. Compton, *International Journal of Electrochemical Science*, 2010, **5**, 407-413.

39. F. W. Campbell, Y.-G. Zhou and R. G. Compton, *New Journal of Chemistry*, 2010, **34**, 187-189.

40. R. Polsky, R. Gill, L. Kaganovsky and I. Willner, *Analytical Chemistry*, 2006, **78**, 2268-2271.

41. H. B. Yildiz, R. Freeman, R. Gill and I. Willner, *Analytical Chemistry*, 2008, **80**, 2811-2816.

42. H. Borchert, D. Fenske, J. Kolny-Olesiak, J. Parisi, K. Al-Shamery and M. Bäumer, *Angewandte Chemie International Edition*, 2007, **46**, 2923-2926.

43. X. Dai and R. G. Compton, *Analyst*, 2006, **131**, 516.

44. W. H. O. (WHO), http://www.who.int/mediacentre/factsheets/fs210/.

45. H. Kim, N. Jeong, S. Lee and K. Song, *Korean Journal of Chemical Engineering*, 2008, **25**, 443-445.

46. J. Shi, X.-S. Li, Y.-Q. Hu and Y.-X. Hua, *Journal of Solid State Electrochemistry*, 2008, **12**, 1555-1559.

47. D.-J. Guo and H.-L. Li, *Journal of Power Sources*, 2006, **160**, 44-49.

48. Z. Wang and K. Qiu, *Electrochemistry Communications*, 2006, **8**, 1075-1081.

49. R. Baron, F. W. Campbell, L. Xiao and R. G. Compton, *International Journal of Electrochemical Science*, 2008, **3**, 556-565.

50. G. Gao, G. Yang, M. Xu, C. Wang, C. Xu and H. Li, *Journal of Power Sources*, 2007, **173**, 178-182.

51. A. Wang, X. Ye, P. He and Y. Fang, *Electroanalysis*, 2007, **19**, 1603-1608.

52. K. A. Guy, H. Xu, J. C. Yang, C. J. Werth and J. R. Shapley, *The Journal of Physical Chemistry C*, 2009, **113**, 8177-8185.

53. P. Burton, D. Lavenson, M. Johnson, D. Gorm, A. Karim, T. Conant, A. Datye, B. Hernandez-Sanchez and T. Boyle, *Topics in Catalysis*, 2008, **49**, 227-232.

54. S. Marx and A. Baiker, *The Journal of Physical Chemistry C*, 2009, **113**, 6191-6201.

55. J. K. Edwards, B. E. Solsona, P. Landon, A. F. Carley, A. Herzing, C. J. Kiely and G. J. Hutchings, *Journal of Catalysis*, 2005, **236**, 69-79.

56. Z. Chang, H. Fan, K. Zhao, M. Chen, P. He and Y. Fang, *Electroanalysis*, 2008, **20**, 131-136.

57. F.-R. Fan, A. Attia, U. K. Sur, J.-B. Chen, Z.-X. Xie, J.-F. Li, B. Ren and Z.-Q. Tian, *Crystal Growth & Design*, 2009, **9**, 2335-2340.

58. P. Zhou, Z. Dai, M. Fang, X. Huang, J. Bao and J. Gong, *The Journal of Physical Chemistry C*, 2007, **111**, 12609-12616.

59. R. Baron, B. ljuki, C. Salter, S. Crossley and R. G. Compton, *Electroanalysis*, 2007, **19**, 1062-1068.

60. J.-Y. Wang, Y.-Y. Kang, H. Yang and W.-B. Cai, *The Journal of Physical Chemistry C*, 2009, **113**, 8366-8372.

61. C. Batchelor-McAuley, C. E. Banks, A. O. Simm, T. G. J. Jones and R. G. Compton, *Chemphyschem*, 2006, **7**, 1081-1085.

62. S. Mubeen, T. Zhang, B. Yoo, M. A. Deshusses and N. V. Myung, *The Journal of Physical Chemistry C*, 2007, **111**, 6321-6327.

63. C. Batchelor - McAuley, C. E. Banks, A. O. Simm, T. G. J. Jones and R. G. Compton, *Analyst*, 2006, **131**, 106-110.

64. X. Ji, C. E. Banks, A. F. Holloway, K. Jurkschat, C. A. Thorogood, G. G. Wildgoose and R. G. Compton, *Electroanalysis*, 2006, **18**, 2481-2485.

65. J. Liu, J. Ye, C. Xu, S. P. Jiang and Y. Tong, *Electrochemistry Communications*, 2007, **9**, 2334-2339.

66. L. Shaidarova, I. Chelnokova, A. Gedmina, G. Budnikov, S. Ziganshina, A. Mozhanova and A. Bukharaev, *Journal of Analytical Chemistry*, 2006, **61**, 375-381.

67. J. Huang, Y. Liu, H. Hou and T. You, *Biosensors and Bioelectronics*, 2008, **24**, 632-637.

68. Y. Liu, J. Zhang, W. Hou and J. J. Zhu, *Nanotechnology*, 2008, **19**, 135707 (135708pp).

69. F. V. Andrade, L. J. Deiner, H. Varela, J. F. R. de Castro, I. A. Rodrigues and F. C. Nart, *Journal of The Electrochemical Society*, 2007, **154**, F159-F164.

70. Y. Tang, Y. Cao, S. Wang, G. Shen and R. Yu, *Sensors and Actuators B: Chemical*, 2009, **137**, 736-740.

71. A. Nemamcha, J.-L. Rehspringer and D. Khatmi, *The Journal of Physical Chemistry B*, 2005, **110**, 383-387.

72. P. K. Khanna and D. Kulkarni, *Synthesis and Reactivity in Inorganic, Metal-Organic, and Nano-Metal Chemistry*, 2008, **38**, 629-633.

73. Y. Wang, M. Du, J. Xu, P. Yang and Y. Du, *Journal of Dispersion Science and Technology*, 2008, **29**, 891-894.

74. M. Zawadzki and J. Okal, *Materials Research Bulletin*, 2008, **43**, 3111-3121.

75. A. Nirmala Grace and K. Pandian, *Materials Chemistry and Physics*, 2007, **104**, 191-198.

76. M. Vanden Brink, M. A. Peck, K. L. More and J. D. Hoefelmeyer, *The Journal of Physical Chemistry C*, 2008, **112**, 12122-12126.

77. M. Tristany, B. Chaudret, P. Dieudonne, Y. Guari, P. Lecante, V. Matsura, M. Moreno-Manas, K. Philippot and R. Pleixats, *Advanced Functional Materials*, 2006, **16**, 2008-2015.

78. W. Chen, D. Ghosh, J. Sun, M. C. Tong, F. Deng and S. Chen, *Electrochimica Acta*, 2007, **53**, 1150-1156.

79. J. Lu, *Carbon*, 2007, **45**, 1599-1605.

80. Y. Motoyama, M. Takasaki, K. Higashi, S.-H. Yoon, I. Mochida and H. Nagashima, *Chemistry Letters*, 2006, **35**, 876-877.

81. S. Yan, P. Qu, H. Wang, T. Tian and Z. Xiao, *Materials Research Bulletin*, 2008, **43**, 2818-2824.

82. M. E. Grass, S. H. Joo, Y. Zhang and G. A. Somorjai, *The Journal of Physical Chemistry C*, 2009, **113**, 8616-8623.

83. M. E. P. Markiewicz and S. H. Bergens, *Journal of Power Sources*, 2008, **185**, 222-225.

84. M. Islam, R. Basnayake and C. Korzeniewski, *Journal of Electroanalytical Chemistry*, 2007, **599**, 31-40.

85. M.-C. Tsai, T.-K. Yeh and C.-H. Tsai, *Materials Chemistry and Physics*, 2008, **109**, 422-428.

86. C.-T. Hsieh, Y.-W. Chou and W.-Y. Chen, *Journal of Alloys and Compounds*, 2008, **466**, 233-240.

87. L. H. Li, W. D. Zhang and J. S. Ye, *Electroanalysis*, 2008, **20**, 2212.

88. G. Zehl, G. Schmihals, A. Hoell, S. Haas, C. Hartnig, I. Dorbandt, P. Bogdanoff and S. Fietcher, *Angewandte Chemie International Edition*, 2007, **46**, 7311-7314.

89. A. Garsuch, X. Michaud, G. Wagner, O. Klepel and J. R. Dahn, *Electrochimica Acta*, 2009, **54**, 1350-1354.

90. A. Garsuch, X. Michaud, K. Böhme, G. Wagner and J. R. Dahn, *Journal of Power Sources*, 2009, **189**, 1008-1011.

91. Delacôte C, Bonakdarpour A, Johnston CM, Zelenay P and W. A, *Faraday Discussions*, 2008, **140**, 297-317.

92. C. Welch, A. Simm and R. Compton, *Electroanalysis*, 2006, **18**, 965-970.

93. X. Dai, G. G. Wildgoose and R. G. Compton, *Analyst*, 2006, **131**, 901-906.

94. A. O. Simm, S. Ward-Jones, C. E. Banks and R. G. Compton, *Analytical Sciences*, 2005, **21**, 667-671.

95. C. Batchelor-McAuley, G. G. Wildgoose, R. G. Compton, L. Shao and M. L. H. Green, *Sensors and Actuators B: Chemical*, 2008, **132**, 356-360.

96. C. Batchelor-McAuley, Y. Du, G. G. Wildgoose and R. G. Compton, *Sensors and Actuators B: Chemical*, 2008, **135**, 230-235.

97. S. Berchmans, T. Vergheese, A. Kavitha, M. Veerakumar and V. Yegnaraman, *Analytical and Bioanalytical Chemistry*, 2008, **390**, 939-946.

98. W.-Y. Ko, W.-H. Chen, C.-Y. Cheng and K.-J. Lin, *Sensors and Actuators B: Chemical*, 2009, **137**, 437-441.

99. S. A. Kumar, P.-H. Lo and S.-M. Chen, *Journal of The Electrochemical Society*, 2009, **156**, E118-E123.

100. X. Wang, N. Kariuki, J. T. Vaughey, J. Goodpaster, R. Kumar and D. J. Myers, *Journal of The Electrochemical Society*, 2008, **155**, B602-B609.

101. X. Kang, Z. Mai, X. Zou, P. Cai and J. Mo, *Analytical Biochemistry*, 2007, **363**, 143-150.

102. G. G. Couto, J. J. Klein, W. H. Schreiner, D. H. Mosca, A. J. A. de Oliveira and A. J. G. Zarbin, *Journal of Colloid and Interface Science*, 2007, **311**, 461-468.

103. L. Bai, F. Yuan and Q. Tang, *Materials Letters*, 2008, **62**, 2267-2270.

104. J. Cheng, X. Zhang and Y. Ye, *Journal of Solid State Chemistry*, 2006, **179**, 91-95.

105. S.-F. Wang, F. Xie and R.-F. Hu, *Analytical and Bioanalytical Chemistry*, 2007, **387**, 933-939.

106. W. Xu, K. Y. Liew, H. Liu, T. Huang, C. Sun and Y. Zhao, *Materials Letters*, 2008, **62**, 2571-2573.

107. Z. Wu, S. Ge, M. Zhang, W. Li and K. Tao, *Journal of Colloid and Interface Science*, 2009, **330**, 359-366.

108. G.-P. Jin, R. Baron, L. Xiao and R. G. Compton, *New Journal of Chemistry*, 2009, **33**, 107-111.

109. M. Yang, Y. Yang, F. Qu, Y. Lu, G. Shen and R. Yu, *Analytica Chimica Acta*, 2006, **571**, 211-217.

110. A. Salimi, E. Sharifi, A. Noorbakhsh and S. Soltanian, *Biosensors and Bioelectronics*, 2007, **22**, 3146-3153.

111. E. Scavetta, S. Stipa and D. Tonelli, *Electrochemistry Communications*, 2007, **9**, 2838-2842.

112. K. E. Toghill, G. G. Wildgoose, A. Moshar, C. Mulcahy and R. G. Compton, *Electroanalysis*, 2008, **20**, 1731-1737.

113. J.-P. Ndobo-Epoy, E. Lesniewska and J.-P. Guicquero, *Analytical Chemistry*, 2007, **79**, 7560-7564.

114. A. O. Simm, X. Ji, C. E. Banks, M. E. Hyde and R. G. Compton, *ChemPhysChem*, 2006, **7**, 704-709.

115. Q. Liu, X. Guo, Y. Li and W. Shen, *Materials Letters*, 2009, **63**, 1407-1409.

116. T. Lin, H. Shao, Z. Guo, J. Luo and J. Hao, *Rare Metals*, 2009, **28**, 241-244.

117. I. Robinson, M. Volk, L. D. Tung, G. Caruntu, N. Kay and N. T. K. Thanh, *The Journal of Physical Chemistry C*, 2009, **113**, 9497-9501.

118. S. Kumar and S. Zou, *Electrochemistry Communications*, 2006, **8**, 1151-1157.

119. F. H. B. Lima, J. F. R. de Castro and E. A. Ticianelli, *Journal of Power Sources*, 2006, **161**, 806-812.

Chapter 3

Voltammetry at Nanoparticle – Modified Electrodes: Theory.

In this section we will discuss some of the fundamental theoretical principles used to explain the electrochemical behaviour of nanoparticles. We will consider isolated particles as well as arrays of nanoparticles.

3.1 Isolated Spherical Particles

A quantitative description of the diffusion to a nanoparticle – modified electrode has been tackled by Streeter et al[1, 2]. Understanding the diffusional behaviour of a NP – array is critical to effectively model such systems. To begin with, the voltammetric response of a single spherical NP on a planar electrode surface is modeled by numerical simulation. The planar electrode is a conducting material providing a point of electrical contact to the particle, with the reaction occurring exclusively at the NP surface. Experimentally, the nanoparticle – modified electrodes are constructed as an array of particles, randomly distributed on a planar surface. An array of spherical particles is shown in **Figure 3.1 (A)** and an array of hemispherical particles is shown in **Figure 3.1 (C)**.

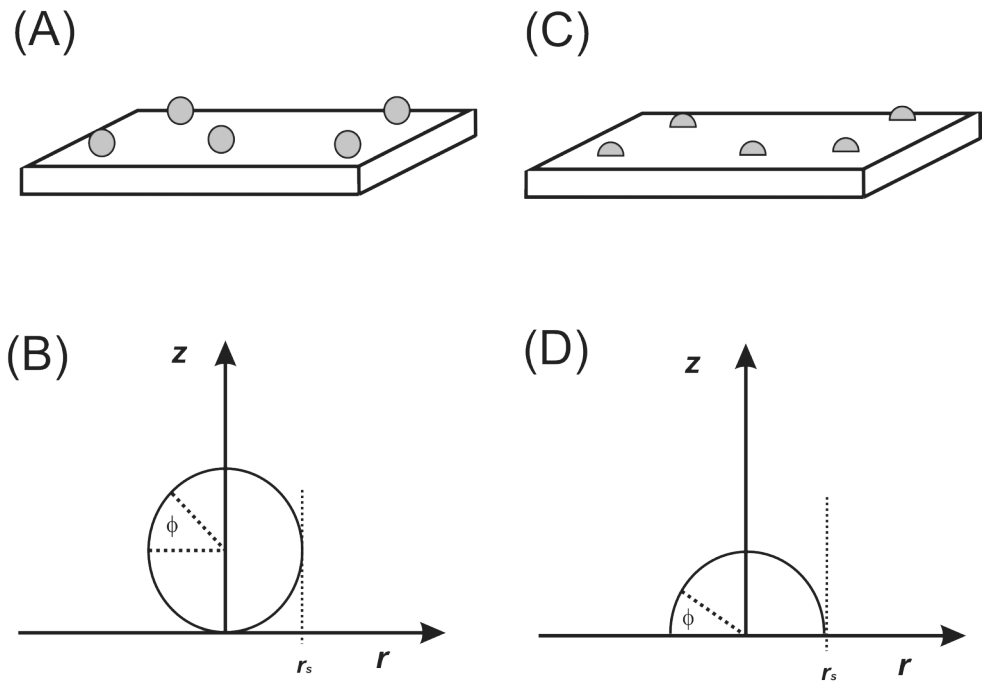


Figure 3.1

Random distribution of nanoparticles immobilized on a substrate electrode: (A) spherical particles, (B) hemispherical particles, (C) single spherical particles and (D) single hemispherical particle (ϕ represents the angle around the particle).

Mass transport to a spherical and hemispherical particle has been described extensively and is well understood.

A spherical particle can be simulated by solving the mass transport equations, in cylindrical polar co – ordinates. This approach can be applied to any curved particle provided it has an axis of symmetry.

The flux profile simulated at a spherical NP under diffusion – limiting conditions, is shown in **Figure 3.2**. The diffusion – limiting current at a spherical particle can be found using the analytical expression shown in **Equation 3.1**.

$$i_{\lim} = -\,8.71nFDr_s[A]_{bulk} \qquad [\mathbf{3.1}]$$

Similarly, the expression for a hemispherical particle is given in **Equation 3.2**.

$$i_{\lim} = -\,2\pi nFDr_s[A]_{bulk}$$

The derivation of these analytical expressions is provided by Streeter et al[1]. Note that the current scales with the NP radius, not the particle area, thus reflecting the convergent nature of diffusion. This expression is applicable at sufficiently slow scan rates. At higher scan rates the diffusion layer becomes increasingly compressed, with the effect of increasing the current and also the uniformity of the local current density as a function of the angle around the NP (**Figure 3.2**). The dimensionless scan rate is defined as $\sigma = \left(\frac{F}{RT}\right)\left(\frac{\upsilon r^2}{D}\right)$. Corresponding results have been obtained for spheroids and hemispheroids

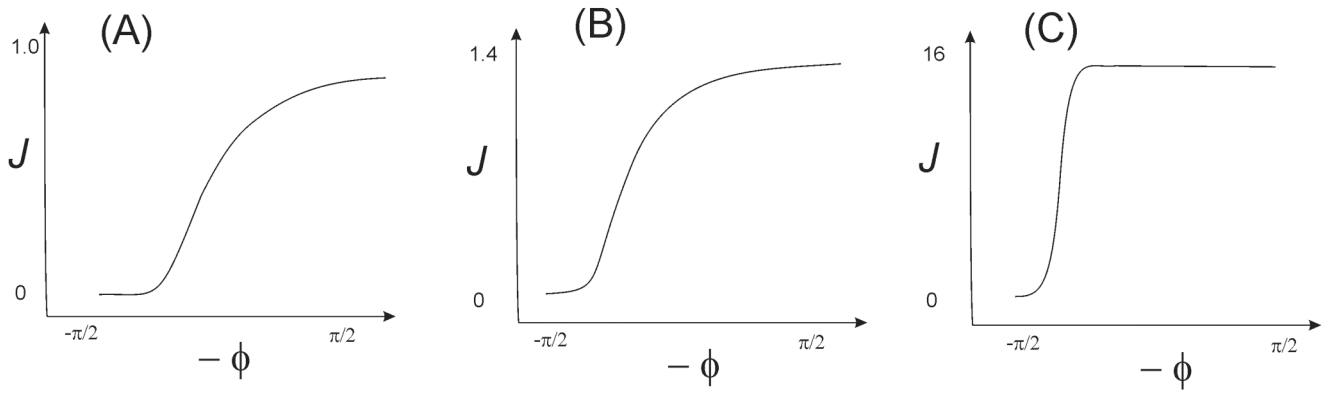


Figure 3.2

Flux profile at a spherical nanoparticle where $\phi = +\pi/2$ represents the top of the sphere and $-\pi/2$ represents the point of contact of the sphere on the substrate: (A) diffusion-limiting,, (B) $\sigma = 1$, (C) $\sigma = 10^3$.

3.2 Diffusion Domain Approximation

The diffusion domain approximation has been applied to simulate regular and random distributions of particles on a substrate electrode. This approach has previously been used to simulate the problem of partially blocked electrodes[3-5] and has since been used for a range of problems including microelectrode arrays[6, 7]. **Figure 3.3 and 3.4** shows the schematic diagram of the diffusion domain approach for a regular and random distribution, respectively.

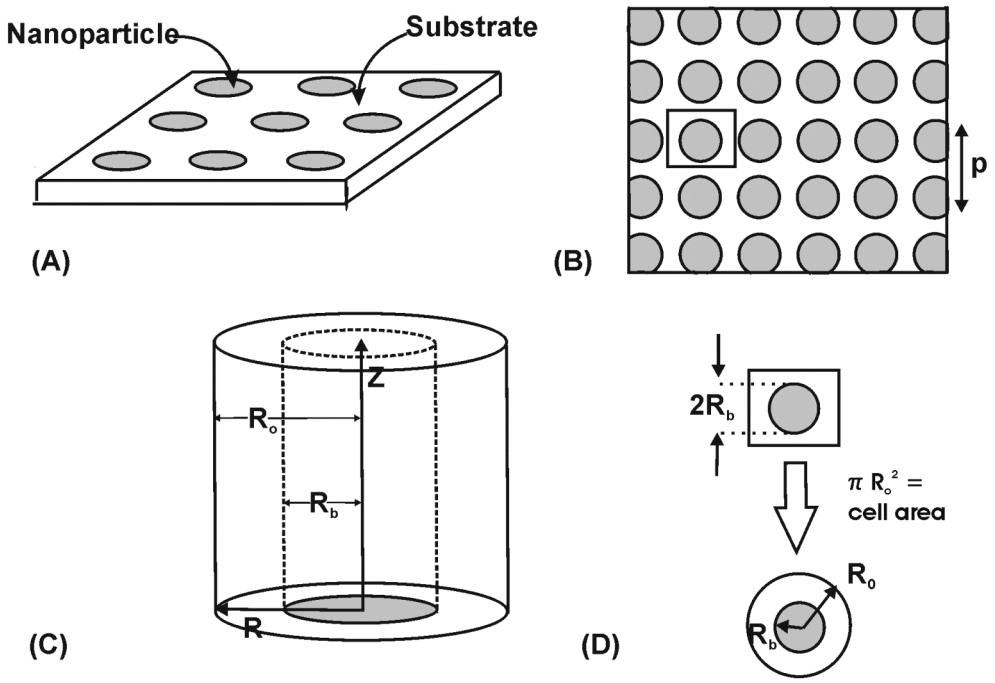


Figure 3.3

Schematic representation of the diffusion domain approximation as applied to a regular array of disks.

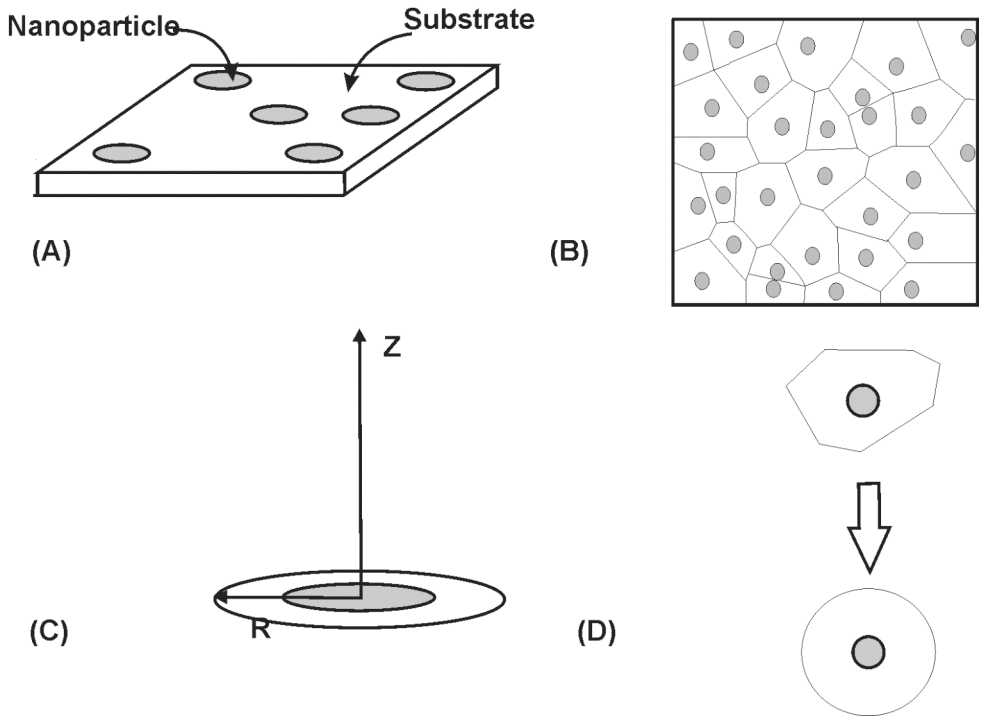


Figure 3.4

Schematic representation of the diffusion domain approximation as applied to a random array of disks.

Voronoi cells are formed from the bi – sectors of each particle and its nearest neighbours and it is assumed that the flux between neighbouring Voronoi cells is zero and so cells are assigned to each individual nanoparticle in the array to be modelled. **Figure 3.4 (C)** shows the approximation of modelling each irregularly shaped Voronoi cell as a cylinder with the same base area as the original cell. This three – dimensional problem can be simplified to two – dimensions as only a single plane as shown in **Figure 3.4 (C)**, needs to be simulated using the *R* and *Z* coordinates. If we have to consider the three – dimensional shape, this can significantly complicate our model.

The random distribution of Voronoi cell areas produced from the random array of nanoparticles on the surface can be approximated using **Equation 3.3** [8]**.**

$$f_{2D}(y) = \frac{343}{15}\sqrt{\frac{7}{2\pi}}y^{5/2}\exp\left(-\frac{7}{2}y\right) \qquad \textbf{[3.3]}$$

where $y = S/\langle S \rangle$ and S is the area of the Voronoi cell.

An average diffusion domain radius, $R_{0,}$ is used in much of this work, as calculation over the whole range of diffusion domain sizes is computationally very time consuming. This value is calculated from the average diffusion domain area, which takes the value of $0.88\left(A_{elec}/N\right)$ where A_{elec} is the total electrode area and N is the number of particles. This represents the median domain area as calculated from the Járai-Szabó and Néda equation[8].

3.3 Numerical Simulation

The single step electron transfer ($A + e^- \rightleftharpoons B$) takes place at the surface of a spherical particle. The mass transport of the electro – active species in solution is given in cylindrical radial co – ordinates (**Equation 3.4**).

$$\frac{\partial c}{\partial t} = D\left(\frac{\partial^2 c}{\partial r^2} + \frac{1}{r}\frac{\partial c}{\partial r} + \frac{\partial^2 c}{\partial z^2}\right) \qquad [3.4]$$

where c is the concentration and D is the diffusion coefficient. We assume that the electron transfer is fast and reversible and that only species A is present in the bulk solution, such that the concentrations of A and B can be calculated by the Nernst equation and that there is sufficient excess supporting electrolyte so transport occurs via diffusion only.

The response is shown to be a function of the dimensionless sweep rate (σ) as shown in **Equation 3.5.**

$$\sigma = \left(\frac{F}{RT}\right)\left(\frac{\upsilon r^2}{D}\right) \qquad [3.5]$$

υ is the voltage scan rate ($V\ s^{-1}$), r is nano – sphere radius and D is the diffusion coefficient of A and B which are assumed to be equal. The dimensionless potential is defined as θ = $E - E_f^0$. Typical responses at a single spherical particle are shown in **Figure 3.5** for scan rates σ = 10^{-3}, 1 and 10^3.

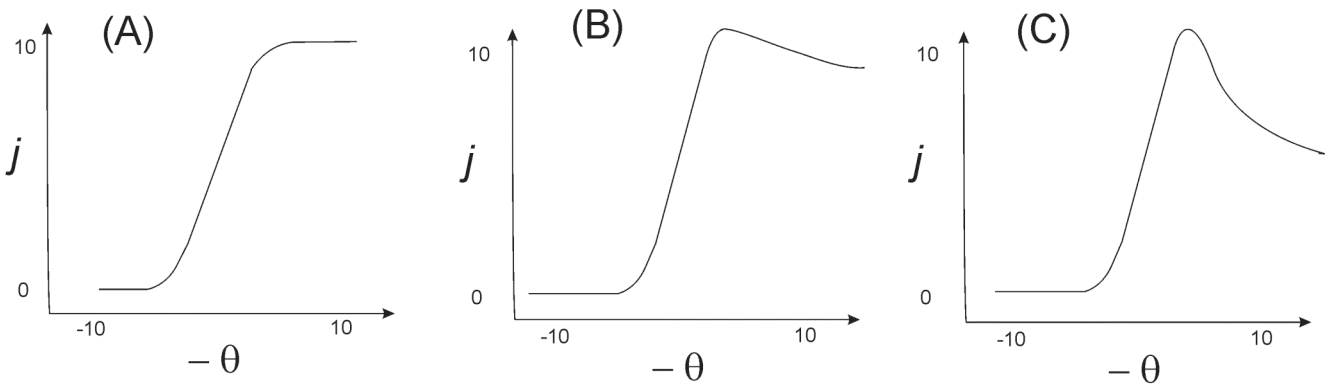


Figure 3.5

Representation of the voltammetry simulated for the reversible electron transfer at a single spherical particle. Scan rate (σ): (A) σ = 10^{-3}, (B) σ =1, (C) σ = 10^{3}. j / mol cm^{-2} s^{-1} represents the rate of transport of material to the electrode surface.

3.4 Categorizing Diffusional Behaviour

When electrodes are modified with a sufficient coverage of nanoparticles such that their diffusion layers interact, the current per nanoparticle is reduced from that predicted for an isolated nanoparticle. In particular, four cases of diffusion behaviour can be identified as reported in the literature by Davies *et al.*[9]. **Figure 3.6** outlines the different categories of diffusion possible at nanoparticle assemblies.

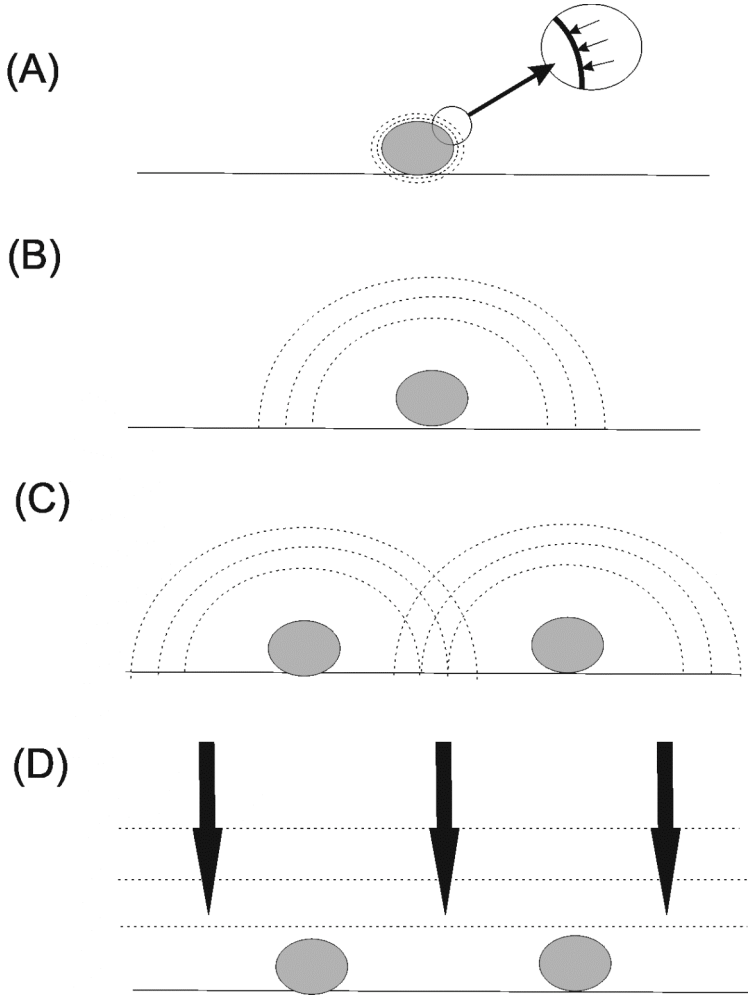


Figure 3.6

Diffusion zones of spherical particles on a planar support: (A) Linear diffusion at an isolated spherical particle over short timescales, (B) Radial diffusion at diffusionally independent spherical particles, (C) Overlap of diffusion zones of neighbouring particles, (D) Heavy overlap of neighbouring diffusion zones leading to overall linear diffusion.

In the case of an isolated spherical particle on a planar substrate, *Case 1* describes the situation at fast scan rates where the diffusion layer is small. At slower scan rates or over a larger experimental time scale the diffusion layer at an isolated particle will expand. This corresponds to *Case 2:* steady state diffusion. In both cases the particles are "diffusionally independent". *Case 3* on the other hand represents the situation where the diffusion layers partially overlap, whilst *Case 4* results when there is very heavy overlap such that the entire electrode effectively experiences linear diffusion. **Figure 3.7** shows typical voltammetry obtained for each of these four diffusional cases.

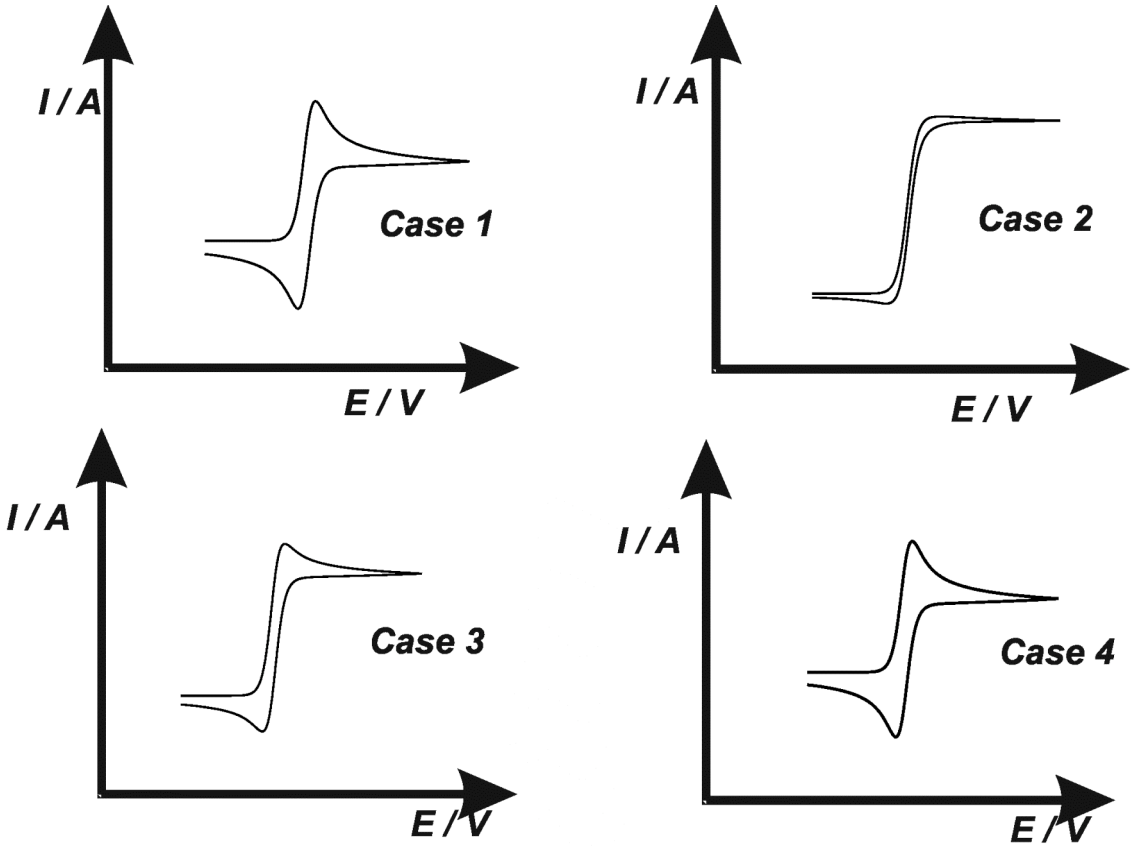


Figure 3.7

Typical voltammetric responses obtained for Case 1, scales with nanoparticle area (A), Case 2, steady – state response (B), Case 3 (C) and Case 4, scales with substrate electrode area (D).

Under conditions where adjacent diffusion layers overlap heavily, *Case 4* diffusion is experienced by the array. In this situation, peak – shaped cyclic voltammetric behaviour is seen and is well modeled by one – dimensional diffusion except that, as predicted by Amatore and Savéant, the peak – to – peak separation reflects an electrochemical rate constant of $k^0\Theta$ where Θ is the coverage of active material and k^0 is the rate constant seen for 100% coverage [10]. The concentration profiles pertaining to *Cases 1 – 4* [6, 9] are shown in **Figure 3.8**.

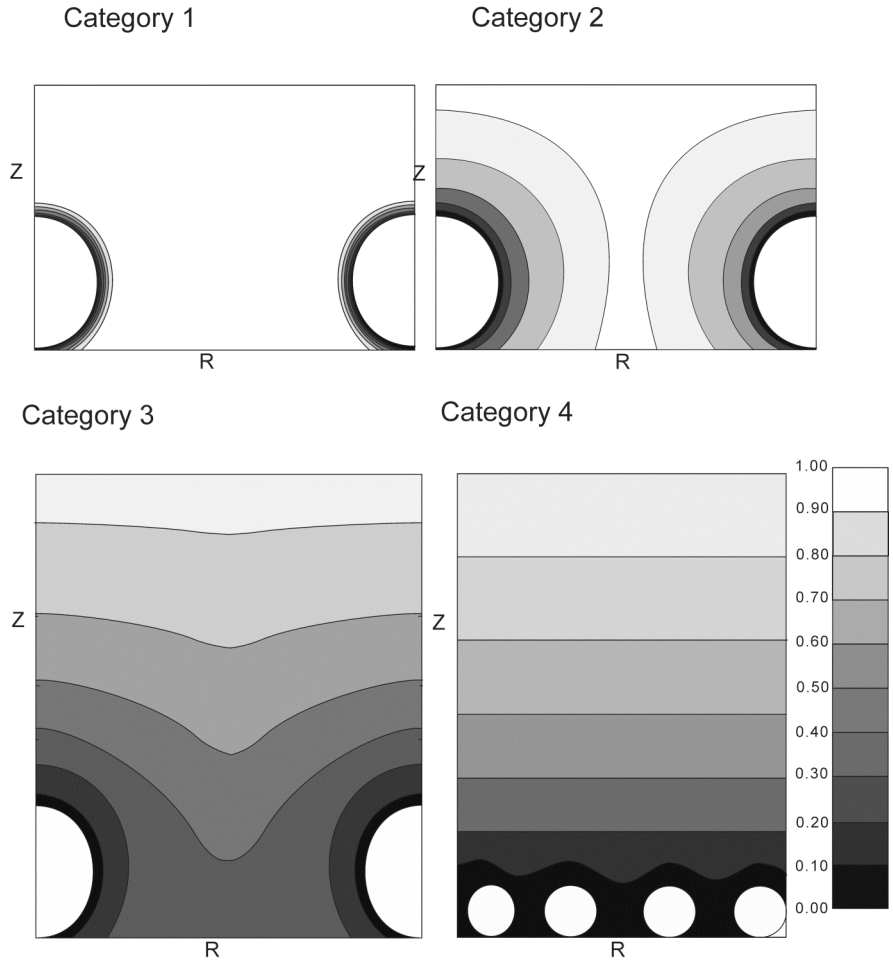


Figure 3.8

Concentration profiles for diffusion domain containing a spherical particle. The four categories of diffusion can be represented with various scan rates: (A) Category 1: $\sigma = 10^3$*, (B) Category 2:* $\sigma = 10$*, (C) Category 3:* $\sigma = 1$*, (D) Category 4:* $\sigma = 0.01$*. Diffusion domain for all categories,* $R_0 = 2$ [11].

3.5 Simulation of Nanoparticle Arrays

Experiments on the reduction of protons at palladium nanoparticles[11] were shown to display the different types of voltammograms identified above with high coverage leading to peak – shaped voltammograms, reflecting the one – dimensional diffusion to the entire surface. However, at low coverage, steady – state voltammetry, characteristic of convergent diffusion to isolated small particles can be observed. This study was simulated by Dr. Ian Streeter and has been extended by Stephen R. Belding to account for finite electrode kinetics [12]. Here numerical simulations have been used to identify how the voltammetric features of NP voltammetry can be influenced by the electrochemical rate constant (k^0) of electron transfer, surface coverage of NPs on the substrate electrode surface (θ) and voltage scan rate (υ). A detailed description of the simulation methods for both the regular and random distribution of electrochemical centres is given in **Appendix 1**. Dr. Ian Streeter, Dr. Sarah E. Ward Jones and Mr. Stephen R. Belding carried out the simulations discussed in this thesis, as indicated in the appropriate chapters.

This method has been applied to electrodes modified with arrays of silver nanoparticles and have been used to study the effects of nanoparticle size and coverage[13-15]. The aim of such studies has been to identify whether or not the electrode kinetics change between the macro – and nano – scales.

In the case of the reduction of hydrogen peroxide at AgNP – arrays, similar transfer coefficients have been reported at the macro – and nano – scales[13]. Therefore, the negative shift in the reduction potential as seen from large to small scale was attributed entirely to the change in the mass transport regime., specifically the transition from planar to convergent diffusion. An increased overpotential exists for arrays of NPs as compared to a bulk silver macro – electrode, due to the partially

convergent diffusion to the NP – array (**Figure 3.9**). This will be discussed in detail in **Chapter 5** of this thesis. In contrast, for the reduction of proton at AgNP – arrays both the rate constant (k^0) and the transfer coefficient (α) changed significantly between the two electrode types[14] . Similarly, this study is covered in details in **Chapter 6** of this thesis.

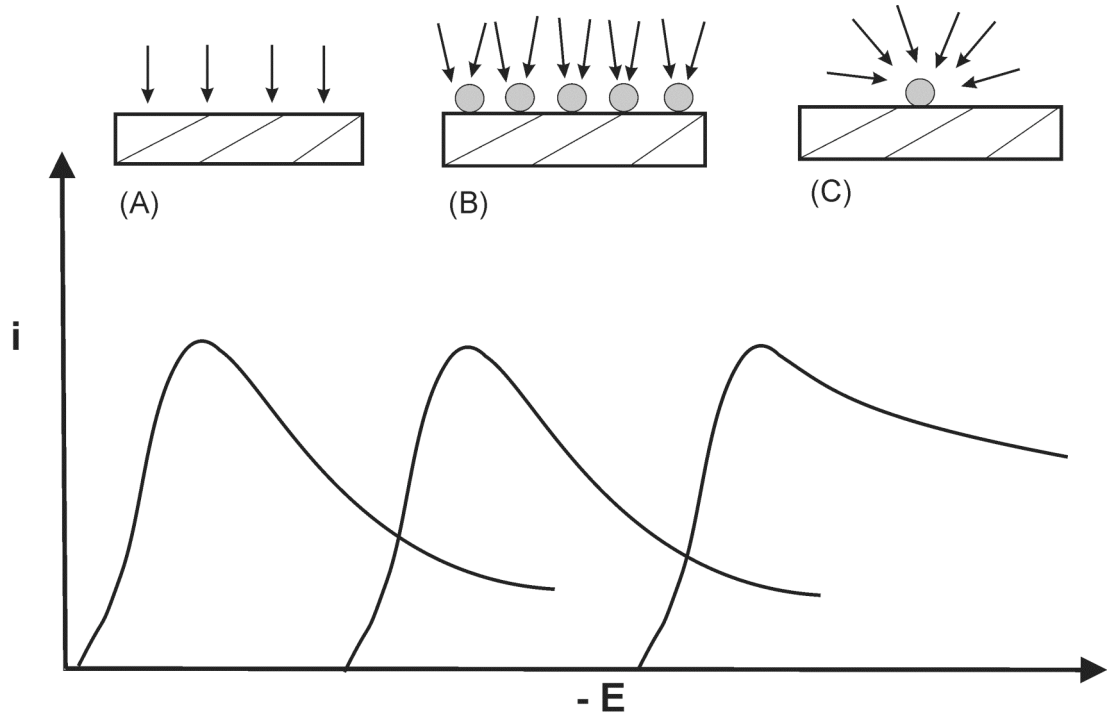


Figure 3.9

Schematic voltammetry outlining the effect of a mass transport on the voltammetry of a fully electrochemically irreversible reduction, reported as a function of electrode type: (A) macroelectrode, (B) NP array (high coverage) and (C) NP array (low coverage).

Chapter 3: References

1. I. Streeter and R. G. Compton, *The Journal of Physical Chemistry C*, 2007, **111**, 18049-18054.

2. I. Streeter, R. Baron and R. G. Compton, *Journal of Physical Chemistry C*, 2007, **111**, 17008-17014.

3. B. A. Brookes, T. J. Davies, A. C. Fisher, R. G. Evans, S. J. Wilkins, K. Yunus, J. D. Wadhawan and R. G. Compton, *Journal of Physical Chemistry B*, 2003, **107**, 1616-1627.

4. T. J. Davies, B. A. Brookes, A. C. Fisher, K. Yunus, S. J. Wilkins, P. R. Greene, J. D. Wadhawan and R. G. Compton, *Journal of Physical Chemistry B*, 2003, **107**, 6431-6444.

5. T. J. Davies, B. A. Brookes and R. G. Compton, *Journal of Electroanalytical Chemistry*, 2004, **566**, 193-216.

6. T. J. Davies and R. G. Compton, *Journal of Electroanalytical Chemistry*, 2005, **585**, 63-82.

7. T. J. Davies, S. Ward-Jones, C. E. Banks, J. del Campo, R. Mas, F. X. Muñoz and R. G. Compton, *Journal of Electroanalytical Chemistry*, 2005, **585**, 51-62.

8. F. Jarai-Szabo and Z. Neda, *arXiv Condens. Matter e-prints*, 2004, **06**, 116.

9. T. J. Davies, C. E. Banks and R. G. Compton, *Journal of Solid State Electrochemistry*, 2005, **9**, 797-808.

10. C. Amatore, J. M. Savéant and D. Tessier, *Journal of Electroanalytical Chemistry*, 1983, **147**, 39-51.

11. I. Streeter, R. Baron and R. G. Compton, *The Journal of Physical Chemistry C*, 2007, **111**, 17008-17014.

12. S. R. Belding, E. J. F. Dickinson and R. G. Compton, *Journal of Physical Chemistry C*, 2009, **113**, 11149-11156.

13. F. W. Campbell, S. R. Belding, R. Baron, L. Xiao and R. G. Compton, *Journal of Physical Chemistry C*, 2009, **113**, 9053-9062.

14. F. W. Campbell, S. R. Belding, R. Baron, L. Xiao and R. G. Compton, *The Journal of Physical Chemistry C*, 2009, **113**, 14852-14857.

15. F. W. Campbell, S. R. Belding and R. G. Compton, *ChemPhysChem*, 2010.

Chapter 4

Experimental Methods.

The aim of this chapter is to give an outline of the experimental procedures used in the work presented in this thesis. Specific details on each individual project are presented in the appropriate chapters.

4.1 Reagents and Materials

A comprehensive list of all chemicals used in these experiments is provided in **Table 4.1** shown below. All chemicals were used as received without further purification unless otherwise stated.

Name	Formula	Purity	Supplier
Sulphuric acid	H_2SO_4	98 %	AnalaR
Hydrogen peroxide	H_2O_2	30 % (w / v)	Fisher Scientific
Silver nitrate	$AgNO_3$	99 %	BDH
Trisodium citrate	$C_6H_5Na_3O_7$	99 %	Aldrich
Monobasic sodium phosphate	$NaH_2PO_4.H_2O$	98 %	Fisher
Dibasic sodium phosphate	$Na_2HPO_4.H_2O$	98 %	Fisher
Perchloric acid	$HClO_4$	70 %	AnalaR
Hydrochloric acid	HCl	37 % (w / w)	Riedel – de Haen
Methanol	CH_3OH	99.99 %	Riedel – de Haen

Potassium Chloride	KCl	99.5 %	Aldrich
L-ascorbic acid		99.5 %	Aldrich
Hexachloroplatinic Acid	H_2PtCl_6	98 %	Sigma – Aldrich
Sodium Hydroxide	NaOH	99 %	Aldrich
4 - Nitrophenol	$C_6H_5NO_3$	98 %	Sigma – Aldrich
Sodium Perchlorate	$NaClO_4$	98 – 102 %	Sigma – Aldrich
Thallium Nitrate	$TlNO_3$	99.9 %	Aldrich
Potassium Nitrate	KNO_3	99.9 %	Aldrich
Sodium Potassium Tartrate	$KNaC_4H_4O_6 \cdot 4H_2O$	99 %	Fluka
Lead Nitrate	$Pb(NO_3)_2$	99 %	AnalaR
Sodium Sulphate	Na_2SO_4	99 %	BDH
Cadmium Sulphate	$CdSO_4$	99 %	Aldrich
Glassy carbon spherical powder (10–20 microns)	-	-	Alfa Aesar
Basal Plane Pyrolytic Graphite (BPPG)	-	-	Le Carbone
Silver wire	Ag	-	Goodfellow
Platinum wire	Pt	-	Goodfellow

Table 4.1

List of reagents and materials used in experiments.

4.2 Solution Preparation

All solutions were prepared using Millipore de-ionised water, with a resistivity no less than 18.2 MΩ cm at 25°C (Vivendi Water Systems, UK). All solutions were purged of oxygen by degassing thoroughly prior to use with an inert gas such as nitrogen (N_2) or argon (Ar). All glassware used was cleaned prior to use with a "piranha" solution of concentrated sulphuric acid and hydrogen peroxide (30% w/v) in a ratio of 4:1.

4.3 Synthesis of Nanoparticles

4.3.1 Colloidal Synthesis

Silver nanoparticles (AgNPs) as used in the following experiments were prepared using a colloidal synthetic approach. The procedure was adapted from the work of Pyatenko *et al.*[1, 2] to prepare spheroidal silver nanoparticles, with controllable dimensions. NPs were synthesized via the citric reduction of a silver salt, such that the citrate acts as both a reducing and capping agent at high temperatures. The detailed procedure is outlined as follows.

25 mL of a 0.01 M silver nitrate ($AgNO_3$) solution was added to 225 mL distilled water in a clean 250 mL flask. The flask was then heated in a bath at 100°C with vigourous magnetic stirring. A solution of trisodium citrate was prepared by dissolving 1g of the salt in 100 mL of distilled water. When the solution reached boiling point, 5 mL of the citrate solution was then added to the flask. Boiling was then allowed to continue for 1 hr and the reaction mixture was then allowed to cool in a cold water bath. This first procedure generated the initial colloid of AgNPs, with the smallest diameter (25 – 40nm).

The initial colloid was then used as a seed particle in subsequent syntheses allowing the growth of larger nanoparticles. The synthesis of nanoparticles of diameter 80 – 120 nm was achieved by adding a small volume (100 μL) of the initial colloidal solution and 5 mL of citrate solution to 25 mL (0.01M) $AgNO_3$ in 225 mL distilled water as it began to boil, and continuing boiling for 1 hr before cooling the flask.

Finally an intermediate size of AgNPs (55 – 75 nm diameter) was synthesised by following the seed particle method as described above but only boiling for 35 minutes before cooling.

For each synthesis it was necessary to separate, wash and re-disperse the nanoparticles to remove any excess chemicals. 1 mL portions of the reaction solution were pipetted into 1.5 mL centrifuge tubes. These tubes were centrifuged at 14,000 RPM for 20 mins. The supernatant liquid was then pipetted off and the remaining solid at the bottom of the centrifuge tube was re-dispersed in 1 mL water. This was repeated three times to thoroughly wash the nanoparticles. Centrifugation was carried out using a Beckman Model J2-21 and Eppendorf 5415 C centrifuge. After washing, the nanoparticles were re-dispersed in 1.5 mL water, giving a yellow colloidal solution, and stored away from direct light.

4.3.2 Electro - less Synthesis

Platinum nanoparticles were synthesized on glassy carbon microspheres and used to study the reduction of protons and methanol. The synthesis was carried out as follows: 100 mg of glassy carbon microspheres were suspended in 50 mL of water. 20 mg of platinum hexachloroplatinate and 46 mg of L – ascorbic acid were added to the solution under vigorous stirring at 70 ºC. The pH of the reaction medium was then adjusted to 5.2 using a 1 M sodium hydroxide solution. The reaction flask was wrapped in aluminium foil and the reaction was allowed to proceed for two hours on a stirrer / hotplate at 70 ºC under stirring[3].

4.4 Nanoparticle Characterisation

4.4.1 UV – vis Spectroscopy

In the case of colloidal silver nanoparticles the surface plasmon resonance associated with colloidal silver nanoparticles allowed UV – vis to be used as an initial means of characterization[4]. As the particle samples were of different sizes it was possible to determine their relative sizes by comparing the optical absorbance of the samples. Smaller particles exhibit an absorbance at shorter wavelength and an increase in size causes the absorbance to shift to longer wavelengths. Colloidal samples were first diluted by a factor of 100 in water. The sample was then inserted into a UV – vis spectrometer and the wavelength scanned from 300 – 700 nm. Silver nanoparticles display a distinct absorbance in the region of 400 nm.

4.4.2 Scanning Electron Microscopy

Scanning electron microscopy (SEM) is an important method of characterization, which allows us to determine the dimensions of the synthesized materials. Images of the particles showed them to be roughly spherical in shape as well as providing the actual sizes of the nanoparticles in each sample. In the case of the PtNP – GCMS material the platinum appears well – dispersed on the carbon substrate with particle diameter of 100 ± 40 nm. The unmodified GCMS material was also imaged by SEM and appeared to be composed of spheres of 15 ± 5 μm. The colloidal AgNPs are sized by SEM imaging as follows: Sample (1): 20 – 40 nm, Sample (2): 50 – 70 nm and Sample (3): 80 – 120 nm. The analysis also provided estimates of the number of NPs per unit area. SEM was performed using a copper grid and a carbon film substrate.

4.5 Electrochemical Experiments

4.5.1 Instrumentation

All electrochemical measurements were carried out using a potentiostat *(μ - Autolab or PGSTAT20, Eco Chemie, Utrecht, Netherlands*) controlled by a desktop PC operating *GPES* PC software. In all experiments a standard three – electrode set – up was employed[5]. The use of this type of experimental set – up is critical in electrochemical experiments as it allows the reaction at one electrode (*working electrode*) to be examined, allowing us to separate and understand the surface reaction at the working electrode and the transport to the electrode. The reaction at the *working electrode (W. E.)* can be controlled by its tuneable potential drop ($\phi_m - \phi_s$) and can be changed by applying a potential difference between the two electrodes (*E*). In order to study this reaction it is essential that the potential of the other electrode remains constant such that a voltage applied between *working electrode* and *reference electrode* will only change ($\phi_m - \phi_s$) for the *working electrode*. For this reason we employ a *reference electrode* (*R. E.*). Some examples of which will be discussed in more detail below. Finally, in order to measure the current (*i*) we require a third electrode, known as the *counter electrode* (*C. E.*). This circuitry allows the current to be passed between the *working electrode* and *counter electrode.* In the studies described in the following chapters, a carbon rod was used as the *counter electrode.* Counter electrodes are often chosen to have high surface area so a high current can be passed. Therefore, the current will be limited by the reaction at the *working electrode.* Another common counter electrode is a platinum gauze electrode. A generalized three – electrode set – up is shown in **Figure 4.1**.

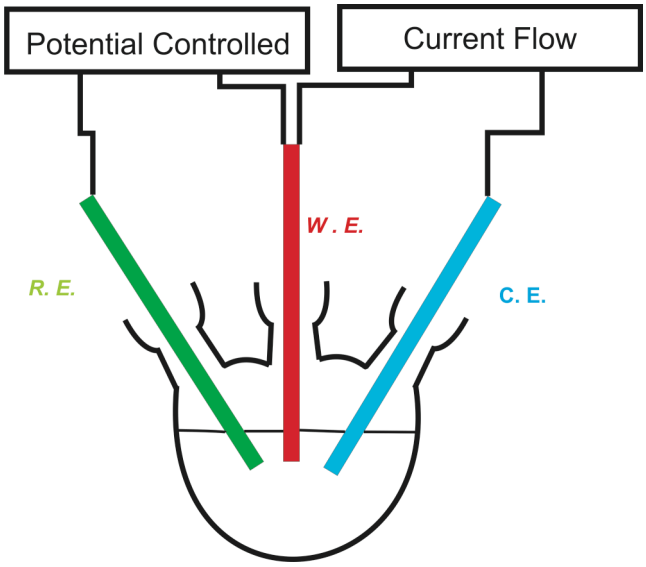


Figure 4.1

Schematic representation of standard three – electrode set – up.

4.5.2 Working Electrodes

The working electrode is that at which the electrochemical reaction being investigated takes place. All working electrodes were fabricated in – house. Metal macro – disk electrodes were constructed by sealing the desired metal wire (sub – mm diameter) inside a glass tube at one end. At the opposite end of the tube, the wire was attached to a thicker copper wire using silver epoxy to provide a means of connecting to the cell. The sealed end of the glass tube could be polished down to reveal a planar metal surface. Carbon basal plane pyrolytic graphite (BPPG) electrodes were also fabricated in – house (*PTCL Workshops, Oxford University*) and consisted of carbon materials encased in a PTFE sheath.

It was necessary to polish the surface of electrodes prior to each electrochemical experiment. Metal electrodes were renewed by polishing on silicon carbide paper followed by alumina with decreasing particle size (3.0, 1.0, 0.3 μm). The BPPG

electrodes were renewed, by pressing cellotape on to the surface thus removing a few layers of graphite.

In the experiments studied in this thesis the working electrodes employed are a silver disc electrode (0.5 mm diameter), platinum disc electrode (0.7 mm diameter) and BPPG electrodes (5 mm diameter).

4.5.3 Reference Electrodes

The reference electrode provides a constant potential against which the potential of the working electrode in the circuit can be measured. In the experiments discussed in the following chapters both a saturated calomel (*SCE, Radiometer, Copenhagen*) and a mercury / mercury oxide (*Hg / HgO, Koslow Scientific, USA*) reference electrode were used with a carbon rod employed as the counter electrode.

Saturated Calomel Electrode (SCE)

$$\tfrac{1}{2} Hg_2Cl_{2(s)} + e^- \rightleftharpoons Hg_{(l)} + Cl^-{}_{(aq)} \qquad \textbf{[4.1]}$$

$$Hg \,\big|\, Hg_2Cl_{2\,(s)} \,\big|\, KCl_{(aq)}$$

The saturated calomel electrode (*SCE*) is commonly used in aqueous media. **Figure 4.2** below shows a schematic diagram of this electrode based on the above reaction. The presence of saturated KCl is critical as it maintains a constant Cl^- concentration over extended periods, affording the high stability essential in a reference electrode.

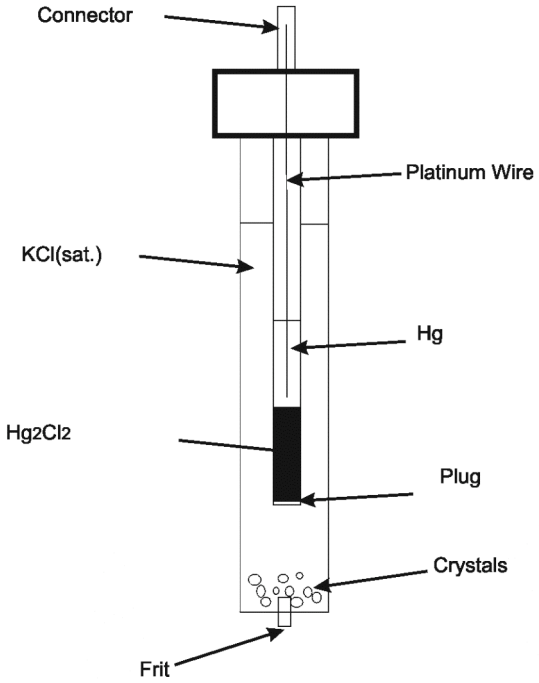


Figure 4.2

Schematic diagram of the saturated calomel reference electrode (SCE).

Mercury / Mercury Oxide (Hg / HgO)

$$HgO_{(s)} + H_2O + 2e^- \rightleftharpoons Hg_{(l)} + 2OH^- \qquad \textbf{[4.2]}$$

$$Hg \left| HgO_{(s)} \right| OH^-_{(aq)}$$

An *Hg / HgO* reference electrode filled with hydroxide (NaOH or KOH, 1 M) can be a useful tool in order to maintain a chloride – free environment. **Figure 4.3** shows a schematic of this reference electrode. Similarly, the presence of high concentration of OH^- maintains stable conditions suitable for reference electrodes.

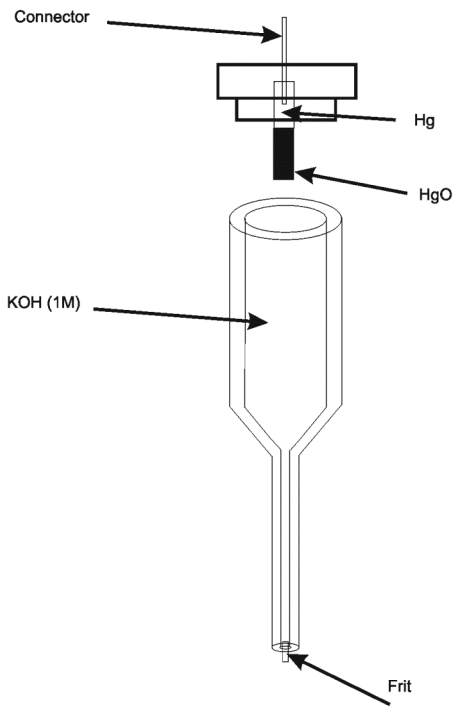


Figure 4.3

Schematic diagram of the mercury / mercury oxide reference electrode (Hg / HgO).

4.6 Electrode Modification

The substrate electrodes (BPPG) were easily modified. In the case of colloidal AgNPs, a volume of suspension was dried on the electrode surface in air. The density of NPs could be easily varied in accordance with the volume of suspension evaporated on the substrate surface. The electrode surface was then rinsed with de – ionized water to remove any material which was not well adsorbed on the surface. Similarly, in the case of PtNP – modified GCMS, the BPPG electrode could be modified by rubbing the electrode in a small quantity of the modified GCMS. This method is referred to as abrasive attachment. When evaporating colloidal suspensions on the electrode surface it was important to sonicate samples for 15 minutes beforehand in order to achieve maximum dispersion of the NPs.

4.7 Techniques

4.7.1 Scanning Electron Microscopy

Understanding the shape and size of nanoparticles is critical in the following work. This is made possible by the use of scanning electron microscopy (SEM). This technique operates on the principle of using electrons to generate an image rather than light as per a conventional microscope. An electron beam is generated, by the heating of a tungsten filament. This beam is then focused and directed via a series of lenses. Tungsten is typically used as its high melting point allows for heating to electron emission. Scanning of the sample is carried out in parallel tracks. As the beam interacts with the sample electrons are ejected by back – scattering and / or secondary emission. These electrons are then collected by detectors and converted to produce an image. Metallic particles show up as illuminated spots in SEM images allowing size and aggregation behaviour to be determined. SEM of nanoparticles was performed using a *JEOL JSM model 6300F* scanning electron microscope.

4.7.2 UV – vis Spectroscopy

UV – vis absorbance measurements were performed on a Perkin – Elmer spectrophotometer in the range 280 – 650 nm wavelengths. The study of visible and UV absorption gives the experimentalist information on the electronic energy levels of the molecules. When electromagnetic radiation falls upon a molecule, electrons can be excited to a higher energy state. If the frequency of the radiation is ν, the difference in energy can be defined according to **Equation 4.3**.

$$\Delta E = h\nu \qquad \textbf{[4.3]}$$

where *h* is Planck's constant. Each photon provides enough energy to excite one electron in a molecule into a different distribution. Provided an empty orbital is available the electron can be excited into it by the incoming radiation, and hence be absorbed. The absorption spectrum is plotted as percentage absorption *vs.* wavelength (nm). The presence of a *d* – metal ion in solution is often responsible for any apparent colour. This can be due to two types of transition. The first is known as a *d* – *d* transition, where an electron is excited from one d – orbital to another of higher energy. As these energy levels are close in energy, this transition can be brought about by the adsorption of visible light. As certain wavelengths of white light are adsorbed, the sample will take on the colour of those complementary to the absorbed light[6].

Chapter 4: References

1. A. Pyatenko, M. Yamaguchi and M. Suzuki, *Journal of Physical Chemistry B*, 2005, **109**, 21608-21611.

2. A. Pyatenko, M. Yamaguchi and M. Suzuki, *Journal of Physical Chemistry C*, 2007, **111**, 7910-7917.

3. R. Baron, F. W. Campbell, L. Xiao and R. G. Compton, *International Journal of Electrochemical Science*, 2008, **3**, 556-565.

4. D. D. Evanoff Jr. and G. Chumanov, *ChemPhysChem*, 2005, **6**, 1221-1231.

5. R. G. Compton and C. E. Banks, *Understanding Voltammetry*, 1st edn., World Scientific, Singapore, 2008.

6. P. Atkins and L. Jones, *Chemical Principles: The Quest for Insight*, 2nd Edition edn., W. H. Freeman, New York, 2002.

Chapter 5

Hydrogen Peroxide Electro – Reduction at a Silver-Nanoparticle Array: Investigating Nanoparticle Size and Coverage Effects.

Abstract

Discussion of the theory relating to nanoparticles has shown that particle size and coverage effects can be very important in determining the nature of the voltammetry. In the case of hydrogen peroxide reduction we observe distinctly different behaviour between the macro – and nano – scales. In this chapter we will compare and contrast the cathodic reduction of hydrogen peroxide (H_2O_2) at a silver macro – electrode (Ag_{macro}) and silver nanoparticle (AgNPs) array. Altered electrochemical behaviour is reported at the different scales. In acidic media, two parallel reduction mechanisms have been reported in the literature, which we will refer to as the "normal" and "autocatalytic" processes.

The "normal" reduction of H_2O_2 is reported at < - 0.4 V and in the presence of H^+ and forms water and the intermediate $OH_{(ads)}$. This $OH_{(ads)}$ intermediate facilitates the "autocatalytic" process. We report some interesting behaviour of AgNPs in this particular system. First, that "autocatalysis" is absent at AgNP – modified electrode. Secondly, at AgNP – modified electrodes, the "normal" reduction also demonstrates a negative peak shift for decreasing NP size as well as a positive peak shift for increased surface coverage. In order to de – convolute this complex behaviour, mass transport models have been developed and implemented to separate size – related diffusional effects from other possible influences. This work has been published in the *Journal of Physical Chemistry*[1].

5.1 Introduction

A wide variety of metallic nano – materials are used in many branches of electrochemistry[2, 3]. There exist significant differences in the physical and chemical properties of nano – materials compared to bulk silver (*e.g.* enhanced mass transport experienced at nanoparticles, high surface area), which can prove advantageous in electro – analysis. Rapid mass transport also facilitates the study of faster electrochemical and chemical processes since mass transport becomes less of a limiting factor. High surface area can promote surface catalysed processes resulting in high current values whilst the expression of particle crystal planes, *e.g.* altered electronic structure, can lead to useful catalytic properties[4].

Nanoparticle arrays can be constructed very easily and are able to generate high currents compared to a single nano – electrode. The current passed for the whole electrode is obtained from a collection of nano – electrodes working electrically in parallel[5]. NP – modified electrodes can play a very important role in electro – analysis due in large part to partial convergent diffusion to the nanoparticle array. Radial diffusion results in a larger current density being 'felt' at individual nanoelectrodes[6] as compared to a macro – electrode. This effect can be of use in electro – analysis as it allows us to achieve lower detection limits for target analytes and a higher sensitivity compared to macro – electrodes of equivalent geometric size.

These properties make NP – array electrodes ideal for the electro – analytical detection of species in solution[7, 8]. NP – arrays constructed on conductive substrates possess a high surface area – to – volume ratio. They are able to catalyse heterogeneous electron transfer, providing a more highly selective analysis than would be available by conventional means[9].

In this chapter we are also concerned with the effect of particle sizes. It is critical to assess the importance of any size effect in order to obtain the optimum conditions for a NP – based device. The literature has shown how metal particle size can affect the performance of alloys and nanocrystalline magnesium for the storage of hydrogen[10, 11], used in fuel cell technology. NP size also plays an important role in determining the stripping potential in anodic linear sweep voltammetry[12]. AgNPs have also demonstrated size dependent cellular interactions, with the work of Carlson and co-workers exhibiting different levels of cytotoxicity for several NP sizes[13]. The kinetics of carbon monoxide electro – oxidation exhibited on PtNPs demonstrates a significant size effect, in the range of 1.8 – 5 nm. Furthermore, size effects are reported in the literature for nano – scale platinum catalysts used in the reduction of oxygen (ORR)[14 15, 16].

The changes observed in the electrochemical behaviour between the macro – and nano – scales have found extensive application as discussed above. Understanding these effects is further complicated by the fact that any or all of the following effects may contribute to the observed electrochemical behaviour: altered mass transport, enhanced surface area or changed electro-catalytic behaviour arising from modified surface crystallographies and / or electronic effects. The rigorous dissection of the physical effects underpinning such a change has rarely been attempted and presents a considerable challenge.

In this chapter we discuss the application of citrate - capped colloidal silver nanoparticles of varying sizes to the reduction of H_2O_2 in acidic and neutral aqueous solutions. By comparing and contrasting the electrochemically irreversible reduction in acidic media at both the silver nano – and macro – electrodes we aim to separate

the mass transport effects from electro – catalytic and / or surface effects. We will also consider the size dependent behaviour of mass transport to an array of nanoparticles and its influence on the observed voltammetry. In particular, shrinkage of the nanoparticles is seen to promote convergent diffusion and so enhances the apparent electrochemical irreversibility of an electrode process. This is accompanied by a concomitant shift of the voltammetric peak to larger overpotentials. Such shifts can arise from mass transport effects alone. Finally, we apply a theoretical model to the reduction of H_2O_2 in order to separate mass transport effects from authentic electro – catalytic or size related effects.

In this chapter, we are particularly concerned with the study of H_2O_2 reduction in acidic solutions. However, polycrystalline silver electrodes have been used to study H_2O_2 reduction in both basic[17-19] and acidic[13, 20] media. The work of Ertl and co – workers suggests two parallel mechanisms of H_2O_2 reduction in operation[21]. The mechanism of the "normal" reduction is outlined in **Equation 5.1** and operates at higher overvoltages (< -0.4 *V vs. Hg / Hg_2SO_4*, $\alpha_N \approx 0.25$), as reported in the literature.

"Normal" H_2O_2 Reduction Pathway

$$H_2O_2 + H^+ + e^- \xrightarrow{slow} OH_{(ads)} + H_2O$$
$$H^+ + OH_{(ads)} + e^- \xrightarrow{fast} H_2O \qquad [\mathbf{5.1}]$$

A second process known as the "autocatalytic" mechanism can be observed at a much smaller overvoltage in the region of - 0.1 V (*vs. Hg / Hg_2SO_4*, $\alpha_A \approx 0.4$). This "autocatalytic" peak is found adjacent to oxide reduction peak. For this secondary

catalytic process to take place at a faster rate, an initial source of $OH_{(ads)}$ is required. This is generated as an intermediate in the "normal" reduction pathway. The "autocatalytic" process occurs as a consequence of the build-up of $OH_{(ads)}$ on the electrode surface. The mechanism of this secondary process is given in **Equation 5.2**:

"Autocatalytic" H_2O_2 Reduction Pathway

$$H_2O_2 + e^- \rightarrow OH_{(ads)} + OH^-$$
$$H_2O_2 + H^+ + OH_{(ads)} + e^- \rightarrow 2OH_{(ads)} + H_2O \qquad [\mathbf{5.2}]$$

Schematic representations of the "normal" and 'autocatalytic" H_2O_2 reductions are shown in **Figure 5.1.** The presence of adsorbed OH, formed as an intermediate in the "normal" reduction process, subsequently increases the rate of the secondary "autocatalytic" reaction resulting in further OH adsorption on the silver surface. We refer to the activated reduction process as "autocatalytic" due to the self – propagating nature of the reaction mechanism. When the two reaction profiles are superimposed, an overall "N – shaped" voltammogram is observed. The "activated" process can only be achieved for a very clean silver surface, free from halide[22] and organic compounds, which are known to contaminate silver sites. Activation of the surface by an initial oxidative scan is also required to observe autocatalysis.

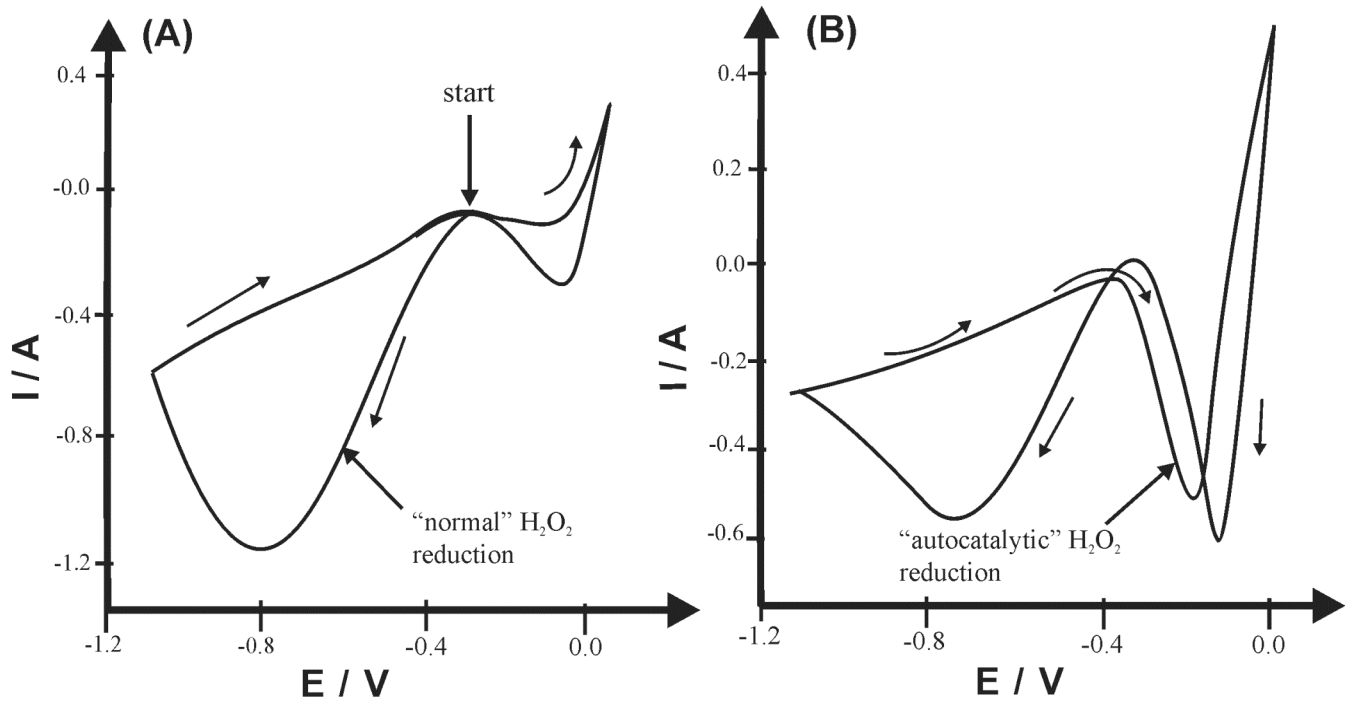


Figure 5.1

Schematic representation of voltammetry at a stationary Ag electrode in an electrolyte of 0.1 M $HClO_4$ + 20 mM H_2O_2, with a scan rate of 100 mV s^{-1}. (A) First scan, beginning at the "start" point and sweeping the potential first in a positive direction. Only "normal" H_2O_2 reduction can be observed in the reverse sweep. (B) Subsequent scans displaying an "autocatalytic" reduction peak at more positive potential as well as the "normal" reduction at a higher overpotential (vs. Hg.HgO)[21].

5.2 Hydrogen Peroxide Reduction at AgNP Arrays

AgNP – arrays were constructed as described in **Section 4.6** by evaporation of a small volume of colloidal suspension on the surface of a BPPG electrode. These AgNP arrays or a silver macro – disk electrode (Ag_{macro}, 3 mm diameter) were then used to investigate the cathodic reduction of hydrogen peroxide.

The experiments were carried out with 6 mM H_2O_2 in 0.1 M $HClO_4$ (pH 1) and in 0.05 M phosphate buffer solution (pH 7.4) *vs.* Hg / HgO electrode at 200 mV s^{-1}. The potential was scanned positively from 0 V giving an oxidation peak, the scan direction was then reversed giving a large and distinctive reduction peak for H_2O_2 reduction.

In this chapter we have also investigated the effects of nanoparticle size and degree of surface coverage on the nature of the experimental voltammetry. Each of the following three sizes of nanoparticles (20 – 40 nm, 50 – 70 nm, 80 – 120 nm) were investigated individually over a range of surface coverages. This allowed us to assess the significance of particle size and coverage on the reduction peak potential. In the case of AgNP – modified electrodes, the cathodic reduction of H_2O_2 was observed at negatively shifted potentials as compared to the Ag_{macro} electrode. For each of the 3 particle sizes, it was therefore necessary to scan the potential negatively from 0 V to up to ~ -1.8 V and reverse back to 0 V. In the presence of 6 mM H_2O_2, the Ag_{macro} displays a reduction wave in the window 0 to – 0.9 V.

Several AgNP – modified electrodes, with varying surface coverage were fabricated by drying volumes of colloidal suspension, between 5 μL and 200 μL on the electrode surface. These electrodes were then applied to the cathodic reduction of H_2O_2.

5.3 Results and Discussion

AgNPs are synthesized as described in **Section 4.3.1** generating particles in three distinct size ranges. All samples used the same citrate capping agent. This is important as any change in the capping agent may, at least in principle, have a marked effect on the behaviour of the NPs. SEM images of the AgNPs are shown in **Figure 5.2**, with sizes in the ranges of 20 – 40 nm, 50 – 70nm and 80 – 120nm.

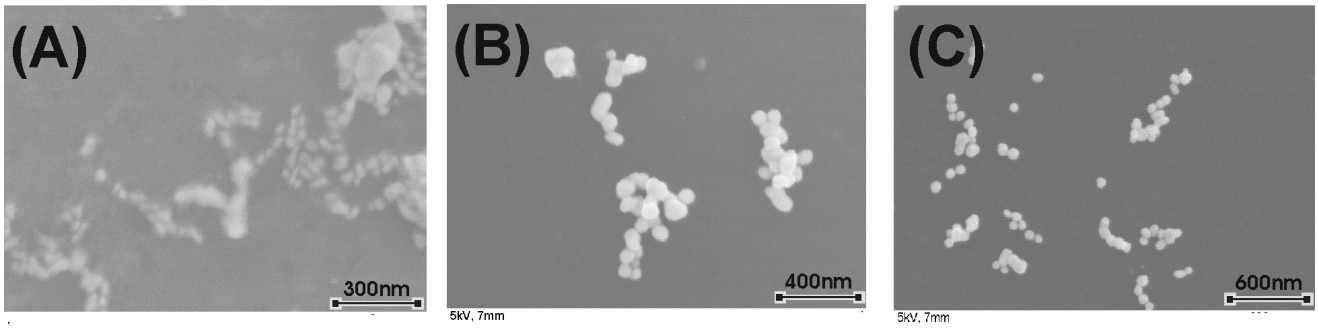


Figure 5.2

SEM images of colloidal citrate-capped AgNPs: (A) 20 – 40 nm, (B) 50 – 70 nm, and (C) 80 – 120 nm. SEM carried out on a carbon film / copper grid substrate.

We have discussed in **Section 5.1** that the "autocatalytic" reduction of H_2O_2 takes place at much smaller overpotentials than the "normal" reduction at a silver macro-electrode and has been well characterized by Ertl et al. The experimental voltammetry recorded for a AgNP – modified electrode is shown in **Figure 5.3**.

It is quite clear that in this case the "autocatalytic" feature is absent from the voltammetric trace. Therefore, the nano – scale material exhibits distinctly different behaviour as compared to a Ag_{macro} electrode as no "autocatalysis" can be observed.

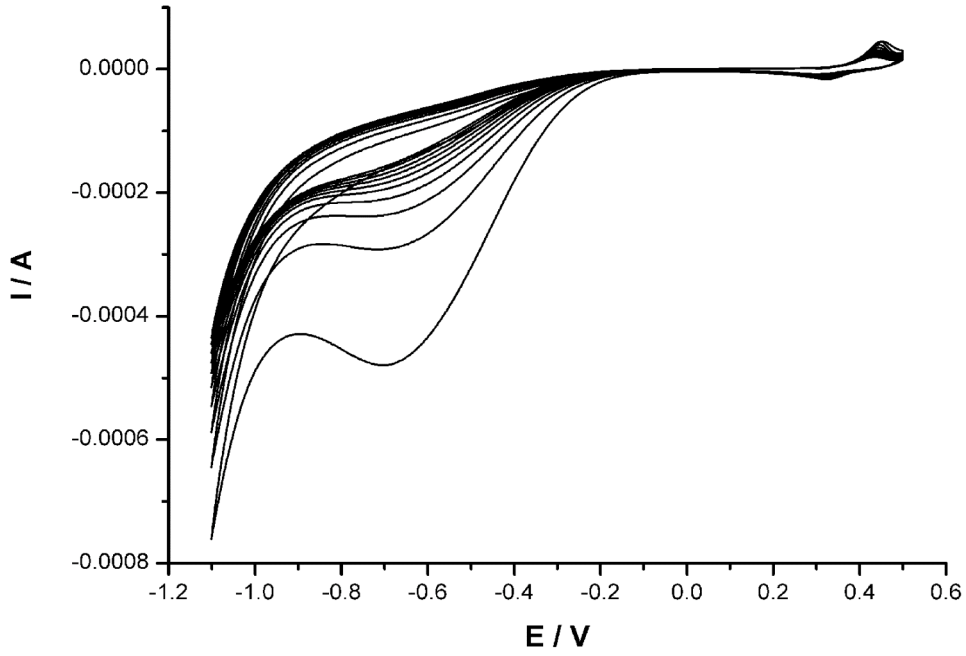


Figure 5.3

Reduction of H_2O_2 at a AgNP – modified electrode (~ 10 % surface coverage, 20 – 40 nm AgNPs): "auto – catalytic" reduction absent in the voltammetry (vs. Hg/HgO).

The reaction mechanism outlined in **Equation 5.1** and **5.2** indicates that the $OH_{(ads)}$ formed as an intermediate in the "normal" reduction of H_2O_2 is vital to facilitate the "autocatalytic" process.

It was initially proposed that the presence of the citrate capping agent on the AgNPs may inhibit the build up of $OH_{(ads)}$ on the NP surface. However, experiments performed in a solution of phosphate buffer containing 0.1 M sodium citrate and 6 mM H_2O_2 using Ag_{macro} electrode displayed similar voltammetry to that recorded in the absence of sodium citrate. Therefore, we can infer that the citrate molecule does not affect the "autocatalytic" process at the silver macro – electrode.

We can therefore infer that the absence of the "autocatalytic" phenomenon at the NP – modified electrode may be due to the nano – scale of the metallic particles rather than any perturbation from the chosen citrate capping agent. $OH_{(ads)}$ is required to initiate

the "autocatalytic" process, which may suggest different levels of adsorption taking place between the macro – and nano – silver. We suggest that at the nano – scale, the $OH_{(ads)}$ is not able to build up by a sufficient amount and therefore no "autocatalysis" is able to take place.

The nanoparticle size and surface coverage proved very significant in determining the nature of the voltammetry. Experimental voltammetry for the H_2O_2 reduction at AgNP – modified electrodes, over a range of surface coverage, is shown in **Figure 5.4**. Only the normal reduction wave is recorded for the NP – modified electrodes as discussed above. As well as the absence of an "autocatalytic" feature, the NP – modified electrodes exhibit some other interesting properties that differ from those at the Ag_{macro}.

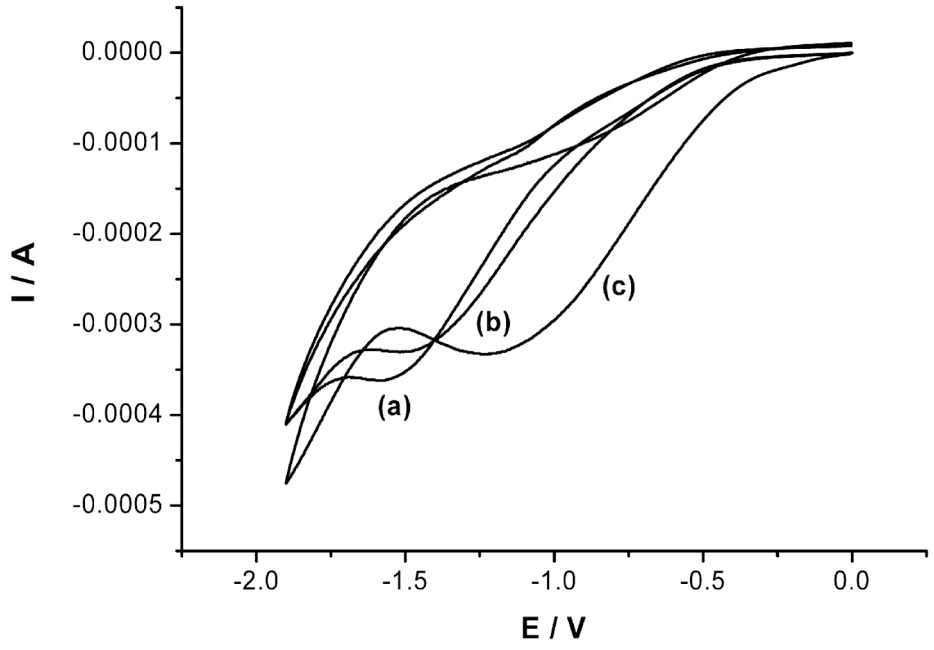


Figure 5.4

Experimental voltammetry for H_2O_2 reduction at AgNP – modified electrode. Curves (a) – (c) represent increasingcoverage ($Q = 0 - 5 \times 10^{-4} C$), resulting in a shift in E_p to smaller overpotentials.

Firstly, at low particle density a clear relationship exists between NP size and reduction peak potential for an essentially isolated particle. Secondly, an unusually large overpotential is observed for the "normal" reduction of H_2O_2, compared to the same reaction at Ag_{macro}. As the surface coverage (θ) increases the reduction peak potential shifts positively, tending towards that recorded at the Ag_{macro}.

NP – arrays also exhibit sensitivity to the degree of surface coverage as well as the variation in E_p with NP radius as previously discussed. The voltammetry obtained for several AgNP – modified electrodes, over a range of surface coverages, is shown in **Figure 5.4**. The curves labelled **(a)**, **(b)** and **(c)** correspond to increasing coverage (θ) of AgNPs on the electrode surface. As we increase θ the reduction peak shifts to smaller overpotentials. This behaviour is observed for all three NP sample sizes (20 – 40 nm, 50 – 70 nm and 80 – 120 nm). As θ increases, the NPs become more densely packed on the electrode surface, such that diffusion layers of adjacent particles begin to overlap. This tends towards linear diffusion as observed at a large disk electrode. Consequently, the voltammetry starts to look more macro – disk – like. The NP size does not dominate contributions to E_p at densely populated NP – arrays.

The reduction of H_2O_2 at the AgNP array was modelled as an array of micro – disks in a regular array, according to the diffusion domain approximation described in detail in **Chapter 1**. In order to assess the influence of nanoparticle coverage and mass transport on the system, varying degrees of nanoparticle separation (p) were considered. Good agreement was found between the simulation and experimental data for all 3 nanoparticle samples as shown in **Figure 5.5**. A best fit was found for $\alpha = 0.25$ and $\frac{k^0}{D}\exp\left[\frac{\alpha F E_f^0}{RT}\right] = 0.4 cm^{-1}$.

The agreement between the experimental data and the numerical simulation confirms that, in the irreversible limit, we are able to effect a shift in the reduction peak potential by altering the distance between neighbouring NPs in an array. Mass transport dictates that the array begins to behave more like a macro – disk, of equivalent size as shown by **Figure 5.5**.

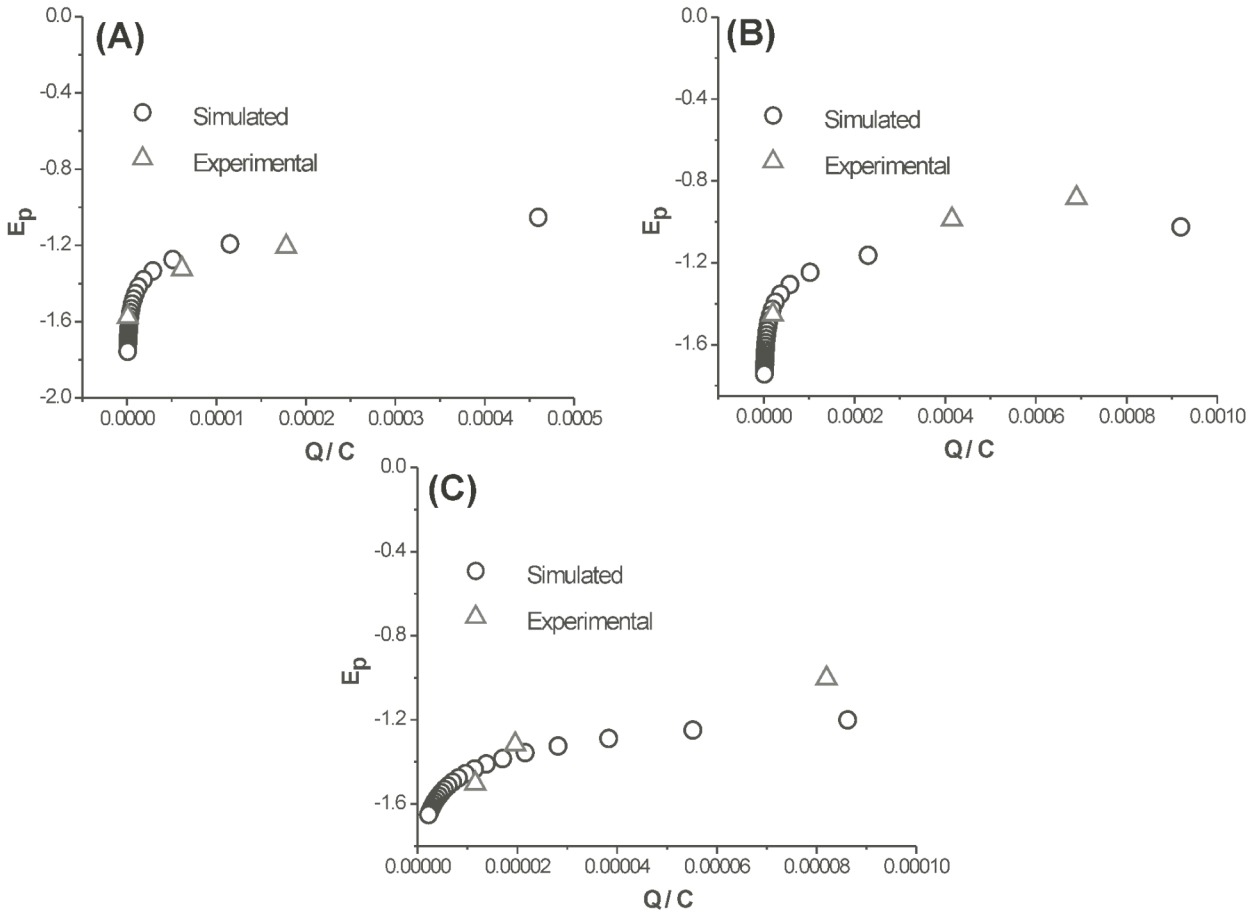


Figure 5.5

Plot of peak potential, E_p calculated for an array of AgNPs, using the model described in Appendix 1, and those obtained experimentally against charge (Q / C), representing the coverage of NPs on the electrode surface. Data plotted for three sizes of NPs with varying degrees of NP coverage, θ: (A) r_{avg} = 15 nm, (B) r_{avg} = 30 nm and (C) r_{avg} = 50 nm.

When the NPs are widely dispersed on the electrode surface such that $\theta \rightarrow 0$, the NPs are considered effectively isolated from each other. In this situation, diffusion to the array as a whole is no longer the dominant force in determining the H_2O_2 reduction peak potential. Instead the NP size becomes the most significant factor influencing the voltammetry. Extrapolation to the essentially isolated case gives a plot of E_p *vs.* $log_{10}\, r_{(avg)}$ shown in **Figure 5.6** for all three particle sizes at very low coverage ($\theta \rightarrow 0$). This plot displays a distinct relationship between the H_2O_2 peak potential (E_p) and the average radius of the NP, with E_p shifting to smaller overpotentials with an increase in the $r_{(avg)}$ of the nanoparticle.

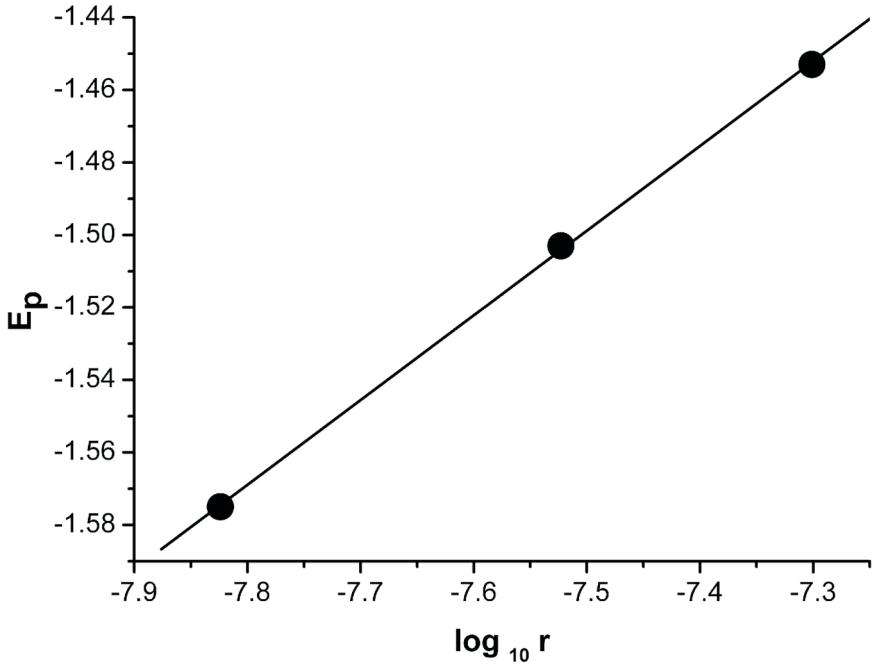


Figure 5.6

Reduction of H_2O_2 at AgNP – modified electrode: E_p vs $log_{10}\, r_{(avg)}$ for isolated nanoparticles; $\alpha = 0.253$.

Analysis of this data showed that:

$$\frac{\partial E_p}{\partial \log_{10} r} = \frac{2.3RT}{\alpha F} = 233\ mV \qquad [\mathbf{5.3}]$$

Fitting of this experimental data returns a value of $\alpha = 0.253$, the transfer coefficient for the "normal" H_2O_2 reduction. This value follows the reported literature values of $\alpha \approx 0.25$ very closely. This shows that where $\theta \rightarrow 0$ (isolated NPs), there exists a clear relationship between the NP size and E_p in the totally irreversible limit of the system.

5.4 Conclusions

In this chapter, AgNP – modified electrodes were used to investigate the electrochemically irreversible reduction of H_2O_2. Distinct differences are reported between the macro – and nano – scale electrodes. The complex behaviour of H_2O_2 reduction at the AgNP array involves a number of factors. First of all, autocatalysis was absent on AgNP – modified electrodes. We have also shown that the voltammetric peak potential / half-wave potential (E_p / $E_{1/2}$) varies logarithmically with NP radius for an electrochemically irreversible process, where the NPs are widely spaced and essentially isolated. The NPs are assumed to be hemispherical or disc shaped. Decreasing the size of the NP promotes convergent diffusion, enhancing the irreversibility of the process, resulting in the shift in E_p to larger overpotentials, compared to the macro – electrode behaviour. By applying a mass transport model to this system we were able to separate the size – related effects from other contributing factors. Experimental data was shown to fit well with that predicted for a simulated array (**Figure 5.6**). Therefore, we conclude that the positive shift with increasing surface coverage occurs as a result of diffusion layers of neighbouring NPs becoming more heavily overlapping, tending towards linear diffusion to and from the electrode surface. In other words, the array begins to behave more like a macro – disk electrode of equivalent size. These insights have significant implications for the development of NP – based sensors. Equally the absence of the "autocatalytic" reduction at the AgNPs is an important observation for the development of the fundamental theory of electron transfer at NP – modified electrodes. We will now go on to consider the reduction of protons at an array of AgNPs of different size and degree of surface coverage.

Chapter 5: References

1. F. W. Campbell, S. R. Belding, R. Baron, L. Xiao and R. G. Compton, *Journal of Physical Chemistry C*, 2009, **113**, 9053-9062.

2. L. Genies, R. Faure and R. Durand, *Electrochimica Acta*, 1998, **44**, 1317-1327.

3. B. Sljukic, R. Baron, C. Salter, A. Crossley and R. G. Compton, *Analytica Chimica Acta*, 2007, **590**, 67-73.

4. M. D. Hughes, Y. J. Xu, P. Jenkins, P. McMorn, P. Landon, D. I. Enache, A. F. Carley, G. A. Attard, G. J. Hutchings, F. King, E. H. Stitt, P. Johnston, K. Griffin and C. J. Kiely, *Nature*, 2005, **437**, 1132-1135.

5. D. W. M. Arrigan, *Analyst*, 2004, **129**, 1157-1165.

6. I. Streeter, R. Baron and R. G. Compton, *The Journal of Physical Chemistry C*, 2007, **111**, 17008-17014.

7. R. G. Compton, G. G. Wildgoose, N. V. Rees, I. Streeter and R. Baron, *Chemical Physics Letters*, 2008, **459**, 1-17.

8. C. M. Welch, C. E. Banks, A. O. Simm and R. G. Compton, *Analytical and Bioanalytical Chemistry*, 2005, **382**, 12-21.

9. C. W. Welch and R. G. Compton, *Analytical and Bioanalytical Chemistry*, 2006, **384**, 601-619.

10. K. Zhong, Y. Liu, M. Gao, J. Wang, H. Miao and H. Pan, *International Journal of Hydrogen Energy*, 2008, **33**, 149-155.

11. O. Friedrichs, L. Kolodziejczyk, J. C. Sánchez-López, A. Fernández, L. Lyubenova, D. Zander, U. Köster, K. F. Aguey-Zinsou, T. Klassen and R. Bormann, *Journal of Alloys and Compounds*, 2008, **463**, 539-545.

12. S. E. W. Jones, F. W. Campbell, R. Baron, L. Xiao and R. G. Compton, *Journal of Physical Chemistry C*, 2008, **112**, 17820-17827.

13. C. Carlson, S. M. Hussain, A. M. Schrand, L. K. Braydich-Stolle, K. L. Hess, R. L. Jones and J. J. Schlager, *The Journal of Physical Chemistry B*, 2008, **112**, 13608-13619.

14. H. Ye, J. A. Crooks and R. M. Crooks, *Langmuir*, 2007, **23**, 11901-11906.

15. S. L. Chen and A. Kucernak, *Journal of Physical Chemistry B*, 2004, **108**, 13984-13994.

16. F. Maillard, E. R. Savinova and U. Stimming, *Journal of Electroanalytical Chemistry*, 2007, **599**, 221-232.

17. M. Honda, T. Kodera and H. Kita, *Electrochimica Acta*, 1983, **28**, 727-733.

18. T. Hurlen, Y. L. Sandler and E. A. Pantier, *Electrochimica Acta*, 1966, **11**, 1463-1473.

19. N. D. Merkulova, G. V. Zhutaeva, N. A. Shumilova and V. S. Bagotzky, *Electrochimica Acta*, 1973, **18**, 169-174.

20. M. Honda, T. Kodera and H. Kita, *Electrochimica Acta*, 1986, **31**, 377-383.

21. G. Flätgen, S. Wasle, M. Lübke, C. Eickes, G. Radhakrishnan, K. Doblhofer and G. Ertl, *Electrochimica Acta*, 1999, **44**, 4499-4506.

22. E. S. Brandt, *Journal of Electroanalytical Chemistry*, 1983, **150**, 97-109.

Chapter 6

The Hydrogen Evolution Reaction at a Silver Nanoparticle Array and a Silver Macro – electrode Compared: Changed Electrode Kinetics between the Macro – and Nano – scales.

Abstract

As discussed in the previous chapter with reference to H_2O_2 reduction, size and coverage effects prove to be very important in determining the nanoparticle behaviour. In this chapter we will continue this discussion by considering the response of silver nanoparticle (AgNP) arrays toward the hydrogen evolution reaction (HER). The HER is based on the electro – reduction of protons (H^+) at a metal electrode surface. This process will be compared at a silver macro – disk electrode and at AgNP – arrays. The AgNPs used were synthesized in colloidal suspension, as detailed in **Chapter 4**. The substrate basal plane pyrolytic graphite (BPPG) electrode was modified by evaporation of the colloidal suspension on the electrode surface. In this chapter we will also consider the effect of NP size and degree of surface coverage on the nature of the voltammetry. The reduction of protons at silver nanoparticle arrays is reported for three sizes of AgNPs, over a range of surface coverages. Electrolysis occurs exclusively at the nanoparticles and not at the underlying BPPG electrode, under the given conditions.

Examination of the voltammetry over a range of surface coverages shows that the onset potential of the HER correlates with the extent of the surface coverage. The experimental data were subsequently simulated numerically for both a regular and

random distribution of particles, allowing for contrasting diffusional effects between the macro – and nano – scales. Numerical simulation of the voltammetry of the HER facilitates the quantification of the kinetic parameters related to this process (*e.g.* electrochemical rate constant (k^0) and the transfer coefficient (α)). From the fitting of the experimental data we were able to demonstrate the altered kinetics (k^0 *and* α) between a silver macro – disk electrode ($\alpha_{macrodisk} \approx 0.36$, $k^0 = 6 \times 10^{-12}$ *cm* s^{-1}) and the AgNP – array ($\alpha_{array} \approx 0.16$, $k^0 = 1 \times 10^{-6}$ *cm* s^{-1}). Therefore, we suggest that the altered kinetics at the nano – scale indicates a specific nano – effect in place. This work has been published in the *Journal of Physical Chemistry*[1].

6.1 Introduction

Nanoparticulate materials are widely used in many areas of electrochemistry. The unique properties exhibited by nanoparticles make them particularly useful in electroanalysis[2]. However, despite the extensive use of nanoparticles in this field little effort has been directed towards explaining the fundamental differences in the electrode kinetics recognized between the macro – and nano – scale. One critical difference is the type of diffusion, as a macro – electrode will experience planar diffusion while an array of nanoparticles will experience a mixture of convergent and linear diffusion depending on the overlap of adjacent diffusion layers. This makes the extraction of the kinetic parameters for a given system somewhat more difficult. Recently, theory implementing the appropriate mass – transport corrections has been developed to facilitate Tafel analysis at NP – arrays. This chapter will build on the theory reported in the literature in order to compare the HER at both silver macro – disk and silver nanoparticle arrays, composed of NPs of varying size, in order to probe the differences that arise between the macro – and nano – scales.

This chapter is focused on the reduction of protons to form dihydrogen, H_2, as shown in **Equation 6.1**.

$$H^+(aq) + e^- \rightarrow \tfrac{1}{2} H_2(g) \qquad \textbf{[6.1]}$$

This reaction has been studied extensively due to its fundamental importance in electrochemistry. Not only is the study of this electrode process of great practical

significance[3] but it can also serve as a simplified model for the study of other, more complex electrode processes.

A great deal of effort has been focused on the study of the electrode kinetics of the HER over a number of decades. The HER has been studied in both acidic[4-6] and alkaline[7, 8] solutions. The effect of the experimental conditions have been examined including the sensitivity of the HER process to temperature[9, 10], pH[11] and the nature of the electrode material. The reaction mechanism has proved to be highly sensitive to the electrode material, proceeding quickly at a platinum surface but very slowly at lead. A wide range of electrode materials have been used to study this reaction including mercury, platinum, gold, tungsten, copper and silver [4-7]. Such sensitivity to electrode material corresponds to the importance of adsorbed hydrogen ($H^{\bullet}$) as an intermediate, as $H^{\bullet}$ is easily adsorbed on Pt compared to Pb. It is quite clear that the specific nature of the electrode / solution interface plays a crucial role in this process.

Studies conducted on the reduction of protons has produced a large body of research, including the work of Marinovic and Despic[12, 13], Trasatti[14, 15], and Conway and Bockris[16]. Kita[17] has also demonstrated that the exchange current density of an electrode displays a dependence on a number of factors such as pre – treatment, solution composition, pre – electrolysis and temperature. The HER exhibits a variation in activity across a range of electrode materials. This can be related to several factors, including the aadsorption enthalpy of hydrogen, work function, etc. Trasatti[14, 15, 18] has considered the mechanism of the HER based on the electrochemical rate constant (k^0) as a function of $\Delta H_{(ads)}$ on different electrodes, the result of which was his famous "volcano curve".

In this chapter we are only concerned with the reaction at silver electrodes. Macagno[7,8] *et al*. have demonstrated enhancement of the rate of the HER for silver electrodes in alkaline solution, following pre – treatment of the electrode. Activation of the electrode has been related to the restructuring of the metal surface during the treatment process. The HER is sensitive to the surface structure as demonstrated by the study of silver single crystal electrodes[19] in aqueous media. Further investigations have been conducted to assess the effects of alcohols[3], chemisorbed sulphur, metallic impurities[20-24] and deposition of sodium[25] on the electrode surface structure and consequently the behaviour of the HER. Quantitative studies of the HER at a silver cathode as carried out by Krishtalik[11] have shown that the corresponding transfer coefficient (α) for this electro – reduction process is ~ 0.3. Trasatti[14, 15, 18] suggests an exchange current density of $\sim 10^{-8}$ $A\ cm^{-2}$ while Kita[26] suggests a wider range of values from $10^{-3.7} - 10^{-7.05}$ $A\ cm^{-2}$, again dependent on the surface structure.

This study was initially prompted by reports of the sensitivity of the HER to the electrode morphology. In this chapter we report the electrode kinetic data pertaining to the HER at silver nanoparticle arrays. Comparison with a silver macro – electrode indicated a significant electrode kinetic effect existing between the nano – and macro – scales, in terms of k^0 and α.

6.2 Theory

In order to fully interpret the experimental data it was necessary to consider the cyclic voltammetry of the random nanoparticle assemblies using numerical simulation methods. A model has been developed in this laboratory[27, 28] to explain the diffusional behaviour taking place at a NP – modified electrode. The simulations are based on the well – established Butler – Volmer (**Equation 6.2**) model[19] for fully irreversible electrode kinetics, applying the diffusion domain approximation[20-24] to the transport to a random distribution of electrochemical centres [29]. For the conversion of *A* to *B*:

$$A + e^{-} \rightarrow B$$

$$k = k^{0} \exp\left[\frac{-\alpha F(E - E_{f}^{0})}{RT}\right] \qquad \textbf{[6.2]}$$

where k is the rate constant; k^0 the standard electrochemical rate constant; α the transfer coefficient; R the gas constant (8.314 $J\ K^{-1}\ mol^{-1}$); T temperature (298 K); E the potential and E_f^o the formal reduction potential for the redox couple A/B.

This problem is based on the different diffusional fields experienced at a macro – electrode, isolated nano – electrode and an array of nanoparticles. The different diffusional fields are shown in **Figure 6.1**. The nano – electrode and nanoparticle arrays are supported on a conducting substrate, which provides electrical contact as

well as acting as a source or sink of electrons. The reaction under investigation is assumed to take place only at the NPs, and not at the supporting substrate material.

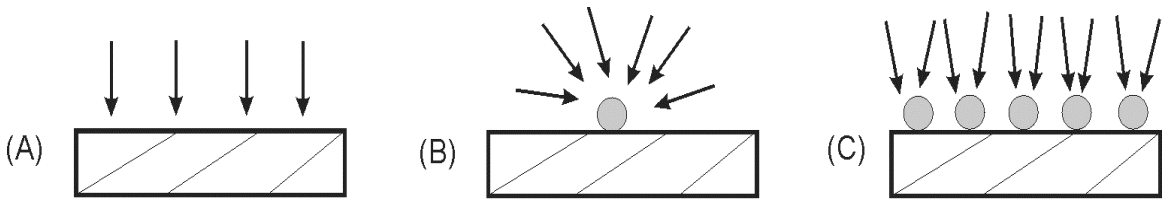


Figure 6.1

The mass transport to: (A) a macro – electrode, (B) an isolated NP and (C) a random array of NPs.

Distinctly different diffusional behaviour is experienced at a macro – electrode (A) and an isolated nano – electrode (B), such that the former experiences planar diffusion and the latter will experience convergent diffusion, a far more effective means of mass transport. A random array of particles (C) will experience diffusional behaviour which is intermediate between planar and convergent diffusion. In this case the degree of surface coverage becomes a critical factor. As the density of particles on the surface increases, the diffusion layers of adjacent particles will overlap to a greater extent, tending towards planar diffusion. It is well understood that for the case of fully irreversible electrode processes[23], the enhanced mass transport in the convergent diffusion regime leads to a greater overpotential than is seen for macro – electrodes undergoing planar diffusion. Therefore, for a reduction, the value of $E_{p,c}$ will be negatively shifted on the isolated NP, relative to a macro – electrode. As a random array of particles will experience intermediate behaviour between planar and convergent behaviour, we expect a greater overpotential for the reduction as

compared to the macro – electrode but less than is seen for the isolated nanoparticle. When we couple this with the effect of surface coverage, we see that as the density of particles increases, the diffusion becomes more planar and less locally convergent, resulting in a decrease in the overpotential, shown schematically in **Figure 6.2**.

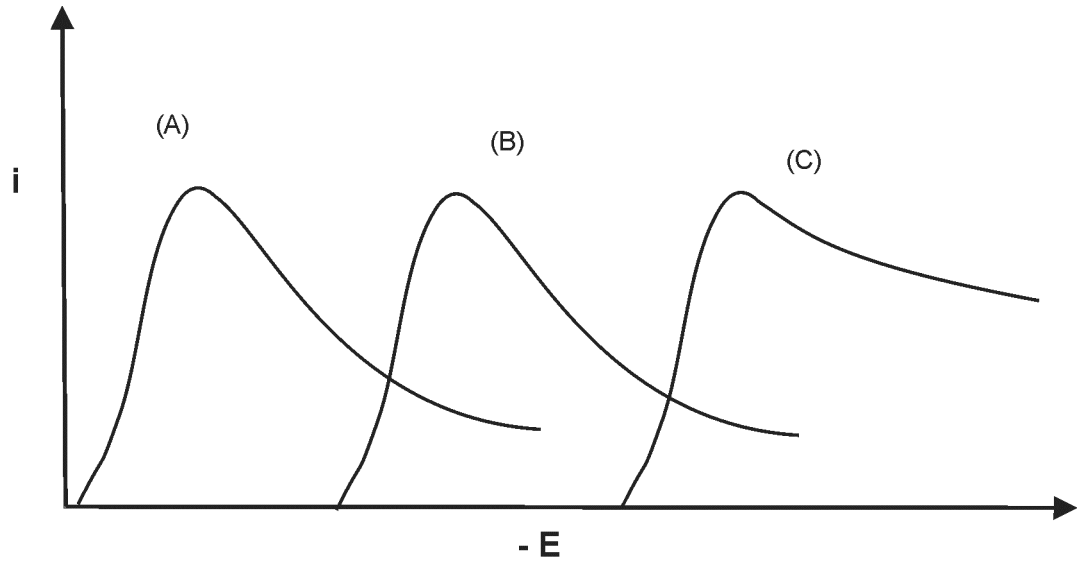


Figure 6.2

The effect of mass transport on the voltammetry of a fully electrochemically irreversible reduction as a function of the electrode type; (A) macro – electrode, (B) NP – array (high coverage) and (C) NP array (low coverage). Note that curve (c) is typically peak – shaped and not sigmoidal at the scan rates required for near diffusional independence.

This effect described above is attributed purely to the difference in the mass transport regime between the macro – and nano – scales. However, it could potentially be mistaken for some sort of "enhanced electro – catalysis" if not considered carefully alongside the corresponding macro – disk behaviour.

The reduction of H^+ at a AgNP – modified BPPG electrode was investigated by a series of numerical simulations[28]. These numerical simulations have been developed from previous work on spherical nanoparticle arrays[30, 31] which approximate the spheres as flat disks. Typical simulation methods model the array based on a regular approximation, (*i.e.* a square array of NPs where the particles are equidistant from one another) under *Case 3 / 4* diffusion. Under such a diffusion regime, there is a significant degree of overlap, corresponding to the experimental conditions. Application of the diffusion domain approximation allows us to solve the diffusion problem, facilitating the numerical simulation of the cyclic voltammetric response, in a matter of minutes. The experimental reality is in fact a random array of NPs on the surface of the substrate electrode. A random assembly of NPs can be treated as flat microdisks wired in parallel, and subsequently divided into a number of Voronoi cells as shown in **Figure 6.3**.

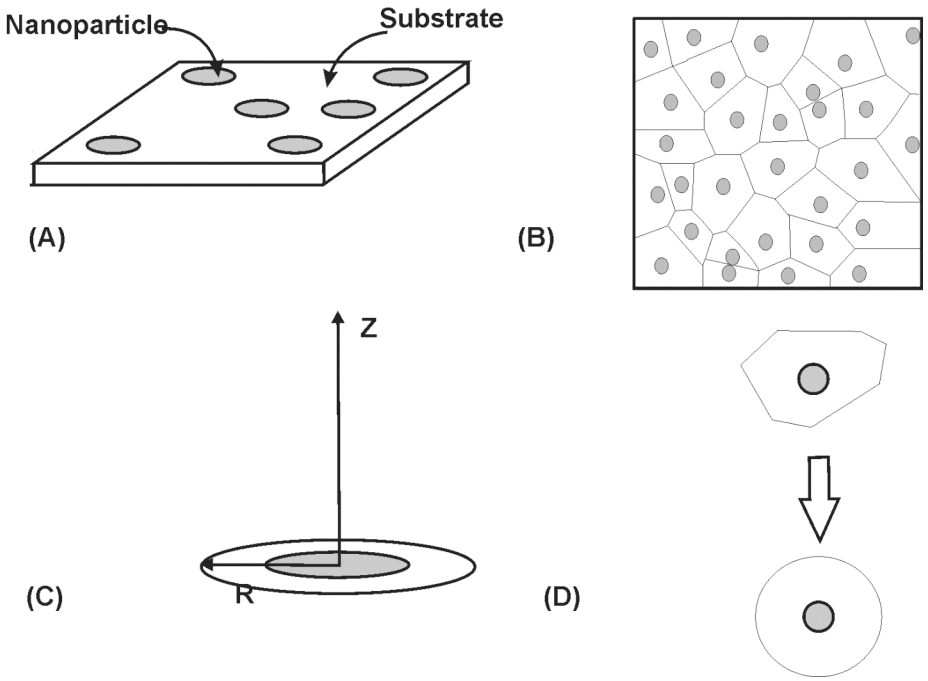


Figure 6.3

Schematic representation of the diffusion domain approximation as applied to a random distribution. (A) random array of microdisks, (B) random array of microdisks divided into Voronoi cells, (C) cylindrical domain, (D) diffusion domain approximation.

The walls of the cell correspond to a no – flux boundary and lie half way between adjacent particles, with each cell containing only one NP. Each Voronoi cell can be treated as diffusionally independent. Similarly, we can then apply the diffusion domain approximation as shown in **Figure 6.3(D)**, to convert the base of the cell to a circle of equivalent area. The flux drawn across the entire assembly of NPs must be the sum of fluxes for every possible diffusion domain radius, weighted according to the frequency distribution for the random assembly for which a Poisson – Voronoi approach was adopted[32] using a two – dimensional approximate distribution as described below as derived by Ferenc on the basis of Monte Carlo simulations. The

weighting is dependent on the average diffusion domain radius ($\langle R_d \rangle$) as shown in **Equation 6.3**;

$$f(y) = \frac{343}{15}\sqrt{\frac{7}{2\pi}}y^{\frac{5}{2}}\exp\left(-\frac{7}{2}y\right) \qquad [\mathbf{6.3}]$$

where

$$y = \left(\frac{R_d}{\langle R_d \rangle}\right)^2$$

Note that for $\langle R_d \rangle \sim 1$, corresponding to near overlap the voltammogram used to compute the weighted averages is that of $R_d = 1$.

All programs were written in C++ and compiled using a Borland compiler. Simulations were run on a desktop PC with a 2.83GHz Pentium processor and 3.25GB of RAM. Full calculations as described above for random arrays are typically very computer time intensive, with run times of ~ 50 hours! On the other hand, simulation of a regular array takes only a few minutes, as only a single diffusion domain needs to be considered. Programs and simulations are credited to Stephen R. Belding. In this chapter we will compare the simulation of the reduction of H^+ at a AgNP – modified BPPG electrode, using both regular and random distribution numerical models. Therefore, we can suggest reasonable conditions under which a random array may be approximated by a regular array of particles.

6.3 Results and Discussion

The voltammetric response of a silver macro – disk electrode was first reported in perchloric acid ($HClO_4$, 0.25M, 50 $mV\ s^{-1}$). This is important for the purpose of comparison with the AgNP – BPPG electrodes. The distinctive irreversible electrochemical behaviour was exhibited for the reduction of protons to dihydrogen (H_2). The corresponding Tafel analysis allowed us to extract the kinetic parameters of the HER. The Tafel plot (*ln i vs. E*) is shown in **Figure 6.4**; from the slope, an experimental value of the transfer coefficient, $\alpha_{macrodisk} \sim 0.36 \pm 0.02$ was obtained and extrapolation of the slope revealed an experimental rate constant of $k^0 = 6 \times 10^{-12} cm\ s^{-1}$. This closely follows the literature value of $\alpha \sim 0.3$ for the HER at a silver macrodisk electrode[7]. It is important to note that due to the extrapolation, the value of k^0 may be subject to a large error whereas the value of α is not.

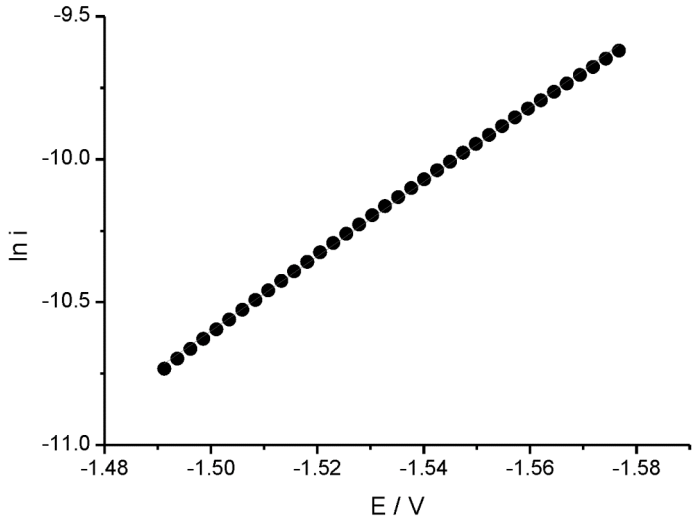


Figure 6.4

Tafel plot of H^+ reduction at a silver macrodisk electrode (0.25 M $HClO_4$ vs. SCE, 50 $mV\ s^{-1}$), $\alpha = 0.36$.

AgNP – arrays were subsequently used to study the hydrogen evolution reaction in $HClO_4$ (0.25 M, 50 $mV\ s^{-1}$). Similarly, the irreversible electro – reduction of protons at potentials more negative than – 1.25 V was observed with the assumed formation of H_2. **Figure 6.5** displays the relationship between the onset of hydrogen evolution and the degree of nanoparticle surface coverage (θ). As θ increases, the onset potential of the HER shifts to smaller overpotentials.

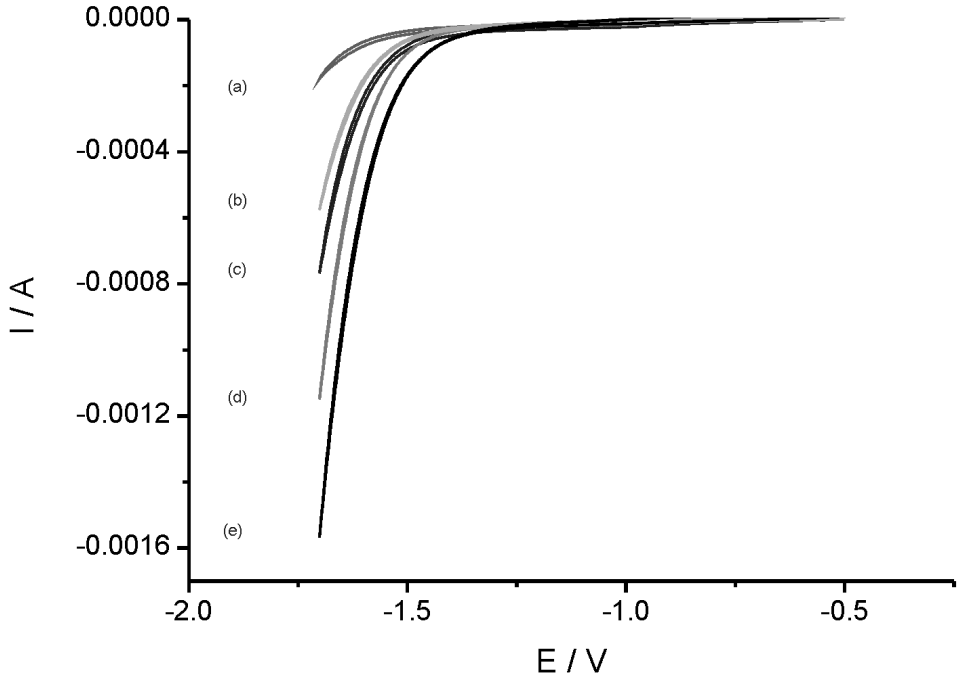


Figure 6.5

Experimental voltammetry of H^+ reduction at a series of AgNP – modified (r = 15 nm) BPPG electrodes, with increasing surface coverage (vs. SCE, 0.25 M $HClO_4$, 50 $mV\ s^{-1}$); (a) 0.87%, (b) 1.8%, (c) 2.6%, (d) 3.0%, (e) 4.0%.

We should also note the increase in current at a fixed potential with increasing coverage. This can be attributed to a reduction in the electrochemical irreversibility of the process but also to an increase in the active surface area of silver available for

the reaction to proceed. Therefore, we can predict that as θ increases, we will be able to recover the macro – electrode response. This type of behaviour was reported for all 3 sizes of AgNP studied over a range of surface coverages (~ 0.1 – 6.0 %). NP size and coverage effects have been discussed in the literature by Campbell et al.[27] and Ward Jones[33] , with respect to H_2O_2 reduction at AgNP – arrays and the stripping of AgNPs, respectively.

The next step was the fitting of the experimental data for each nanoparticle size. The formal potential for the H^+/ H_2 couple is fixed as $E_f^o = 0\ V$. The current at – 1.7 V was fitted for a given surface coverage. Due to the shape of the HER voltammetry, this potential corresponds to the ascending part of the current – voltage curve, rather than the peak current. This process was modeled for both a regular and a random array of AgNPs. A standard irreversible electrochemical rate constant of $k^0 = 1 \times 10^{-6} cm\ s^{-1}$ was deduced from the data fitting, for a series of α values. The fitting of the experimental data for both the regular and random array models, over a range of coverages, is shown in **Figures 6.6** and **6.7**.

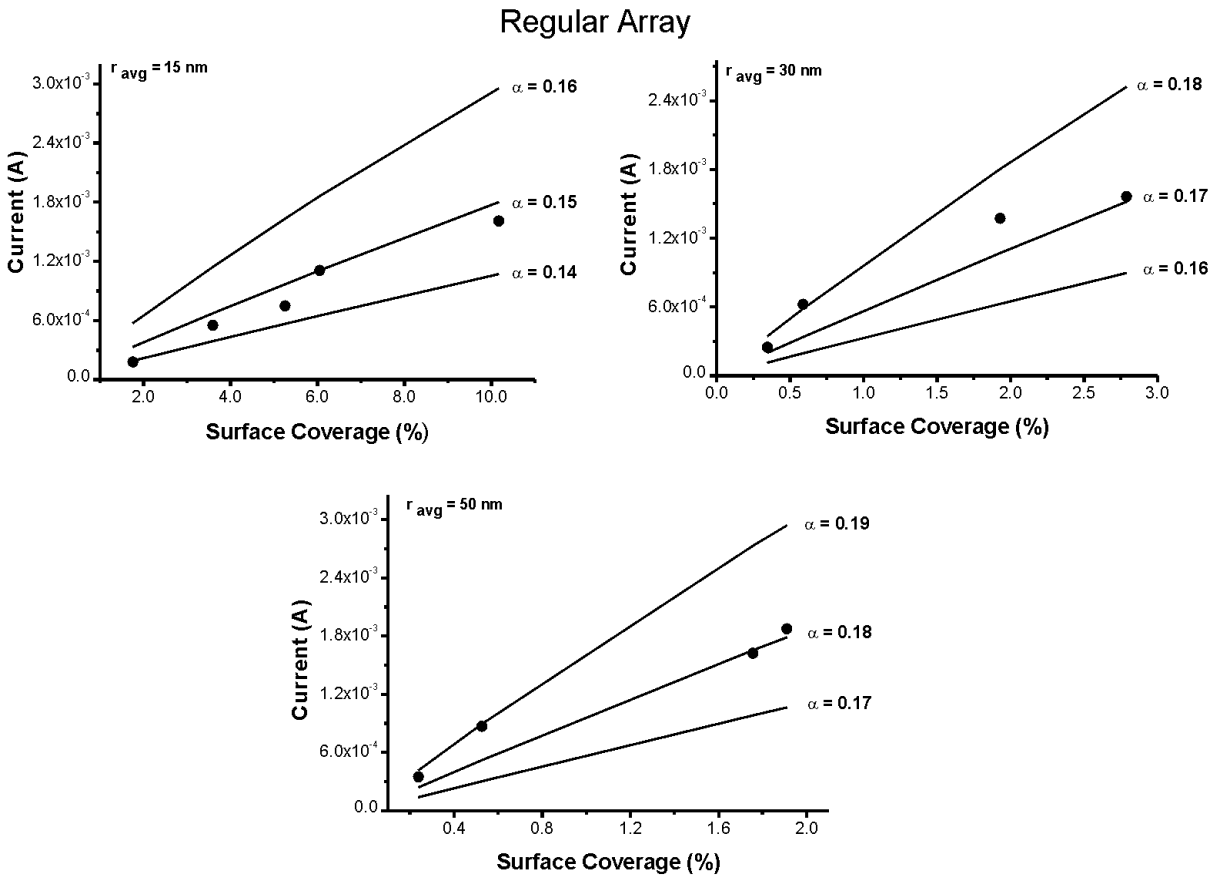


Figure 6.6

Regular array model of particles: Numerical simulations of a AgNP – modified electrodes for 3 sizes of NP (r = 15 nm, 30 nm, 50nm), using several values of α to fit experimental data (black dots). Fitting of experimental data correct to 2 significant figures shows: α_{array}*(15 nm) = 0.15;* α_{array}*(30 nm) = 0.17;* α_{array}*(50 nm) = 0.18,* $k^0 = 1 \times 10^{-6} cm\, s^{-1}$.

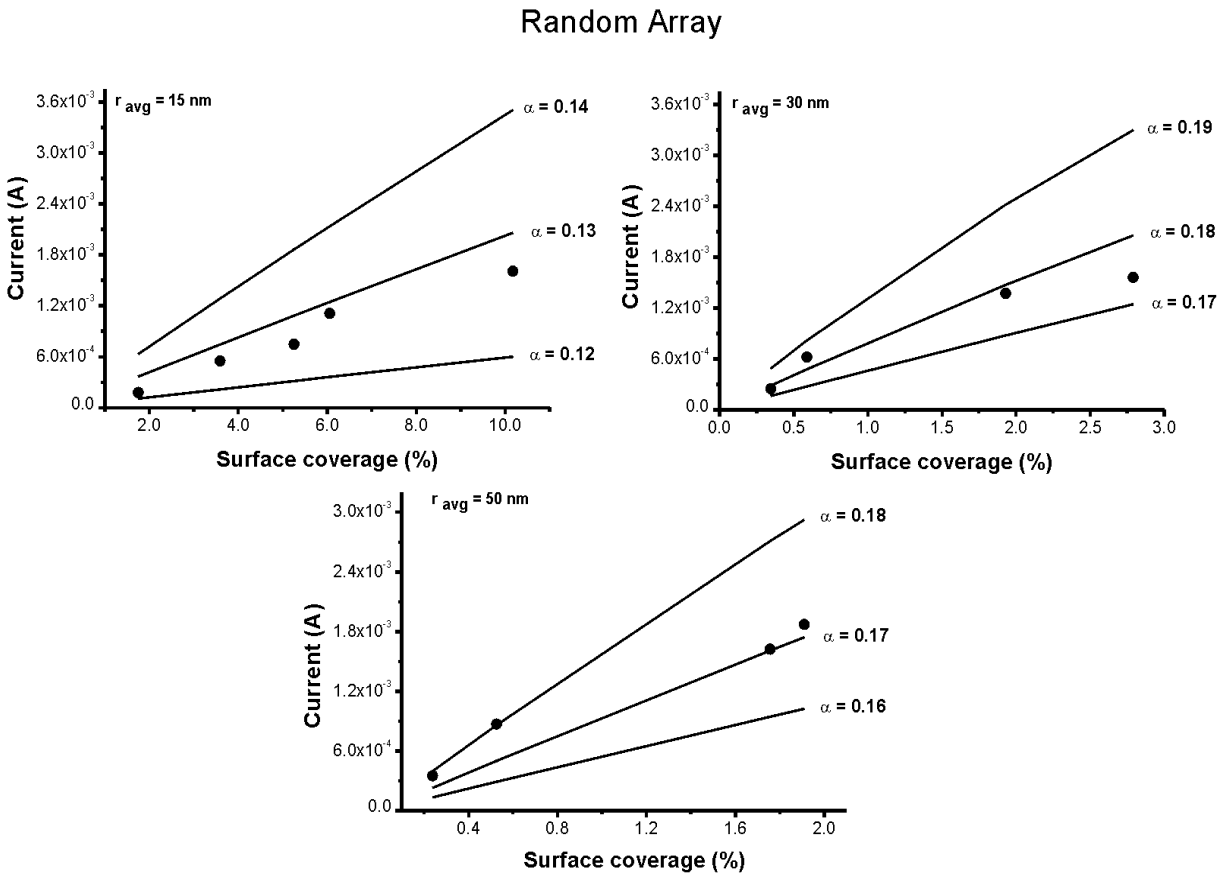


Figure 6.7

Random array model of particles: Numerical simulations of a AgNP – modified electrodes for 3 sizes of NP (r = 15 nm, 30 nm, 50nm), using several values of α to fit experimental data (black dots). Fitting of experimental data correct to 2 significant figures shows: α_{array}*(15 nm) = 0.13;* α_{array}*(30 nm) = 0.18;* α_{array}*(50 nm) = 0.17,* $k^0 = 1 \times 10^{-6} cm\, s^{-1}$.

The simulations for various α values were carried out for each of the 3 sizes of AgNPs. For a regular array, α values ranging from 0.14 – 0.19 were calculated and for a random array, α values in the range of 0.12 – 0.19. The fitted values of α for each NP size are given in **Table 6.1** below.

Regular Array Simulation		**Random Array Simulation**	
Average NP radius (nm)	**α_{array}**	**Average NP radius (nm)**	**α_{array}**
15	0.15	15	0.13
30	0.17	30	0.18
50	0.18	50	0.17

Table 6.1

Fitted value of α for both the regular and random array simulations, for all 3 nanoparticle sizes.

The table above clearly indicates that as the NP size decreases from $r_{(avg)}$ = 50 nm to $r_{(avg)}$ = 15 nm, α decreases accordingly from *ca*. 0.18 to *ca*. 0.13. Comparison of the results obtained for α_{array} shows that the regular and random models agree quite conclusively, well within the range of any experimental error.

This conclusion demonstrates an experimental proof, agreeing with previous theoretical studies of random and regular arrays of NPs[2]. In this instance the diffusion has been categorized as *Case 3*, such that the adjacent diffusion layers overlap extensively. Under these conditions, the distribution of NPs plays a minor role in determining the electrode kinetics of the process. Specifically, the maximum deviation in the kinetic parameters, between random and regular distributions are

defined as a factor of 2 for the rate constant (k^0) and 0.02 for the value of the transfer coefficient (α).

Tafel analysis of the voltammetry at a AgNP – arrays can be conducted such that apparently straight lines can be determined at low currents. However, this reveals α values which display a strong dependence on surface coverage. In principle, by recording α at very low currents, we should be able to attain mass transport free data. However, in the system studied here, the presence of small background currents makes this approach unreliable.

Under these given conditions (*i.e.* surface coverage < 10 %), it is perfectly reasonable to approximate a random array of particles by a regular approximation, for the reduction of protons at a AgNP – array, thus providing a fast and accurate means of numerical simulation. We can use this approach to investigate the influence of kinetic parameters (k^0 and α) on the voltammetric features. The effect of surface coverage (θ) on the nature of the voltammetry can also be investigated.

The altered kinetics between the macro – disk and the NP – array is indicative of a specific kinetic nano – effect, with the values α_{array} and k^0 varying significantly from those for the macro – disk. Using DIGISIM™[34] we can apply the kinetics determined at the NP – array ($\alpha_{array} \sim 0.16$, $k^0 = 1 \times 10^{-6} cm\ s^{-1}, E_f^0 = 0\ V$) to an equivalent macro – disk electrode under the same conditions (50 $mV\ s^{-1}$, $[H^+]$ = 0.25M). Comparison of this simulation with that obtained using the experimentally determined kinetic parameters for the silver macro – disk ($\alpha_{macrodisk} \sim 0.36$, $k^0 = 6 \times 10^{-12} cm\ s^{-1}, E_f^0 = 0\ V$), we observe an interesting phenomenon. When the NP – array kinetics are applied to a macro – electrode, a significantly less negative overpotential (~ 145 mV) is required for the electro – reduction process to take place. This implied faster electrode kinetics

at the NP – array as compared to an equivalent macro – disk. The increase in the value of k^0 from the macro – scale to the nano – scale is likely to reflect an increase in the density of active sites available for $H^{\bullet}$ adsorption. On the other hand, the reduced value of α for the NP – array may suggest that the potential distribution near the NPs is altered from that at a macro – electrode.

6.4 Conclusions

In conclusion, this chapter has discussed the importance of the hydrogen evolution reaction in the field of electrochemistry. Furthermore, we have also considered the properties of the HER in relation to AgNP – array electrodes. We have compared and contrasted the voltammetry obtained for a AgNP – modified electrode and a silver macro – electrode for the reduction of H^+, under the same conditions.

At a silver macro – disk, in acidic media, the HER displayed typically irreversible behaviour. Tafel analysis of the voltammetry revealed a value of $\alpha_{macrodisk} \sim 0.36 \pm 0.02$. This value agrees with the reported literature value[8] of $\alpha \sim 0.3$.

For all three sizes of particles, the AgNP – arrays exhibited a clear relationship between the degree of surface coverage and current. More specifically, the cathodic current increases with density of NPs on the BPPG electrode surface. This effect is attributed to increased electro – active surface area of the AgNPs and a decrease in the irreversibility of the electrode process.

We further investigated this system by a series of numerical simulations conducted for both a regular and random array of nanoparticles. The simulated cyclic voltammetry at AgNP – modified electrode displayed good agreement with the experimental data, for both a regular and random model. The parameters extracted from these numerical simulations are detailed in **Table 6.1**. The agreement between the regular and random array models is a particularly relevant result as it shows that for this system, a regular approximation of a random distribution of particles provides a fast and reliable result, thus removing the problem associated with the time – intensive simulation of random nanoparticle distributions.

To summarise, by numerical simulation of the cyclic voltammetry of the AgNP – arrays for the reduction of H^+, we have demonstrated that altered kinetics exist between the silver macro – disk and the AgNP – array. An unusually low value of α_{array} = 0.13 - 0.18 fits our experimentally obtained data for the AgNP – arrays at various surface coverages. This differs significantly compared to the value for the macro – disk, reported as $\alpha \sim 0.3$. In the following chapter we consider the study of proton reduction at arrays of platinum nanoparticles immobilised on glassy carbon microspheres.

Chapter 6: References

1. F. W. Campbell, S. R. Belding, R. Baron, L. Xiao and R. G. Compton, *The Journal of Physical Chemistry C*, 2009, **113**, 14852-14857.

2. C. W. Welch and R. G. Compton, *Analytical and Bioanalytical Chemistry*, 2006, **384**, 601-619.

3. A. A. Gürten, K. Kayakirilmaz, B. Yazici and M. Erbil, *International Journal of Hydrogen Energy*, 2003, **28**, 1083-1088.

4. C. Batchelor-McAuley, C. E. Banks, A. O. Simm, T. G. J. Jones and R. G. Compton, *Chemphyschem*, 2006, **7**, 1081-1085.

5. D. Marin, F. Mendicuti and C. Teijeiro, *Journal of Chemical Education*, 1994, **71**, A277-A278.

6. J. O. Bockris, I. A. Ammar and A. K. M. S. Huq, *Journal of Physical Chemistry*, 1957, **61**, 879-886.

7. H. M. Villullas, G. I. Lacconi, A. S. Gioda and V. A. Macagno, *Electrochimica Acta*, 1987, **32**, 1657-1659.

8. G. I. Lacconi, A. S. Gioda and V. A. Macagno, *Electrochimica Acta*, 1985, **30**, 211-215.

9. U. Frese and U. Stimming, *Journal of Electroanalytical Chemistry*, 1986, **198**, 409-416.

10. M. Cappadonia, S. Krause and U. Stimming, *Electrochimica Acta*, 1997, **42**, 841-848.

11. L. I. Krishtalik, *Charge Transfer Reactions in Electrochemical and Chemical Processes*, 1st edn., Consultants Bureau, 1986.

12. V. Marinovic and A. R. Despic, *Journal of Electroanalytical Chemistry*, 1997, **431**, 127-132.

13. V. Marinovic and A. R. Despic, *Russian Journal of Electrochemistry*, 2004, **40**, 995-999.

14. S. Trasatti, *Journal of the Chemical Society-Faraday Transactions I*, 1972, **68**, 229-&.

15. S. Trasatti, *Journal of Electroanalytical Chemistry*, 1972, **39**, 163-184.

16. B. E. Conway and J. O. Bockris, *Journal of Chemical Physics*, 1957, **26**, 532-541.

17. H. Kita, *Journal of the Electrochemical Society*, 1966, **113**, 1095-1111.

18. S. Trasatti, *Journal of Electroanalytical Chemistry*, 1971, **33**, 351-378.

19. R. G. Compton and C. E. Banks, *Understanding Voltammetry*, 1st edn., World Scientific, Singapore, 2008.

20. H. Reller, F. Kirowa-Eisner and E. Gileadi, *Journal of Electroanalytical Chemistry*, 1982, **138**, 65-77.

21. M. Pagels, C. E. Hall, N. S. Lawrence, A. Meredith, T. G. J. Jones, H. P. Godfried, C. S. J. Pickles, J. Wilman, C. E. Banks, R. G. Compton and L. Jiang, *Analytical Chemistry*, 2005, **77**, 3705-3708.

22. B. J. Seddon, Y. Shao and H. H. Girault, *Electrochimica Acta*, 1994, **39**, 2377-2386.

23. C. Amatore, J. M. Savéant and D. Tessier, *Journal of Electroanalytical Chemistry*, 1983, **147**, 39-51.

24. T. J. Davies and R. G. Compton, *Journal of Electroanalytical Chemistry*, 2005, **585**, 63-82.

25. T. Yamazaki and M. Enyo, *Electrochimica Acta*, 1990, **35**, 523-527.

26. H. Kita, *Journal of the Electrochemical Society*, 1966, **113**, 1095-&.

27. F. W. Campbell, S. R. Belding, R. Baron, L. Xiao and R. G. Compton, *Journal of Physical Chemistry C*, 2009, **113**, 9053-9062.

28. S. R. Belding, E. J. F. Dickinson and R. G. Compton, *Journal of Physical Chemistry C*, 2009, **113**, 11149-11156.

29. T. J. Davies, C. E. Banks and R. G. Compton, *Journal of Solid State Electrochemistry*, 2005, **9**, 797-808.

30. I. Streeter, R. Baron and R. G. Compton, *Journal of Physical Chemistry C*, 2007, **111**, 17008-17014.

31. I. Streeter and R. G. Compton, *The Journal of Physical Chemistry C*, 2007, **111**, 18049-18054.

32. J.-S. Ferenc and Z. Néda, *Physica A: Statistical Mechanics and its Applications*, 2007, **385**, 518-526.

33. S. E. W. Jones, F. W. Campbell, R. Baron, L. Xiao and R. G. Compton, *Journal of Physical Chemistry C*, 2008, **112**, 17820-17827.

34. M. Rudolph, D. P. Reddy and S. W. Feldberg, *Analytical Chemistry*, 1994, **66**, 589A-600A.

Chapter 7

Facile Method for the Construction of Random Nanoparticle Arrays on a Carbon Support for the Development of Well – Defined Catalytic Surfaces.

Abstract

In this chapter we discuss a simple method of producing platinum nanoparticle (PtNPs) arrays on a carbon substrate. The ability to obtain PtNPs, which are both well – dispersed on the carbon substrate and of homogenous size, is of key importance in this study. This particular synthetic procedure allowed us to generate well – dispersed and well – defined spherical PtNPs with diameter of 100 ± 40 nm, on glassy carbon microspheres (GCMS). This material exhibits a number of catalytic properties as outlined in the following electrochemical experiments. The PtNP – GCMS material was used to develop a Pt nanoelectrode array sensor for the detection of protons in aqueous media. The oxidation of methanol was also studied as Pt electrodes have proved to be very useful in the development of fuel cells. We propose a simple approach to the synthesis of well – defined catalytic surfaces. This work has been published in *International Journal of Electrochemical Science*[1].

7.1 Introduction

A number of advances in the area of nanotechnology have been made in recent years. This has led to the development of a diverse range of nano – scale materials. Furthermore, the development of nanoparticle arrays with potential applications in catalysis has received considerable attention[2-4]. The catalytic properties often exhibited by nanoparticle arrays can potentially be incorporated into fuel cell technologies and sensor devices[5]. Specific properties arising as a result of the reduction in size of the NPs and details of their synthesis have been discussed in **Chapter 2**. In this chapter we discuss a straightforward synthetic technique. Many synthetic approaches discussed in the literature require specialist equipment and can be relatively complex[6-8]. Therefore, a simple and low cost method of producing nanoparticle arrays is highly sought after. Previous studies have implemented electro – less deposition procedures. However, such methods often result in poor control over the NP size and dispersion on the substrate material. In this study we were able to synthesize metallic NPs on a conductive carbon support (GCMS) in a random array. The association of metallic nanoparticles with bulk carbon substrates is of particular interest. Carbon is a very attractive substrate material due to its high conductivity, relative stability and low cost. Furthermore, it was reported that nanoparticles sometimes have higher catalytic properties than the corresponding bulk material[9].

The electro – less deposition of metal nanoparticles on carbon substrates has been achieved recently[10-17]. This technique as described in detail in **Chapter 4** allowed us to synthesise well – dispersed spherical PtNPs, on the surface of the GCMS. The synthesized PtNPs have a diameter of 100 ± 40 nm. The catalytic properties of this material were demonstrated by a series of electrochemical studies. The PtNP – arrays

were subsequently applied to the detection of protons. Where the species of interest is only electro – active at the metallic NPs and inactive at the substrate material, the nanoparticle array can be considered as a nanoelectrode array. Additionally, methanol oxidation was studied to exemplify potential use of this platinum material in fuel cells.

7.2 Results and Discussion

7.2.1 Electrode Characterisation

SEM analysis of the bare GCMS (**A**) and the platinum modified GCMS (**B)** and **(C**) was carried out and the images are shown in **Figure 7.1**. The glassy carbon microspheres have a diameter of 15 ± 5 μm and were used as the carbon support in this study. This shows that the PtNPs have a diameter of 100 ± 40 nm and that they are relatively well spread on the surface of the carbon microspheres with an interparticle distance of between 0 and 220 nm. The material was further characterized by Energy Dispersive X-ray Analysis (EDX), in order to confirm the identity of the metal particles.

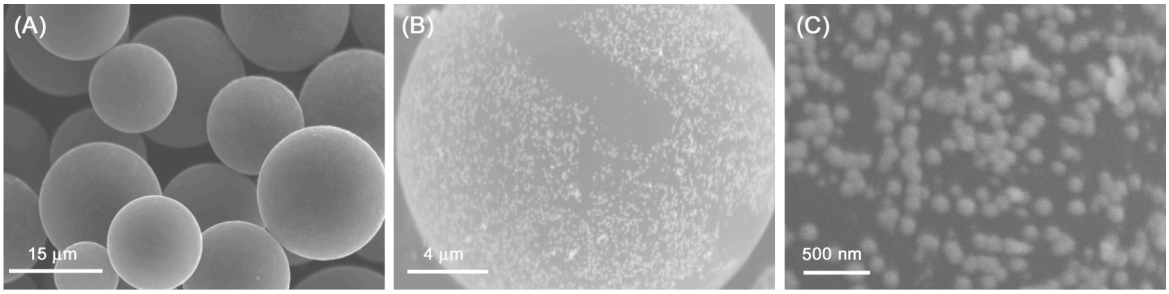


Figure 7.1

SEM images of (A) non-modified glassy carbon microspheres (GCMS), (B) and (C) platinum nanoparticles on glassy carbon microspheres (PtNPs-GCMS).

The GCMS are attached to the BPPG electrode by abrasive attachment, a quick and simple procedure to generate a nanoparticle array[8] as it takes only a matter of minutes to construct. The result is a nanoparticle array that is not expected to produce

agglomerates. A schematic representation of the electrode architecture obtained is presented below in **Figure 7.2**.

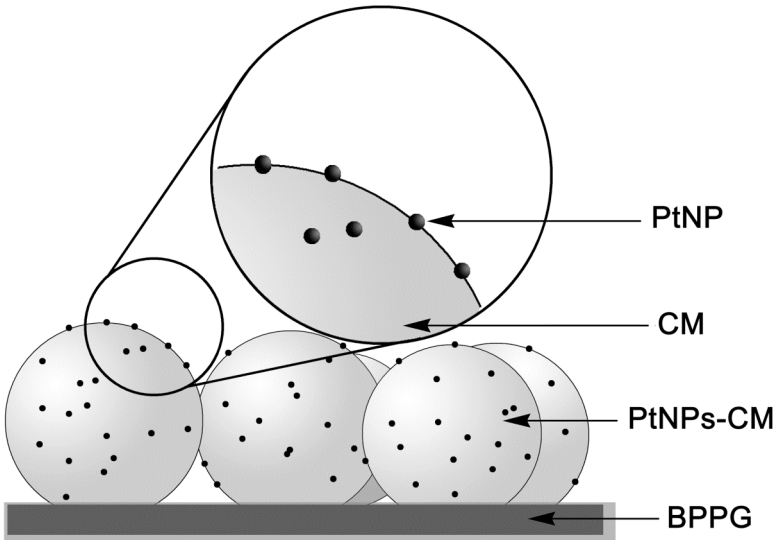


Figure 7.2

A schematic representation of the PtNP – arra,y on a BPPG substrate electrode.

The electrode as described above could subsequently be used in all studies discussed in this chapter. Cyclic voltammetry using these modified electrodes was conducted in a solution of 0.5 M H_2SO_4. The voltammetry obtained is shown in **Figure 7.3.**

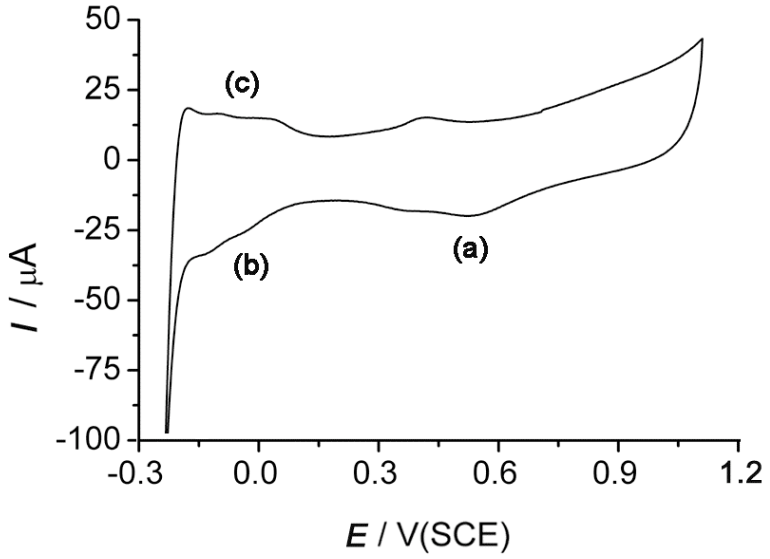


Figure 7.3

The cyclic voltammetry of a 5 mm diameter platinum nanoparticle array: (0.5 M H_2SO_4 at 100 mV s^{-1}, A = 0.123 cm^2).

When we compared the PtNP – BPPG electrode voltammetry to that for a platinum macro – electrode, it clearly exhibits the same characteristic features we would expect of a platinum electrode. An oxidative feature and the corresponding reduction of platinum oxides is reported at peak **(a)** ~ 0.5 V (*vs. SCE*). A further voltammetric feature is recorded in the backward scan, **(b)** ~ - 0.1 V, corresponding to the adsorption of hydrogen. Finally, peak **(c)** observed upon reversing the scan direction once again is characteristic of the hydrogen desorption. From this electrochemical characterization we are able to confirm the presence of platinum on the electrode surface and that it is electrically connected to the electrode. By the integration of the hydrogen adsorption peak, using a literature value of 208 μC cm^{-2}, we are able to estimate the total surface coverage of platinum[18]. The total surface area of 0.123 cm^2 was estimated for the modified electrode used in **Figure 7.3**. It is worth emphasizing that for this experiment a platinum wire was in fact used as the reference electrode

instead of the *SCE* so as to avoid the transfer of chloride ions in the electrolyte. Once the cyclic voltammogram was recorded a further recording was made using the *SCE* electrode to obtain the peak potentials *vs. SCE*. Such precautions have to be taken so as to get a viable estimation of the platinum surface from the integration of the peaks that correspond to the hydrogen adsorption [19].

7.2.2 The Redox Behaviour of Ferro / Ferricyanide at PtNP Arrays

Figure 7.4 outlines the response of the PtNP – array to the ferrocyanide / ferricyanide redox couple. The voltammetry shown in **Figure 7.4** exhibits clearly reversible electrochemical behaviour both at a bare basal plane pyrolytic electrode (BPPG) electrode (**Figure 7.4 (A)**) and at a PtNP – modified BPPG electrode (**Figure 7.4 (B)**). Closer examination of this voltammetry at the unmodified and modified electrodes (scan rate = 100 mVs^{-1}) shows that the peak – to – peak separation is 0.180 V at the unmodified electrode compared to 0.085 V at the PtNP – array. We can attribute this large peak – to – peak separation to a decrease in the electron transfer kinetics resulting from oxygenation of the edge plane sites on the BPPG surface, as reported in the literature [20]. The result is a deviation from the predicted Randles – Ševčík plot, as shown in **Figure 7.4(A) inset**. The Randles – Ševčík plot is calculated using a diffusion coefficient, $D = 0.76 \times 10^{-5}\ cm^2\ s^{-1}$ [21].

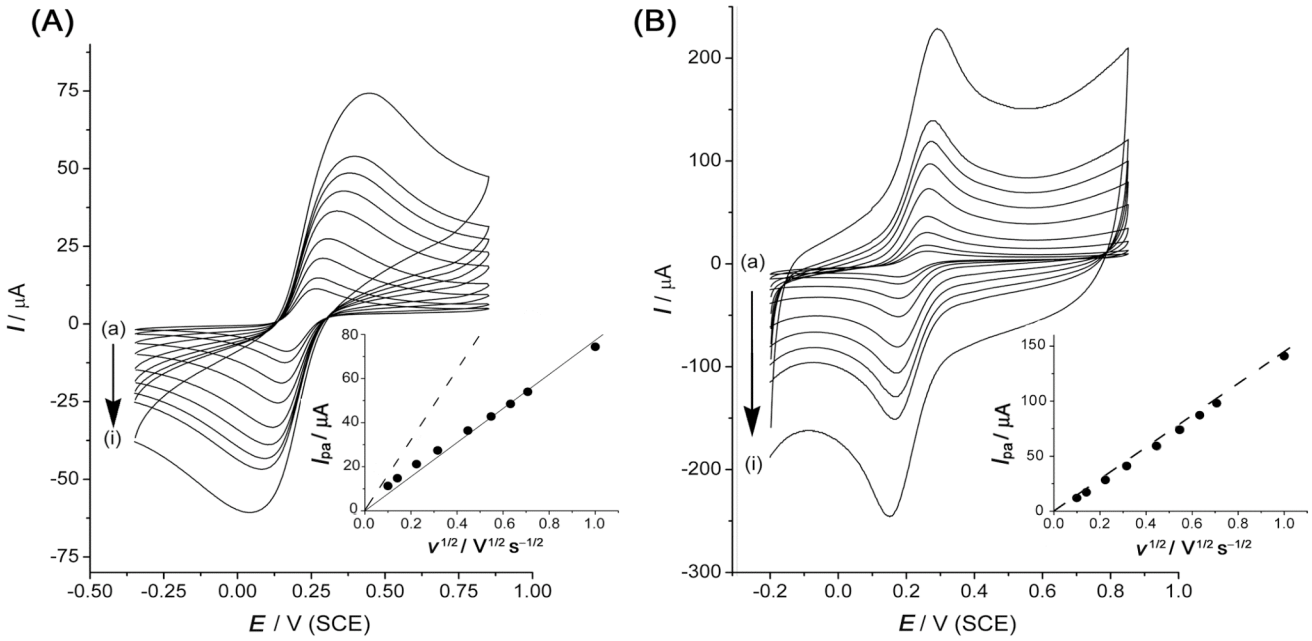


Figure 7.4

Cyclic voltammetry of 1 mM potassium ferrocyanide and 0.1 M KCl, (A) at a 5 mm diameter BPPG electrode (B) at a 5 mm diameter BPPG electrode modified with glassy carbon microspheres decorated with platinum nanoparticles (PtNPs – GCMS) (total PtNPs loading of 0.100 cm^2). The voltammograms were recorded at (a) 10, (b) 20, (c) 50, (d) 100, (e) 200, (f) 300, (g) 400, (h) 500 and (i) 1000 mV s^{-1}. Insets: plot of I_{pa} versus $v^{½}$. Dashed line: expected plot using the Randles – Ševčík formula.

The immobilisation of the PtNP – GCMS on the BPPG substrate appears to restore the fast electron transfer kinetics. Furthermore, the plot of peak current versus square root of scan rate (i_p *vs.* $v^{1/2}$) shows good agreement with the current calculated by the Randles – Ševčík formula (**Figure 7.4(B), Inset**). At a modified BPPG electrode, the measured current is a combination of the current at the PtNPs – GCMS and that obtained at the BPPG surface. In this system, the PtNP – arrays behave as macrodisk electrodes as the species of interest is electro – active at both the substrate and the PtNPs – GCMS.

7.2.3 Proton Reduction at Platinum Nanoparticle Arrays

The PtNP – arrays were then used to study the reduction of protons in aqueous media. In this case, proton reduction only takes place at the platinum surface, with no electro – activity at the BPPG or GCMS surfaces in the potential range of interest. Therefore, the properties of the NP – array can be investigated using this particular system. **Figure 7.4(A)** shows the voltammetry obtained at a BPPG electrode modified with PtNP – GCMS, over a range of scan rates (10 – 500 $mV\,s^{-1}$). In the range of – 0.2 to – 0.6 V (*vs. SCE*) a well – defined redox couple is recorded at $E_{p,c}$ = - 0.55 V, $E_{p,a}$ = - 0.38 V. This process is the adsorption and subsequent desorption of hydrogen on the platinum surface. The electrode reaction mechanism involves the transfer of one electron per proton (H^+), the neutral hydrogen atom being adsorbed (H_{ads}) on the platinum surface. The loading of platinum on the electrode surface can be varied simply by using a different quantity of the modified GCMS powder in the abrasive attachment step. Three BPPG electrodes with different PtNP – GCMS loadings were constructed and applied to the reduction of protons. The corresponding plots of i_p *vs*. $\upsilon^{1/2}$ are given in **Figure 7.4(B)**. The dashed line represents the plot as calculated by a Randles – Ševčík method. The degree of deviation from this calculated value is clearly related to the density of PtNPs, such that the lowest NP density **(a)** shows the greatest deviation from the predicted plot.

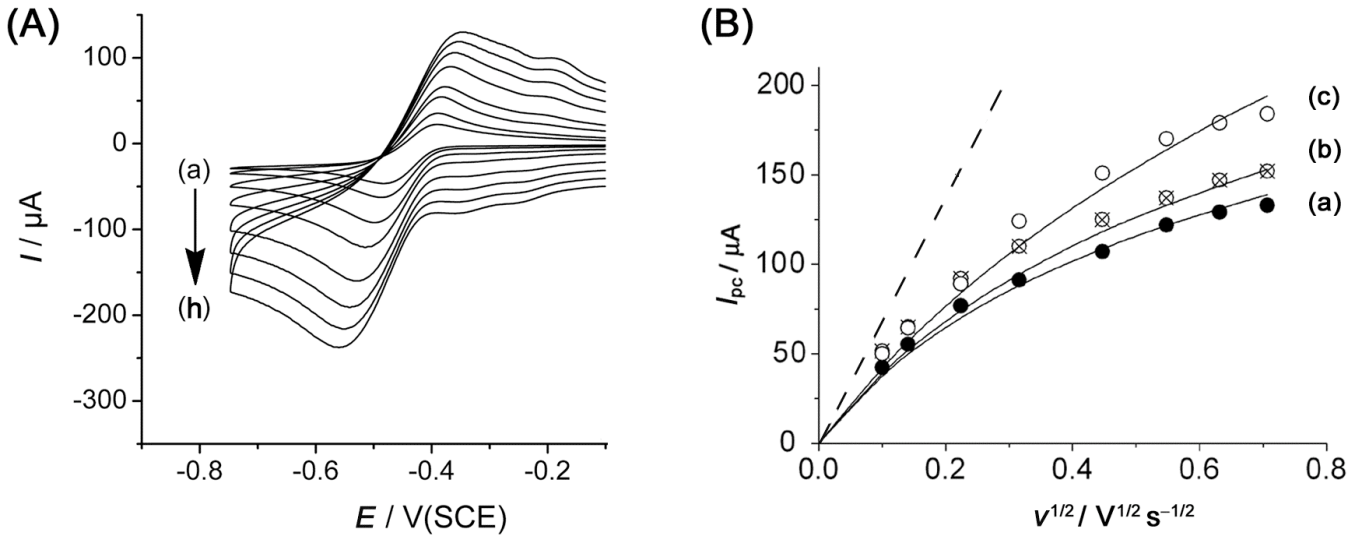


Figure 7.4

(A) Cyclic voltammetry at a 5 mm diameter platinum nanoparticle array (total PtNPs loading of 0.123 cm^2) in 1 mM HCl and 0.1 M KCl at (a) 10, (b) 20, (c) 50, (d) 100, (e) 200, (f) 300, (g) 400, (h) 500 mV s^{-1}. (B) Plot of $i_{p,c}$ vs. $v^{½}$ for various total platinum loadings (a), 0.123 (b) 0.186 and (c) 0.196 cm^2; the points and the curves correspond respectively to the experimental and the modeled peak currents. Dashed line: expected plot using the Randles – Ševčík formula.

Theoretical modeling of isolated nanoparticles or microparticles[22] and random arrays of micro – and nano – particles[23] has been achieved in our laboratory in recent years. The model considers the electron transfer occurring at the surface of a spherical particle supported on an electro – inactive planar surface. The mass transport equation for the electro – active species is solved by finite difference methods. The diffusion domain approximation is used to model a randomly distributed array of spheres on the electrode surface. By employing the diffusion domain approach it is possible to model the diffusional current at a random array of particles based on the particle dimensions and distance between neighbouring particles. The electron transfer is assumed to be fast and reversible. It is also assumed that both the reactant and

product of the electron transfer are soluble and have equal diffusion coefficients. The PtNP diameter (100 ± 40 nm) and the inter – particle distance (0 – 220 nm) as determined from the SEM imaging were used to model the nanoparticle array using a diffusion coefficient of, $D = 7.9 \times 10^{-5} cm^2 s^{-1}$ [24, 25]. The result of the numerical simulation indicated a high degree of diffusional overlap between adjacent particles in the array, equivalent to linear diffusion across the array as a whole. As the electrode architecture consists of carbon microspheres attached to a BPPG substrate, we can consider the GCMS and the PtNPs separately. As the GCMS are decorated with a high density of PtNPs, they will behave as if coated in a layer of platinum. Therefore, we describe the diffusional behaviour at the surface of the GCMS as *Case 4* [26-28]. When immobilized on the BPPG surface, the diffusion domains of adjacent GCMS will overlap to some extent but not completely, such that the diffusion can be categorized as *Case 3*[26-28].

A schematic representation of the diffusion both at a decorated carbon microsphere surface and at the modified – BPPG surface is given in **Figure 7.5**.

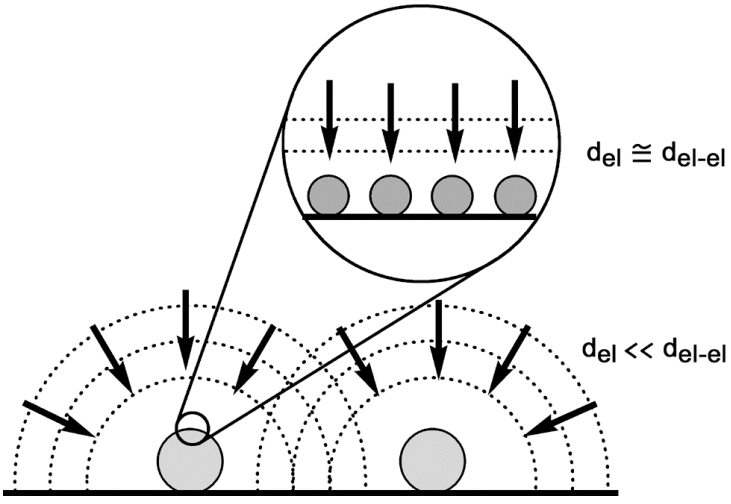


Figure 7.5

Schematic representation of the diffusion zones at spherical nanoparticles (PtNPs) on microspheres (CMs diameter << distance between CMs) on a supporting planar

surface.

A full modelling of the peak currents was performed and it can be seen from **Figure 7.4(B)** that a reasonable fitting of the experimental data was obtained. The modelling allowed us to estimate the number of decorated microspheres that are present on the whole BPPG electrode surface. For the modified electrodes used in **Figure 7.4(B)** curves **(a)**, **(b)** and **(c)** the number of microspheres immobilized on the whole electrode surface was estimated to be 2900, 3289 and 4621, respectively.

7.2.4 pH Determination

As a distinct proton reduction is seen to take place at the PtNP array, it was possible to explore the potential of this material in the determination of pH. **Figure 7.6(A)** and **Figure 7.6(C)** show the voltammetric response obtained at 100 $mV\ s^{-1}$ for 0.1 and 1 mM additions, respectively. The corresponding calibration curves are presented, respectively, in **Figure 7.6(B)** and **Fig. 7.6(D)**. A sensitivity of 0.46 $mA\ mol^{-1}$ and a detection limit of 200 μM were obtained. The peak current increases linearly for concentrations between 0.1 mM and 10 mM. This method can therefore be used to give precise pH measurements within the range $pH = 1 - 3$. The limit of detection was calculated from a standard addition method consisting of 5 additions of 200 μM HCl ($LOD = 3\sigma/N$).

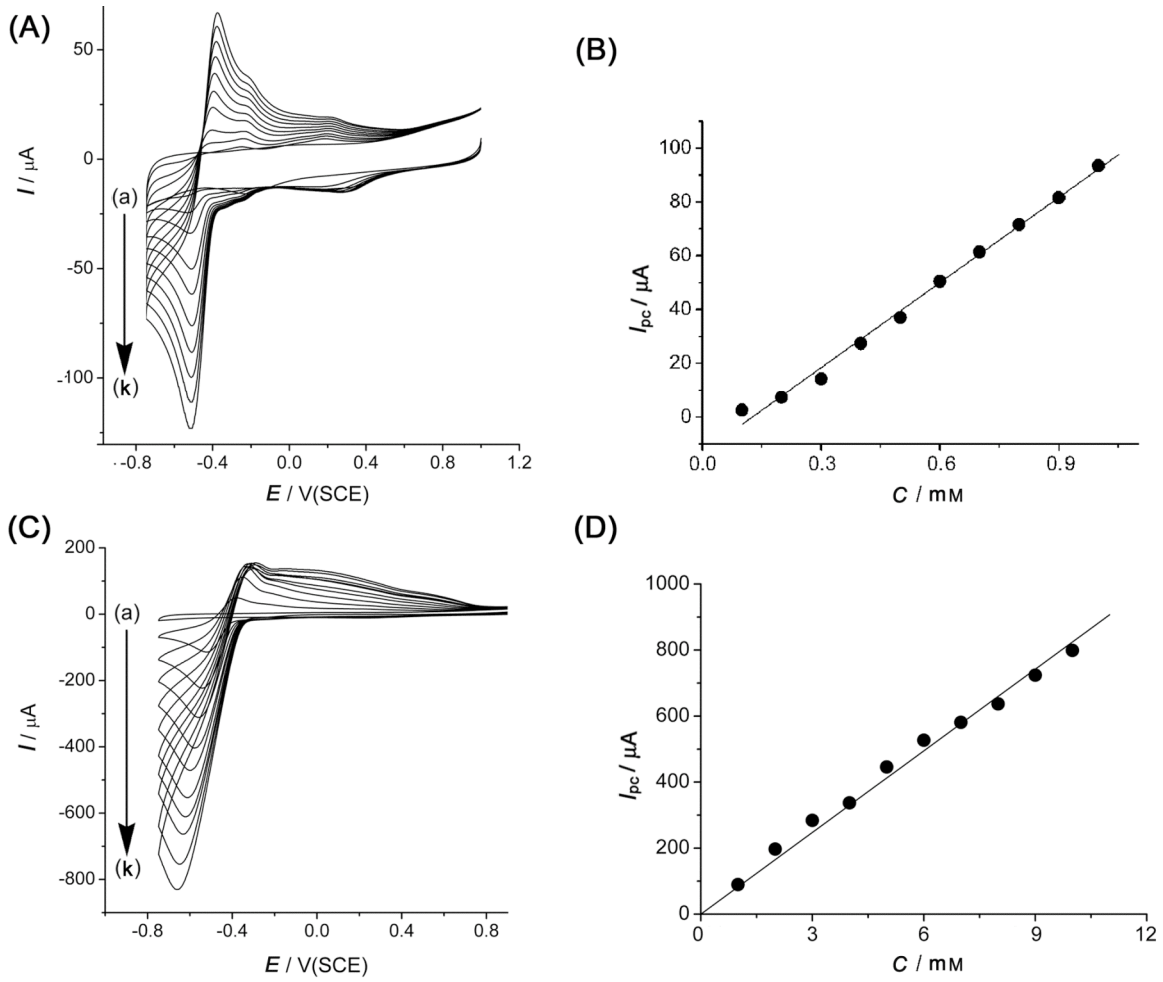


Figure 7.6

Cyclic voltammetry at a 5 mm diameter platinum nanoparticle array (total PtNPs loading of 0.123 cm^2) in 0.1 M KCl at 100 mV s^{-1} for various concentrations of HCl; (A) (a) 0, (b) 0.1, (c) 0.2, (d) 0.3, (e) 0.4, (f) 0.5, (g) 0.6, (h) 0.7, (i) 0.8, (j) 0.9, (k) 1 mM; (C) (a) 0, (b) 1, (c) 2, (d) 3, (e) 4, (f) 5, (g) 6, (h) 7, (i) 8, (j) 9, (k) 10 mM; (B) and (D) are the corresponding calibration curves.

7.2.5 The Oxidation of Methanol at Platinum Nanoparticle Arrays.

We also considered the potential of these PtNP arrays in the oxidation of methanol, which may have applications in fuel cell technologies. **Figure 7.7** shows the oxidative cyclic voltammetry obtained in aqueous alkaline media in the presence of methanol.

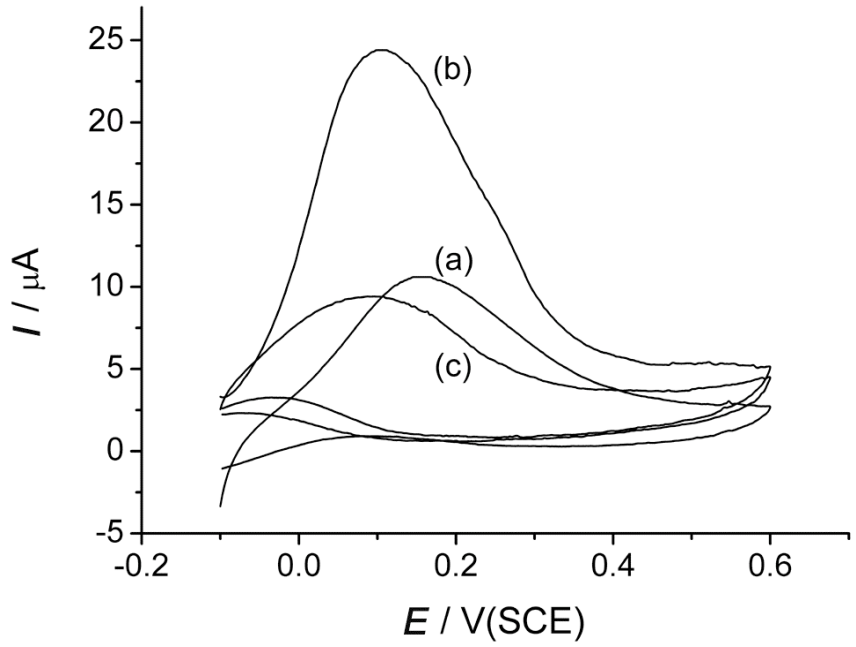


Figure 7.7

Cyclic voltammetry at a 5 mm diameter platinum nanoparticle array (total PtNPs loading of 0.340 cm^2) at 5 mV s^{-1} in 1 M KOH and methanol (a) 0.5 M, (b) 1 M (1st cycle) and (c) 1 M (2nd cycle).

The oxidation of methanol does not take place at either the BPPG or GCMS substrate materials within the potential region of interest. However, when the BPPG electrode is modified with PtNPs – GCMS a large oxidation peak was recorded at ~ 0.15 *V* (*vs. SCE*). The electrode surface rapidly becomes poisoned with further oxidative scans when in the presence of high methanol concentrations. As less than half of the current

remained after two cycles in 1 M methanol. This observation is in good agreement with previous methanol oxidation studies at PtNPs[29].

7.3 Conclusions

In this chapter we have detailed the simple construction of a platinum nanoparticle array on a carbon matrix support. The array is fabricated by the electro – less deposition of platinum on glassy carbon microspheres. These decorated microspheres were then used to modify a BPPG electrode by abrasive attachment. This provides a well – defined catalytic surface for the study of a variety of electrochemical systems. In this case we have applied these electrodes to the ferro – / ferri cyanide redox couple and to the detection of protons. The electrodes will behave as a macrodisk electrode for species that are electro – active at both platinum and the substrate material (*e.g.* ferro – / ferricyanide). On the other hand, for species that are only active at platinum (*e.g.* H^+, methanol), the electrode will behave as a nano – electrode array. The electro – activity of protons proved to be useful in the precise determination of pH within the range of *pH 1 – 3*. An important feature of this method is that the procedure can very easily be generalized to construct nanoparticle arrays consisting of other metallic particles, so long as the NPs can be synthesized on GCMS. In **Chapter 8** we will further consider the effects of size and coverage in the voltammetric response of silver nanoparticle arrays. This study will look at the reduction of 4 – nitrophenol and the apparently changed mechanism between the macro – and nano – scales.

Chapter 7: References

1. R. Baron, F. W. Campbell, L. Xiao and R. G. Compton, *International Journal of Electrochemical Science*, 2008, **3**, 556-565.

2. A. N. Shipway, E. Katz and I. Willner, *ChemPhysChem*, 2000, **1**, 18-52.

3. A. Haryono and W. H. Binder, *Small*, 2006, **2**, 600-611.

4. S. I. Yoo, J. H. Kwon and B. H. Sohn, *Journal of Materials Chemistry*, 2007, **17**, 2969-2975.

5. D. W. M. Arrigan, *Analyst*, 2004, **129**, 1157-1165.

6. M. P. Nagale and I. Fritsch, *Analytical Chemistry*, 1998, **70**, 2902-2907.

7. M. E. Sandison and J. M. Cooper, *Lab on a Chip*, 2006, **6**, 1020-1025.

8. P. Ugo, N. Pepe, L. Maria Moretto and M. Battagliarin, *Journal of Electroanalytical Chemistry*, 2003, **560**, 51-58.

9. C. W. Welch and R. G. Compton, *Analytical and Bioanalytical Chemistry*, 2006, **384**, 601-619.

10. X. Dai, G. G. Wildgoose, C. Salter, A. Crossley and R. G. Compton, *Analytical Chemistry*, 2006, **78**, 6102-6108.

11. X. Dai, G. G. Wildgoose and R. G. Compton, *Analyst*, 2006, **131**, 1241-1247.

12. B. Sljukic, R. Baron, C. Salter, A. Crossley and R. G. Compton, *Analytica Chimica Acta*, 2007, **590**, 67-73.

13. R. Baron, B. ljuki, C. Salter, S. Crossley and R. G. Compton, *Electroanalysis*, 2007, **19**, 1062-1068.

14. R. Baron, B. Sljukic, C. Salter, A. Crossley and R. G. Compton, *Russian Journal of Physical Chemistry*, 2007, **81**, 1443-1447.

15. L. E. Barrosse-Antle, L. Xiao, G. G. Wildgoose, R. Baron, C. J. Salter, A. Crossley and R. G. Compton, *New Journal of Chemistry*, 2007, **31**, 2071-2075.

16. C. Xu, L. Cheng, P. Shen and Y. Liu, *Electrochemistry Communications*, 2007, **9**, 997-1001.

17. C. W. Xu, Y. L. Liu and D. S. Yuan, *International Journal of Electrochemical Science*, 2007, **2**, 674-680.

18. J. M. Doña Rodríguez, J. A. Herrera Melián and J. Pérez Peña, *Journal of Chemical Education*, 2000, **77**, 1195-1197.

19. J. M. Doña Rodríguez, J. A. Herrera Melián and J. Pérez Peña, *Journal of Chemical Education*, 2000, **77**, 1195-1197.

20. X. B. Ji, C. E. Banks, A. Crossley and R. G. Compton, *Chemphyschem*, 2006, **7**, 1337-1344.

21. A. J. Bard and L. R. Faulkner, *Electrochemical Methods: Fundamentals and Applications*, 2nd edn., John Wiley & Sons, Inc., New York, 2001.

22. I. Streeter and R. G. Compton, *The Journal of Physical Chemistry C*, 2007, **111**, 18049-18054.

23. I. Streeter, R. Baron and R. G. Compton, *The Journal of Physical Chemistry C*, 2007, **111**, 17008-17014.

24. J. V. Macpherson and P. R. Unwin, *Analytical Chemistry*, 1997, **69**, 2063-2069.

25. S. Daniele, I. Lavagnini, M. A. Baldo and F. Magno, *Journal of Electroanalytical Chemistry*, 1996, **404**, 105-111.

26. I. Streeter, R. Baron and R. G. Compton, *Journal of Physical Chemistry C*, 2007, **111**, 17008-17014.

27. T. J. Davies, C. E. Banks and R. G. Compton, *Journal of Solid State Electrochemistry*, 2005, **9**, 797-808.

28. T. J. Davies and R. G. Compton, *Journal of Electroanalytical Chemistry*, 2005, **585**, 63-82.

29. B. Beden, F. Hahn, S. Juanto, C. Lamy and J. M. Leger, *Journal of Electroanalytical Chemistry*, 1987, **225**, 215-225.

Chapter 8

A Changed Electrode Reaction Mechanism between the Nano – and Macro – Scales: The Reduction of 4 – Nitrophenol in Aqueous Solution at Silver Electrode.

Abstract

Altered electrode kinetics have been discussed in previous chapters for the irreversible reduction of H_2O_2 and protons at silver nanoparticle (AgNP) arrays. The reduction of nitrophenol compounds at silver electrodes typically displays irreversible behaviour. This presents another system worthy of comparative investigation at the macro – and nano – scales. In this chapter we will consider the altered electrode kinetics reported at the bulk silver macro – electrode and at AgNP – arrays for the reduction of 4 - nitrophenol. Kinetic data for the electro – reduction of 4 – nitrophenol in aqueous solution is obtained by fitting of the experimental data using a series of numerical simulations. AgNP – arrays are constructed for a range of nanoparticle sizes, ranging from 15 – 50 nm average radius. Following on from this, we discuss the influence that the changed electrode kinetics may have on the mechanism of the electrode process. This study has been published in *ChemPhysChem*[1].

8.1 Introduction

Metallic nanoparticles (NPs) can be employed as electro – catalysts in a diverse range of electrolytic processes. Suitable examples include those used in fuel cell technology[2-6] (*e.g.* catalysis of the H^+/H_2 reaction at PtNPs[7]) and in chemical sensing[8,12] (*e.g.* H_2O_2 reduction at AgNPs[13, 14]). A considerable body of work exists investigating the effects of changed morphology and electronic structure between the macro – and nano – scales and the potential for correspondingly altered electrode reactions and mechanisms. In this work we have attempted to address the failure of previous research to quantitatively compare the electrode kinetics between the macro – and nano – scales. There currently exists little basis for comparing electrode reaction mechanisms between the two size scales.

The electrochemical properties of nanoparticles are generally studied as arrays of NPs, rather than as isolated particles. The NPs tend to be supported on a conductive electrode substrate, which also acts as a source or sink of electrons. However, the substrate tends to electrolytically inactive towards the reaction of interest. Thus, the process under investigation will occur exclusively on the nanoparticles. This makes the measurement of the electrode kinetics at these NP – arrays somewhat more difficult than the equivalent measurements performed at a macro – electrode. Such undertakings are central in order to attempt any further discussion of the mechanisms occurring at the macro – and nano – scales. Where Tafel analysis is used to extract the transfer coefficient (α) and the standard electrochemical rate constant (k^0), as defined according to the Butler – Volmer model, it is necessary to apply mass transport corrections[15] as the electro – active species must first diffuse to the electrode surface

before an electron transfer event can take place. These corrections at a NP – array are further complicated as the mass transport regime is largely dependent on the NP surface coverage. More specifically, at very dilute coverages the nanoparticles can effectively be considered as isolated and, therefore will experience fully convergent diffusion and corresponding transport limited currents rather than a peak – shaped voltammetric response. At the opposite end of the scale, if the substrate electrode is densely covered with NPs, planar diffusion will dominate and the voltammetry will be a typical cyclic voltammetric response, the magnitude of which will reflect the geometric area of the substrate electrode rather than the active area of the NPs. Intermediate coverages will show a response intermediate between steady state convergent diffusion and transient linear (planar) diffusion. This is the so – called *Case 3* type response which has been previously characterised[16].

In this laboratory we have published a series of papers[14, 17-20] aimed at the quantitative extraction of Butler – Volmer parameters from NP – arrays. These have been covered in **Chapters 5** and **6**. This has been achieved by means of the numerical simulation of NP – array voltammetry, as a function of coverage, k^0 and α. Using this work as a base we can search for altered electrode kinetics and mechanistic behaviours between the nano – and macro – scale electrodes. In this chapter we consider the reduction of 4-nitrophenol in acidic media at an array of AgNPs. We are therefore able to establish the differences that arise in k^0 and α compared to the same process at a silver macro – electrode.

8.2 Results and Discussion

AgNPs were synthesized according to the adapted citrate – mediated colloidal synthesis as detailed in **Chapter 4**. The citrate – capped AgNPs were then used to modify a basal plane pyrolytic graphite (BPPG) electrode by evaporation of the colloidal suspension on the electrode surface (**Chapter 4**). The response of the AgNP – modified electrode towards the presence of 4-nitrophenol in acidic media was examined using cyclic voltammetry by sweeping the potential from – 0.2 *V* to – 1.0 *V* (*vs. SCE*). Stripping voltammetry then allowed us to estimate the surface coverage and NP distribution on the electrode surface, by integration of the area beneath the stripping peak. Stripping experiments were performed in a solution of $NaClO_4$ (0.1 M) at 20 $mV\ s^{-1}$ and the electrode potential was swept from 0 *V* to + 1.0 *V* (*vs. SCE*) bringing about the quantitative dissolution of Ag to Ag^+. All voltammetric experiments were performed at 25 °C.

As has been discussed extensively in previous chapters, the electrochemical behaviour of nanoparticles can differ from that of macro – electrodes for a variety of reasons. One significant difference is that as the nano – scale the size of the diffuse double layer and the diffusion layer can be similar and hence diffusion and migration are strongly coupled. Recent work carried out in our laboratory has simulated the diffuse double layer at nano – spheres. This work has shown that for the sizes of nanoparticles discussed above, and in the concentration of electrolyte reported, any "Frumkin corrections[21]" will be minor. Therefore, the observed kinetic effects can be effectively described in terms of the diffusion model without further complications. For smaller NPs or lower electrolyte concentrations, this approximation may break down.

The reduction of 4-nitrophenol was then examined in acidic media at both a silver macrodisk electrode and AgNP – modified electrodes. The reduction of various nitrobenzene derivatives have been studied on materials such as bismuth[22], copper[23], palladium colloids[24, 25], mercury[26], carbon[27] and gold[28]. The overall reaction pathway is outlined in **Figure 8.1** and is thought to be an irreversible process whereby four electrons are transferred to the 4-nitrophenol (4 – NP) to produce 4 – hydroxyphenylhydroxylamine[29].

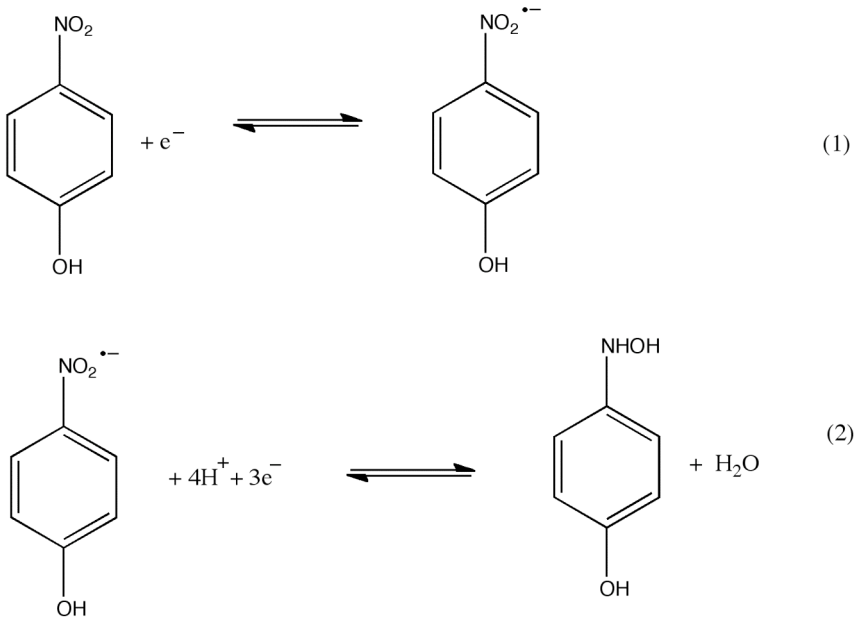


Figure 8.1

The mechanism of 4-nitrophenol reduction at a silver nanoparticle array: (1) rate – determining electron transfer step (2) fast follow – up chemical and further electron transfer step.

The kinetic parameters (α and k^0) as reported in the literature refer to the first step as shown in **Figure 8.1(1)**. Although four electrons are transferred overall, at a AgNP – BPPG electrode, the first electron transfer is believed to be rate – determining.

Casella[30] has reported the reduction of a series of nitrophenol compounds on globular silver particles, electrodeposited on a glassy carbon electrode under pulsed potential conditions. Silver nanoshell – coated polystyrene beads have also proven to be a good catalysts for the reduction of 4-nitrophenol[31].

We first considered the irreversible reduction of 4-nitrophenol at a silver macrodisk electrode (0.7 mm diameter; $A = 3.85 \times 10^{-3} cm^2$). The experiment was performed in a 10 mM solution of perchloric acid ($HClO_4$) and 100 mM sodium perchlorate ($NaClO_4$) in the presence of 3 mM 4-nitrophenol (scan rate: 50 $mV\ s^{-1}$). The experimental voltammetry is shown in **Figure 8.2**.

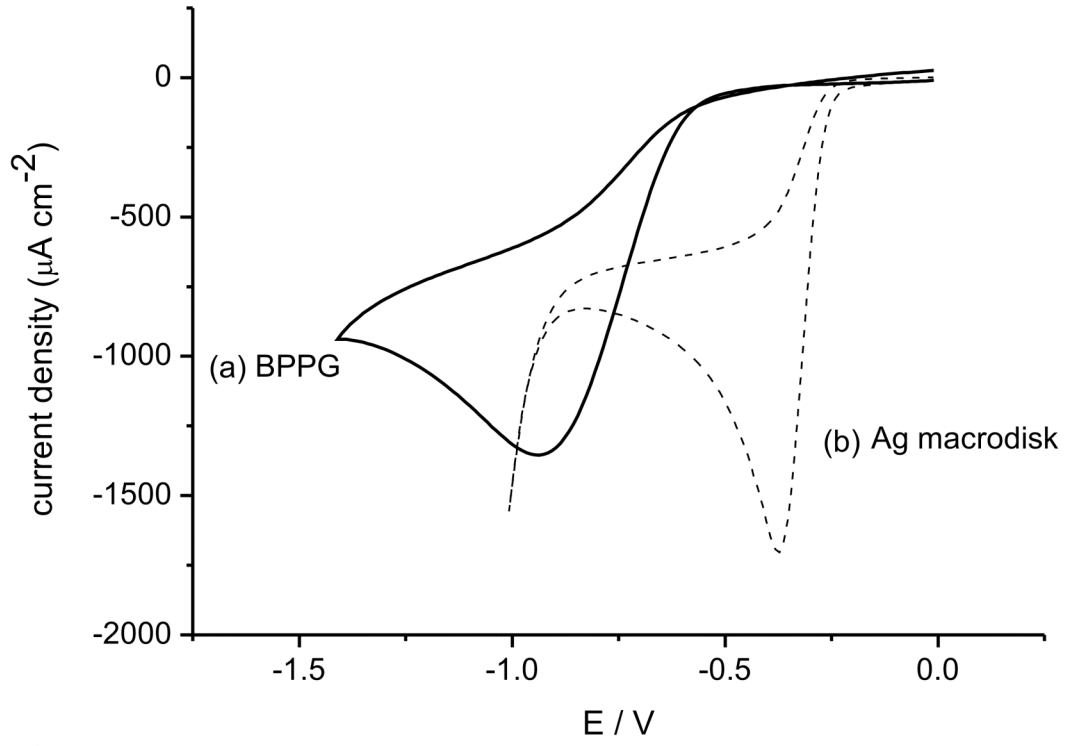


Figure 8.2

The reduction of 4-nitrophenol at: (a) a bare BPPG electrode curve (5mm diameter, area = 0.196 cm^2; E_p ~ - 0.95 V vs. SCE), (b) a silver macro – disk electrode (0.7 mm diameter, A = 3.85 x 10^{-3} cm^2; E_p ~ - 0.375 V vs. SCE). Experimental conditions: 10 mM $HClO_4$ + 100 mM $NaClO_4$ + 3 mM 4-NP (50 mV s^{-1}).

A distinct reduction wave is observed at E_p = – 0.375 *V* (*vs. SCE*). Tafel analysis (*ln I vs. E*) of the 4-nitrophenol reduction wave at the Ag macrodisk electrode was then performed and a transfer coefficient of α = 0.85 ± 0.15 was calculated, assuming the first electron transfer to be rate limiting. This follows the value of α quoted in the literature for a lithium modified glassy carbon electrode[32], α = 0.95.

Several AgNP – modified BPPG electrodes were then studied under the same conditions in order to assess the effect of increasing the AgNP density. A bare BPPG electrode (diameter = 5 mm*; A = 0.196 cm*^{2}) is shown to be electro – active towards the reduction of 4-nitrophenol in acidic media, at a relatively high overpotential, E_p = - 0.95 *V* (*vs. SCE*). The voltammetry of a AgNP – modified BPPG electrode towards 4 – nitrophenol reduction displays a dependence on the nanoparticle density. At a dilute surface coverage of ~ 1 %, the reductive wave is recorded at a high overpotential (- 0.8 *V vs. SCE*). In the case of small nanoparticles (r_{avg} = 15 nm), by increasing the nanoparticle density to ~ 8 % we effect a positive shift in the peak potential by ~ 0.25 *V*. This behaviour is shown in **Figure 8.3**, with a shift to lower overpotentials with increasing nanoparticle density

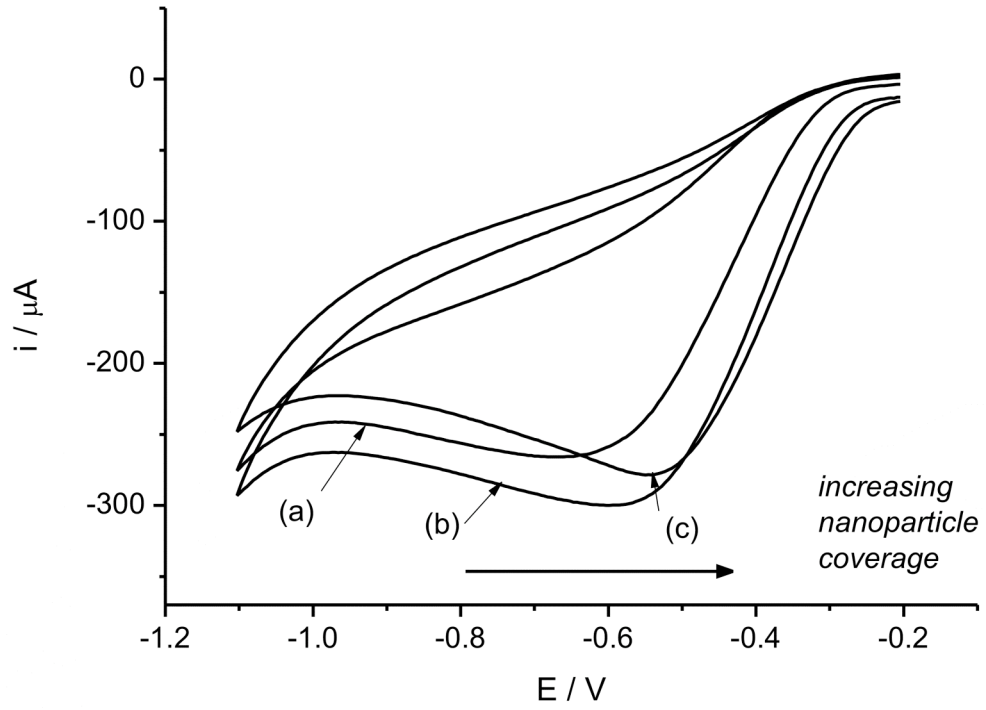


Figure 8.3

Experimental voltammetry recorded for the reduction of 4-nitrophenol at a silver nanoparticle array (r_{avg} = 15 nm), with increasing surface coverage: (a) 4.7 % (b) 5.3 % (c) 7.5 %. Experimental conditions: 10 mM $HClO_4$ + 100 mM $NaClO_4$ +3 mM 4-NP (vs. SCE). Scan rate: 50 mV s^{-1}.

This behaviour was found to be a consistent for all three samples of AgNPs (r_{avg} = 15, 30 and 50 nm) over a range of surface coverages. This implied that the AgNPs exhibit changed electrode kinetics towards nitrophenol reduction, resulting in the reduction wave occurring at a significantly lower overpotential.

Numerical simulations were conducted in order to examine the kinetics of the AgNP – arrays with respect to the 4-nitrophenol reduction. The peak potentials of 4-nitrophenol reduction were modelled as a function of surface coverage, α and k^0 parameters, for a random array of silver particles. This model is based on the Butler –

Volmer model which has been very well established[33]. The diffusion problem can subsequently be solved by applying the diffusion domain approximation[34-36, 37] to a random distribution of electrochemical centres[38]. The basis of this model has been discussed in depth in the literature[18, 39]. This approach allowed us to quickly simulate a response within a few minutes, using a desktop PC. The peak potential at a NP – array varies with scan rate, rate constant, and surface coverage as shown in **Figure 8.4** for a surface coverage of 1% in which α = 0.5 and:

$$\theta_{peak} = (E_p - E^0_f) \qquad [\mathbf{8.1}]$$

$$\sigma = \nu \frac{\left(F/RT\right) r_e^2}{D_A} \qquad [\mathbf{8.2}]$$

$$K^0 = \frac{\left(k^0 r_e\right)}{D_A} \qquad [\mathbf{8.3}]$$

In the limit of electrochemical irreversibility (*low* K^0), the value of θ_{peak} plotted in **Figure 8.4** scales directly with the value of the transfer coefficient (α). It follows from the description given in the introductory section that at very low scan rates the *Case 4* limit is obtained and θ_{peak} becomes less negative as σ is reduced.

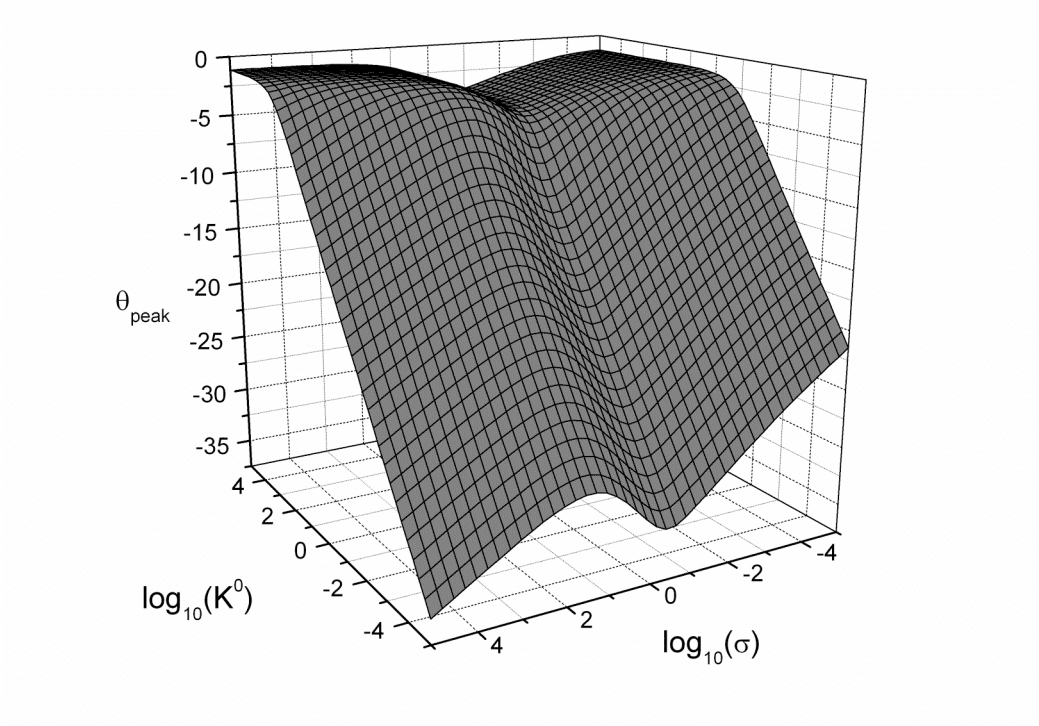


Figure 8.4

Plot of θ_{peak} as a function of σ and K^0 (1 % surface coverage, α = 0.5).

We can therefore, measure the peak potential, at low scan rate, over a range of surface coverages in order to determine the value of the kinetic and thermodynamic parameters.

The reduction of 4-nitrophenol was considered at 2 different acid concentrations **(**10^{-3} M and 10^{-2} M**)** and for all three nanoparticle sizes (r_{avg} = 15, 30 and 50 nm). **Figure 8.5** shows the fittings of E_{peak} for each size, over a range of surface coverages at both acid concentrations. The experimental data points were fitted very well alongside the simulation of a random array of particles. The kinetic parameters ($k^0 \exp\left(\frac{+\alpha F E_f^0}{RT}\right)$ and α) returned by the simulations at each acid concentration are outlined in **Table 8.1**.

AgNP – BPPG **r_{avg} = 15 – 50 nm**	**10^{-3} M $HClO_4$** **0.1M $NaClO_4$**	**10^{-2} M $HClO_4$** **0.1M $NaClO_4$**
$k^0 \exp\left(\frac{\alpha F E_f^0}{RT}\right) m\ s^{-1}$	$7.5 \pm 1.5 \times 10^{-7}$	$2.2 \pm 1.1 \times 10^{-6}$
α	0.32 ± 0.03	0.30 ± 0.01

Table 8.1

Kinetic parameter obtained from fitting of experimental data by simulation of a random array of particles.

As the formal potential (E_f^o) is unknown in this case, we have fitted the values of $k^0 \exp\left(\frac{+\alpha F E_f^0}{RT}\right)$ for all three nanoparticle sizes. The low values of α = 0.30 – 0.32 were confirmed by classical Tafel analysis of the experimental voltammograms using the very low current region exclusively. Linear Tafel plots were obtained and the inferred α values were close to those obtained by the simulation of the voltammograms as observed above.

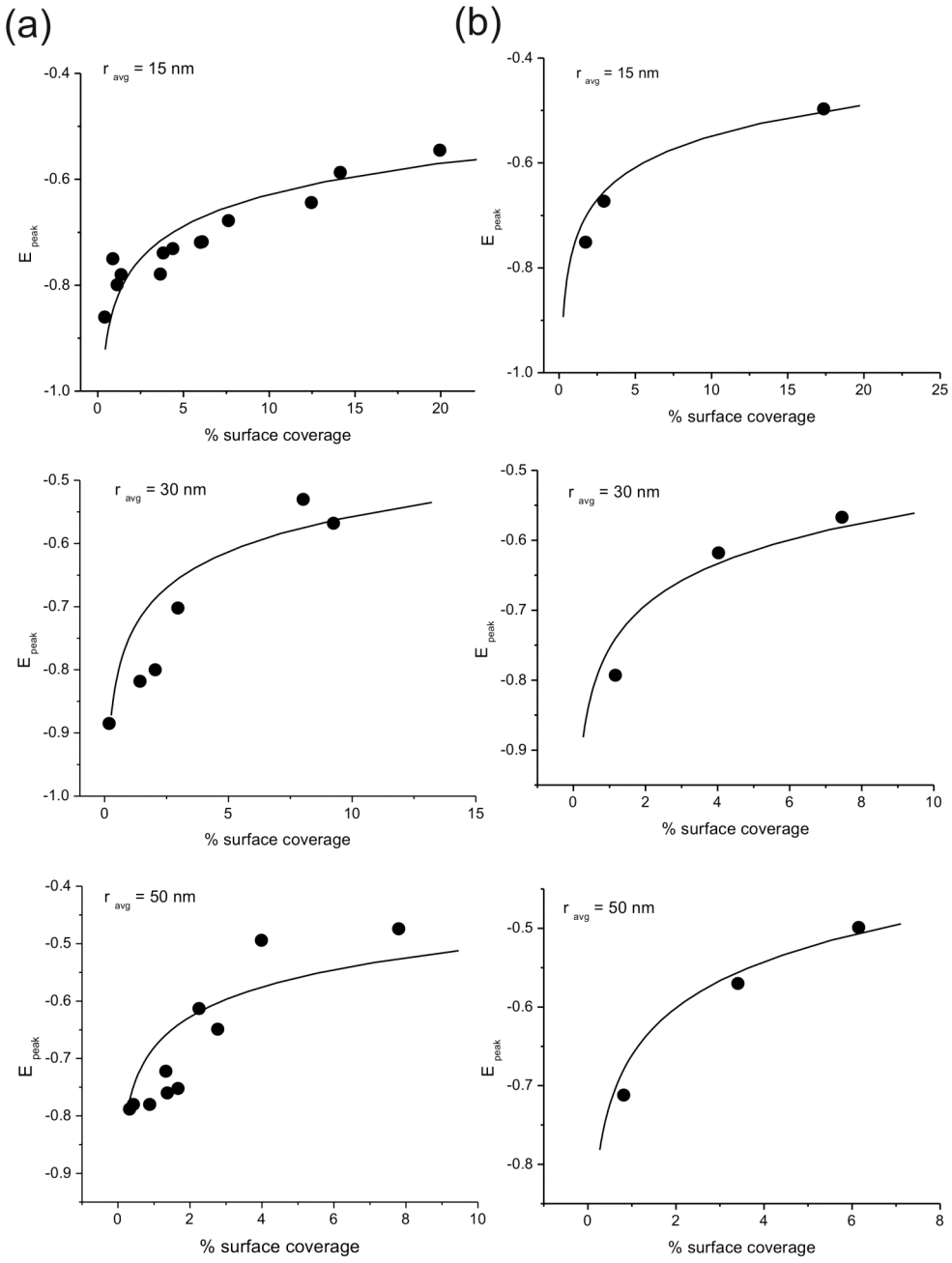


Figure 8.5

Fitting of peak potential (E_{peak}) with increasing surface coverage for silver nanoparticle arrays: (a) 10^{-3} M $HClO_4$ + 10^{-2} M $NaClO_4$ + 4 – NP (3 mM); (b) 10^{-2} M $HClO_4$ + 10^{-2} M $NaClO_4$ + 4 – NP (3 mM). Black dots represent experimental data points and line represents simulation of a random array of particles.

Comparison of the kinetic parameters extracted for 10^{-3} M and 10^{-2} M acid (both with 0.1 M supporting electrolyte) indicates that the concentration of protons does not

significantly alter the system kinetics. This in turn implies that the rate – determining step does not involve protonation of the species and is therefore more likely to be a simple electron transfer step as indicated by step (1) in **Figure 8.1**, followed by a chemical step, probably protonation.

Comparison with the transfer coefficient recorded for a silver macro – disk electrode ($\alpha = 0.85 \pm 0.15$) clearly demonstrated that the altered surface structure of the nanoparticle array, as compared to a planar disk electrode, has a marked effect on the kinetic behaviour and thus the reaction mechanism of the rate – determining step in this system. In particular we speculate that the closeness of the α value for a macro – electrode to unity may suggest the formation of the radical anion of 4-nitrophenol followed by a slow rate determining chemical step. In contrast the first electron transfer is evidently rate – determining in the case of the nanomaterial and the low value of alpha, may indicate a significant role of adsorption in the process.

In particular we have recently studied[40] the underpotential deposition (*UPD*) adsorption of species such as thallium (I) on silver nanoparticles and found that whilst particles of size greater than r_{avg} = 50 nm behave as a macro – electrode with *UPD* being observed as at the larger scale, no such adsorption is seen to occur for the case of the smaller silver nanoparticles. It is therefore possible to speculate that the observed behaviour in the case of 4-nitrophenol reduction results from a similar case of adsorption so that with smaller particles the anion radical is formed in solution, not as part of an adsorption based process.

8.3 Conclusions

To conclude this chapter we suggest that following the study of 4-nitrophenol reduction in acidic media at silver nanoparticle arrays, we were able to fit the experimental data by means of a numerical simulation of a random distribution of particles. The electrode kinetics at two different acid concentrations could be extracted by fitting of the experimental data. Comparison of these data sets allowed us to determine that for the nanoparticle arrays, the mechanism is likely to be a rate – determining electron transfer followed by a chemical step. Critically, the nanoparticle arrays displayed significantly altered electrode kinetics from that obtained at the silver macro – disk. We can therefore, infer a change in the mechanism of the rate – determining step for the reduction of 4 – nitrophenol between the macro – and nano – scales. The significance of nanoparticle size and the density of particles in the array have been discussed extensively in previous chapters. As such they have proved critical in explaining the cyclic voltammetric response of NP – arrays. As such NP size and surface coverage are also likely to influence the stripping voltammetry of NPs as discussed in the following chapter.

Chapter 8: References

1. F. W. Campbell, S. R. Belding and R. G. Compton, *ChemPhysChem*, 2010, **11**, 2820-2824.

2. M. S. Saha, M. N. Banis, Y. Zhang, R. Li, X. Sun, M. Cai and F. T. Wagner, *Journal of Power Sources*, 2009, **192**, 330-335.

3. S. C. Zignani, E. Antolini and E. R. Gonzalez, *Journal of Power Sources*, 2009, **191**, 344-350.

4. Z. Bai, L. Yang, L. Li, J. Lv, K. Wang and J. Zhang, *The Journal of Physical Chemistry C*, 2009, **113**, 10568-10573.

5. H. Bunazawa and Y. Yamazaki, *Journal of Power Sources*, 2009, **190**, 210-215.

6. Y. S. Kim, H. J. Kim and W. B. Kim, *Electrochemistry Communications*, 2009, **11**, 1026-1029.

7. R. Baron, F. W. Campbell, L. Xiao and R. G. Compton, *International Journal of Electrochemical Science*, 2008, **3**, 556-565.

8. B. Sljukic, R. Baron, C. Salter, A. Crossley and R. G. Compton, *Analytica Chimica Acta*, 2007, **590**, 67-73.

9. R. Baron, B. ljuki, C. Salter, S. Crossley and R. G. Compton, *Electroanalysis*, 2007, **19**, 1062-1068.

10. K. E. Toghill, G. G. Wildgoose, A. Moshar, C. Mulcahy and R. G. Compton, *Electroanalysis*, 2008, **20**, 1731-1737.

11. G.-P. Jin, R. Baron, L. Xiao and R. G. Compton, *New Journal of Chemistry*, 2009, **33**, 107-111.

12. K. E. Toghill, L. Xiao, G. G. Wildgoose and R. G. Compton, *Electroanalysis*, 2009, **21**, 1113-1118.

13. C. M. Welch, C. E. Banks, A. O. Simm and R. G. Compton, *Analytical and Bioanalytical Chemistry*, 2005, **382**, 12-21.

14. F. W. Campbell, S. R. Belding, R. Baron, L. Xiao and R. G. Compton, *Journal of Physical Chemistry C*, 2009, **113**, 9053-9062.

15. J. Albery, *Electrode Kinetics*, Clarendon, Oxford, 1975.

16. T. J. Davies, C. E. Banks and R. G. Compton, *Journal of Solid State Electrochemistry*, 2005, **9**, 797-808.

17. F. W. Campbell, S. R. Belding, R. Baron, L. Xiao and R. G. Compton, *The Journal of Physical Chemistry C*, 2009, **113**, 14852-14857.

18. S. R. Belding, E. J. F. Dickinson and R. G. Compton, *Journal of Physical Chemistry C*, 2009, **113**, 11149-11156.

19. I. Streeter, R. Baron and R. G. Compton, *Journal of Physical Chemistry C*, 2007, **111**, 17008-17014.

20. I. Streeter and R. G. Compton, *The Journal of Physical Chemistry C*, 2007, **111**, 18049-18054.

21. A. J. Bard and L. R. Faulkner, *Electrochemical Methods: Fundamentals and Applications*, 2nd edn., John Wiley & Sons, Inc., New York, 2001.

22. E. Hutton, B. Ogorevc and M. R. Smyth, *Electroanalysis*, 2004, **16**, 1616-1621.

23. K. Polat, M. L. Aksu and A. T. Pekel, *Journal of Applied Electrochemistry*, 2002, **32**, 217-223.

24. S.-D. Oh, M.-R. Kim, S.-H. Choi, J.-H. Chun, K.-P. Lee, A. Gopalan, C.-G. Hwang, K. Sang-Ho and O. J. Hoon, *Journal of Industrial and Engineering Chemistry*, 2008, **14**, 687-692.

25. C.-G. Hwang, K. Sang-Ho, O. J. Hoon, M.-R. Kim and S.-H. Choi, *Journal of Industrial and Engineering Chemistry*, 2008, **14**, 864-868.

26. A. Baeza, J. Ortiz and I. González, *Journal of Electroanalytical Chemistry*, 1997, **429**, 121-127.

27. V. A. Pedrosa, L. Codognoto and L. A. Avaca, *Journal of Brazilian Chemical Society*, 2003, **14**, 530-535.

28. K. Kuroda, T. Ishida and M. Haruta, *Journal of Molecular Catalysis A: Chemical*, 2009, **298**, 7-11.

29. A. M. Heras, E. Muñoz, J. L. Avila, L. Camacho and J. L. Cruz, *Journal of Electroanalytical Chemistry*, 1988, **243**, 293-307.

30. I. G. Casella and M. Contursi, *Journal of The Electrochemical Society*, 2007, **154**, D697-D702.

31. S. Jana, S. K. Ghosh, S. Nath, S. Pande, S. Praharaj, S. Panigrahi, S. Basu, T. Endo and T. Pal, *Applied Catalysis A: General*, 2006, **313**, 41-48.

32. R. de Cássia Silva Luz, F. S. Damos, A. B. de Oliveira, J. Beck and L. T. Kubota, *Talanta*, 2004, **64**, 935-942.

33. R. G. Compton and C. E. Banks, *Understanding Voltammetry*, 1st edn., World Scientific, Singapore, 2008.

34. H. Reller, F. Kirowa-Eisner and E. Gileadi, *Journal of Electroanalytical Chemistry*, 1982, **138**, 65-77.

35. M. Pagels, C. E. Hall, N. S. Lawrence, A. Meredith, T. G. J. Jones, H. P. Godfried, C. S. J. Pickles, J. Wilman, C. E. Banks, R. G. Compton and L. Jiang, *Analytical Chemistry*, 2005, **77**, 3705-3708.

36. B. J. Seddon, Y. Shao and H. H. Girault, *Electrochimica Acta*, 1994, **39**, 2377-2386.

37. C. Amatore, J. M. Savéant and D. Tessier, *Journal of Electroanalytical Chemistry*, 1983, **147**, 39-51.

38. T. Davies, C. Banks and R. Compton, *Journal of Solid State Electrochemistry*, 2005, **9**, 797-808.

39. J.-S. Ferenc and Z. Néda, *Physica A: Statistical Mechanics and its Applications*, 2007, **385**, 518-526.

40. F. W. Campbell, Y.-G. Zhou and R. G. Compton, *New Journal of Chemistry*, 2010, **34**, 187-189.

Chapter 9

Particle Size and Surface Coverage Effects in the Stripping Voltammetry of Silver Nanoparticles: Theory & Experiment.

Abstract

Previous chapters have outlined the importance of both nanoparticle size and coverage in determining the nature of the observed voltammetric reponse. This also applies to the stripping of nanoparticles from the surface of a substrate electrode as discussed as follows. In this chapter we explore the stripping behaviour of silver nanoparticles (AgNPs) from BPPG electrodes with varying NP sizes and degrees of surface coverage. We present an overview of a mathematical model for the stripping of a random distribution of AgNPs, based on two – dimensional diffusion. Theoretical results are compared with both the reversible and irreversible limits of the approximate analytical expression as derived by Brainina[1-3]. The theoretical model used to model the experimental stripping of AgNPs, considers the individual particle environments as opposed to the model proposed by Brainina, which applies an average coverage of material across the whole electrode surface. The experimental stripping of different sizes of AgNPs over a range of surfaces coverages was investigated. By comparison of the experimental data with our theoretical model we are able to explain the trends in stripping peak potential, indicating the electrochemically reversible nature of the Ag / Ag^{+} couple.

9.1 Introduction

Stripping voltammetry is a commonly used technique in electro – analysis. This technique can be coupled with NP – modified electrodes for the detection of trace heavy metals such as arsenic[4, 5]. Nanoparticles can also be used as molecular tags for the quantitative detection of biological molecules via the stripping voltammetry of nanoparticles[6]. The experimental work discussed in this chapter uses AgNPs generated by a colloidal synthesis abrasively attached on a BPPG electrode substrate[7, 8].

The voltammetry at metal nanoparticle arrays for a simple heterogeneous electron transfer has been previously modelled for both isolated particles and for random distributions[9, 10]. However, other than the work of Mouhandess[11-13] and Grygar[14, 15], the dissolution of particles from an electrode surface is still relatively unexplored. The "thick layer" stripping voltammetry theory presented by Ward Jones *et al*.[16] has been extended to look at the stripping over a range of surface coverages and nanoparticle sizes. The reversible and irreversible limits for the model are compared to those in the form derived by Brainina *et al.* for the stripping of metal particles from carbon paste electro – active electrodes (*CPEEs*) [1-3]. The model presented by Brainina considers one – dimensional diffusion from the electrode surface, such that the concentration of metal is averaged over the entire electrode surface.

9.2 Theory

9.2.1 Introduction

As discussed in **Section 9.1** we have a applied an adapted version of the "thick layer" stripping model[16] to model this system. This model provides a good starting point for the modelling of AgNP stripping voltammetry as the literature[17, 18] suggests the stripping of silver in aqueous solution displays a similar sharp drop in current at the end of the stripping peak, which is characteristic of the "thick layer" stripping model. Despite the small dimensions of these AgNPs, we consider them to behave as bulk metal composed of layers of silver atoms. This is likely to be true for the majority of the stripping process. However, towards the end of the NP dissolution, the inherently strained surface structure is likely to result in different behaviour from the bulk metal. The literature suggests that ~ 20 atoms are required in order to generate "bulk character"[19-22]. Calculation of the number of atoms in spherical NPs with diameter in the range of 25 – 100 nm suggests that this is a reasonable approximation. By assuming that the nanoparticles are perfect spheres, the volumes of single 25, 50 and 100 nm diameter particles are calculated to be 8.2×10^{-18}, 6.5×10^{-17} and $5.2\times10^{-16}\,cm^3$ respectively. Taking the density of the nanoparticle to be that of bulk silver[23], 10.5 $g\,cm^{-3}$, the molar mass to be 107.9 $g\,mol^{-1}$ and the Avogadro constant to be $6.022\times10^{23}\,mol^{-1}$, the approximate number of atoms in the nanoparticles can be calculated. For 25, 50 and 100 nm diameter particles the approximate number of atoms per particle are calculated as 4.80×10^{5}, 3.84×10^{6} and 3.07×10^{7} respectively. Therefore, we can expect the standard potential, E^0, of silver to apply as this value is quoted for all species in their standard states. In the case of silver the standard state is

the pure crystalline bulk metal. When dealing with clusters of containing less than 20 atoms, E_n^0 is very different from that for the bulk metal ($n >> 20$) [19-22]

The range of particle sizes considered in this particular study is narrow. We can therefore assume that the activities and therefore the standard potential will be the same for all different NP sizes. Furthermore, we also assume that any errors arising from this approximation will be small compared to the effect of changing the initial particle size. Towards the end of the NP dissolution changes in the activity and standard potential of such small particles may become more relevant.

9.2.2 Diffusion Domain Approximation

The diffusion domain approximation has been applied to simulate the random distribution of spherical NPs on a substrate electrode. This approach has previously been used to simulate the problem of partially blocked electrodes[24-26] and has since been used for a range of problems including microelectrode arrays[27, 28]. **Figure 9.1** shows the schematic diagram of the diffusion domain approach. Voronoi cells are formed from the mid – point between each particle and its nearest neighbours, and as such it is assumed that the flux between neighbouring Voronoi cells is zero and one is assigned to each individual nanoparticle in the array to be modelled. **Figure 9.1 (c)** shows the approximation of modeling each irregularly shaped Voronoi cell as a cylinder with the same base area as the original cell. This three – dimensional problem can be simplified to two – dimensions as only a single plane as shown in **Figure 9.1 (d)** needs to be simulated using the R and Z coordinates. A spherical particle can be modeled approximately as a flat disk of the same radius and coverage distribution as shown in **Figure 9.1 (e)**. This two – dimensional simplification is used

as during the stripping step, the size of the particle will shrink. If we have to consider the three – dimensional shape, this can significantly complicate our model.

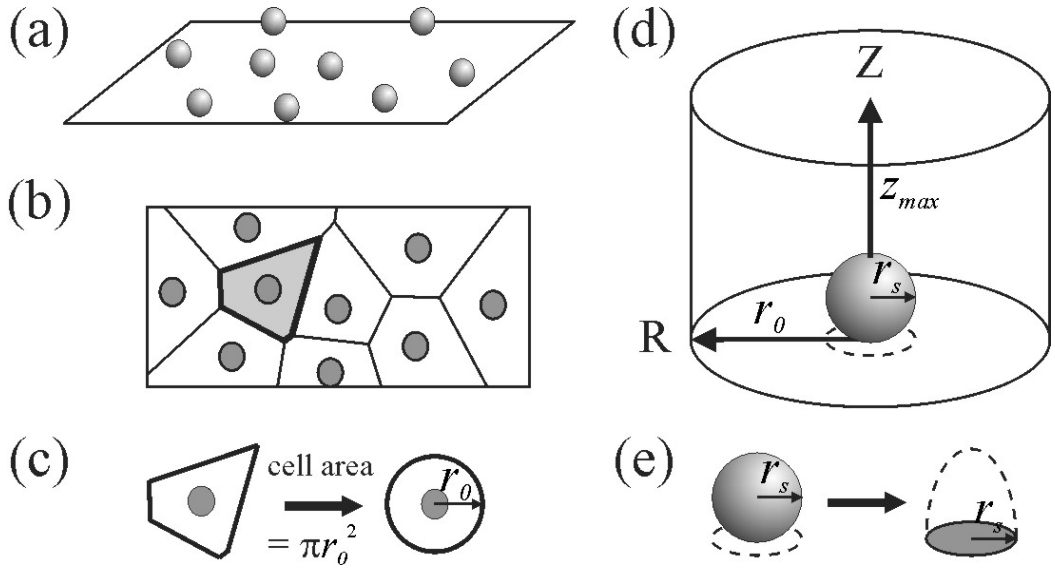


Figure 9.1

Schematic diagram of the diffusion domain approach for the problem of randomly distributed nanoparticles on an electrode surface: (a) random distribution of spherical particles on electrode surface; (b) electrode surface divided into Voronoi cells: (c) diffusion domain approximation; (d) cylindrical co – ordinates R and Z; (e) approximation of a sphere as a flat disk.

Both the distribution of domains and the spherical distribution round off the peak – shape and broaden the peak when compared to regularly spaced particles with a uniform coverage as the material runs out at different points on the electrode at different times during the stripping voltammetric scan.

The random distribution of Voronoi cell areas produced from the random distribution of nanoparticles on the surface can be approximated using **Equation 9.1**[29]**.**

$$f_{2D}(y) = \frac{343}{15}\sqrt{\frac{7}{2\pi}}y^{5/2}\exp\left(-\frac{7}{2}y\right) \quad \textbf{[9.1]}$$

where $y = S/\langle S \rangle$ and S is the area of the Voronoi cell.

An average diffusion domain radius, $R_{0,}$ is used in much of this work, as calculation over the whole range of diffusion domain sizes is computationally very time consuming. This value is calculated from the average diffusion domain area, which takes the value of $0.88\left(A_{elec}/N\right)$ where A_{elec} is the total electrode area and N is the number of particles. This represents the median domain area as calculated from the Járai-Szabó and Néda equation[29]. This approximation is reasonable for this stripping voltammetry work as the peak shape is very similar in different domains. This is in contrast to voltammetry where both the reactant and product form solution species, where the distribution of domain sizes has a large effect on the peak shape.

9.2.3 Adapted "Thick Layer" Mathematical Model

In this chapter a brief overview is discussed. A detailed description of this model can be found in the literature[16]. All nanoparticles within a given sample are assumed to be spheres and have the same radius, r_s. The dissolution of the silver nanoparticles is described by a simple one – electron transfer (**Equation 9.2)**:

$$Ag^{+}_{(aq)} + e^{-} \rightleftharpoons Ag_{(s)} \quad \textbf{[9.2]}$$

The diffusion of Ag^+ in solution to the electrode surface follows the behaviour described by Fick's second law. **Equation 9.3** describes the cylindrical coordinate system used in this model as shown in **Figure 9.1 (d)**:

$$\frac{\partial[Ag^+]}{\partial t} = D_{Ag^+}\left(\frac{\partial^2[Ag^+]}{\partial r^2} + \frac{1}{r}\frac{\partial[Ag^+]}{\partial r} + \frac{\partial^2[Ag^+]}{\partial z^2}\right) \qquad \textbf{[9.3]}$$

The silver stripping is assumed to follow Bulter – Volmer kinetics where the rate constant for deposition of silver on the electrode surface, k_c, and dissolution of the metal, k_a are given by **Equations 9.4** and **9.5**, respectively:

$$k_c = k^0 \exp\left(-\frac{\alpha F}{RT}(E - E_f^0)\right) \qquad \textbf{[9.4]}$$

$$k_a = k^0[A]^* \exp\left(\frac{(1-\alpha)F}{RT}(E - E_f^0)\right) \qquad \textbf{[9.5]}$$

Where k^0 is the standard rate constant, $[A]^*$ is equal to $1.0 \times 10^{-3} mol\ cm^{-3}$ and is a standard concentration, α is the transfer coefficient, F is Faraday's constant (96485 $C\ mol^{-1}$), R is the ideal gas constant (8.314 $J\ mol^{-1}\ K^{-1}$), T is the temperature (298 K for the work in this paper), E is the potential and E_f^0 is the formal potential, both measured in V.

The potential, E, is varied using a sweep from an initial potential, E_1, to a final potential, E_2, at a scan rate, υ, according to **Equation 9.6**, where t is the time in seconds since the sweep started

$$E = E_1 + \upsilon t \qquad \textbf{[9.6]}$$

The initial and boundary conditions for the model are given in **Table 9.1**.

Equations	Boundary region	
Initial boundary conditions		
$[Ag^+] = 0$	$0 \le r \le r_0$	$0 \le z \le z_{\max}$
$\Gamma_{Ag} = 2d(\sqrt{r_s^2 - r^2})$	$0 \le r \le r_s$	$z = 0$
General boundary conditions		
$[Ag^+] = 0$	$0 \le r \le r_0$	$z = z_{\max}$
$\partial[Ag^+]/\partial r = 0$	$r = 0$	$0 \le z < z_{\max}$
$\partial[Ag^+]/\partial r = 0$	$r = r_0$	$0 \le z < z_{\max}$
$\partial[Ag^+]/\partial z = 0$	$r_s < r \le r_0$	$z = 0$
$\frac{\partial \Gamma_{Ag}}{\partial t} = D_{Ag^+} \frac{\partial [Ag^+]}{\partial z} = k_a [Ag^+]_{z=0} - k_d$	$0 \le r \le r_s$	$z = 0$
$k_d \partial t = -\partial \Gamma_{Ag} + k_a \left[Ag^+ \right]_{Z=0} \partial t$	If $\frac{\partial \Gamma_{Ag}}{\partial t} > k_a \left[Ag^+ \right]_{Z=0} - k_d$	

Table 9.1

Initial conditions and boundary conditions for the mathematical model presented.

The nanoparticles are assumed to have the same density, *d*, as that of bulk silver. The initial position dependent coverage of solid silver, Γ_{Ag}, is assigned a value at each point so that the spherical nature of the particle is represented in the distribution of material over the disk used to model the particle. Surface conditions result in a sharp drop in current. The current can be calculated from the change in the surface coverage with time given by **Equation 9.7**:

$$i = -2\pi F \int_0^{r_d} \frac{\partial \Gamma}{\partial t} r \, \partial r \qquad [9.7]$$

9.3 Results and Discussion

9.3.1 Experimental Results

Figure 9.2 shows the experimental voltammetry obtained during the stripping of several AgNP arrays over a range of surfaces coverages. As the degree of surface coverage is increased we observe a positive shift in the stripping peak potential (E_p). This trend is observed over all three NP size ranges. In order to understand this behaviour we have compared our experimental results with the stripping model described by Brainina and co – workers as well as the two – dimensional model discussed.

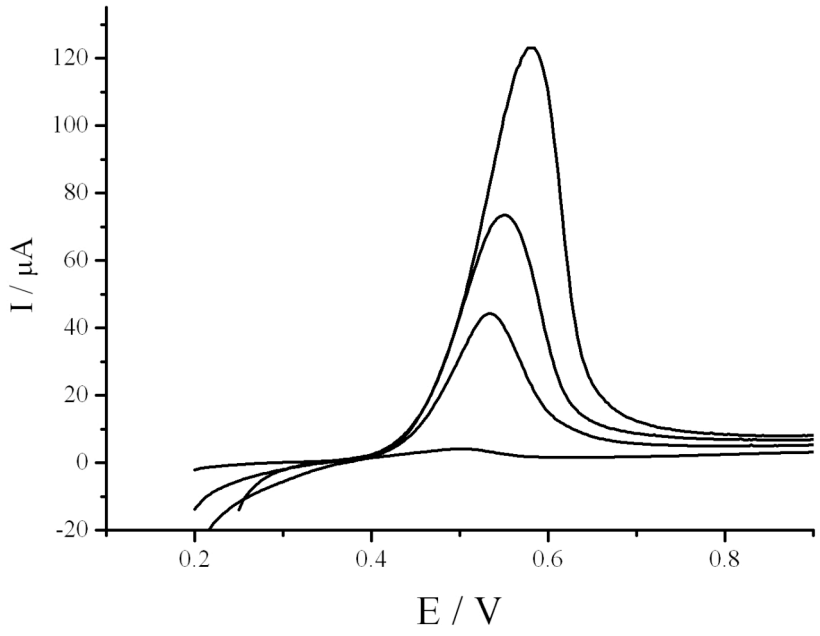


Figure 9.2

Stripping voltammetry for four different loadings of 80 – 120 nm diameter nanoparticles stripped into a 0.1 M $NaClO_4$ solution at a scan rate υ = 20 mV s^{-1} (vs. Hg/HgO).

9.3.2 Computation

The dissolution of AgNPs, r_{avg} = 50 nm is described in **Figure 9.3** as a function of rate constant, k^0, and diffusion domain radius, r_0. Simulation parameters are given in **Table 9.2**. This computational program and simulations are credited to Dr. Sarah E. Ward Jones[30].

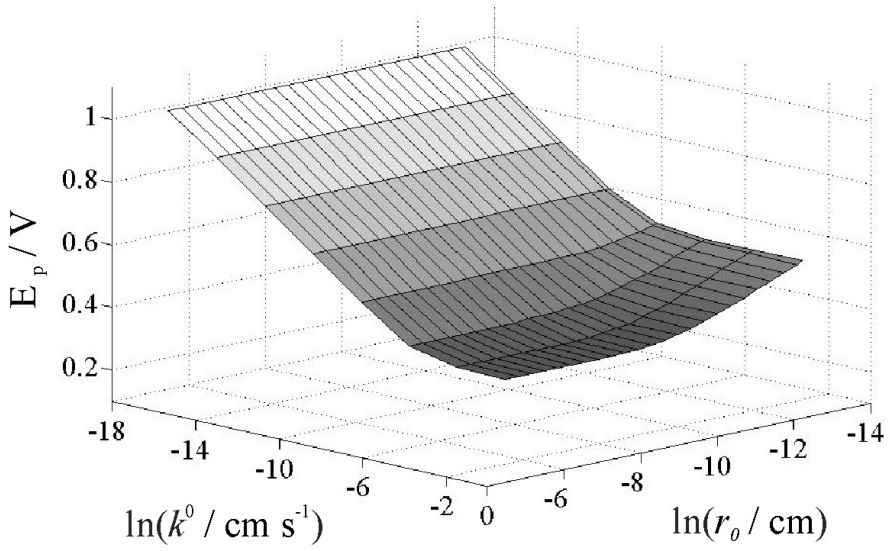


Figure 9.3

*Plot of the simulated peak potential, E_p, against $ln(k^0)$ and $ln(r_0)$ for the stripping a sphere radius, r_s = 50 nm. k^0 values range from 1 cm s^{-1} to 1 x 10^{-7} cm s^{-1} and r_0 from $5\times10^{-6} cm$ to 1×10^{-3}. All other parameters used in the simulation are listed in **Table 9.2**.*

Parameter	Value
Starting potential, E_1	0.2 V
End potential, E_2	1.2 V
Formal potential, E_f^0	0.65 V
Diffusion coefficient of Ag^+, D_{Ag+}	$1.2\times10^{-5} cm^2 s^{-1}$
Transfer coefficient, α	0.5
Scan rate, υ	0.02 V s^{-1}

Table 9.2

Simulation parameters used for the numerical simulations presented.

As we can see above (**Figure 9.2**), the peak potential (E_p) decreases with increasing k^0, reaching a plateau as kinetics get very fast and the reversible limit is approached. On the other hand, with correspondingly slower kinetics, the plateau is reached at more positive potentials when the diffusion domain radius, r_0, is smaller. This is due to the extensive overlap of diffusion layers between adjacent particles resulting in planar diffusion across the array as a whole. This in turn restricts the dissolution process more so than radial diffusion. Consequently, the peak potential is shifted positively.

As the kinetics becomes more irreversible, a corresponding increase in E_p is expected as the particle is stripped away more slowly. In the irreversible limit, E_p is independent of the particle separation as the deposition process is negligible. Therefore, the concentration and the associated diffusion of ions in solution do not play a part in the recorded current.

Figure 9.1 describes the approximation of spherical particles as disks, with the position – dependent coverage representing the distribution of material on the electrode surface. Such an approximation is most accurate in the reversible limit where planar diffusion dominates. For widely distributed, essentially isolated particles, the NP morphology plays a significant role with respect to the diffusional behaviour. By mathematical modelling of the voltammetry of solution species at NP – modified electrodes, Streeter *et al.*, have shown that the reversible limiting current (**Equation 9.8**) for a NP – modified electrode is 2.18 times greater than for the equivalent micro – disk electrode[10].

$$i_{\lim} = -8.71nFDr_s[A_{bulk}] \qquad \textbf{[9.8]}$$

Where n is the number of electrons; F is the Faraday constant, D is the diffusion coefficient; r_s is the particle radius and $[A]_{bulk}$ is the bulk concentration of species A. This implies that a similar increase in the net flux may be applied to the metal ions during the dissolution process. This faster rate of particle dissolution would result in a lower value of E_p at the isolated particles in the reversible limit than that predicted for the flat disk equivalent.

9.3.3 Comparison of Theories

The work of Brainina *et al.* [1-3] is based on an average coverage of metal on the electrode and one – dimensional diffusion across the whole electrode surface. For reversible kinetics we expect this to be valid at slow scan rate, reasonably high particle coverage, smaller particle size and small inter – particle separations. The electrochemically reversible and irreversible cases are given in **Equations 9.9** and **9.10**. **Equation 9.10** for the electrochemically irreversible dissolution is expected to hold for all coverages. These equations have been adapted so that the formal potential has the same definition as that used in our adapted "thick layer" model. The spherical morphology of the particles is accounted for and assumes the particle can be modeled as a flat disk.

Reversible Limit:

$$E_p = E_f^0 + \frac{RT}{nF}\ln\frac{2c^0 r_s}{[A]^*}\sqrt{\frac{nF}{RTD}} + \frac{RT}{2nF}\ln\upsilon \qquad \textbf{[9.9]}$$

Where E_p is the peak potential, c^0 is the average concentration of metal on the electrode surface, equal to $4\pi r_s^2 dN/6A_{elec}$ where N is the total number of particles and all other parameter are defined as before.

Irreversible Limit:

$$E_p = E_f^0 + \frac{RT}{\beta nF}\ln\frac{4\beta nFr_s d}{3RTk^0[A]^*} + \frac{RT}{\beta nF}\ln\upsilon \qquad \textbf{[9.10]}$$

This model is based on two – dimensional diffusion at the electrode surface and accounts for the changing particle separation and the transition between the limits of reversible and irreversible systems. Rather than an average distribution of material across the electrode surface as a whole, this model is based on position – dependent distribution of particles, taking into account radial diffusion to individual particles as well as the proximity of adjacent particles.

9.3.4 Electrochemically Irreversible Stripping

Figure 9.4 shows a plot of peak potential, E_p, calculated for the reversible limit as given by **Equations 9.9** and that predicted by the mathematical model described (k^0 = 1 $cm\ s^{-1}$), against the domain radius, $r_{0,}$ for the stripping particles with a radius of r_s = 12.5, 25 and 50 nm. All other parameters used in the simulation are listed in **Table 7.2**.

Figure 9.4 highlights the effect of nanoparticle radius and the size of the diffusion domain. Brainina's reversible limit (**Equation 9.9)** indicates very good agreement for a high density of NPs on the electrode surface. However, as the diffusion domain

increases we see a deviation from this reversible limit. Where particles are widely separated, they can behave as diffusionally independent of the neighbouring particles. Therefore, values will tend towards those observed at isolated particles. At dilute coverages, Brainina's theory begins to break down due to the shift to a two – dimensional diffusion regime and the significance of the individual particle sizes. Where this deviation between the two models starts to occur will depend on parameters such as the diffusion coefficient (D) and scan rate (υ) used in the experiment. When differently sized particles are placed within the same size of diffusion domain the peak potential is seen to increase with increasing particle size.

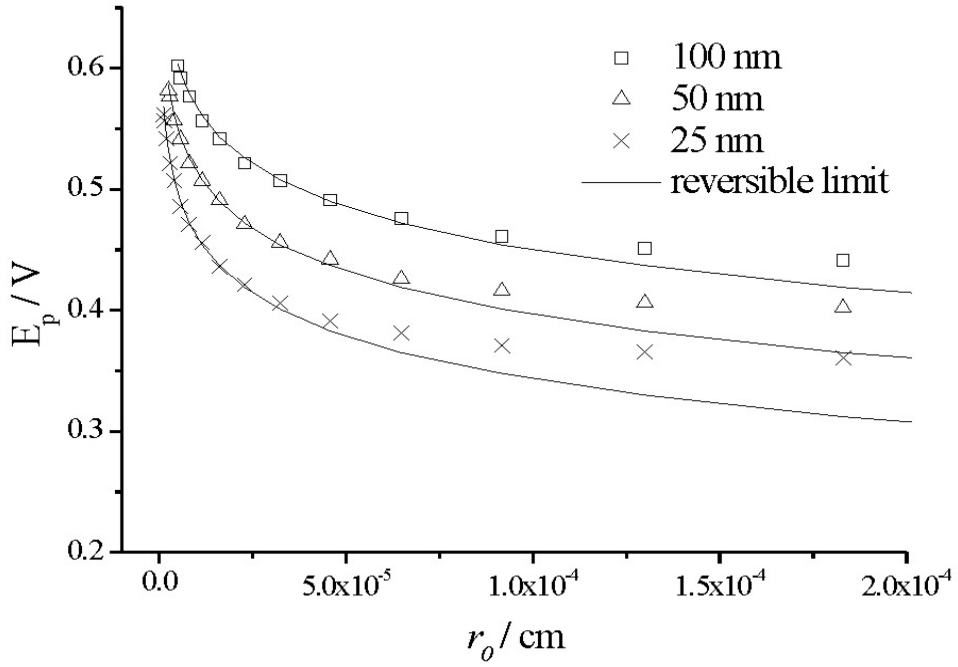


Figure 9.4

Plot of the theoretical peak potential, E_p, calculated for the reversible limit as given by ***Equation 9.9*** *derived by Brainina (solid lines) and that predicted by the computational model described in this chapter (symbols, k^0 = 1 cm s^{-1}), against the domain radius, $r_{0,}$ for the stripping particles of radius, r_s = 12.5, 25 and 50 nm. All other parameters used in the simulation are listed in* ***Table 9.2.***

Equation 9.9 predicts that E_p depends on the initial average concentration of metal on the electrode surface, c^0. The value of $c^0 r_s$ can in turn be related to the stripping charge, (Q) by **Equation 9.11**

$$2c^0 r_s = \frac{Q}{nFN\pi r_0^2} = \frac{Q}{nFA_{elec}} \qquad \textbf{[9.11]}$$

as

$$N = \frac{A_{elec}}{\pi r_0^2} \qquad \textbf{[9.12]}$$

Where Q is the total stripping charge, N is the number of particles and A_{elec} is the total electrode area. It is therefore predicted from **Equation 9.9** that E_p should depend on $\left(\frac{RT}{F}\ln(Q)\right)$ and be independent of the size of the individual particles in the reversible limit. This equation therefore predicts that the peak potential drops to negative infinity as the surface coverage tends towards zero and as the value of c^0 decreases in proportion to the total stripping charge, Q.

Figure 9.5 shows a plot of the peak potential, E_p, calculated by **Equation 9.9** and those predicted by our adapted "thick layer" stripping model under electrochemically reversible conditions, (k^0 = 1 $cm\ s^{-1}$), as a function of Q,

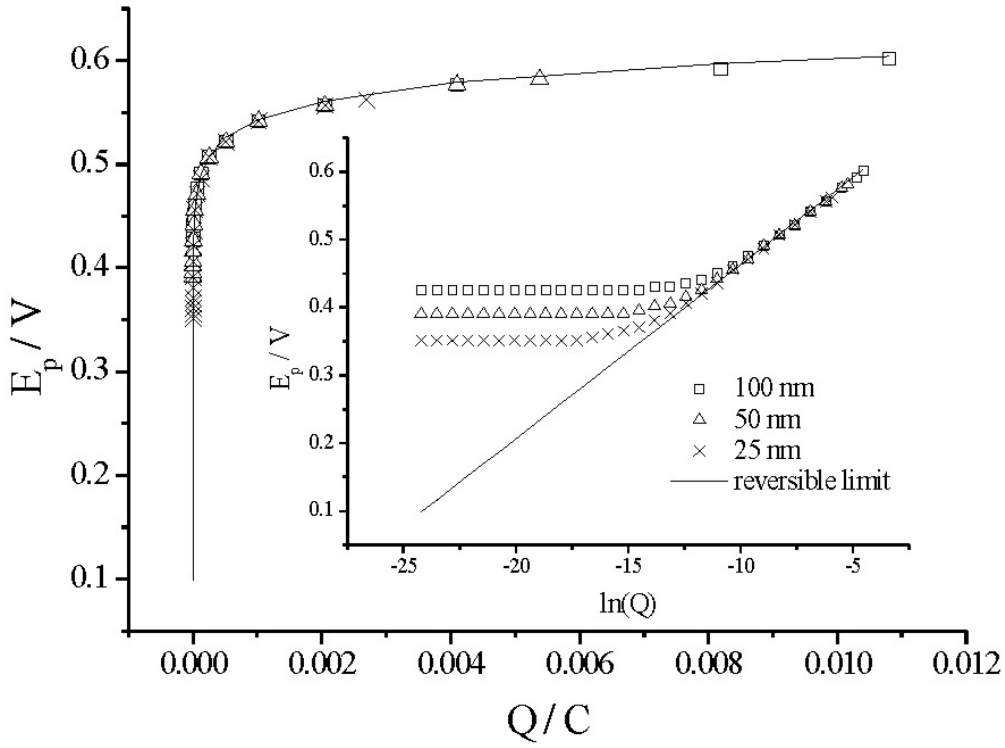


Figure 9.5

Plot of peak potential, E_p, calculated for the reversible limit as given by ***Equation 9.9*** *derived by Brainina (solid line) and those predicted by the computational model described in this chapter (symbols, k^0 = 1 cm s^{-1}) against the stripping charge, Q for the stripping particles of radius, r_s = 12.5, 25 and 50 nm. All other parameters used in the simulation are listed in* ***Table 9.2****. Inset shows the same data plotted against ln(Q).*

Brainina predicts that E_p is independent of the particle size at all values of Q. At high values of Q, we observe good agreement between both models. In this case the diffusion zones overlap heavily, effectively averaging the metal coverage across the whole array, undergoing planar diffusion. Whereas Brainina predicts a linear relationship between Q and E_p, our mathematical model predicts a plateau at a constant E_p at dilute surface coverages. Experimentally, we would not expect to follow Brainina's theory as at some point the individual particles must become far

enough away to have no effect on each other. As the particles become diffusionally independent, the peak potential becomes independent of any further change in the surface coverage. **Figure 9.6 (inset)** shows that a fixed peak potential is reached for each NP size, at low values of Q. Clearly, at low Q the particle size becomes critical in determining the peak potential. Particle size does not directly affect peak potential at high coverage; only the total amount of material on the surface, as measured by the stripping charge, has an effect and so E_p scales with $\left(\frac{RT}{F}\ln(Q)\right)$.

9.3.5 Comparison between Theory and Experiment

Figure 9.6 shows the comparison of peak potentials observed experimentally with the simulation results, using the parameters in **Table 9.3,** for a range of particle sizes and coverages as measured by charge passed during the stripping phase, Q. **Figure 9.6 (a)**, **(b)** and **(c)** shows the results for 12.5, 25 and 50 nm average radius AgNPs respectively, produced in colloidal suspension as described in **Chapter 4**. For each sample a range of different particle loadings, as measured from the peak charge, are considered.

Parameter	**Value**
Starting potential, E_1	0.2 V
End potential, E_2	0.9 V
Formal potential, E_f^0	0.69 V
Diffusion coefficient of Ag^+, D_{Ag+}	$1.2\times10^{-5} cm^2 s^{-1}$
Transfer coefficient, α	0.5
Scan rate, υ	0.01 V s^{-1}, 0.02 V s^{-1}, 0.1 V s^{-1}
Rate constant, k^0	1 cm s^{-1}

Table 9.3

Parameters used for numerical simulations to fit with experimental data.

For all particle sizes it can be seen that the peak potential increases with the increasing amount of metal initially on the electrode surface. This is characteristic of reversible kinetics and therefore the theoretical data presented in **Figure 9.6** are for fast kinetics. As we have discussed the increase in E_p is due to the planar diffusion resulting from the extensive overlap of diffusion layers during the dissolution process. Planar diffusion restricts the diffusion compared to the case of isolated particles and therefore results in a higher peak potential. The surface coverages investigated are less than 12%. At 12% coverage it seems there is significant diffusional overlap such that rate of stripping is mainly controlled by planar diffusion of Ag^+ away from the whole electrode surface.

In order to give a clearer picture of the experimental data as compared to the mathematical model, all particle sizes were plotted *vs. ln(Q)*, as shown in **Figure 9.6(d)**. Across the experimental range, the size of the individual particles does not have a significant effect on the peak potential due to the degree of overlap. The stripping process is controlled by the diffusion process across the whole electrode rather than the diffusional environment very close to each individual particle and therefore the exact distribution of the silver on the electrode surface does not affect the stripping peak, only the total amount present is important. At the most dilute NP densities we expect to see a constant E_p value for each NP size. However, such low surface coverages are difficult to achieve experimentally.

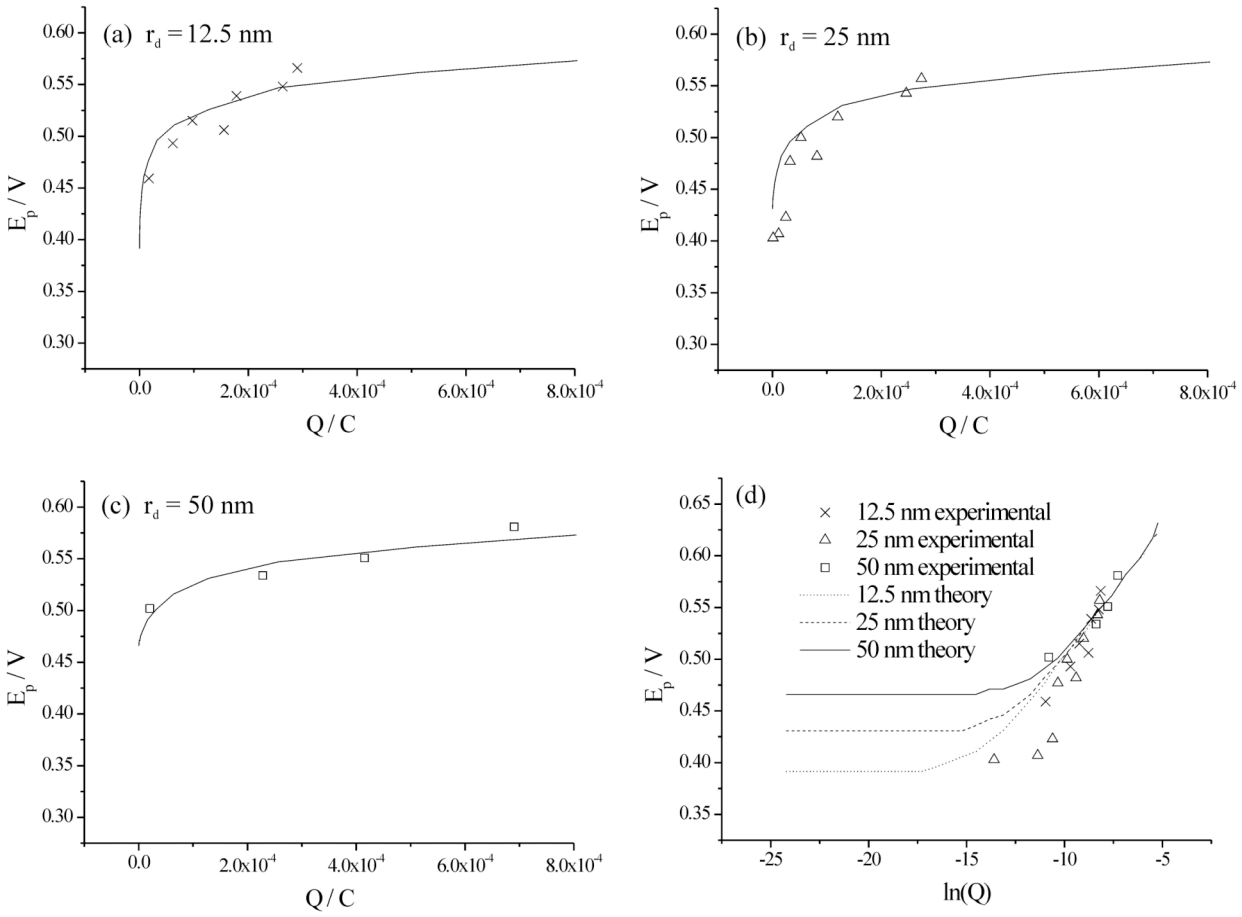


Figure 9.6

*Plots of peak potential, E_p, measured experimentally (symbols) and the values predicted by the computational model described in this chapter (solid line, parameters given in **Table 9.3**) against the stripping charge, Q. Nanoparticle radius (a) r_s = 12.5 nm (Sample 1), (b) r_s = 25 nm (Sample 2) and (c) r_s = 50 nm (Sample 3). (d) shows the same data plotted against ln(Q). In all cases the scan rate, υ, is 0.02 V s^{-1}.*

This model is based on a number of assumptions as previously described. Furthermore, we assume the NPs are distributed on the electrode surface in an incomplete monolayer. However, experimentally NPs may clump together forming some larger particles. The presence of some larger, more widely spaced particles is likely to result in some deviation as calculations are based in the distribution and size

originally prepared. This larger size distribution is unaccounted for in the model. Such approximations may result in differences between theory and experiments.

Scan rate dependence of the peak potential for the stripping of AgNPs (r_{avg} = 12.5 nm) is shown in **Figure 9.7**.

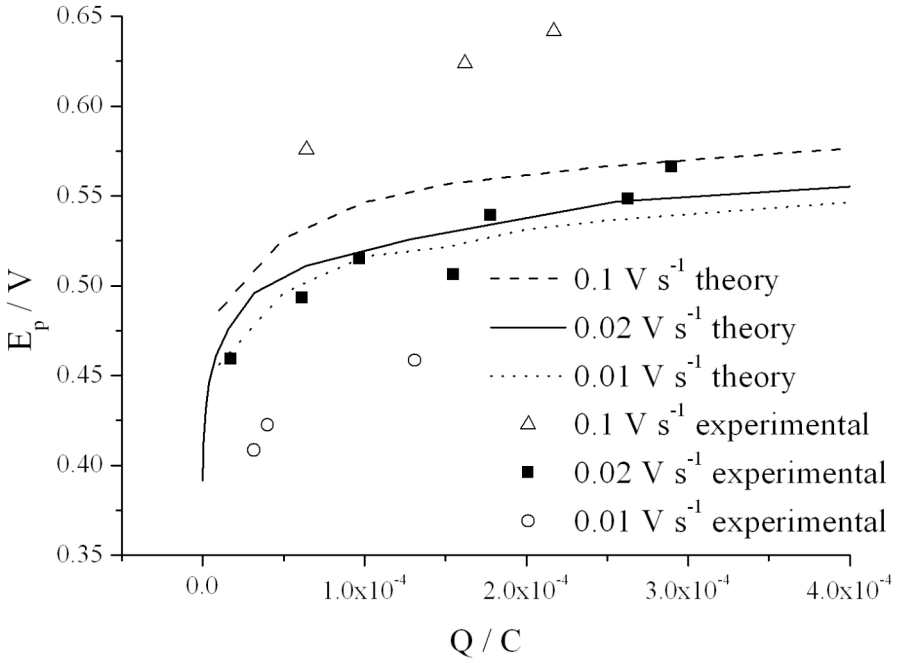


Figure 9.7

*Plots of peak potential, E_p, measured experimentally (symbols) and the values predicted by the mathematical model (solid line, parameters given in **Table 9.3**) against the stripping charge, Q, for r_s = 12.5 nm (sample 1) nanoparticles stripped at three different scan rates, υ = 0.01 V s^{-1}, 0.02 V s^{-1} and 0.1 V s^{-1}.*

The dependence of the stripping peak potential on the stripping charge can be seen at all the scan rates, suggesting that there is still extensive overlap of the diffusion layers even at a scan rate of 0.1 $V\ s^{-1}$. The average diffusion domain radius is calculated to be less than $1\times10^{-5} cm$, considerably smaller than the predicted value of

approximately $3 \times 10^{-3} cm$ (υ = 0.1 $V\ s^{-1}$). The approximate diffusion layer thickness is equal to $\sqrt{Dt}$ where $t = 0.1/\upsilon$, with 0.1 V being the approximate difference between the start of the stripping peak and the peak potential.

Comparison of theory and experiment indicates the qualitative trend: an increase in E_p with Q and ν in the experimental data. However, the theory is only able to approximate this dependence. We are unable to obtain a good agreement in this case such as that obtained for E_p *vs.* Q data at a fixed value of υ. This is due to the fact that changing the scan rate means that assumptions in respect of particle shape change systematically with scan rate and are thus less effective under this type of comparison.

9.4 Conclusions

In this chapter we have presented both experimental data and a theoretical interpretation for modelling the voltammetry of stripping silver nanoparticles from the surface of an electrode. Critically, this model incorporates both radial diffusion and the proximity of the particles to each other, unlike previous models. The reversible and irreversible limits of the Brainina [1-3] model are compared. This latter model considers only one – dimensional diffusion and an average metal concentration across the whole electrode.

The study of stripping voltammetry at AgNP – modified electrodes has shown that the equations derived by Brainina are appropriate at an array of NPs with high coverage, undergoing essentially planar diffusion. However, at the opposite end of the spectrum, where NPs in an array are widely dispersed and essentially isolated, radial diffusion to the individual particles and the NP size begins to dominate their behaviour. In this case Brainina's model is no longer appropriate and we must consider the two – dimensional mathematical model. The trends observed with changing coverage and particle size have been explained by the theory presented and suggest the Ag^+ / Ag couple has reversible kinetics.

In the following chapter we will discuss the size – dependent adsorption behaviour of macro – and nano – silver towards the underpotential deposition (*UPD*) of a series of heavy metals.

Chapter 9: References

1. K. Z. Brainina, *Talanta*, 1971, **18**, 513-539.

2. K. Z. Brainina and R. P. Lesunova, *Zhurnal Analiticheskoi Khimii*, 1972, **29**, 1302-1308.

3. K. Z. Brainina and M. B. Vydrevich, *Journal of Electroanalytical Chemistry*, 1981, **121**, 1-28.

4. X. Dai and R. G. Compton, *Analytical Sciences*, 2006, **22**, 567-570.

5. X. Dai and R. G. Compton, *Electroanalysis*, 2005, **17**, 1325-1330.

6. K. Brainina, A. Kozitsina and J. Beikin, *Analytical and Bioanalytical Chemistry*, 2003, **376**, 481-485.

7. F. W. Campbell, S. R. Belding, R. Baron, L. Xiao and R. G. Compton, *Journal of Physical Chemistry C*, 2009, **113**, 9053-9062.

8. F. W. Campbell, S. R. Belding, R. Baron, L. Xiao and R. G. Compton, *The Journal of Physical Chemistry C*, 2009, **113**, 14852-14857.

9. I. Streeter and R. G. Compton, *The Journal of Physical Chemistry C*, 2007, **111**, 18049-18054.

10. I. Streeter, R. Baron and R. G. Compton, *The Journal of Physical Chemistry C*, 2007, **111**, 17008-17014.

11. M. T. Mouhandess, F. Chassagneux and O. Vittori, *Journal of Electroanalytical Chemistry*, 1982, **131**, 367-371.

12. M. T. Mouhandess, F. Chassagneux, O. Vittori, A. Accary and R. M. Reeves, *Journal of Electroanalytical Chemistry*, 1984, **181**, 93-105.

13. M. Mouhandess, F. Chassagneux, B. Durand, Z. Sharara and O. Vittori, *Journal of Materials Science*, 1985, **20**, 3289-3299.

14. T. Grygar, *Journal of Solid State Electrochemistry*, 1998, **2**, 127-136.

15. T. Grygar, F. Marken, U. Schroder and F. Scholz, *Collection Czech Chemical Communications*, 2002, **67**, 163.

16. S. E. Ward Jones, F. G. Chevallier, C. A. Paddon and R. G. Compton, *Analytical Chemistry*, 2007, **79**, 4110-4119.

17. B. J. Murray, J. T. Newberg, E. C. Walter, Q. Li, J. C. Hemminger and R. M. Penner, *Analytical Chemistry*, 2005, **77**, 5205-5214.

18. M. Hourani, *Analyst* 1994, **119**, 1975-1978.

19. A. J. Bard and L. R. Faulkner, *Electrochemical Methods: Fundamentals and Applications*, 2nd edn., John Wiley & Sons, Inc., New York, 2001.

20. A. Henglein, Editon edn., 1988, pp. 113-180.

21. A. Henglein, *Chemical Reviews*, 1989, **89**, 1861-1873.

22. A. Henglein, *Berichte der Bunsen-Gesellschaft*, 1990, **94**, 600-603.

23. *Revised Nuffield Advanced Science Book of Data*, Longman, London, 1984.

24. B. A. Brookes, T. J. Davies, A. C. Fisher, R. G. Evans, S. J. Wilkins, K. Yunus, J. D. Wadhawan and R. G. Compton, *Journal of Physical Chemistry B*, 2003, **107**, 1616-1627.

25. T. J. Davies, B. A. Brookes, A. C. Fisher, K. Yunus, S. J. Wilkins, P. R. Greene, J. D. Wadhawan and R. G. Compton, *Journal of Physical Chemistry B*, 2003, **107**, 6431-6444.

26. T. J. Davies, B. A. Brookes and R. G. Compton, *Journal of Electroanalytical Chemistry*, 2004, **566**, 193-216.

27. T. J. Davies and R. G. Compton, *Journal of Electroanalytical Chemistry*, 2005, **585**, 63-82.

28. T. J. Davies, S. Ward-Jones, C. E. Banks, J. del Campo, R. Mas, F. X. Muñoz and R. G. Compton, *Journal of Electroanalytical Chemistry*, 2005, **585**, 51-62.

29. J.-S. Ferenc and Z. Néda, *Physica A: Statistical Mechanics and its Applications*, 2007, **385**, 518-526.

30. S. E. Ward Jones, F. W. Campbell, R. Baron, L. Xiao and R. G. Compton, *Journal of Physical Chemistry C*, 2008, **112**, 17820-17827.

Chapter 10

The Underpotential Deposition of Heavy Metals on Silver Nanoparticles: Size – Dependent Adsorption Behaviour.

Abstract

It has been well established that the macro – and nano – scales exhibit some distinctly different behaviours. We have previously discussed the importance of NP size in stripping voltammetry and the cathodic reduction of various species. Adsorption to the electrode material has proved to be an important feature of the reaction mechanisms previously discussed. Therefore, it is important to compare the adsorption behaviour between the macro – and nano – scales in order to fully understand the voltammetric behaviour. This chapter reports the apparent size – dependent adsorption behaviour of silver nanoparticles (AgNPs) towards the underpotential deposition (*UPD*) of a selection of heavy metals. We have considered the *UPD* of thallium, lead and cadmium at silver nanoparticle arrays. Distinctive *UPD* behaviour is observed at large nanoparticles and bulk silver electrodes. However, significantly altered *UPD* behaviour is observed at nanoparticles below ~ 50 nm in diameter. Similar behaviour is reported for all three heavy metals investigated. We suggest that this phenomenon occurs partly due to the change in morphology or electronic (work function) properties between the macro – and nano – scales. In this chapter we report some of the first examples of size – dependent adsorption phenomena.

10.1 Introduction

The use of nanoparticles in electrochemistry provides a number of advantages over their corresponding bulk materials. One obvious difference, which will prove to be extremely relevant in this chapter, is the higher active surface area provided by nanoparticulate materials. This can in turn lead to improved selectivity and signal – to – noise ratio, which has proven to be highly advantageous in some electro – analytical applications[1-3]. The reduction in size can also lead to changed surface and electronic properties. Crystal faces exposed at the nano – scale, and not seen at the macro – scale, may lead to improved current responses and catalytic properties; the converse might also be true. Nanoparticles have therefore found extensive use in catalytic and sensing[4, 5] applications. However, the adsorption of species on nanoparticulate material is still relatively unexplored by comparison. In an electrochemical environment, the adsorption on macro – and nano – gold supported on carbon nanotubes has been shown to change qualitatively with no adsorption seen on small nanoparticles[6, 7]. Furthermore, the size – dependent charging of gold nanoparticles[8], improved tolerance to electrode fouling[8] and varied capacity for hydrogen storage[9, 10] also show dependence on the particle size.

Underpotential deposition (*UPD*) is the deposition of a monolayer, or sub – monolayer, of a metal onto a different substrate metal electrode at potentials more positive than the equilibrium (Nernst) potential for bulk deposition of the metal. It is possible to deposit a wide variety of metals on to an electrode substrate by *UPD*. Most relevant to this study is *UPD* of thallium, lead and cadmium on macro – sized silver electrodes[11-13], which have been extensively reported in the literature. However, the *UPD* of metals such as bismuth, copper, nickel and zinc[14-18] have also

been reported on a variety of silver substrates. Studies have also examined the *UPD* behaviour of two co – depositing species (*e.g.* thallium and lead[14, 19]). Thallium *UPD* has also be reported on gold[20, 21], platinum[22, 23] and copper[24, 25] electrodes. The potential difference between *UPD* and bulk deposition can be related to the different work functions associated with the substrate material and the deposit. This can in turn result in partial charging of the adatoms. Since the work function of the nanoparticles may be size – related this offers a further mechanism by which changed electrochemical behaviour may arise at the nano – scale.[26-29]

The study of *UPD* is important as it commonly results in the deposition of a monolayer or sub – monolayer of material. Such layers can be highly significant in the mechanism of electrocatalytic processes. Study of the deposition of metals is necessary to fully understand adsorbate – substrate interactions in the design of bi – metallic catalysts and in the study of alloys. Accordingly the investigation of adsorption effects on nanoparticulate materials is required for the development of these materials for both synthetic and analytical applications.

10.2 Results and Discussion

10.2.1 Thallium Underpotential Deposition

A number of thallium deposition studies have been performed on macro – sized silver single crystal electrodes, each of which displays its own distinct features. The reduction of Tl^+ to an adsorbed layer of thallium metal is represented in **Equation 10.1**.

$$Tl^{+}_{(aq)} + e^{-} \rightleftharpoons Tl_{(metal)} \qquad \textbf{[10.1]}$$

The structure of a surface is seen to control the ease with which thallium can be deposited: Ag(111) > Ag(100) > Ag(110) > polycrystalline Ag[30, 31]. This evidence clearly indicates that the adsorption of thallium is highly sensitive to the detailed surface structure of a silver electrode.

Little detailed research can be found in the literature relating to the *UPD* adsorption of metal atoms such as thallium, on nanoparticulate materials[32, 33] or indeed of the adsorption of molecules in general on nanoparticles. In this section we will compare the deposition of thallium on silver macro – disk electrodes and AgNPs, examining the influence of both nanoparticle size and electrode coverage on the bulk and underpotential deposition of thallium.

We have chosen to examine the underpotential and bulk deposition of thallium on AgNPs of varying sizes. AgNPs were synthesized by a well documented[12, 13] seed – mediated citrate reduction process. This method allows us to synthesise AgNPs with the following sizes: 20 – 40 nm, 50 – 70 nm and 80 – 120 nm diameter[13]. The as

synthesized colloidal AgNPs were then used to modify a basal plane pyrolytic graphite (BPPG) electrode.

Thallium deposition was carried out in a solution of KNO_3 (1.5 M) and $TlNO_3$ (10 mM) at 50 $mV\ s^{-1}$. **Figure 10.1** displays the underpotential deposition [E_p = - 0.545 *V* (*vs. SCE*)] and stripping [E_p = - 0.440 *V* (*vs. SCE*)] of thallium on a silver macro – disk (*diameter = 0.7 mm*) under the same conditions described above. Thallium deposition was also examined on a bare BPPG (*diameter = 5 mm*) electrode and showed no *UPD* and a bulk deposition taking place at E_p = - 0.822 *V*, with a corresponding stripping peak at E_p = -0.637 *V*.

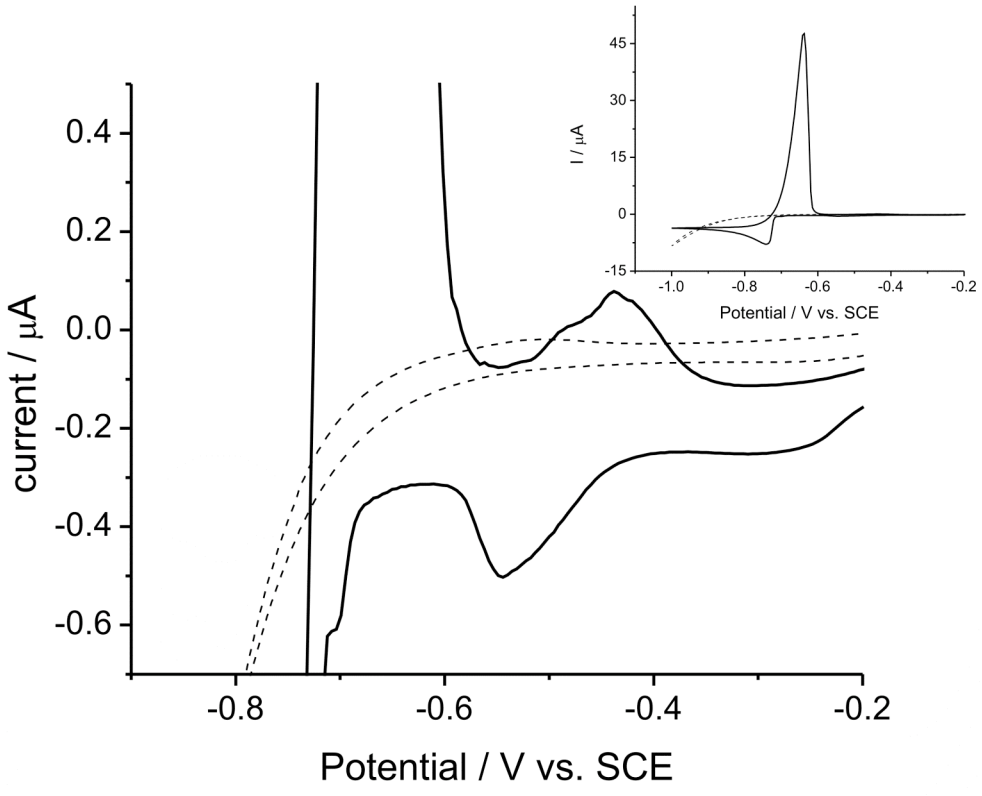


Figure 10.1

Thallium deposition on a silver macrodisk electrode. Experimental conditions: KNO_3 (1.5 M) + $TlNO_3$ vs. SCE. Scan rate: 50 mVs^{-1}. (Solid line: 10 mM $TlNO_3$; Dashed line: 0 mM $TlNO_3$). Inset: demagnification showing bulk deposition.

When we compare this with a BPPG electrode modified with AgNPs (20 – 40 nm) we can see that the bulk deposition peak shifts positively from that of a BPPG bulk deposition to that of silver bulk deposition, as shown in **Figure 10.2 (inset)**. Furthermore, when we closely examine the region of *UPD* it is clear that on the small AgNPs (20 – 40 nm), no appreciable UPD or stripping of thallium takes place, while we still observe a bulk deposition wave at E_p = -0.777 *V* (*vs. SCE*) and the corresponding dissolution at E_p = -0.633 *V* (*vs. SCE*) as shown in **Figure 10.2**.

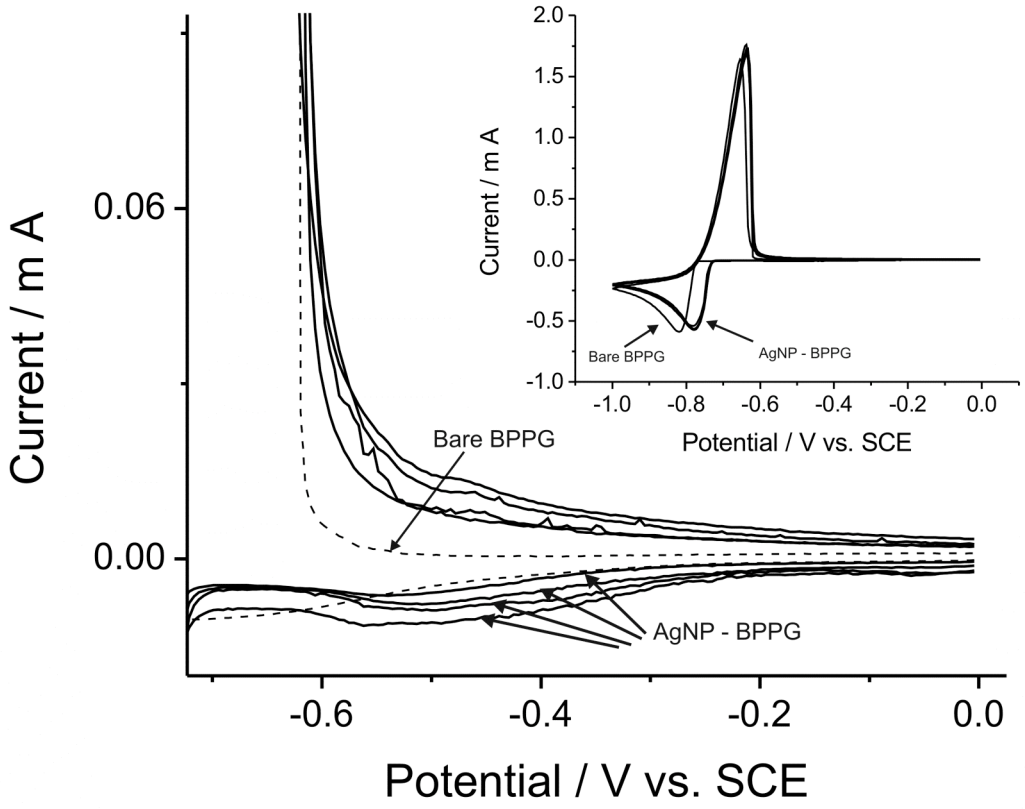


Figure 10.2

Thallium deposition on AgNP – BPPG (20 – 40 nm) electrode. Experimental conditions: KNO_3 (1.5 M) + $TlNO_3$ vs. SCE. Scan rate: 50 mVs^{-1}. (Solid line: AgNP – BPPG (20 – 40 nm) electrode; Dashed line: bare BPPG). Inset: demagnification showing shift in bulk deposition potential between bare BPPG and AgNP – BPPG.

The same effect is recorded for a range of AgNP surface coverages of AgNPs on the BPPG electrode, between 0.5 and 3%. The degree of surface coverage could be altered in accordance with the volume of colloidal suspension evaporated on the electrode surface, (*i.e.* by increasing the volume the NP density is increased). Following the deposition and stripping of thallium we are able to quantify the amount of silver on the electrode surface by linear sweep stripping voltammetry (*LSV*) in $NaClO_4$ (0.1 M) as shown in **Figure 10.3**.

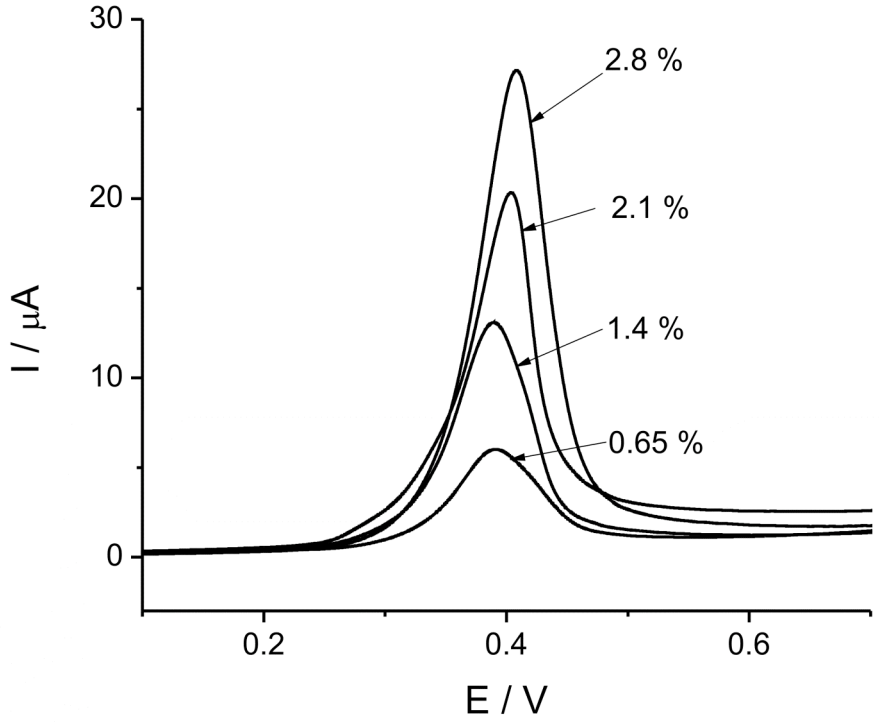


Figure 10.3

Stripping voltammetry recorded for increasing surface coverage of AgNPs (20 – 40 nm, 0.5 and 3.0 %). Experimental conditions: $NaClO_4$ (0.1 M), vs. SCE. Scan rate: 20 mVs^{-1}.

When the same experiment was repeated using larger AgNPs (80 – 120 nm) (**Figure 10.4**) a similar effect was observed with respect to the shift in the position of the bulk

deposition peak. However, unlike the small AgNPs (20 – 40 nm), the larger AgNPs (80 -120 nm) exhibited distinct deposition and stripping peaks in the thallium *UPD* region, corresponding to those reported on bulk silver. As no *UPD* is observed for bare BPPG we can attribute this to the presence of AgNPs (80 – 120 nm). In this case the increased AgNP density on the electrode surface corresponds to an increase in the thallium deposition and stripping peak heights (**Figure 10.4**), due to the greater surface area available for thallium adsorption.

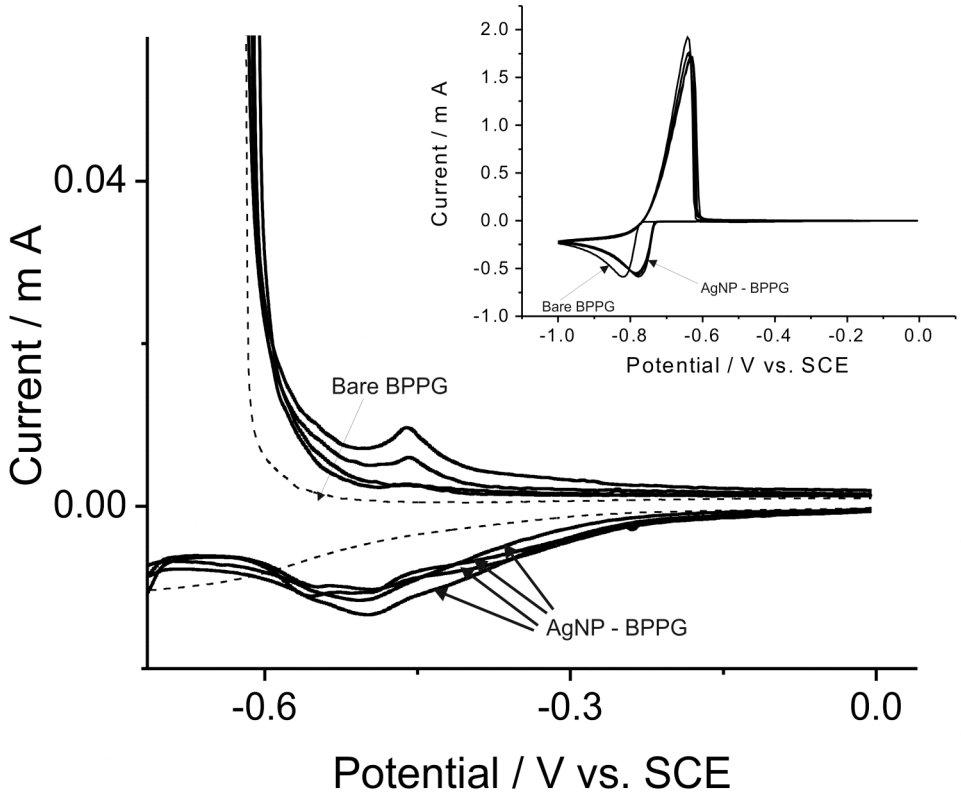


Figure 10.4

Thallium deposition on AgNP – BPPG (80 – 120 nm) electrode. Experimental conditions: KNO_3 (1.5 M) + $TlNO_3$ (10 mM) vs. SCE. Scan rate: 50 mVs^{-1}. (Solid line: AgNP – BPPG (80 – 120 nm) electrode; Dashed line: bare BPPG). Inset: demagnification showing entire deposition range at bare BPPG and AgNP – BPPG and corresponding shift in bulk deposition potential between them.

10.2.2 Lead Underpotential Deposition

The *UPD* behaviour on AgNPs was further studied by the deposition of lead at AgNP – arrays composed of small (*20 – 40* nm) and large (*80 – 120* nm) nanoparticles. Lead has repeatedly been studied on silver electrodes in the presence of co – depositing species, such as thallium on polycrystalline silver electrodes[19]. In this case the deposition appears strongly dependent on the composition of the supporting electrolyte. The presence of adsorbing anions in solution can also affect the deposition process[34, 35]. Furthermore, the *UPD* of lead and cadmium adsorbates has been examined on gold and silver single crystal surfaces [15, 34, 36-38] as well as modified silver electrodes[39]. The results of such studies have indicated that deposition can be very sensitive to the solution composition and the electrode surface structure. Similarly, the work functions associated with the substrate material and the deposit may also be related to the particle size.

In this section we focus on the electrochemical underpotential and bulk deposition of lead on silver macro – electrodes and AgNP – arrays composed of varying sizes of particles. The reduction of lead to form an adsorbed layer of metal is represented by **Equation 10.2**.

$$Pb^{2+}{}_{(aq)} + 2e^{-} \rightleftharpoons Pb_{(metal)} \qquad \textbf{[10.2]}$$

As discussed, we can distinguish the *UPD* process from that of the bulk deposition, at potentials positive of the reversible Nernst potential.

Cyclic voltammetry for the deposition of lead at a silver macrodisk is shown in **Figure 10.5**. A distinct *UPD* process is recognizable at E_p = - 0.43 *V*, with the

formation of a sub – monolayer and the corresponding stripping peak at E_p = - 0.39 *V*. The bulk deposition of lead takes place on silver electrodes at potentials negative of – 0.6 *V*, with the corresponding stripping peak at – 0.54 *V*. The bulk deposition does not produce a distinct peak but rather appears as a continuation of the *UPD* peak. The number of layers deposited in the bulk process can be increased by extending the deposition time or by scanning to more negative potentials. We are able to record only the *UPD* peak without any bulk deposition by scanning from 0 to – 0.6 *V* and reversing the scan direction.

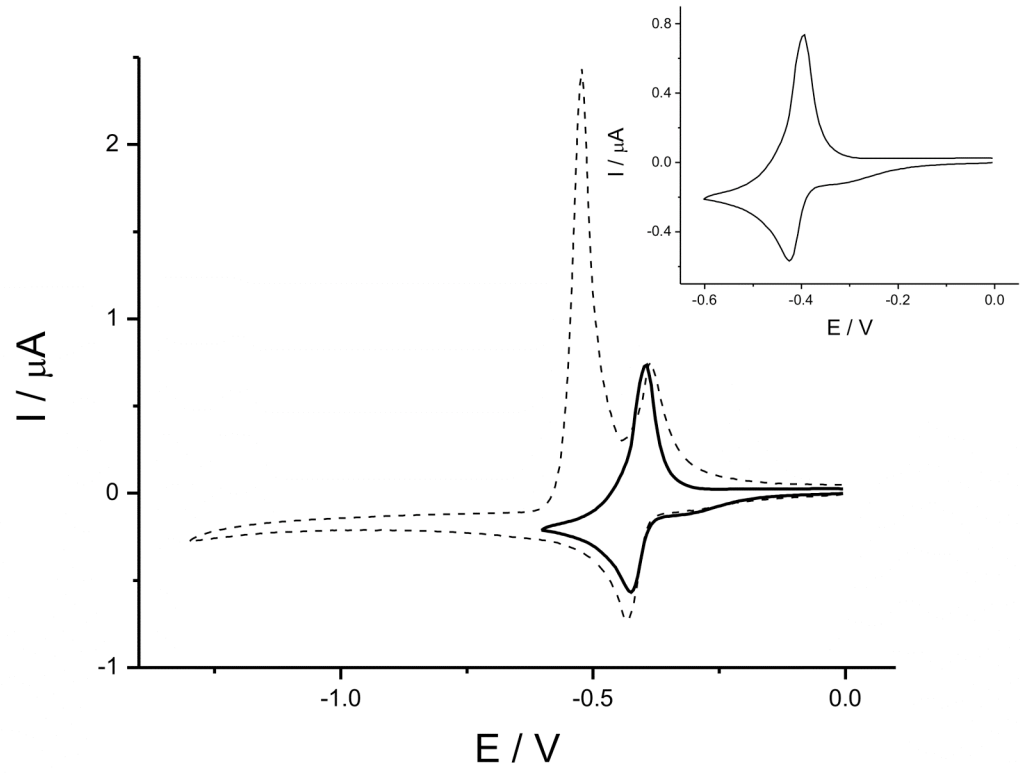


Figure 10.5

Lead deposition on silver macro – disk electrode (A = $3.85\times10^{-3} cm^2$*) from a solution of sodium potassium tartrate (0.1 M) + H_2SO_4 (0.01M) + $Pb(NO_3)_2$ (*$3\times10^{-3} M$*). Scan rate: 50 mVs^{-1}, vs. SCE. (Inset: magnification of the solid line showing only UPD region).*

The lead deposition at a silver nanoparticle array is shown in **Figure 10.6**. The solid line shows the voltammetry obtained for large AgNPs (80 – 120 nm) and the dashed line shows the same for smaller particles (20 – 40 nm).

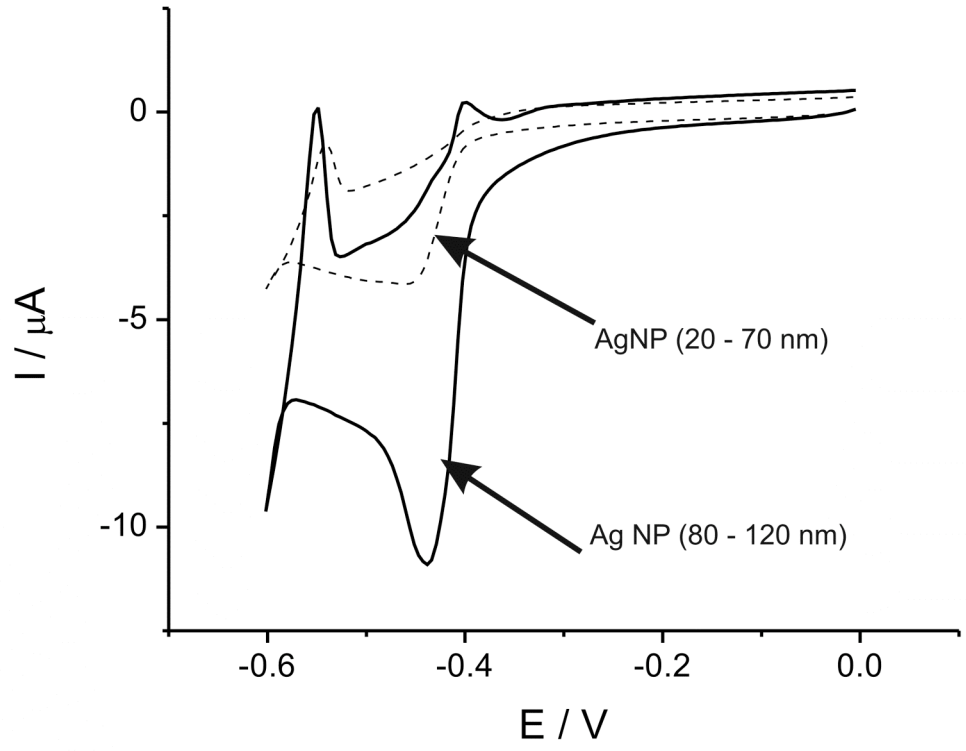


Figure 10.6

Lead deposition on AgNP – modified BPPG electrode. Solid line: AgNP – BPPG 80 - 120 nm; Dashed line: AgNP – BPPG 20 – 70 nm. Scan rate: 50 mV s^{-1}, vs. SCE.

It is clear that for the larger nanoparticles, as for the macro – disk, distinct underpotential deposition and stripping peaks are observed at – 0.43 *V* and – 0.39 *V*, respectively. On the other hand, for the small AgNPs distinctive deposition and stripping peaks are absent in the *UPD* region.

10.2.3 Cadmium Underpotential Depostion

A similar behaviour can be observed for the deposition of cadmium on silver electrodes. The deposition of cadmium cations in aqueous solution to cadmium metal on the electrode surface is outlined in **Equation 10.3**.

$$Cd^{2+}_{(aq)} + 2e^- \rightleftharpoons Cd_{(metal)} \qquad \textbf{[10.3]}$$

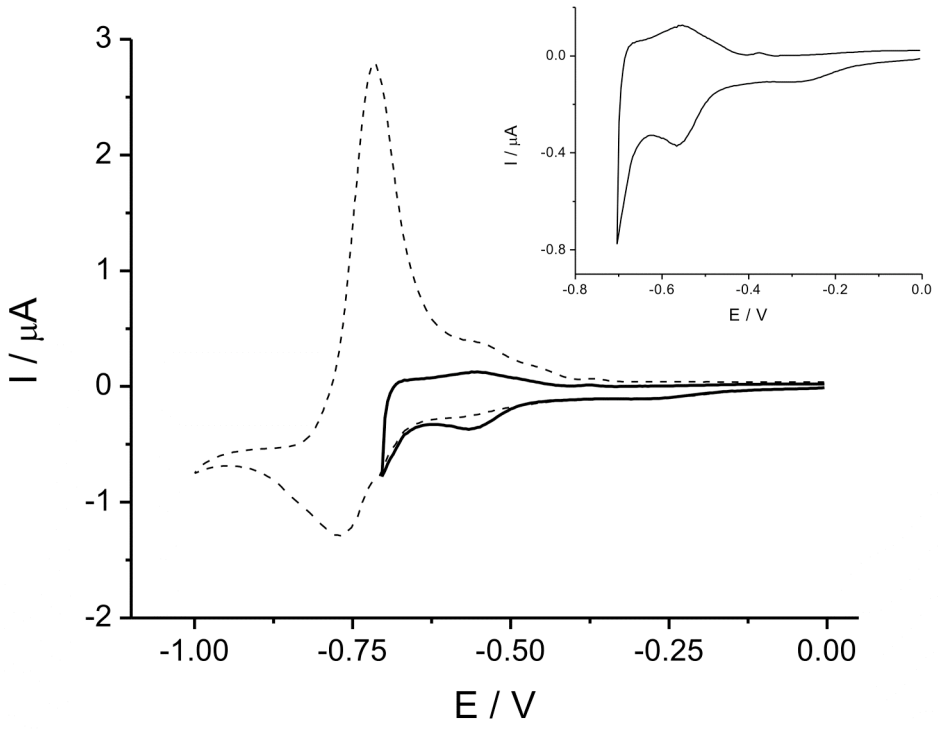


Figure 10.7

Cadmium deposition on a silver macro – disk electrode ($A = 3.85 \times 10^{-3} cm^2$) from a solution of Na_2SO_4 (0.5 M) + H_2SO_4 (0.01 M) + $CdSO_4$ ($2 \times 10^{-3} M$). Scan rate: 50 mVs^{-1}, vs. SCE. (Inset: magnification of solid line showing only UPD region).

The deposition of cadmium on a silver macro – electrode is displayed in **Figure 10.7**. The bulk deposition takes place at E_p = – 0.77 V with the corresponding stripping

peak at $E_p = -0.72\ V$ (*vs. SCE*). The *UPD* process takes place at $E_p = -0.57\ V$, with stripping at $E_p = -0.55\ V$. We are able to record the isolated *UPD* process by scanning negatively to – 0.7 *V* and reversing the scan direction.

AgNP – arrays composed of 80 – 120 nm diameter nanoparticles display *UPD* behaviour, similar to that occurring at the silver macro – electrode. **Figure 10.8** displays the behaviour of AgNP – BPPG (80 – 120 nm) as a solid line, underpotential deposition taking place at potentials very close to that of the macro –electrode, with $E_p = -0.56\ V$ and stripping at $E_p = -0.54\ V$. The dashed line in **Figure 10.8** shows the absence of distinctive cadmium *UPD* and stripping processes for a AgNP – BPPG (20 – 40 nm). The sharp peaks superimposed on the deposition / stripping waves may be due to deposition on the different crystal faces of the larger NPs.

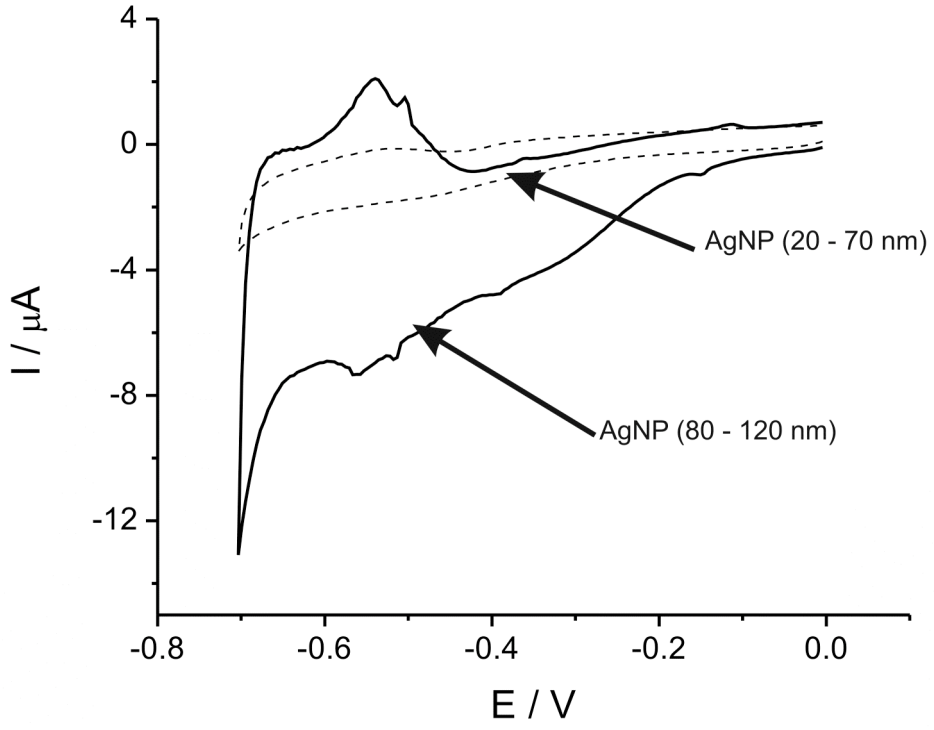


Figure 10.8

Cadmium deposition on silver nanoparticle modified BPPG electrode. Solid line: AgNP – BPPG 80 -120 nm; Dashed line: AgNP – BPPG 20 – 70 nm. Scan rate: 50 mVs^{-1}, vs. SCE.

In the case of thallium, lead and cadmium deposition on AgNPs, the intermediate nanoparticle size (50 – 70 nm) behaves much like the smaller size (20 – 40 nm), with no obvious underpotential deposition process.

This *UPD* behaviour is exhibited by AgNPs of varying size as reported for all three heavy metals investigated (thallium, lead and cadmium).

In the case of the larger AgNPs (80 – 120 nm) it seems that more material is deposited than is stripped off in the underpotential region. This could possibly indicate the occurrence of alloy formation or an incomplete stripping process at the nano – scale material. This process may also contribute to the behaviour of the smaller NPs (20 –

40 nm), resulting in the absence of the distinct *UPD* / stripping features in the voltammetry. The high surface energy of smaller NPs may promote alloying, incorporating deposited material into the particle making it inaccessible during the stripping step. This is a distinctly different behaviour from that observed at the macro – scale electrode.

10.3 Conclusions

Investigation of the electrochemical deposition of the heavy metals thallium, lead and cadmium on silver nanoparticles has allowed us to conclude that silver nanoparticles show qualitatively different adsorption behaviour below a size threshold of *ca.* 50 nm. A minimum diameter of *ca.* 50 nm is required in order to clearly observe the underpotential deposition and corresponding stripping processes for all three heavy metal deposits discussed in this chapter. Where the array is composed of small particles, with a diameter of less than *ca.* 50 nm, the *UPD* and stripping processes are essentially absent. In certain cases, it appears that some *UPD* occurs at small particles without any stripping peak, in the reverse scan. We suggest this may arise due to a contribution from possible alloy formation or an incomplete stripping process taking place at the nano – scale, which is not possible at the large particles or macro – scale. The evidence so far suggests this may be a general behaviour for the case of underpotential deposition of heavy metals on silver nanomaterials; in particular the change of surface structure and / or work function at the nano – scale may qualitatively alter the observed electrochemistry.

Chapter 10: References

1. C. Batchelor-McAuley, Y. Du, G. G. Wildgoose and R. G. Compton, *Sensors and Actuators B: Chemical*, 2008, **135**, 230-235.

2. L. Xiao, G. G. Wildgoose and R. G. Compton, *Analytica Chimica Acta*, 2008, **620**, 44-49.

3. X. Dai, G. G. Wildgoose, C. Salter, A. Crossley and R. G. Compton, *Analytical Chemistry*, 2006, **78**, 6102-6108.

4. F. W. Campbell and R. Compton, *Analytical and Bioanalytical Chemistry*, 2010, **396**, 241-259.

5. C. Welch and R. Compton, *Analytical and Bioanalytical Chemistry*, 2006, **384**, 601-619.

6. C. Batchelor - McAuley, G. G. Wildgoose and R. G. Compton, *New Journal of Chemistry*, 2008, **32**, 941-946.

7. H. Ye, J. A. Crooks and R. M. Crooks, *Langmuir*, 2007, **23**, 11901-11906.

8. F. Maillard, M. Martin, F. Gloaguen and J. M. Léger, *Electrochimica Acta*, 2002, **47**, 3431-3440.

9. O. Friedrichs, L. Kolodziejczyk, J. C. Sánchez-López, A. Fernández, L. Lyubenova, D. Zander, U. Köster, K. F. Aguey-Zinsou, T. Klassen and R. Bormann, *Journal of Alloys and Compounds*, 2008, **463**, 539-545.

10. K. Zhong, Y. Liu, M. Gao, J. Wang, H. Miao and H. Pan, *International Journal of Hydrogen Energy*, 2008, **33**, 149-155.

11. T. C. Girija and M. V. Sangaranarayanan, *Journal of Applied Electrochemistry*, 2006, **36**, 531-538.

12. V. Daujotis and E. Gaidamauskas, *Journal of Electroanalytical Chemistry*, 1998, **446**, 151-157.

13. E. Herrero, L. J. Buller and H. D. Abruña, *Chemical Reviews*, 2001, **101**, 1897-1930.

14. Y. V. Bokshits, N. P. Osipovich, E. A. Strel'tsov and G. P. Shevchenko, *Colloids and Surfaces A: Physicochemical and Engineering Aspects*, 2004, **242**, 79-83.

15. Y. Bonfil, M. Brand and E. Kirowa-Eisner, *Analytica Chimica Acta*, 2002, **464**, 99-114.

16. K. O. Thiel, M. Hintze, A. Vollmer and C. Donner, *Journal of Electroanalytical Chemistry*, 2008, **621**, 7-12.

17. S. Morin, A. Lachenwitzer, F. A. Moller, O. M. Magnussen and R. J. Behm, *Journal of The Electrochemical Society*, 1999, **146**, 1013-1018.

18. J. Miragliotta and T. E. Furtak, *Surface and Interface Analysis*, 1989, **14**, 53-58.

19. S. Bharathi, V. Yegnaraman and G. Prabhakara Rao, *Journal of Applied Electrochemistry*, 1994, **24**, 981-988.

20. A. Montes-Rojas and E. Chainet, *Journal of the Chilean Chemical Society*, 2007, **52**, 1130-1137.

21. D. Poskus and G. Agafonovas, *Journal of Electroanalytical Chemistry*, 2000, **493**, 50-56.

22. K. Bamba, K. B. Kokoh, K. Servat and J. M. Leger, *Journal of Applied Electrochemistry*, 2006, **36**, 233-238.

23. D. R. Wheeler, J. X. Wang and R. R. Adzic, *Journal of Electroanalytical Chemistry*, 1995, **387**, 115-119.

24. D. A. Berg, D. S. Nadezdhin and R. G. Barradas, *Journal of Electroanalytical Chemistry*, 1993, **355**, 165-179.

25. D. A. Berg, V. A. Vandernoot, R. G. Barradas and E. P. C. Lai, *Journal of Electroanalytical Chemistry*, 1994, **369**, 33-37.

26. D. M. Kolb, M. Przasnyski and H. Gerischer, *Journal of Electroanalytical Chemistry*, 1974, **54**, 25-38.

27. D. M. Kolb and H. Gerischer, *Surface Science*, 1975, **51**, 323-327.

28. H. Gerischer, D. M. Kolb and M. Przasnyski, *Surface Science*, 1974, **43**, 662-666.

29. W. J. Plieth, *The Journal of Physical Chemistry*, 1982, **86**, 3166-3170.

30. B. W. Mao, Z. Q. Tian and M. Fleischmann, *Electrochimica Acta*, 1992, **37**, 1767-1770.

31. J. X. Wang, R. R. Adzic, O. M. Magnussen and B. M. Ocko, *Surface Science*, 1995, **344**, 111-121.

32. K. E. Toghill, G. G. Wildgoose, A. Moshar, C. Mulcahy and R. G. Compton, *Electroanalysis*, 2008, **20**, 1731-1737.

33. K. E. Toghill, L. Xiao, G. G. Wildgoose and R. G. Compton, *Electroanalysis*, 2009, **21**, 1113-1118.

34. V. D. Jovic, B. M. Jovic and A. R. Despic, *Journal of Electroanalytical Chemistry*, 1990, **288**, 229-243.

35. V. D. Jovic and B. M. Jovic, *Electrochimica Acta*, 2002, **47**, 1777-1785.

36. M. F. Toney, J. G. Gordon, M. G. Samant, G. L. Borges, O. R. Melroy, D. Yee and L. B. Sorensen, *The Journal of Physical Chemistry*, 1995, **99**, 4733-4744.

37. H. Bort, K. Jüttner, W. J. Lorenz and G. Staikov, *Electrochimica Acta*, 1983, **28**, 993-1001.

38. L. P. Bicelli, B. Bozzini, C. Mele and L. D'Urzo, *International Journal of Electrochemical Science*, 2008, **3**, 356-408.

39. J. W. F. Robertson, D. J. Tiani and J. E. Pemberton, *Langmuir*, 2007, **23**, 4651-4661.

Chapter 11

Conclusions

In conclusion, the study of the voltammetry of metallic nanoparticles has given rise to several significant results. The study of nanomaterials is an important area of current research, with a wide range of practical applications in areas such as catalysis, sensing devices, biological and fuel cell technologies.

The work discussed in this thesis indicates the importance of both nanoparticle size and nanoparticle surface coverage in determining the nature of the voltammetric response. The reduction of hydrogen peroxide and the hydrogen evolution reaction, as investigated at silver nanoparticle arrays display altered kinetics between the macro – and nano – scales. Furthermore, the reduction of 4-nitrophenol at silver nanoparticle arrays suggests an altered mechanism of the rate - determining step between the silver macro – disk and the silver nanoparticle array.

Size – dependent adsorption behaviour has been reported for the first time in relation to the deposition of heavy metals (*e.g.* thallium, lead and cadmium) at silver nanoparticles of varying size. Small particles do not display the typical UPD characteristics of the corresponding bulk material. It is suggested this may be due to altered surface structure and / or work function at the nano – scale. A size – effect is also noted for the voltammetric stripping of silver nanoparticles. In this case it becomes necessary to apply a two – dimensional diffusion model for essentially isolated particles to account for the apparent shift towards convergent diffusion.

This work indicates that nanoparticles possess a variety of properties specific to the nano – scale, differing from the corresponding bulk materials. We have shown this

includes both size and coverage specific effects relating to the change in diffusion regime between an isolated particle and a densely packed array. Altered electrode kinetics, size – specific stripping behaviour, electrode mechanisms and adsorption behaviour have also been reported. The latter suggests the importance of surface structure in the nature of the voltammetry reported.

The study of nano – materials continues to be a promising and exciting field and is certainly deserving of further investigation.

Glossary

W.E.	*Working Electrode*
R.E.	*Reference Electrode*
C.E.	*Counter Electrode*
SCE	*Saturated Calomel Electrode*
SHE	*Standard Hydrogen Electrode*
NHE	*Normal Hydrogen Electrode*
QRE	*Quasi – Reference Electrode*
Hg/HgO	*Mercury / Mercury Oxide Reference Electrode*
E	*Potential (V)*
E_p	*Peak potential (V)*
$E_{1/2}$	*Half – wave potential*
E^0	*Standard potential (V)*
$E^{0'}$	*Formal potential (V)*
E_f^0	*Formal potential of redox couple (V)*
$(E - E_f^0)$	*Applied potential (V)*
G_{sys}	*Gibbs free energy of system (J mol^{-1})*
ΔG^0	*Standard Gibbs free energy change (J mol^{-1})*
K	*Equilibrium constant*
R	*Gas constant (8.314 J K^{-1} mol^{-1})*
F	*Faraday constant (96485 C mol^{-1})*
T	*Temperature (K)*
P	*Pressure (Pa)*
ϕ_m	*Potential of metal electrode (V)*
ϕ_s	*Potential of solution (V)*
$\Delta\phi_{m/s}$	*Potential drop across electrode / solution interface (V)*

$\bar{\mu}_A$	*Electrochemical potential*
μ_A	*Chemical Potential*
z_A	*Charge on molecule A*
a_A	*Activity of species A*
γ_A	*Activity coefficient*
iR	*Electrical resistance of solution*
j	*Flux (mol cm^{-2} s^{-1})*
i	*Current (A)*
$[\,]_0$	*Concentration at electrode surface*
$[\,]_{bulk}$	*Bulk solution concentration*
$\partial c / \partial x$	*Concentration gradient*
D	*Diffusion coefficient (cm^2 s^{-1})*
E_A	*Activation energy (kJ mol^{-1})*
t	*Time (secs)*
δ	*Diffusion layer thickness (cm)*
m_T	*Mass transport coefficient (D/δ) (cm s^{-1})*
k_c	*Cathodic / reductive rate constant*
k_a	*Anodic / oxidative rate constant*
$\Delta G^{\ddagger}$	*Standard free energy of activation (J mol^{-1})*
$\ddagger$	*Transition state*
$\Delta S^{\ddagger}$	*Entropy change (J K^{-1} mol^{-1})*
$\Delta H^{\ddagger}$	*Enthalpy change (J mol^{-1})*
k^0	*Standard electrochemical rate constant (cm s^{-1})*
α, β	*Transfer coefficient*
$i_{p,\,a}$	*Anodic peak current (A)*
$i_{p,\,c}$	*Cathodic peak current (A)*
υ	*Sweep rate (V s-1)*

n	*Number of electrons*
i_{lim}	*Diffusion limiting current (A)*
r	*Radius of particle (cm)*
θ	*Surface coverage*
p	*Nanoparticle centre – to – centre separation (cm)*
R_d	*Diffusion domain radius (cm)*
$[A]^*$	*Standard concentration (mol cm^{-3})*
Q	*Stripping charge (C)*
IHP	*Inner Helmholtz Plane*
OHP	*Outer Helmholtz Plane*

Appendix 1

Simulation Methods used to Model Regular and Random Arrays of Nanoparticles.

Overview

The simulation of these systems of nanoparticle arrays should be credited to Stephen R. Belding (*PTCL, Oxford*).

We consider the case of an electrochemically quasi-reversible or irreversible processes:

$$Ox + e^- \rightleftharpoons Red \qquad [1]$$

Both *Ox* and *Red* are solution phase species, and we assume that Butler – Volmer kinetics are followed so that:

$$k_c = k^0 \exp\frac{-\alpha F}{RT}(E - E_f^0) = k^0 e^{-\alpha(\theta - \theta_f)} \qquad [2]$$

$$k_a = k^0 \exp\frac{\beta F}{RT}(E - E_f^0) = k^0 e^{\beta(\theta - \theta_f)} \qquad [3]$$

The value k^0 is the standard electrochemical rate constant; E_f^0 is the formal potential of the redox couple; α and β are transfer coefficients such that $\alpha + \beta = 1$, and *R, T, F* have

their usual meaning. The dimensionless potentials are represented by the quantity θ, and $\theta = FE/RT$ and $\theta_f = FE_f^0/RT$.

1.1 Isolated electrodes

We consider first reaction [**1**] at isolated hemispheres and micro – discs of arbitrary radius, r_e. By 'isolated' we mean the electrodes are sufficiently far apart as to be diffusionally independent. Assuming that sufficient electrolyte is present to suppress migration effects, the relevant form of Ficks' Second Law of Diffusion is given by [**4**] and [**5**]:

Hemisphere: $$\frac{\partial c}{\partial t} = D\frac{\partial^2 c}{\partial r^2} + \frac{2D}{r}\frac{\partial c}{\partial r} \qquad [4]$$

Microdisc: $$\frac{\partial c}{\partial t} = D\frac{\partial^2 c}{\partial r^2} + \frac{D}{r}\frac{\partial c}{\partial r} + D\frac{\partial^2 c}{\partial z^2} \qquad [5]$$

The co – ordinate systems are shown in **Figure 1**, c is the concentration of electro – active species (*i.e.* [*Ox*] or [*Red*]) and D is the relevant diffusion coefficient.

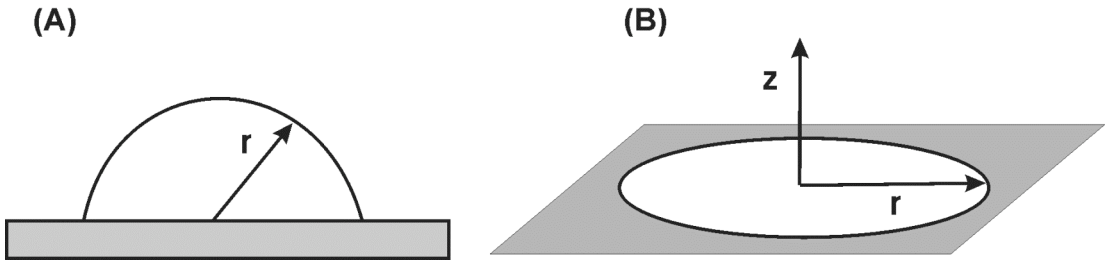


Figure 1

Schematic representation of the coordinate systems for (A) a hemisphere and (B) a disk.

The equations given in [**4**] and [**5**] can be solved subject to the following boundary conditions:

Hemisphere:

$$r \to \infty \quad [Ox] \to [Ox]_{bulk}$$
$$[Red] \to 0$$

$$r = r_e \quad D_{ox}\frac{\partial [Ox]}{\partial r} = k_c[Ox] - k_a[Red] \qquad [6]$$

Disc:

$$z \to \infty, \text{ all } r \quad [Ox] \to [Ox]_{bulk}$$
$$[Red] \to 0$$

$$z=0,\ r > r_e \quad \frac{\partial [Ox]}{\partial z} = \frac{\partial [Red]}{\partial z} = 0 \qquad [7]$$

$$z=0,\ r \le r_e \quad D_{ox}\frac{\partial [Ox]}{\partial z} = k_c[Ox] - k_a[\mathrm{Re}\,d]$$

We further assume that the diffusion coefficients of *Ox* and *Red* are identical such that $D_{ox} = D_{\mathrm{Red}} = D$. Note the assumption that there is sufficient supporting electrolyte to suppress migration effects is unlikely to be valid for particles of size less than ten nanometres since the double layer and diffusion layer will then be comparable in size. However, for the nanoparticles considered, this assumption is likely to be valid.

It is known that the steady – state fluxes at the two electrode types are given by [**8**] and [**9**]:

$$\text{Hemisphere}: \quad j_{ss}^{h} / mol\ cm^{-2}s^{-1} = D\frac{[Ox]_{bulk}}{r_e} \qquad [\mathbf{8}]$$

$$\text{Disc}: \quad j_{ss}^{d} / molcm^{-2}s^{-1} = \frac{2}{\pi} D\frac{[Ox]_{bulk}}{\sqrt{r_e^{\,2} - r^2}} \qquad [\mathbf{9}]$$

The flux is uniform over the hemisphere but not over the disc surface. The corresponding steady – state currents for a reduction are given according to [**10**] and [**11**].

$$\text{Hemisphere}: \quad \mathrm{I}_{ss}^{h} / A = 2\pi r_e FD[Ox]_{bulk} \qquad [\mathbf{10}]$$

$$\text{Disc}: \quad I_{ss}^{d} / A = 4 r_e FD[Ox]_{bulk} \qquad [\mathbf{11}]$$

In the problem of interest, *viz* the linear sweep voltammetry of electrochemically quasi – reversible and irreversible processes, the potential is swept according to [**12**]:

$$E = E_{initial} - \nu t \qquad [12]$$

The resulting voltammograms can be presented in dimensionless form of $\tilde{I}$ *vs.* $\tilde{\Theta}$, where $\tilde{\Theta} = \Theta - \Theta_f$. The dimensionless current is shown in [**13**]:

$$\tilde{I}^m = \frac{I^m}{I_{ss}^m} \qquad [13]$$

such that $m = h$ *or* d and I^m is the current, $\tilde{I}^m$ is the dimensionless current of the hemisphere ($m = h$) or micro – disc ($m = d$).

The resulting voltammograms are one of two types. For sufficiently small electrodes and slow scan rates, then 'steady – state' voltammograms are observed in which the current increases monotonically as the potential is swept until attaining a steady – state limiting current, I_{ss}^m. Otherwise, for larger electrodes and faster scan rates, a peaked current-voltage trace is observed. In the former case, the voltammogram is partially characterized by the dimensionless half – wave potential ($\Theta_{1/2} - \Theta_f$) corresponding to the current as given in [**14**]:

$$I^m = \frac{1}{2} I_{ss}^m \qquad [14]$$

In the latter case, the dimensionless potential ($\Theta_p - \Theta_f$) corresponds to the peak current that partly characterizes the voltammogram and this is the potential corresponding to the condition:

$$\frac{\partial I^m}{d\Theta} = 0 \qquad [15]$$

Dimensional analysis shows that:

$$\Theta_{1/2} - \Theta_f = f\ (K,\ \sigma) \qquad [16]$$

and

$$\Theta_p - \Theta_f = g\ (K,\ \sigma) \qquad [17]$$

As shown above, *f* and *g* are functions and the parameters *K* and σ are a dimensionless rate constant

$$K^0 = \frac{k^0 r_e}{D} \qquad [18]$$

and a dimensionless scan rate

$$\sigma = \left[\frac{F\upsilon}{RT}\right]\frac{r_e^2}{D} \qquad [19]$$

Simulations were carried out using DIGISIM™[1] in the case of the hemispherical electrode and using the approach described here for the case of the micro – disc electrode. In the former case quantitative agreement with the work of Diao and Zhang[2] was observed, although the latter chose to present their results using different normalized variables. Specifically they use the parameters Ψ and Λ where $\Psi = (K^2/\sigma)^{1/2}$ and $\Lambda = K$.

Figure 2 shows the working surfaces for $\Theta_{1/2} - \Theta_f$ for both hemisphere and disc electrodes as a function of K and σ.

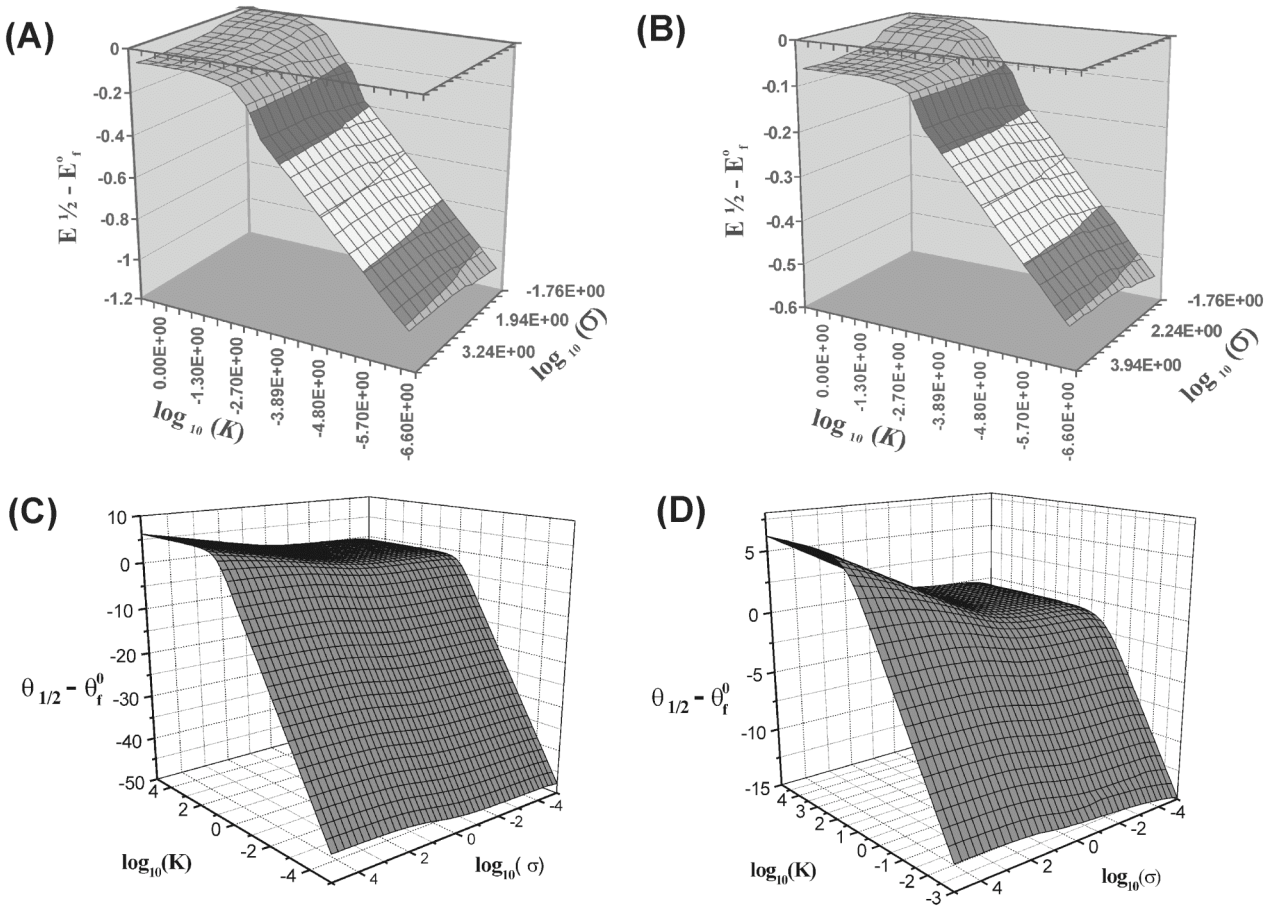


Figure 2

Three – dimensional working surfaces for $\Theta_{1/2}$- Θ_f as a function of K and σ for an isolated hemisphere: (A) α = 0.25, (B) α = 0.5. For an isolated disk: (C) α = 0.25, (D) α = 0.5.

Figure 3 analogously shows $\Theta_p - \Theta_f$ against *K* and σ. The working surfaces contain the information required to explore how $E_{1/2} - E_f^o$ or $E_p - E_f^o$ vary with the hemisphere or micro – disc radius, r_e.

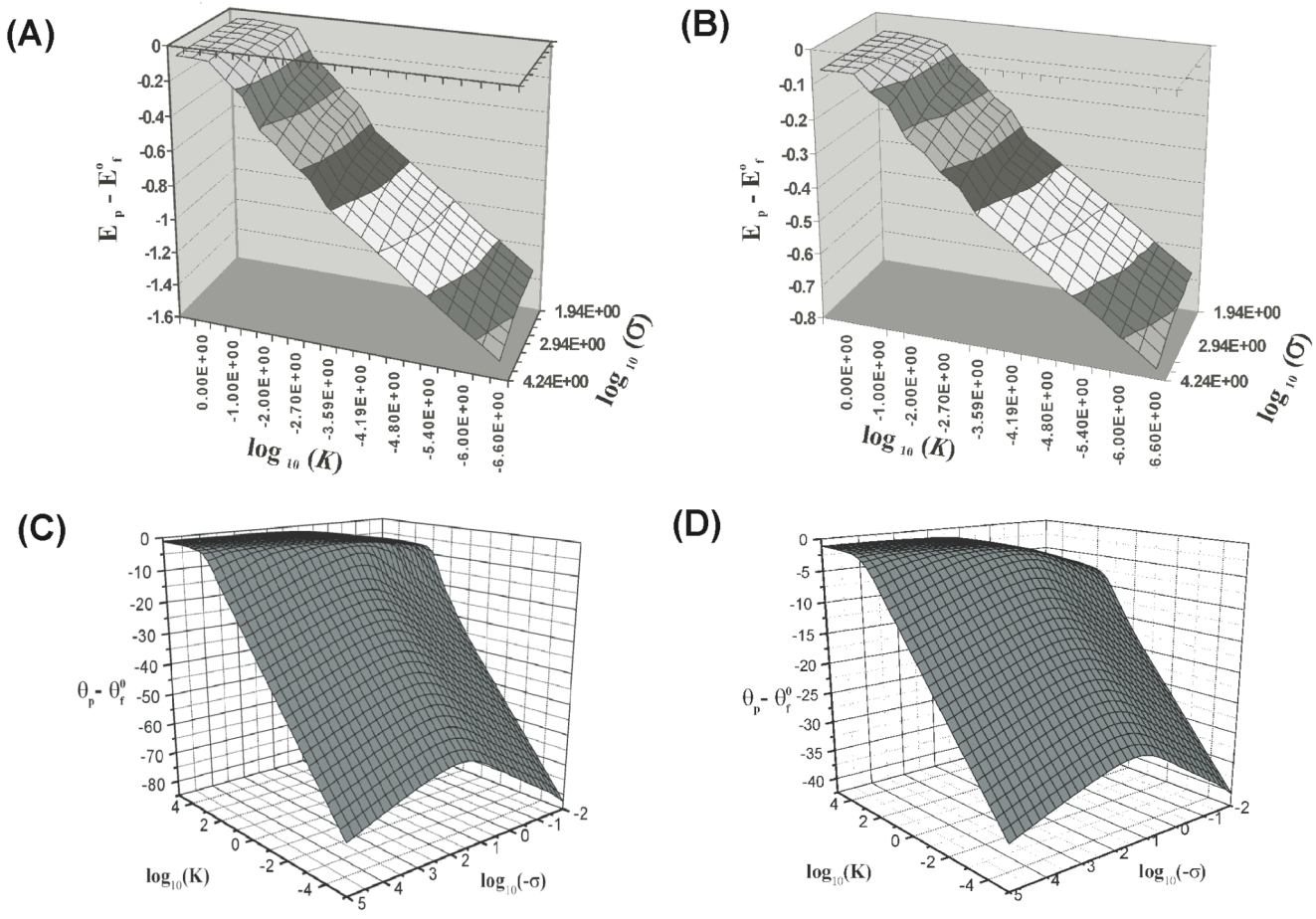


Figure 3

Three – dimensional working surfaces for $\Theta_p - \Theta_f$ *as a function of K and σ for an isolated hemisphere: (A) α = 0.25, (B) α = 0. 5 and for an isolated disc: (C) α = 0.25, (D) α = 0.5.*

In particular since,

$$dE_{½} = \frac{dE_{½}}{dK} dK + \frac{dE_{½}}{d\sigma} d\sigma \qquad [\mathbf{20}]$$

it follows that

$$\frac{\partial E_{½}}{\partial \ln r} = \frac{\partial E_{½}}{\partial \ln K} + \frac{2\partial E_{½}}{\partial \ln \sigma} \quad [21]$$

and similarly

$$\frac{\partial \mathrm{E}_{p}}{\partial \mathrm{lnr}} = \frac{\partial E_{p}}{\partial \ln K} + \frac{2\partial E_{p}}{\partial \ln \sigma} \quad [22]$$

In the 'nanoparticle limit', where $r_e \rightarrow 0$, inspection of **Figures 2** and **3** show that:

$$\frac{\partial E_{p}}{\partial \ln \sigma} = \frac{\partial E_{½}}{\partial \ln \sigma} = 0 \quad [23]$$

and

$$\frac{\partial E_{p}}{\partial \ln K} = \frac{\partial E_{½}}{\partial \ln \sigma} = \frac{RT}{\alpha F} \quad [24]$$

so that

$$\frac{\partial E_{p}}{\partial \ln r} = \frac{\partial E_{½}}{\partial \ln r} = \frac{RT}{\alpha F} \quad [25]$$

for both systems.

1.2 Arrays of Disc Shaped Nanoparticles

The results obtained in the previous section related to isolated hemispheres or micro – discs. Experimentally, an electrode surface is likely to be created by modifying an otherwise inactive surface with an array of nanoparticles. Such fabrication of nanoparticle arrays will generate random distributions of nanoparticles on the electrode surface. It is necessary to consider where particles are close enough together such that their diffusion layers will overlap with those of neighbouring particles. In such cases the conclusions drawn for isolated particles must be adapted, as the voltammetry will become sensitive to the degree of surface coverage (θ) of the electrode surface with nanoparticles.

$$\theta = N\frac{\pi r_e^{\,2}}{A} \qquad [26]$$

A is the substrate area, N is the number of particles and r_e is the nanoparticle radius.

Figures 4 and **5** illustrate the regular and random distribution of particles, respectively.

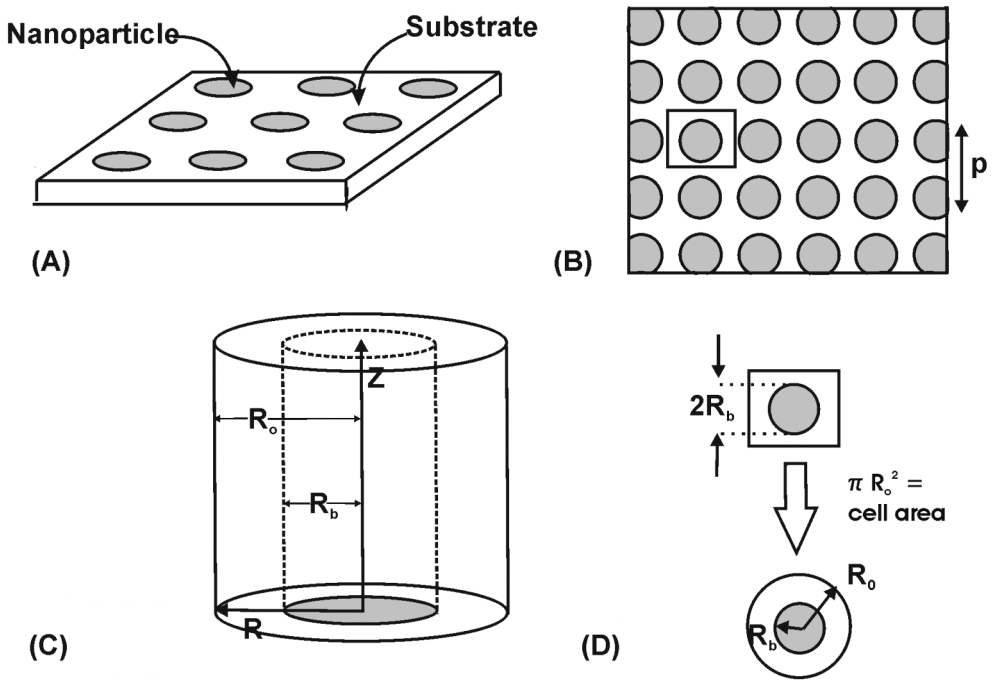


Figure 4

Schematic representation of the diffusion domain approximation as applied to a regular array of disks.

In the case of a square array of particles, the centre – to – centre distance between adjacent particles is described as the quantityl p. In order to solve the diffusion problem to the disc surface, we employ the diffusion domain approximation and consider a cylindrical domain of radius, r_0, such that:

$$r_0 = 0.564\,p \qquad [27]$$

A random distribution of particles is described by **Figure 5**. The array is considered as a number of Voronoi cells formed from the bi – sectors of each particle and its nearest neighbours. The irregular Voronoi cell is modelled by approximating it as a cylinder

with the same base area as original cell. The three – dimensional model can be simplified to single plane (*R* and *Z*) co – ordinates (**Figure 5 (C)**).

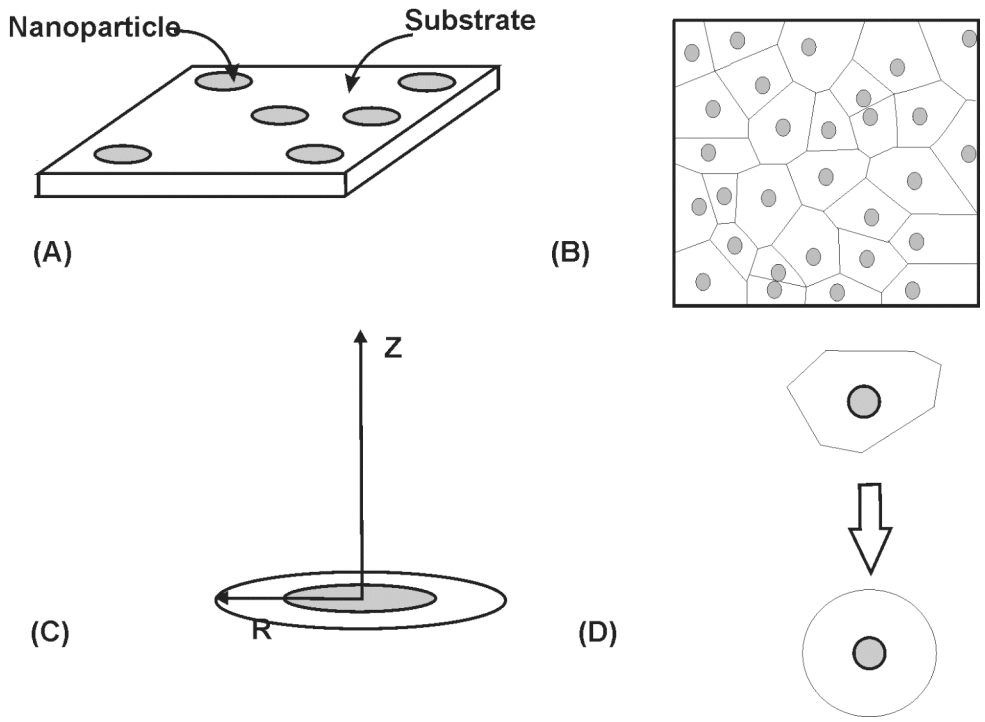


Figure 5

Schematic representation of the diffusion domain approximation as applied to a regular array of disks.

An average diffusion domain radius (r_0) is applied as calculation across the entire range can be very computer time intensive.

We can solve Fick's 2nd Law with the diffusion domain using a no flux boundary condition at the sides of the domain (**Equation 28**), supplementing the boundary conditions already specified for the isolated case.

$$\frac{\partial c}{\partial r} = 0 \text{ at } r = r_0 \text{ for all } z \qquad [28]$$

Figure 6 displays the effects of decreasing the disc separation. As disc separation decreases, the diffusion zones overlap to a greater extent leading to a smaller flux.

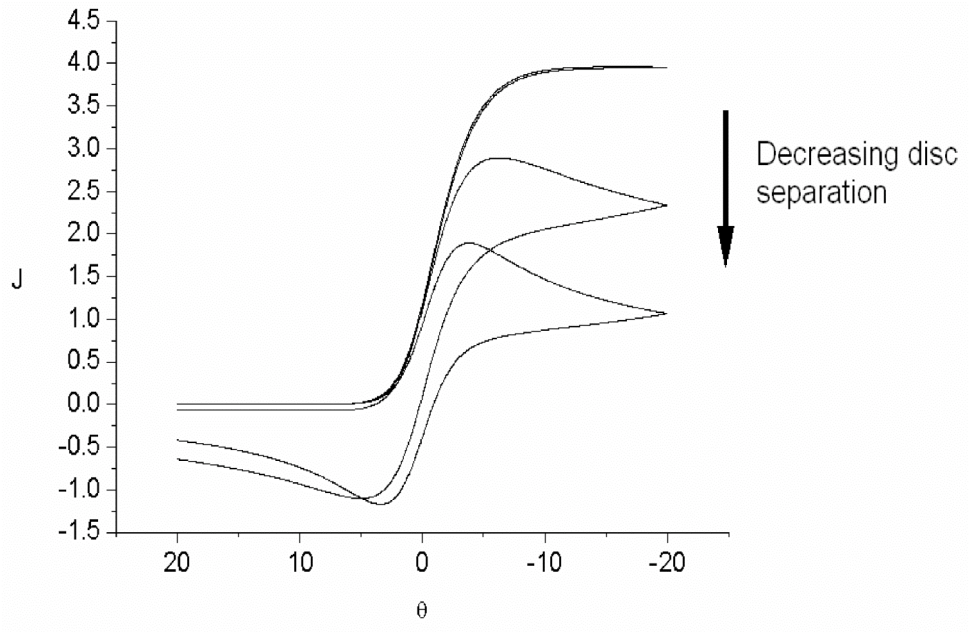


Figure 6

Simulated voltammograms at various values of electrode separations for a cubic array of micro – discs (α = 0.5, σ = -0.001, K^0 = 1).

The theory outlined in this section is used below to account for coverage effects observed in the experimental voltammetry.

1.3 Simulation of Isolated Microelectrodes

We consider a simple one – electron reduction:

$$A + e^- \underset{k_a}{\overset{k_c}{\rightleftharpoons}} B \qquad [29]$$

The numerical simulations are based on a circular disc electrode inlaid on an insulating support as shown in **Figure 4** and **5**. When solving numerical problems it is standard practice to express equations only in terms of dimensionless parameters such that the solutions are more general owing to the removal of (known) scaling factors. The dimensionless parameters used in this paper are defined in **Table 1.1**. The problem amounts to solving Fick's second law:

$$\frac{\partial a}{\partial \tau} = \frac{\partial^2 a}{\partial R^2} + \frac{1}{R}\frac{\partial a}{\partial R} + \frac{\partial^2 a}{\partial Z^2} \qquad [30]$$

In order to account for the symmetry of the situation, cylindrical co – ordinates are used. This equation is solved subject to several boundary conditions. The behaviour of the system at the interface between electrode and solution, is quantified by the Butler – Volmer equation:

$$j = K^0 a_0 \exp\left[-\alpha\theta\right] - K^0 b_0 \exp\left[(1-\alpha)\theta\right] \qquad [31]$$

At very large distances from the electrode surface $a = 1$ and $b = 0$. The values of Z_{max} and R_{max} are chosen so as to contain the entire diffusion layer. The expressions used here are:

i

$$Z_{\max} = 6\sqrt{\tau_{total}} \qquad [32]$$

$$R_{\max} = 1 + 6\sqrt{\tau_{total}} \qquad [33]$$

In addition, there is assumed to be zero flux through the symmetry axis or through the insulating surface surrounding the electrode. The boundary conditions are summarised below:

$R = 0$	$\frac{\partial a}{\partial R} = 0$	$\frac{\partial b}{\partial R} = 0$	
$R = R_{\max}$	$\frac{\partial a}{\partial R} = 0$	$\frac{\partial b}{\partial R} = 0$	
$Z = Z_{\max}$	$\frac{\partial a}{\partial Z} = 0$	$\frac{\partial b}{\partial Z} = 0$	[34]
$Z = 0 \quad R \le 1$	Equation 3		
$Z = 0 \quad R > 1$	$\frac{\partial a}{\partial Z} = 0$	$\frac{\partial b}{\partial Z} = 0$	

The problem is solved numerically using the Alternating Direct Implicit method (ADI)[3, 4]. This requires discretization in both space and time. Simulation efficiency is increased by using an expanding spatial mesh. The mesh is chosen so as to leave a high density at the singularities, *i.e.* the edge of the electrode and the symmetry axis. An exponentially expanding mesh is used. The nature of the expansion is identical to that used by Gavaghan[4].

Once the simulation is run across a 2D spatial segment the flux over the entire electrode is calculated:

$$j_{total} = 2\pi \int_0^1 j_{segment} R \partial R \qquad [35]$$

This integral is solved numerically using the trapezium rule[5].

1.4 Simulation of Microelectrode Arrays

The simulation procedure for a microelectrode in an array is identical to that described above except the value of R_{max} must be chosen so as to characterize the separation of the electrodes of the array. Electrode separation is calculated assuming a regular square grid. Each microelectrode can be considered as being at the centre of a unit cell as shown in the **Figure 4(B)**. Each cell is diffusionally independent. The square base of each cell is taken to be equivalent to a circle of equal area. This is called the diffusion domain approximation and is illustrated in **Figures 4(C)** and **4(D)**. The current over the entire array is calculated by summing together the contribution from each microelectrode.

Dimensionless Parameter	Definition
R	r / r_e
Z	z / r_e
τ	$D_A t / r_e^2$
a	$[A]/[A]_{bulk}$
b	$[B]/[A]_{bulk}$
a_0	$[A]_0/[A]_{bulk}$
b_0	$[B]_0/[A]_{bulk}$
J	$i / (nF[A]_{bulk}D_A r_e)$
K^0	$k^0 r_e / D_A$
θ	$(F/RT)(E - E^0_f)$
σ	$(F/RT)(v)(r^2/D)$

Table 1.1

List of the dimensionless parameters used in simulation methods described above.

Dimensional Parameter	Definition
r_e	*Electrode radius (m)*
F	*Faraday constant ($Cmol^{-1}$)*
R	*Universal gas constant ($J\,K^{-1}mol^{-1}$)*
T	*Temperature (K)*
A	*Electrode area (m^2)*
$[A]_0$	*Concentration of species A at the electrode surface ($mol\ m^{-3}$)*
$[B]_0$	*Concentration of species B at the electrode surface ($mol\ m^{-3}$)*
$[A]_{bulk}$	*Concentration of species A in bulk solution ($mol\ m^{-3}$)*
$[B]_{bulk}$	*Concentration of species B in bulk solution ($mol\ m^{-3}$)*
α	*Transfer coefficient (unitless)*
k^0	*Electrochemical rate constant ($m\ s^{-1}$)*
E	*Applied potential (V)*
E^0_f	*Formal reduction potential (V)*
D_A	*Diffusion coefficient of species A (m^2s^{-1})*
D_B	*Diffusion coefficient of species B (m^2s^{-1})*
j	*Flux across the electrode ($mol\ m^{-2}\ s^{-1}$)*
i	*Current (A)*
m	*i/i_{lim} on a steady-state voltammogram (unitless)*
υ	*Scan rate ($V\ s^{-1}$)*

Table 1.2

List of the dimensional parameter used in the simulation methods described above.

1.5 Computation

All programs were written in C++ and compiled using a Borland compiler. The simulations were run on a desktop PC with a 3.4 GHz Pentium processor and 2 GB of RAM. Approximately 2 minutes of CPU time were required to simulate a single voltammogram. The integrity of the source code and efficiency of the program were investigated by comparing simulations for an isolated disc at steady state with the Saito equation[6]. The program was converged to yield better than 0.1% accuracy.

Appendix 1: References

1. M. Rudolph, D. P. Reddy and S. W. Feldberg, *Analytical Chemistry*, 1994, **66**, 589A-600A.

2. G. Diao and Z. Zhang, *Journal of Electroanalytical Chemistry*, 1996, **410**, 155-162.

3. J. Heinze, *Journal of Electroanalytical Chemistry*, 1981, **124**, 73-86.

4. D. J. Gavaghan, *Journal of Electroanalytical Chemistry*, 1998, **456**, 25-35.

5. G. Stephenson, *Mathematical Methods for Science Students*, Pearson, Prentice Hall, Harlow, England, 1973.

6. Y. Saito, *Review of Polarography*, 1968, **15**, 177.